

ADVANCES IN PHYSICS

**Molecular Quantum Materials:
Electronic Phases and Charge Dynamics
in Two-Dimensional Organic Solids**

Martin Dressel^a and Silvia Tomić^b

^a*1. Physikalisches Institut, Universität Stuttgart, Stuttgart, Germany;*

^b*Institut za fiziku, Zagreb, Croatia*

(Compiled November 25, 2021)

This review provides a perspective on recent developments and their implications for our understanding of novel quantum phenomena in the physics of two-dimensional organic solids. We concentrate on the phase transitions and collective response in the charge sector, the importance of coupling of electronic and lattice degrees of freedom and stress an intriguing role of disorder. After a brief introduction to low-dimensional organic solids and their crystallographic structures, we focus on the dimensionality and interactions and emergent quantum phenomena. Important topics of current research in organic matter with sizeable electronic correlations are Mott metal-insulator phase transitions, charge order and ferroelectricity. Highly frustrated two-dimensional systems are established model compounds for studying the quantum spin liquid state and the competition with magnetic long-range order. There are also unique examples of quantum disordered state of magnetic and electric dipoles. Representative experimental results are complemented by current theoretical approaches.

Keywords: Molecular materials; organic conductors and superconductors; two-dimensional electron system, electronic correlations, phase transitions

Contents

1	Introduction	3
2	Structural Aspects	4
2.1	BEDT-TTF salts	4
2.1.1	α -(BEDT-TTF) ₂ I ₃	6
2.1.2	β'' -(BEDT-TTF) ₂ SF ₅ RSO ₃	7
2.1.3	θ -(BEDT-TTF) ₂ RbZn(SCN) ₄	8
2.1.4	κ -(BEDT-TTF) ₂ X salts	9
2.2	Other molecular compounds	11
2.2.1	β' -EtMe ₃ Sb[Pd(dmit) ₂] ₂	11
2.2.2	κ -H ₃ (Cat-EDT-TTF) ₂	12
3	Charge Order and Ferroelectricity	13
3.1	Phase diagrams of quarter-filled systems	16
3.2	Ferroelectricity driven by charge order in weakly dimerized solids . . .	18
3.2.1	Semi-metallic state at high temperatures	19
3.2.2	Metal-insulator transition into the charge-ordered state	21

3.2.3	Character of the metal-insulator phase transition	23
3.2.4	Origin of the charge-order phase transition	24
3.2.5	Charge-ordered states with no ferroelectricity	26
3.3	States nearby charge order	27
3.3.1	Charge glass	27
3.3.2	Dirac electrons	31
3.4	Electrodynamics of weakly dimerized ferroelectrics	36
3.4.1	Polarization switching	36
3.4.2	Dielectric response	37
3.4.3	Domain walls	38
3.4.4	Non-linear effects and ultra-fast response	40
3.5	Ferroelectricity driven by charge order in dimerized solids	43
4	Mott Metal-Insulator Phase Transition	47
4.1	Antiferromagnetic Mott insulator	49
4.1.1	Mott quantum criticality	49
4.1.2	Coexistence regime	52
4.2	Frustrated Mott insulator	54
4.3	Coherent transport	59
4.3.1	Fermi-liquid behavior	60
4.3.2	ω - T scaling	63
4.3.3	Bad-metal regime and Ioffe-Regel-Mott limit	64
4.4	Effects of disorder on the Mott transition	66
5	Quantum Spin Liquid versus Magnetic Order	70
5.1	Properties	71
5.2	Gapless quantum spin liquid?	72
5.3	6 K-anomaly	75
5.4	Valence-bond solid	77
5.5	Randomness	80
6	Coupling of Quantum Electric and Magnetic Dipoles	82
6.1	Quantum electric dipoles	83
6.2	Ferroelectric signatures in quantum spin liquid and afm states	86
6.3	Quantum electric dipoles in a quantum spin liquid	88
6.4	Quantum electric dipoles with glassy signatures	91
6.4.1	Quantum electric dipole lattice	91
6.4.2	Glassy behavior	91
6.4.3	Coupling to magnetic degrees of freedom	92
7	Summary and Prospects	94
7.1	Electronic ferroelectricity	95
7.2	Dirac electrons	96
7.3	Mott metal-insulator phase transition	97
7.4	Quantum spin liquid versus magnetic order	99
7.5	Quantum states of electric and magnetic dipoles	101
7.6	Outlook	102
8	Acknowledgements	103

1. Introduction

When molecular solids and in particular organic conductors started flourishing in the 1970s and 1980s, the spotlight was directed on their strong electronic anisotropy down to one dimension and subsequently the superconducting phases in the TMTSF and BEDT-TTF salts [1–24]. While these are still thrilling topics with many unresolved questions, for the last ten years or so the focus of interest shifted towards novel electronic properties that are related to the strong electron-electron correlations present in these compounds. By now, organic conductors are recognized as versatile molecular quantum materials, which exhibit numerous exciting and unprecedented features. In comparison to inorganic compounds, molecular conductors are cleaner and easier to tune by chemical and physical means; hence they are well established as model compounds for the investigation of several fundamental problems. Since the field has been steadily covered by monographies and compilations [20,25–35], we restrain ourselves from presenting a comprehensive and balanced overview on the entire field. Instead we select the outstanding themes and issues: those which – from our point of view – are of paramount importance to and have the largest impact on condensed matter physics in general.

In prototypical strongly correlated materials, such as heavy fermions or transition metal compounds, f - and d -electrons with their rather narrow bands govern the electronic properties. Often the Fermi surface is very complex and multiple bands compete. Molecular materials, on the other side, are characterized by delocalized π -electrons that are distributed over the extended organic molecule. If the almost planar molecules are stacked or assembled face-to-face in certain patterns constituting bulk crystals, the protruding orbitals of adjacent molecules overlap slightly, forming narrow electronic bands. Although the unit cell of molecular crystals contains many atoms, it consists of a small number of molecules. In most cases, only one electronic band cuts the Fermi energy, leading to rather simple Fermi surfaces [36]. Typical bands consist only of lowest unoccupied molecular orbital (LUMO) and highest occupied molecular orbital (HOMO), which often are isolated from other bands. Therefore, the effective Coulomb interaction between electrons on the HOMO and LUMO orbitals is poorly screened by other bands. These two factors (small bandwidth and ineffective screening) make the molecular conductors mostly strongly correlated electron systems.

Since heavy fermions are intermetallic compounds with delocalized electrons, strong electronic correlations are adequately captured by simple renormalization of the Fermi-liquid parameters [37]. Transition metal compounds are most successfully described by the Hubbard model, *i.e.* a lattice fermion model including onsite and intersite interaction as required. Here strong electronic repulsion causes a metal insulator transition that takes place either by diverging mass or – more commonly – by vanishing carrier number [38]. In many transition metal oxides, hybridization with the oxygen p orbitals takes place and the character of low-energy charge excitations changes; these Mott insulators are actually charge transfer insulators. In this regard organics represent the best examples of Mott-Hubbard insulators with the lowest energy excitation between the lower and upper Hubbard bands. Here the quasi-particle mass increases significantly as the Mott transition is approached.

By now it became clear that molecular conductors are an original class of strongly correlated electron systems. They possess several features that makes them a diverse playground for the study of quantum many body physics and the properties of quantum materials. Organic solids are available as extremely pure single crystals of millimeter size and stable under ambient conditions. The energy scales fall in an easily

accessible range, as far as temperature, magnetic field and pressure is concerned: superconductivity occurs around 10 K; but can be destroyed by applying less than 20 T; the typical bandwidth is less than 1 eV; due to the large compressibility of organic compounds, pressure of less than 1 GPa already leads to significant alterations of the physical properties. Due to different organic molecules that can be combined with a number of counterions and the numerous stacking pattern possible in two-dimensions, a variety of prototypical behaviors of correlated electron systems can be achieved and easily modified by chemical means.

But there are some caveats that have to be mentioned: Several of the methods, which have been advanced over the last decades to investigate the electronic and magnetic properties of inorganic materials cannot easily be applied to molecular compounds. Limited crystal size and the presence of hydrogen essentially prevent neutron scattering experiments, the most powerful tool for exploration of magnetic properties and dispersion. Furthermore, scanning tunneling methods as well as photoemission spectroscopy are challenging due to the surface properties and ionic structure. Nevertheless, the study of organic crystals has significantly profited from the enormous progress in instrumentation seen over the last years and spectacular achievements are reported on a regular basis.

We start in Chapter 3 with a survey given on charge order and ferroelectricity in two-dimensional molecular solids, in particular covering the experimental achievements and theoretical insight gained over the last decade or so. By now, dimerized BEDT-TTF salts are widely recognized as the prime examples for studying the metal-insulator transition driven by onsite Coulomb repulsion. Hence in Chapter 4 we cover various aspects of the Mott transition, starting from the scaling behavior around the critical endpoint and followed by the spatial coexistence of metallic and insulating regions at the first-order Mott transition. In the following Chapter we consider the highly-frustrated magnetic state leading to the quantum spin liquid ground state. In Chapter 6 we turn our attention to charge degrees of freedom and explore their interplay with magnetic degrees of freedom and how varying dimerization and geometrical frustration results in the particular ordered and liquid ground states. The Chapters should be self-contained with numerous cross-references that allow the reader to select certain topics of particular interest.

2. Structural Aspects

Before proceeding to the detailed discussion of the electronic properties of molecular quantum materials, in this Chapter we want to summarize briefly some structural aspects of those compounds most prominent in this regards.

2.1. *BEDT-TTF salts*

In succession of the Fabre salts based on TMTTF (tetramethyl-tetrathiafulvalene) and Bechgaard salts based on TMTSF (tetramethyl-tetraselenafulvalene) molecule, the BEDT-TTF molecules become the widely used building block for the two-dimensional organic superconductors and molecular quantum materials. Here BEDT-TTF or sometimes simply ET, stands for bis(ethylenedithio)tetrathiafulvalene ($C_{10}H_8S_8$) and was first synthesized by Saito *et al.* in 1982 [39]; as depicted in Figure 1, the core is still the TTF-unit, but now extended by two sulfur and two ethylene groups on each side. Owing to the extended size, the molecule is not completely flat anymore but the two terminal

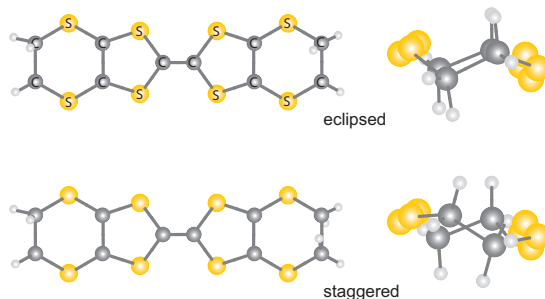


Figure 1. Molecular structure of BEDT-TTF or ET, which stands for bis(ethylenedithio)tetrathiafulvalene. The eight sulfur atoms are indicated by yellow, the carbon atoms by dark grey balls, the hydrogens are depicted by light gray. The molecule is not absolutely flat, but the endgroups are tilted either in eclipsed or staggered fashion, as indicated.

groups are slightly twisted. This can be done in the same direction, called eclipsed, or opposite directions (staggered); opening the possibility of intrinsic disorder being present. In the case of the organic superconductor κ -(BEDT-TTF) $_2$ Cu[N(CN) $_2$]Br, for instance, the crystals exhibit ordering of the ethylene endgroups upon cooling: While at room temperature 70% of the molecules are in the eclipsed configuration, it becomes 29% at $T = 100$ K [40].

As pointed out by Girlando [41], the symmetry of the BEDT-TTF molecule is often assumed D_{2h} , implying a completely planar molecule [42–44], in order to reduce the 72 independent vibrational degrees of freedom when calculating the molecular vibrations. The actual symmetry, however, is D_2 in the case of a staggered molecule, and C_{2h} in the case of eclipsed. As a matter of fact, the neutral molecule acquires a boat conformation with C_2 symmetry [45,46], but this aspect is commonly neglected in the ionic crystal.

In order to vary the electronic orbitals, some of the sulfur atoms can be substituted. Replacing the four central S by Se, for instance, leads to BEDT-TSF or BETS, *i.e.* bis(ethylenedithio)tetraselenafulvalene. Alternatively, the substitution can be performed only on one side, resulting in the asymmetric BEDT-STF, *i.e.* bis(ethylenedithio)selenathiafulvalene. This will be utilized in several studies presented in Section 4.2.

Typically the compounds grow as (BEDT-TTF) $_2$ X, where X stands for a monovalent anion. The electronic charge of half a hole per BEDT-TTF molecule is distributed over the entire molecule, with the highest density around the central C=C, followed by the other two carbon double bonds. In most of the (BEDT-TTF) $_2$ X salts, the organic donor molecules are packed more-or-less upright in layers; they are held together by strong in-plane covalent bonds but weak out-of-plane van der Waals forces. The molecular layers alternate along the third direction with sheets of monovalent anions or polymeric networks. The interface between the donor and acceptor layers is determined by a hydrogen-bond network constituted by the terminal ethylene groups. Commonly, anions are considered to serve as spacer and as charge reservoir, but the role of donor-anion interaction in stabilization of diverse electronic phases has been emphasized [47].

Due to the larger number of orbitals and extended size compared to the TMTSF-molecule, multiple polymorphs can be found for most BEDT-TTF compounds, labeled by Greek letters [26,48–51]. Figure 2 displays some of the packing motives of relevance here. In the case of the α - β - and θ -phase, the organic molecules are arranged in stacks, while in κ -salts pairs of molecules so-called dimers are formed that are almost orthogonal. Within the stacks of the β -phase, neighboring molecules are slightly shifted with

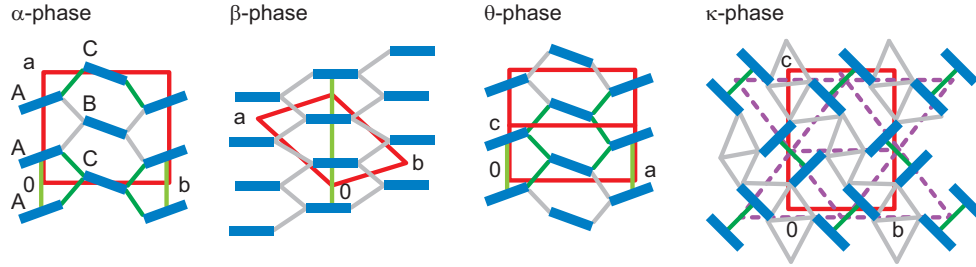


Figure 2. Schematic representation of some of the $(\text{BEDT-TTF})_2X$ packing motives by looking at the quasi-two-dimensional layer. The pattern labeled as α -, β -, θ - and κ -phase possesses a different degree of dimerization. Only the strongest inter-donor interactions are indicated. While in the α - β - and θ -polymorphs chains of BEDT-TTF molecules can be identified, the lattice of the κ -phases consists of pairs of molecules so-called dimers arranged almost perpendicular to each other. Here an effective triangular lattice of dimeric units can be identified as indicated by the dashed purple lines (suggested by [47]).

respect to each other; for the α - and θ -phase they are alternatively tilted. As indicated, neighboring stacks are coupled, resulting in two-dimensional, almost isotropic properties. The dimers of the κ -lattice compose an effective triangular lattice giving way to frustration, as we will see in Chapter 5.

2.1.1. α - $(\text{BEDT-TTF})_2\text{I}_3$

In the case of α - $(\text{BEDT-TTF})_2\text{I}_3$, the triclinic crystal structure (space group $P\bar{1}$) is an alternation of insulating I_3^- anion layers and conducting layers of donor molecules $\text{BEDT-TTF}^{0.5+}$, displayed in Figure 3(a) [52]. The BEDT-TTF molecules form a herringbone pattern and are organized in a triangular lattice with two types of stacks. At room temperature, stack I is weakly dimerized and composed of crystallographically equivalent molecules A and A' related by an inversion center, while the stack II is a uniform chain composed of distinct B and C molecules, shown in Figure 3(b). These two types of stacks are interconnected by many $\text{S}\cdots\text{S}$ short contacts that provide the electronic delocalization within the ab -layer. The I_3^- anions form two distinct chains, labeled by chain 1 and chain 2, illustrated in panel (c). Thus the unit cell contains four BEDT-TTF molecules. At high temperatures, the system is a semimetal with

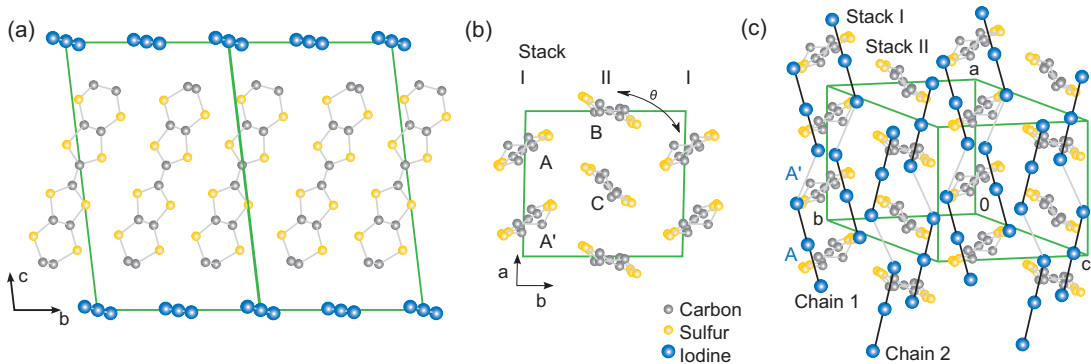


Figure 3. Crystal structure of α - $(\text{BEDT-TTF})_2\text{I}_3$. (a) The BEDT-TTF molecules are arranged in the ab -layers with the molecular axis not normal but slightly tilted to this layer. Sheets of I_3^- -anions separate these layers in c -direction. (b) View along the molecular axis reveals two distinct stacks. Stack I contains the BEDT-TTF molecules A and A', which are identical by symmetry. The molecules B and C in stack II are distinct to the rest. A dihedral angle between BEDT-TTF molecules in neighboring stacks is labeled by θ . (c) Axiometric view of α - $(\text{BEDT-TTF})_2\text{I}_3$ with the unit cell indicated in green. There are two arrangements of the I_3^- anions, labelled as chain 1 and chain 2.

small electron and hole pockets in the Fermi surface [48,53]. There is a slight charge disproportionation (among B and C molecules, while there is none among A and A') already at ambient condition that gets considerable when cooled below the charge-ordering phase transition temperature at $T_{CO} = 135$ K, as discussed in Section 3.2.

2.1.2. β'' -(BEDT-TTF) $_2$ SF $_5$ RSO $_3$

The β'' -(BEDT-TTF) $_2$ SF $_5$ RSO $_3$ compounds with different groups R are isostructural, crystallizing in the P1 triclinic system, with two formula units per unit cell [54,55]. The structure is characterized by layers of BEDT-TTF in the ab -crystal plane, separated by the all-organic anions, shown in Figure 4. Within the cation layer, the BEDT-TTF are arranged in tilted stacks, typical of the β'' -packing motif [49] with the strongest interaction along the crystallographic b -axis, *i.e.* perpendicular to the stacks. Along the stacking direction a , two BEDT-TTF molecules are related by inversion symmetry (A and A'; B and B'); and the two pairs in neighboring stacks, AA' and BB', are crystallographically independent. Figure 4(c) presents four different anions constituting systems that have been subject of intense investigations discussed in Section 3.2: β'' -

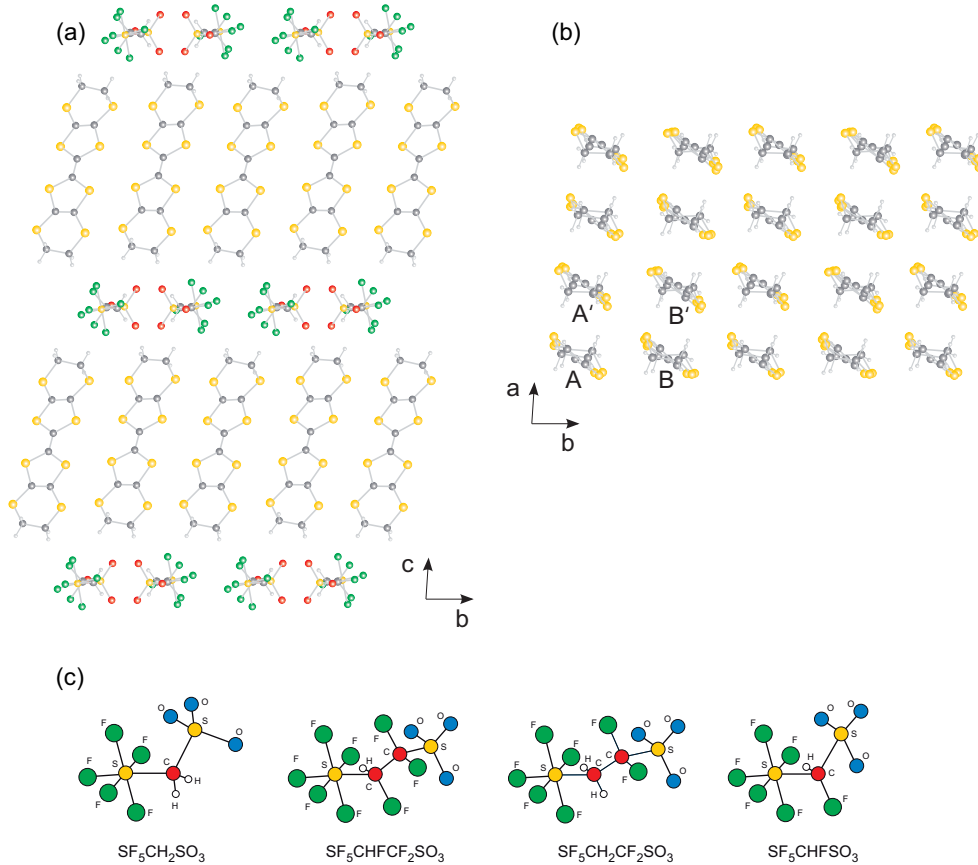


Figure 4. Crystal structure of β'' -(BEDT-TTF) $_2$ SF $_5$ RSO $_3$. (a) View onto the bc -plane illustrates how the BEDT-TTF molecules form layers, separated in c -direction by sheets of the all-organic anions. (b) Within the ab -plane, the BEDT-TTF molecules are arranged in two slightly distinct stacks along the a -direction with uniform distance. (c) The four anions SF $_5$ RSO $_3^-$ differ by the central entity: R equal CH $_2$, CHFCF $_2$, CH $_2$ CF $_2$ and CHF, respectively.

(BEDT-TTF) $_2$ SF $_5$ CH $_2$ SO $_3$ (denoted β'' -I) is a charge-ordered insulator, β'' -(BEDT-TTF) $_2$ SF $_5$ CHF CF_2 SO $_3$ (β'' -MI) undergoes a metal-insulator transition at 180 K, β'' -(BEDT-TTF) $_2$ SF $_5$ CH $_2$ CF $_2$ SO $_3$ (β'' -SC) is a superconductor at $T_c = 5$ K driven by charge fluctuations, and β'' -(BEDT-TTF) $_2$ SF $_5$ CHFSO $_3$ (β'' -M) remains metallic down to low temperatures. The phase diagram of Figure 13 summarizes the ground states of this family. At $T = 300$ K the crystal structure of β'' -I exhibits some degree of disorder in the terminal ethylene groups [54]. No disorder is observed in the structure of β'' -SC, which, however, has been collected at $T = 123$ K.

2.1.3. θ -(BEDT-TTF) $_2$ RbZn(SCN) $_4$

θ -(BEDT-TTF) $_2$ RbZn(SCN) $_4$ crystallizes in the higher symmetry orthorhombic structure (space group I222) with four BEDT-TTF $^{0.5+}$ molecules and two [RbZn(SCN) $_4$] $^-$ anions per unit cell, shown in Figure 5. All BEDT-TTF molecules are crystallographically equivalent and stack along the a -axis. Since the molecules are strongly tilted with respect to each other, there is a large orbital overlap between neighboring stacks leading to a two-dimensional conductivity in the ac -plane [50]; in b -direction the layers are separated by the anions as shown in panel(b). This two-dimensional RbZn(SCN) $_4^-$ network is built from two (SCN) $_2$ chains, connected by a Rb $^+$, in which Zn $^{2+}$ is tetrahedrally coordinated to the SCN $^-$ groups. At high temperatures the system is characterized by degenerated bands and a two-dimensional closed Fermi surface with three-quarter filling, resulting in a metallic conductivity behavior within the molecular planes [56]. Similar to α -(BEDT-TTF) $_2$ I $_3$, charge disproportionation develops in the metallic state and when cooled slowly a phase transition into the long-range charge-order state sets in at $T_{CO} = 190$ K, as discussed in Section 3.2. Conversely, rapid cooling inhibits order and a charge glass state is formed, as discussed in Section 3.3.1.

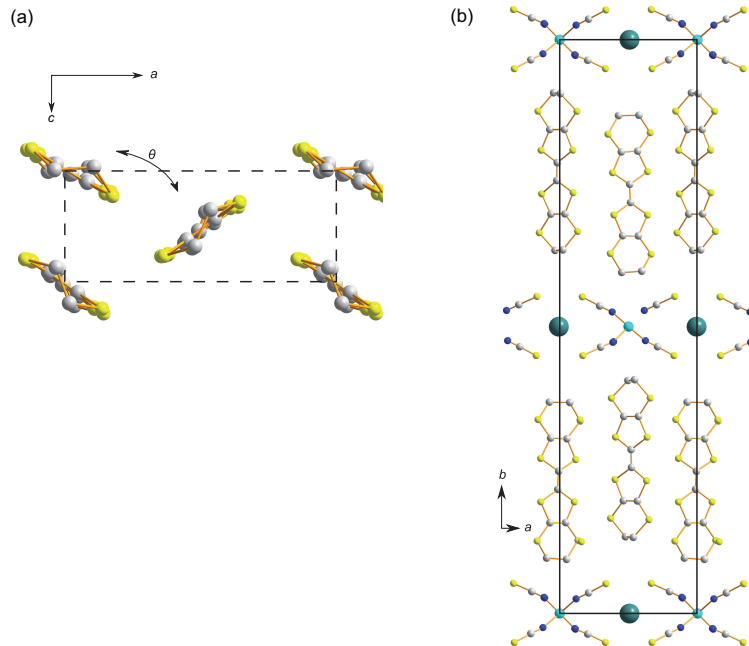


Figure 5. Crystallographic structure of θ -(BEDT-TTF) $_2$ RbZn(SCN) $_4$. (a) View of BEDT-TTF molecules from one out of two cation layers in the ac -plane showing their triangular arrangement. They are tilted by a dihedral angle θ with respect to each other. (b) Unit cell of θ -(BEDT-TTF) $_2$ RbZn(SCN) $_4$ containing four BEDT-TTF molecules and two RbZn(SCN) $_4^-$ entities.

2.1.4. κ -(BEDT-TTF)₂X salts

The κ -(BEDT-TTF)₂X salts are characterized by the BEDT-TTF dimers, which are almost orthogonal to each other. Due to the strong dimerization, the κ -salts are prime examples of half filled Mott systems. The intradimer coupling t_d is a fair estimate of the on-site Coulomb repulsion U [57,58]. Advancing previous calculations [49,59–67], Scriven and Powell computed the effective Coulomb interaction within the BEDT-TTF dimers by density functional theory (DFT) [68].

As usual, the organic molecules are arranged in layers separated by the anion sheets. In the case of κ -(BEDT-TTF)₂Cu[N(CN)₂]Cl and κ -(BEDT-TTF)₂Cu[N(CN)₂]Br the BEDT-TTF dimers are tilted in alternating directions [Figure 6(a)]. In each of two organic layers, related by mirror symmetry, all four BEDT-TTF molecules are equivalent. Hence, κ -(BEDT-TTF)₂Cu[N(CN)₂]Cl crystallizes in the space group Pnma. The BEDT-TTF layers are separated by polymeric Cu[N(CN)₂]Cl[−] anions along the

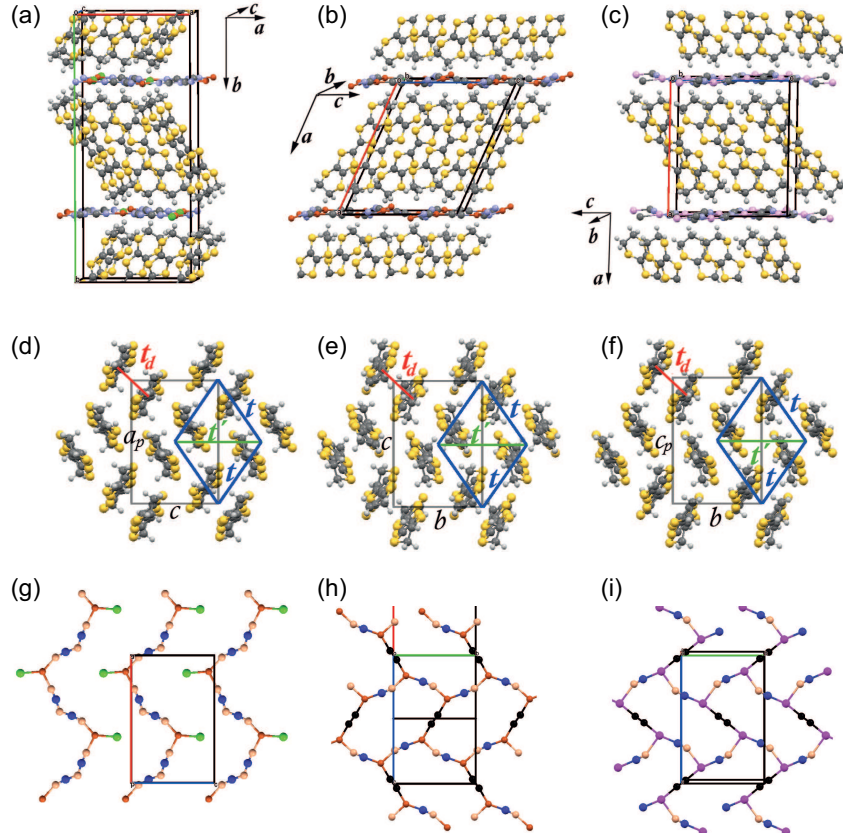


Figure 6. Crystal structure of three κ -phase salts: (a,d,g) κ -(BEDT-TTF)₂Cu[N(CN)₂]Cl, (b,e,h) κ -(BEDT-TTF)₂Cu₂(CN)₃ and (c,f,i) κ -(BEDT-TTF)₂Ag₂(CN)₃. The lines mark the unit cell. In panels (d,g) for clarity reasons only one out of two cation and anion layers constituting the unit cell is shown. (d,e,f) View of BEDT-TTF dimers arranged in anisotropic triangles in the two-dimensional planes. Carbon, sulfur and hydrogen atoms of the BEDT-TTF molecule are colored in dark gray, yellow and light gray, respectively. The interdimer transfer integrals are denoted by t and t' , and the intradimer transfer integral by t_d . The ratio t'/t measures the degree of frustration. (g,h,i) View of the anion network in the two-dimensional planes. Chlorine, copper, silver, carbon and nitrogen are colored in green, red, pink, blue and orange, respectively. Ordered cyanide (CN)[−] groups exist in all three systems, while CN[−] groups (labeled by black) located at inversion centers are present only in κ -(BEDT-TTF)₂Cu₂(CN)₃ and κ -(BEDT-TTF)₂Ag₂(CN)₃ and are source of intrinsic disorder. Note that for κ -(BEDT-TTF)₂Cu[N(CN)₂]Cl the anion network reveals a kind of linear bonding scheme, while for κ -(BEDT-TTF)₂Cu₂(CN)₃ and κ -(BEDT-TTF)₂Ag₂(CN)₃ the anion network displays two-dimensional bonding arrangement.

b-direction. Figure 6(b) and (c) display the extended unit cell of κ -(BEDT-TTF)₂-Cu₂(CN)₃ and κ -(BEDT-TTF)₂Ag₂(CN)₃, respectively. The space group is commonly solved in monoclinic P2₁/c, in which all four BEDT-TTF molecules are equivalent [69,70]. However, the P2₁/c is only the average structure, while the exact structure presents a triclinic symmetry with two non-equivalent crystallographic sites [71,72]. In the panel (d) to (f) the projection of one of the layers is shown. Neighboring dimers are rotated by about 90° with respect to each other. The ratio t'/t of next-nearest-neighbor (t') and nearest-neighbor (t) coupling between the dimers measures the degree of frustration. For κ -(BEDT-TTF)₂Cu[N(CN)₂]Cl $t'/t \approx 0.5$ is rather small, while for the spin liquid candidates κ -(BEDT-TTF)₂Cu₂(CN)₃ and κ -(BEDT-TTF)₂Ag₂(CN)₃ the ratio $t'/t \approx 0.85$ indicates high frustration on the anisotropic triangle. Using tight-binding analysis, it was demonstrated that also the molecular conformation of the ethylene endgroups has some influence on the electronic structure [73]. Panels (g) to (i) show the anion networks. In κ -(BEDT-TTF)₂Cu[N(CN)₂]Cl all cyanide (CN) groups positioned between the copper atoms are ordered in a zigzag line along the *a*-axis so that the anion layer consists of one-dimensional chains [panel (g)]. In contrast to that, in κ -(BEDT-TTF)₂Cu₂(CN)₃ and κ -(BEDT-TTF)₂Ag₂(CN)₃ in addition to ordered CN groups (so-called chain CN) between Cu/Ag atoms in the chains along the *b*-axis, there are CN groups (so-called bridging CN) located at the inversion centers. These bridging CN groups connect Cu/Ag atoms along the *c*-axis so that the anion network is formed in two-dimensions [panels (h) and (i)]. The triangular coordination of Cu and Ag implies frustration since each Cu/Ag atom can be linked either to two N and one C atom, or to one N atom and two C atoms introducing intrinsic disorder. This ambiguity was eliminated in the recently synthesized salt κ -(BEDT-TTF)₂Cu[Au(CN)₂]Cl that is highly frustrated $t'/t = 1.19$ but possesses no disorder in the polymeric anions [74]. The properties of κ -(BEDT-TTF)₂Cu[N(CN)₂]Cl, κ -(BEDT-TTF)₂Cu₂(CN)₃ and κ -(BEDT-TTF)₂Ag₂(CN)₃ are discussed in Chapters 4 and 5, and Section 6.2.

The crystal structure of κ -(BEDT-TTF)₂Hg(SCN)₂Cl and κ -(BEDT-TTF)₂Hg(SCN)₂Br corresponds to space group C2/c [75]. It consists of alternating layers of BEDT-TTF radical cations and anions along the crystallographic *a*-axis, as shown in Figure 7(a). The anionic layer contains [Hg(SCN)₂Cl]_∞⁻ and [Hg(SCN)₂Br]_∞⁻ chains in the case of κ -(BEDT-TTF)₂Hg(SCN)₂Cl and κ -(BEDT-TTF)₂Hg(SCN)₂Br, respectively. It is worth to note that in contrast to many other BEDT-TTF salts, in the present family, *i.e.* in κ -(BEDT-TTF)₂Hg(SCN)₂Cl and the bromine-containing sister compound, the anions are not completely flat, but have a sizable width. This implies that the BEDT-TTF layers are separated more than usually.

As illustrated in panel (b), in κ -(BEDT-TTF)₂Hg(SCN)₂Cl as well as in κ -(BEDT-TTF)₂Hg(SCN)₂Br the dimers form a triangular lattice with rather large frustration $t'/t \approx 0.80$ [75,76]. The κ -type packing motif is slightly distorted compared to the previous ones in κ -(BEDT-TTF)₂Cu[N(CN)₂]Cl or κ -(BEDT-TTF)₂Cu₂(CN)₃. The large number of S ··· S intermolecular interactions between dimer units leads to a pretty strong *V*. For that reason, for κ -(BEDT-TTF)₂Hg(SCN)₂Cl and κ -(BEDT-TTF)₂Hg(SCN)₂Br the interdimer interaction becomes so important, that the system cannot be treated by the simple Hubbard model with a half-filled conduction band. Another distinction is that within the dimer, the BEDT-TTF molecules are slightly shifted with respect to each other, leading to a reduced intradimer transfer integral t_d and thus smaller *U*.

For κ -(BEDT-TTF)₂Hg(SCN)₂Cl and κ -(BEDT-TTF)₂Hg(SCN)₂Br there is one crystallographically unique BEDT-TTF molecule in the unit cell. In the case of κ -

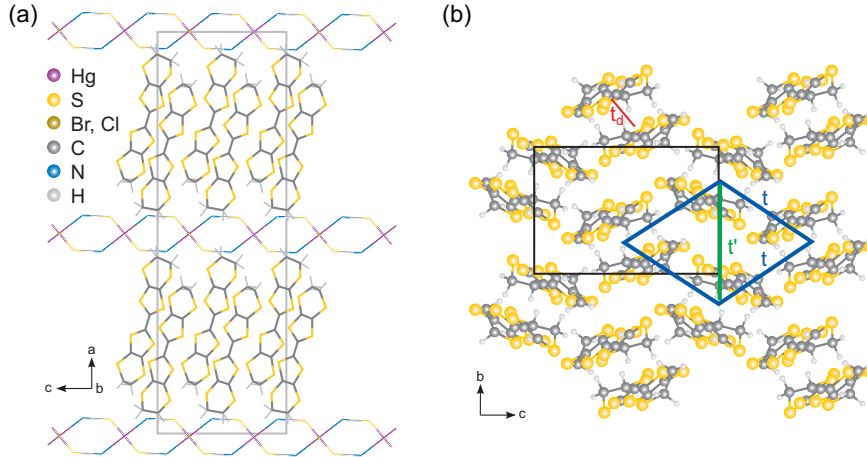


Figure 7. Crystal structure of κ -(BEDT-TTF) $_2$ Hg(SCN) $_2$ Cl and κ -(BEDT-TTF) $_2$ Hg(SCN) $_2$ Br. (a) The molecular layers along the conducting bc -plane are separated by the $[\text{Hg}(\text{SCN})_2\text{Cl}]_\infty^-$ anions and $[\text{Hg}(\text{SCN})_2\text{Br}]_\infty^-$ in the case of κ -(BEDT-TTF) $_2$ Hg(SCN) $_2$ Cl and κ -(BEDT-TTF) $_2$ Hg(SCN) $_2$ Br, respectively. Note that within a dimer the two molecules are displaced along the molecular axis, leading to a reduced transfer integral t_d . (b) Two face-to-face BEDT-TTF molecules form dimer with intra-dimer transfer integral t_d . The dimers are arranged on an anisotropic triangular lattice with effective transfer integrals t and t' .

(BEDT-TTF) $_2$ Hg(SCN) $_2$ Cl at room temperature, both ethylene end-groups are disordered, but below $T = 100$ K a staggered conformation prevails. Interestingly, the unit cell is slightly larger than in the sister compound κ -(BEDT-TTF) $_2$ Hg(SCN) $_2$ Br [77]; this trend is just opposite than expected from the larger Br ion compared to Cl. However, there seems to be no possibility to transform the physical properties of κ -(BEDT-TTF) $_2$ Hg(SCN) $_2$ Br towards those of κ -(BEDT-TTF) $_2$ Hg(SCN) $_2$ Cl, but also not *vice versa*. The two structurally similar compounds display different low-temperature behavior. κ -(BEDT-TTF) $_2$ Hg(SCN) $_2$ Cl undergoes a pronounced metal-insulator transition due to charge ordering at $T_{\text{CO}} = 30$ K, as discussed in Section 3.5, whereas κ -(BEDT-TTF) $_2$ Hg(SCN) $_2$ Br when cooled below metal-insulator transition at $T_{\text{CO}} = 80$ K develops quantum dipole liquid state with glassy signatures, as discussed in Section 6.4.

2.2. Other molecular compounds

During the last decades there have been numerous alternative attempts towards organic superconductors, most of them with rather limited success. The molecular conductors based on the anion radicals $[M(\text{dmit})_2]$ ($M = \text{Ni}$ and Pd) synthesized by R. Kato [78] is probably the most prominent family as it exhibits several interesting properties. More recently H. Mori suggested an even other approach via a H-bonded molecular unit-based organic conductor with a fused structure of short hydrogen bonds and stacked π -electron systems.

2.2.1. β' -EtMe $_3$ Sb[Pd(dmit) $_2$] $_2$

β' -EtMe $_3$ Sb[Pd(dmit) $_2$] $_2$ radical anion salt is based on the metal dithiolene complex Pd(dmit) $_2$ [79]. The crystal has a layered structure along the c -axis with symmetry space group $C2/c$ (Figure 8). Two Pd(dmit) $_2$ molecules form a dimer with one negative charge, and the dimers are arranged to form an almost isotropic triangular lattice with the ratio $t'/t \approx 0.8$. There are two equivalent anion layers consisting of four

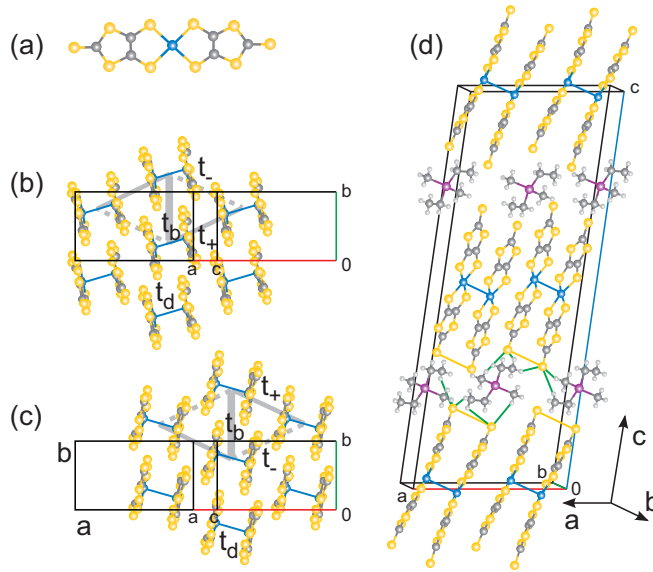


Figure 8. Crystal structure of β' -EtMe₃Sb[Pd(dmit)₂]₂. (a) Sketch of the molecule (1,3-dithiole-2-thione-4,5-dithiolate), Pd(dmit)₂: yellow, grey and green circles denote sulfur, carbon, and palladium atoms, respectively. (b) and (c) View of Pd(dmit)₂ dimers in the *ab*-plane projected along the direction tilted 17° away from the *c*-axis. The panels show dimers in two neighboring layers which have $(a + b)$ and $(a - b)$ stacking directions, respectively. An almost isotropic triangular lattice is denoted by gray lines, the interdimer transfer integrals are labeled by *t_b* (thick gray) and *t₊* (thin gray), and *t₋* (dashed gray), while the intradimer transfer integral is labeled by *t_d*. (d) Side view of the extended unit cell. Antimony and hydrogen atoms are denoted by violet and light grey circles. Possible hydrogen bonds between the end S ions of the Pd(dmit)₂ molecules and H of Et (CH₂-CH₃) or Me (CH₃) groups of the cations are indicated by full green lines.

molecular dimers (two in the central and two in the side layers), where dimers stack face-to-face along two diagonal directions [110] and [1 $\bar{1}$ 0]. There are four monovalent cations EtMe₃Sb; each cation consists of three methyl CH₃ groups labeled as Me₃ and one ethyl CH₂-CH₃ group labeled as Et, which can occupy one of two different equally probable orientations. The latter indicates that the formation of several crystallographic configurations is possible. Quantum spin liquid is suggested as the ground state of β' -EtMe₃Sb[Pd(dmit)₂]₂; its properties are discussed in Chapters 4 and 5.

2.2.2. κ -H₃(Cat-EDT-TTF)₂

In comparison to the previous radical cation (BEDT-TTF) and anion [Pd(dmit)₂] salts, κ -H₃(Cat-EDT-TTF)₂ and its deuterated isotopologue κ -D₃(Cat-EDT-TTF)₂ do not contain counter-ion species. κ -H₃(Cat-EDT-TTF)₂ consists of two crystallographically equivalent catechol-fused ethylenedithio-tetrathiafulvalene (Cat-EDT-TTF) molecules linked by a symmetric anionic [O \cdots H \cdots O]⁻-type strong hydrogen-bond as shown in Figure 9(a) [80–83]. H-bonded hydrogen is located at the central position between two oxygen atoms and these H-bonds result in the generation of holes (+0.5) on both Cat-EDT-TTF molecules. The crystal holds C2/*c* symmetry. These conductors enabled the construction of an unprecedented packing structure where the two-dimensional π -electron conducting layers shown in Figure 9(c) are connected by the H-bonds [panel (b)]. In these layers there are four kinds of inter-molecular interactions (*b*1, *b*2, *p*, and *q*); among them the strongest interaction is *b*1 from the face-to-face π - π stacking. Two face-to-face Cat-EDT-TTF molecules are paired in a dimer and the dimers form a two-dimensional triangular lattice in the *bc*-plane. The degree of frustration measured by

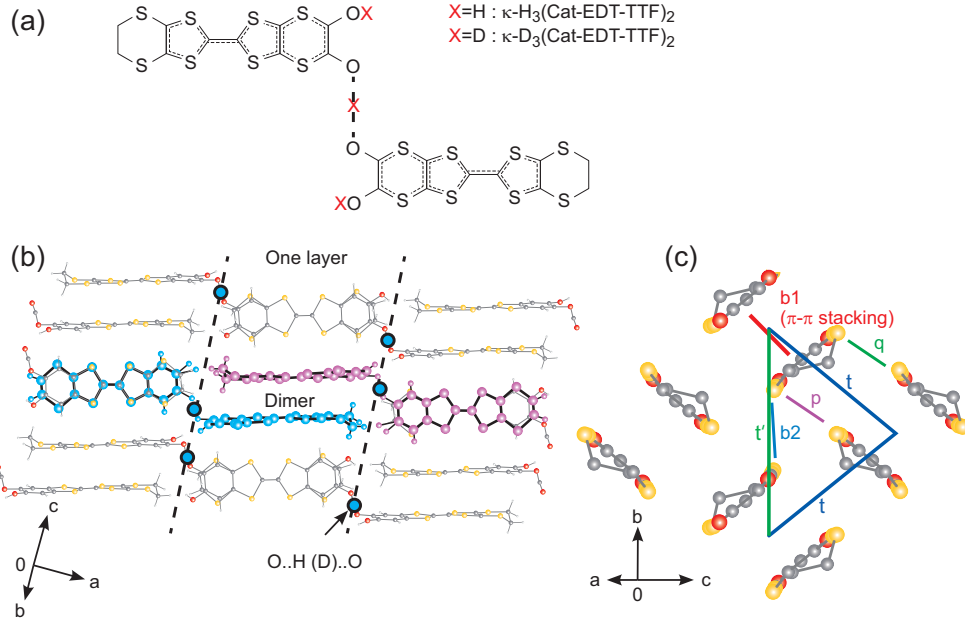


Figure 9. Crystal structure of $\kappa\text{-H}_3(\text{Cat-EDT-TTF})_2$ and $\kappa\text{-D}_3(\text{Cat-EDT-TTF})_2$. (a) Hydrogen-bonded molecular unit of the $\kappa\text{-X}_3(\text{Cat-EDT-TTF})_2$, where X stands for either a hydrogen or deuterium atom, in the case of $\kappa\text{-H}_3(\text{Cat-EDT-TTF})_2$ and $\kappa\text{-D}_3(\text{Cat-EDT-TTF})_2$, respectively. Two Cat-EDT-TTF molecules are related by twofold rotational symmetry with respect to the central hydrogen atom, and are thus crystallographically equivalent to each other. (b) Packing arrangement of the molecular $\kappa\text{-H}_3(\text{Cat-EDT-TTF})_2$ and $\kappa\text{-D}_3(\text{Cat-EDT-TTF})_2$ units. Two face-to-face Cat-EDT-TTF molecules, colored by pink and light blue, form a dimer. (c) View of the two-dimensional crystal structure in the layer shown in panel (b). There are four different kinds of inter-molecular interactions in the two-dimensional layer; the corresponding transfer integrals are labeled as $b1$ (face-to-face $\pi\text{-}\pi$ stacking), $b2$, p , and q . The dimers are arranged on an anisotropic triangular lattice in the (b, c) plane. The interdimer transfer integrals are denoted by t and t' , and the intradimer transfer integral by t_d . The ratio t'/t measures the degree of frustration. All hydrogen atoms are omitted for the simplicity reasons (after [83]).

the ratio of the couplings between dimers $t'/t \approx 1.25$ is slightly one-dimensional unlike t'/t values found in $\kappa\text{-(BEDT-TTF)}_2X$. $\kappa\text{-H}_3(\text{Cat-EDT-TTF})_2$ is suggested as a quantum spin liquid candidate with simultaneously developed quantum disordered state of electric dipoles, while $\kappa\text{-D}_3(\text{Cat-EDT-TTF})_2$ undergoes a metal-insulator transition to a charge-ordered state at $T_{\text{CO}} = 185$ K. We discuss their properties in Sections 5.1 and 6.3.

3. Charge Order and Ferroelectricity

Among the quantum phenomena emerging in organic low-dimensional solids with strong electron correlations, ferroelectricity driven by charge order is probably the most prominent one. Ferroelectricity was discovered 100 years ago [84]; nowadays it is of great fundamental and technological importance, widely exploited in modern devices such as memory storage elements, filters, high-performance insulators, and most recently in the energy harvesting technologies [85]. Ferroelectrics exhibit a spontaneous electric polarization that can be reversed by applying an external electric field. Conventional ferroelectrics are commonly classified into two groups termed as displacive and order-disorder ferroelectrics [86]. In the former, the polarization originates in the relative shift of positive and negative ions due to lattice distortion, while the polar-

ization in the latter case arises from the collective alignment of permanent electric dipoles. The most important developments in electronic technology, *viz.* the size and switching time reduction, and functional improvement of mobile electronic components, require novel ferroelectric materials with properties that enable overcoming the present limitations in designing new generations of energy efficient electronic devices. A promising route may lie in materials with strongly correlated electrons [87,88]. These materials undergo various phase transitions into broken-symmetry electronic ground states, including electronic ferroelectricity and multiferroicity, due to a fine interplay of charge, spin, lattice and orbital interactions [89–96].

Electronic ferroelectricity is basically charge-driven, meaning that the macroscopic electric polarization primarily depends on electron correlations and is closely related to charge ordering. In contrast to conventional displacive ferroelectrics, the mass of charge particles responsible for polarization is therefore very small and large lattice distortions are not expected. This implies the existence of strong dielectric fluctuations and polar domains of small size. Novel collective modes of excitation are also expected to provide ultrafast optical responses. Another distinction from conventional ferroelectric materials arises from the interplay of several competing electronic interactions involved in the charge ordering phase transition resulting in paraelectric-ferroelectric phase separation and causing relaxor-like dispersion in the dielectric behavior. A universal signature of the relaxor is a broad frequency-dependent peak in the real part of the temperature-dependent dielectric susceptibility. The latter is commonly observed in relaxor ferroelectrics, which exists in a random field state due to internal heterogeneities and disorder [97–99]. Notably, signatures of anomalous relaxor-like behavior and inherent randomness have also been observed in organic solids hosting charge ordering and electronic ferroelectricity, however, a full understanding is still missing.

The charge-driven ferroelectricity originating from an electronic phase transition was first shown theoretically to occur in the strongly correlated insulating phase of the Falicov-Kimball model [100]. More recently, the basic mechanism by which the charge ordering can lead to ferroelectricity was elucidated by Efremov *et al.* [101] and van den Brink and Khomskii [102]: it depends on the simultaneous presence of non-equivalent sites and bonds as depicted in Figure 10. It is worth noting that non-equivalent sites and bonds are not necessarily associated with the site-centered and bond-centered charge ordering; rather they may be simply due to the presence of charge sites with different valences and native dimerized structure, respectively.

Electronic ferroelectricity can be also spin-driven, implying that the macroscopic electric polarization is primarily due to spin frustration and closely related to magnetic ordering [103,104]. The materials with magneto-electric coupling, in which ferroelectricity and magnetism coexist, commonly known as multiferroics, open prospects of charge control by applied magnetic fields (and *vice versa*). In the 21st century the flurry of activity in the subject of multiferroicity is considerably rising worldwide due to both the intriguing fundamental physics problems and the technological importance in designing new generation of spintronics devices [105–108]. There exist several extensive review articles on multiferroicity, e.g. [102,109,110] to name only a few. Multiferroicity and magnetoelectric coupling of electrical and magnetic properties, which is a more common phenomenon [111,112], have been identified mostly among magnetic oxides and chalcogenides. However, ferroelectric and magnetic properties may also be intertwined in some low-dimensional organic solids. Notably, magneto-dielectric effects have been detected in several two-dimensional organic solids albeit no sign of the charge-ordering phase transition has been found. These materials show signatures of relaxor ferroelectricity, and multiferroicity was suggested involving the coupled order-disorder

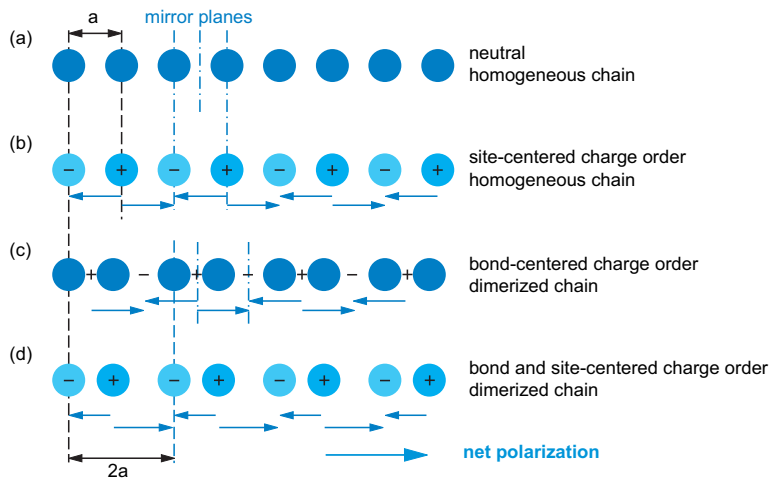


Figure 10. Schematic explanation of the basic mechanism by which charge ordering in a one-dimensional chain gives rise to electronic ferroelectricity (following [102]). The blue arrows denote dipolar moments. Site-centered charge order breaks the inversion symmetry between the sites (b), but only together with bond-centered charge order resulting in a lattice dimerization (c), charge order leads to a complete loss of inversion symmetry and a net polarization is established (d).

ferroelectric and magnetic order. Several theoretical approaches assuming the presence of quantum electric dipoles due to inherent frustration of molecular dimer units have been developed to explain the experimental observations. They all proposed the important role of spin-charge coupling in the formation of low-temperature phases in charge and spin sectors. This intriguing topic will be addressed in Chapter 6.

Charge-driven ferroelectricity has been proposed to be realized in a number low-dimensional molecular organic solids based on the structural dimer units and charge ordering phase transitions (see Figure 10). Quasi-one-dimensional $(\text{TMTTF})_2X$ and TTF-CA materials are considered as prototype examples of electronic ferroelectrics whose properties are rather well understood after the years of extensive research. Here TMTTF stands for tetramethyltetrathiafulvalene which forms a charge-transfer salt with centrosymmetric anions X^- such as PF_6^- , AsF_6^- , SbF_6^- , Br^- and noncentrosymmetric anions X^- such as ReO_4^- , BF_4^- . The Fabre salts $(\text{TMTTF})_2X$ are dimerized Mott insulators consisting of the dimer units of two neighboring TMTTF molecules, and of anions along the segregated quasi-one-dimensional chains with one hole per TMTTF dimer at high temperatures. A charge-ordering phase transition, in which TMTTF molecules within a dimer become non-equivalent, involves coupling of the electronic TMTTF subsystem with the anion lattice. The charge ordering phase transition and the low-temperature state show some typical fingerprints of ferroelectricity including structural changes and charge disproportionation due to symmetry breaking, and dielectric response. Several extensive review papers cover experimental and theoretical aspects of electronic ferroelectricity in these systems intensively studied during the first decade of the present century [113–116].

Another family of organic ferroelectrics are mixed-stack compounds, the most prominent being TTF-CA. Here TTF stands for tetrathiafulvalene and CA for tetrachloro-p-benzoquinone called chloranil. The planar TTF or its derivatives, together with chloranil or its variants form a single chain with alternating π -electron donor and acceptor molecules. At ambient conditions, the material is basically neutral but under elevated pressure or temperature or photoexcitation the TTF-CA becomes ionic. At the first-order phase transition the change of ionicity and dimerization appear

simultaneously, resulting in symmetry breaking and a sudden increase of the dielectric constant. Ferroelectricity is also manifested in polarization hysteresis, strong nonlinear effects and ultra-fast optical response. Several papers provide an overview of ferroelectricity in these systems [115,117,118]. In addition, development of novel routes for design and applications of organic ferroelectrics based on single-component polar organic molecules, hydrogen-bonded supramolecules and charge-transfer complexes with TTF, has been presented by an extensive review and articles by Horiuchi and Tokura [119,120].

Although the signatures of electronic ferroelectricity, such as large dielectric constant, characteristic dielectric dispersion, hysteresis, second-harmonic generation, ultra-fast dynamics, switching, bistable resistance and domain-wall dynamics have also been observed in two-dimensional organic solids, a complete characterization and full understanding as in conventional ferroelectrics is often missing. Considerable efforts have been devoted to elucidate the nature of collective charge excitations in the charge-driven ferroelectric phases as well as their coupling to applied dc and ac fields. And while some of their features – such as screened Arrhenius-like dispersion – resemble the well-established electrodynamics of charge-density waves in one- and two-dimensions [121–123], others – like giant nonlinear conductivity and negative differential resistance – appear different and have not been encountered until now. Distinct mechanisms to explain these remarkable effects have been suggested ranging from melting of charge order to dielectric breakdown and sliding. Diverse approaches have been proposed concerning the mechanism behind charge-ordering phase transition and associated ferroelectricity, ranging from the purely Coulomb-driven to cation-anion hydrogen bonding interactions. Most important, a vital role of geometrical frustration in the formation of ferroelectric phase, related to a triangular arrangement of organic molecules in two-dimensional organic solids, has been recently reviewed in two publications [92,110].

In this Chapter we present the current state of research and give a survey of the relevant work performed in the studies of charge order and ferroelectricity in two-dimensional molecular solids during the last decade. For further details we refer the reader to three review papers published a few years ago [115,116,124]. We focus on three major quarter-filled systems that have drawn most attention during this period: α -(BEDT-TTF)₂I₃, θ -(BEDT-TTF)₂RbZn(SCN)₄ and β'' -(BEDT-TTF)₂SF₅RSO₃ (Sections 3.1, 3.2 and 3.4). In the final Section 3.5, we will have a look at κ -(BEDT-TTF)₂Hg(SCN)₂Cl, where charge order with ferroelectric signatures occurs in a dimerized compound with an effectively half-filled band.

3.1. *Phase diagrams of quarter-filled systems*

Two-dimensional organic materials based on BEDT-TTF molecule hosting electronic ferroelectricity driven by charge order possess extremely rich phase diagrams; their origin lies in the competition between the tendency of electrons to delocalize and strong interactions between charge, spin and lattice. In the conducting layers, BEDT-TTF molecules form a geometrically frustrated triangular lattice and each molecule accommodates half a hole so that the conduction bands are quarter filled. In contrast to dimer Mott insulators at half filling, which are mainly governed by the on-site Coulomb repulsion U , here the combined action of a U and a sizeable inter-site Coulomb repulsion V , analyzed within an extended Hubbard model, is expected to lead to the formation of a charge-ordered ground state [90,125–128]. Indeed, it turns out that V is strong

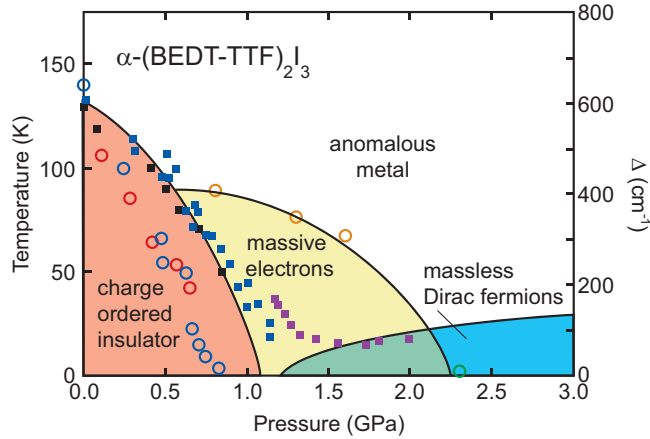


Figure 11. The phase diagram of α -(BEDT-TTF)₂I₃ shows how with varying pressure and temperature different phases and boundaries develop. The charge-ordered transition T_{CO} is suppressed by pressure as probed by various methods (squares, left scale); concomitantly the charge gap Δ closes as extracted from thermal activated conductivity and optical properties (circles, right axis). The charge-ordered insulator and an anomalous metal coexist at high temperatures and low pressures, whereas they share the common boundary with the massless Dirac fermionic state at lower temperature and higher pressure (after [132]).

enough so that charge-ordered states are observed in numerous materials based on the BEDT-TTF molecule possessing different types of crystal morphologies, labelled by α , θ and β'' [26,49–51], as depicted in Figure 2. On the other hand, in materials with κ -pattern, in which molecules are paired in dimers (s.c. dimerized materials), the Mott physics plays important role (see Chapters 4 and 5), so that no tendency towards charge order has been expected. However, this common view has been recently challenged by a discovery of charge ordered ferroelectricity in κ -(BEDT-TTF)₂Hg(SCN)₂Cl [75,76,129]. The charge ordered state is quickly suppressed by a rather low pressure, however without any trace of superconductivity [130,131].

The charge-ordered ferroelectric α -(BEDT-TTF)₂I₃ is certainly of utmost importance among the class of two-dimensional molecular materials with quarter filling, thanks to its rich phase diagram with a number of exotic quantum phenomena ranging from electronic ferroelectricity to superconductivity, from non-linear transport to zero-gap semiconductivity and ferrimagnetism characterized by massless Dirac fermions [132–135]. Superconductivity with $T_c \approx 7$ K is reported to occur under 0.2 GPa of uniaxial strain applied along the in-plane stacking a -axis [136]. A stable superconducting phase with $T_c = 8$ K can be achieved by tempering the crystals at 70°C for a few days [137]. The most outstanding feature of the α -(BEDT-TTF)₂I₃ phase diagram is that a charge-ordered ferroelectricity lies nearby a massless Dirac fermions state, as displayed in Figure 11. At ambient pressure, charge-ordering develops below the metal-insulator phase transition $T_{CO} = 135$ K with inversion symmetry broken and charge disproportionated between neighboring sites. Increasing pressure suppresses charge order and a massless Dirac fermions phase emerges, thus making α -(BEDT-TTF)₂I₃ the first bulk material, in which the impact of electron correlations on the Dirac-point conductance can be studied [132,138,139] (see Section 3.3.2).

Another prominent example of electronic ferroelectricity due to charge order is θ -(BEDT-TTF)₂RbZn(SCN)₄. A remarkable feature of this material is that charge order sets in right at the boundary of the charge-glass in the phase diagram (Figure 12). The competition between charge-ordered phase and charge glass is governed by geometrical frustration. Increasing the degree of frustration by replacing the RbZn(SCN)₄⁻ anions

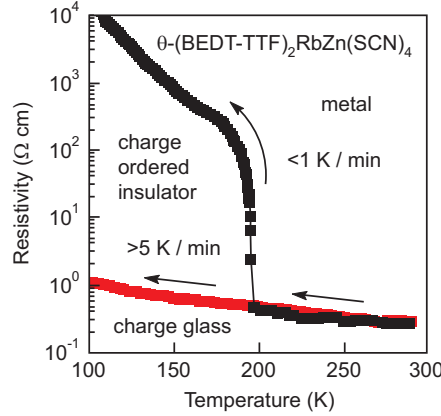


Figure 12. Temperature-dependent resistivity of θ -(BEDT-TTF) $_2$ RbZn(SCN) $_4$ measured with different cooling rates. Slow cooling leads to a sharp metal-insulator transition at $T_{CO} = 190$ K into the charge-ordered state. Rapid cooling (less than 1 K per minute) prevents this order leaving space to charge glass formation (after [140]).

by $\text{CsZn}(\text{SCN})_4^-$, which form nearly isotropic triangular lattice, completely suppresses the formation of charge order [141]. In θ -(BEDT-TTF) $_2$ RbZn(SCN) $_4$ charge order develops at long-range scale only under sufficiently slow cooling conditions (cooling speed slower than 1 K/min). Similarly to α -(BEDT-TTF) $_2$ I $_3$, a charge-ordered state builds up below the metal-insulator transition $T_{CO} = 190$ K with the inversion symmetry broken and charge imbalance between neighboring sites. On the other hand, when cooled rapidly, the charge ordering is avoided and a charge glass with slow dynamics is formed below $T_g = 170$ K [140] (see Section 3.3.1).

Among other weakly dimerized compounds with charge order, the BEDT-TTF family of β'' -(BEDT-TTF) $_2$ SF $_5$ RSO $_3$ has attracted a lot of attention because they constitute an all-organic superconductor with large polyfluorinated anions [Figure 4(c)] built with H \cdots F hydrogen bonding [55]. Some years ago, Merino and McKenzie suggested these materials for investigating the interplay between charge order and superconductivity [142,143]. However, only recently, a generalized phase diagram has been established showing that both the charge disproportionation and the temperature of the charge-ordering phase transition scale with intersite repulsion V , as theoretically expected [144–149]. Starting at the strongly correlated side β'' -I ($R = \text{CH}_2$) is an insulator up to the room temperature, followed by β'' -MI ($R = \text{CHF}_2$) which undergoes a metal-to-insulator phase transition at 170 K, β'' -SC ($R = \text{CH}_2\text{CF}_2$) becomes a superconductor at $T_c = 5.5$ K, while β'' -M ($R = \text{CHF}$) is metal at all temperatures. Most remarkably, a superconducting state occurs close to the charge-ordered insulating state as plotted in the phase diagram of Figure 13; an enhanced charge disproportionation leads to an increase of superconducting transition temperature T_c indicating a critical role of charge fluctuations in its formation.

3.2. Ferroelectricity driven by charge order in weakly dimerized solids

Ferroelectricity driven by a charge-order phase transition is predominantly established in weakly dimerized solids with quarter-filled bands. Among them α -(BEDT-TTF) $_2$ I $_3$ represents the most outstanding example, which has attracted strong interest among researchers worldwide since it was introduced to the community by Schweitzer and collaborators in 1984 [52,53]. At ambient pressure, α -(BEDT-TTF) $_2$ I $_3$ undergoes

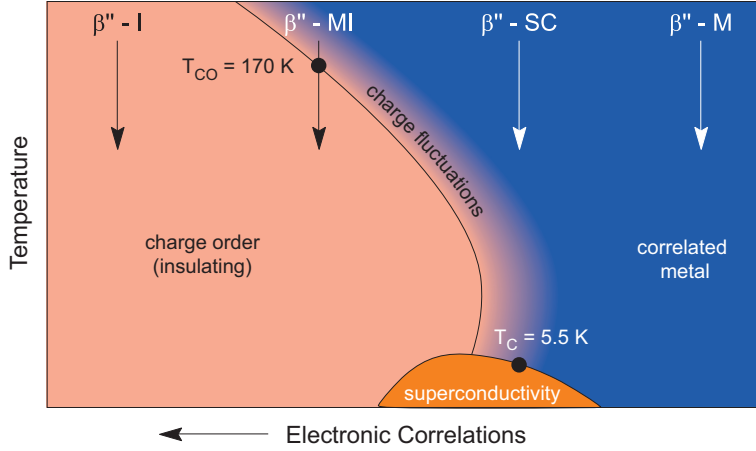


Figure 13. Phase diagram of β'' -(BEDT-TTF) $_2$ SF $_5$ RSO $_3$: as electronic correlations get weaker, the charge order is gradually suppressed and superconductivity sets in. β'' -I, β'' -MI, β'' -SC and β'' -M stand for materials with R equal CH $_2$, CHF CF_2 , CH $_2$ CF $_2$ and CHF, respectively; cf. Figure 4(c) (adopted from [144]).

a metal-insulator phase transition from a high-temperature semimetallic state to a charge-ordered at $T_{CO} = 135\text{ K}$. Below this temperature, a striped pattern of charge disproportionation sets in. The inversion symmetry is broken, the charge is disproportionated between the molecular sites within the dimerized stack of the unit cell and consequently a net polarization is created resulting in ferroelectricity.

In the present and the subsequent Section 3.4, we give a comprehensive presentation of the relevant findings in α -(BEDT-TTF) $_2$ I $_3$ and compare them with the results obtained in the studies of ferroelectricity in slowly cooled θ -(BEDT-TTF) $_2$ RbZn(SCN) $_4$ wherever appropriate. For completeness reasons, we briefly address β'' -(BEDT-TTF) $_2$ SF $_5$ CHF CF_2 SO $_3$, in which charge order does not lead to ferroelectricity; inversion symmetry persists at all temperatures and ferroelectricity cannot be established.

3.2.1. Semi-metallic state at high temperatures

We first address the semi-metallic state at high temperatures. Here, α -(BEDT-TTF) $_2$ I $_3$ [52,53] crystallizes in non-polar space group $P\bar{1}$. As is described in Section 2, the unit cell contains four BEDT-TTF $^{0.5+}$ molecules and two I $_3^-$ anions. Commonly, two stacks are distinguished: within column I, which is weakly dimerized, BEDT-TTF molecules, denoted as A and A', are related through an inversion center and thus are equivalent; column II consists of two different types of molecules, denoted as B and C, which are uniformly spaced and lie at the crystallographic inversion centers [Figure 14 (a)].

According to the density functional calculations [138], as well as extended Hückel molecular-orbital calculations [48], the system is a semi-metal with very small electron and hole pockets; this results in an experimentally observed weakly metal-like conductivity within the molecular plane [52,53,133]. The direct experimental proof for semimetallicity is provided by recent Hall effect and magnetoresistance measurements, which show that dc transport is governed by the high mobility of electrons and holes resulting in an almost temperature-independent conductivity. The value of the Hall coefficient confirms the idea of a quarter-filled band; the dominantly inter-pocket scattering equalizes the mobilities of the two types of charge carriers [150].

Notably, a striped charge pattern is observed at room temperature by scanning tun-

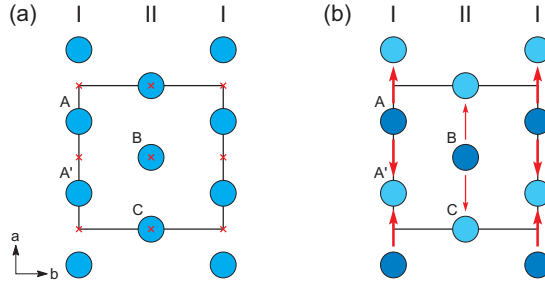


Figure 14. (a) Schematic representation of the in-plane molecular structure of α -(BEDT-TTF) $_2$ I $_3$ in the high-temperature semi-metallic state. Within the (ab) -plane the BEDT-TTF molecules form stacks along the a -direction in a herringbone way and exhibit a triangular arrangement with adjacent stacks. Molecules belonging to weakly dimerized stack I and non-dimerized stack II are denoted as A, A', and B, C, respectively. Crosses denote the inversion center relating A and A' molecules. (b) Charge-density distribution in the in-plane molecular layer of α -(BEDT-TTF) $_2$ I $_3$ in the low-temperature charge-ordered state. Molecules with higher (charge-rich) and lower (charge-poor) charge density are shown by dark and light blue circles, respectively. Electric dipoles are indicated by arrows: importantly, only dipoles in stack I contribute to a net polarization, while those in stack II cancel each other out.

neling microscopy [151]. Partial charge disproportionation and charge fluctuations already present at $T = 300$ K persist all the way down to the charge-ordering phase transition. The charge imbalance was first suggested based on nuclear-magnetic-resonance (NMR) measurements by Takahashi and collaborators [152,153] and was later deduced from x-ray diffraction measurements [154] using empirical relationship between intramolecular bond lengths and charge density [155] and confirmed by optical vibrational measurements [156–158]. The best local probes utilized in these experiments are the highly charge-sensitive stretching modes of the BEDT-TTF molecules, such as the symmetric Raman-active ν_3 mode, and the asymmetric infrared-active ν_{27} mode of the outer C=C bonds [41,159–162]. The $\nu_{27}(b_{1u})$ band at high temperatures is shown in the inset in Figure 15 [163]. The result corresponds well to the one reported previously [115,158]. With an – in a first approximation – linear shift of 140 cm^{-1} per unit charge, the charge disproportionation $2\delta_\rho$ is calculated from

$$2\delta_\rho = \frac{\delta\nu_{27}(b_{1u})}{140 \text{ cm}^{-1}/e} \quad , \quad (1)$$

where $\delta\nu_{27}$ is the difference in frequency positions between the two ν_{27} vibration bands associated with two non-equal BEDT-TTF molecules, i.e $2\delta_\rho = \rho_{\text{rich}} - \rho_{\text{poor}}$ [161]. For the BEDT-TTF cations, an increase in positive charge loosens the bonds, *i.e.* the vibrational features are redshifted.

The broad absorption band observed in the infrared spectra at about 1445 cm^{-1} , corresponding to an average charge of $+0.5e$ per molecule hides a non-uniform site charge distribution. Resolving the associated splitting indicates that charge imbalance is present only within stack II and is rather small $2\delta_\rho < 0.2e$ (Figure 15); a similar result is deduced from x-ray scattering measurements [115,154]. The values of charge density at different molecular sites A, A', B and C agree well with results obtained by density functional theory (DFT) calculations: $+0.52e$ (A, A'), $+0.55e$ (B) and $+0.38e$ (C) [138,164].

The question remains how to explain the charge disproportionation at elevated temperatures. Kakiuchi *et al.* discard the local electric potential distribution originating from the iodine ion in the anionic layer and suggest that the charge disproportionation may be due to distribution of transfer integrals among the BEDT-TTF molecules

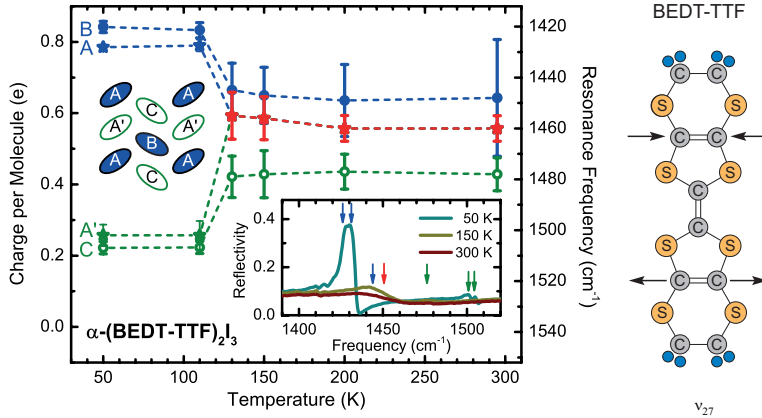


Figure 15. Temperature dependence of the charge distribution (left axis) and the frequency position of $\nu_{27}(b_{1u})$ stretching mode (right axis) of α -(BEDT-TTF) $_2$ I $_3$. Below the phase transition temperature of $T_{CO} = 135$ K, the charge per molecule changes drastically for all four sites. The inset shows reflectivity in the frequency range of the $\nu_{27}(b_{1u})$ vibrations. The positions of the vibrational modes are illustrated by the colored arrows, corresponding to the dots in the main frame. At 300 K, blue color indicates the low-frequency vibration of the B molecule, green the C molecule at high frequencies, and the red color the molecules A and A' located in between. The charge ordering phase transition is visible by the splitting of the peak: now two features are present each one with a double-peak structure (from [163]). The sketch on the right illustrates the structure of the BEDT-TTF molecule and the antisymmetric vibrations of the outer C=C double bond involved in the $\nu_{27}(b_{1u})$ mode leading to an alternating charge flow along the molecular axis.

[154]. Their view was challenged by the findings of Alemany *et al.* [138], who argue that the hole concentration in the highest-occupied molecular orbitals is intrinsically related to the strength of hydrogen bonding between the terminal hydrogens of BEDT-TTF molecules and the anions. They conclude that molecules A and B participate in a number of very short H-bonds with anions, whereas molecules C are not involved in those; instead they make the strongest sulfur-sulfur contacts insuring in this way the stability and electronic delocalization within molecular layers.

At the end, we note that short-range charge disproportionation and charge fluctuations at high temperatures also develop in slowly cooled θ -(BEDT-TTF) $_2$ RbZn(SCN) $_4$ as evidenced by NMR line broadening and diffuse x-ray scattering [165–167].

3.2.2. Metal-insulator transition into the charge-ordered state

In the following, we address the charge-ordering phase transition and the charge-ordered state which develops upon cooling. When the temperature reaches $T_{CO} = 135$ K, several striking changes in the physical properties, electronic as well as in structural, take place.

Optical second-harmonic generation provides the definite proof that inversion symmetry is lost. As displayed in Figure 16, the SHG signal sets in abruptly at T_{CO} and develops gradually with further decreasing temperature [168,169]. In addition, large polar domains develop with several 100 μm in size and opposite polarization as detected by interferometric experiments of the second-harmonic signal [170]. These findings agree perfectly with the results of x-ray diffraction measurements: At T_{CO} lattice deformation breaks the inversion symmetry; the symmetry is reduced from $P\bar{1}$ space group at high temperatures to polar space group P1 and twin, right-handed and left-handed domains are formed due to the acentric structure [154].

Remarkably, upon cooling the charge distribution changes drastically right at T_{CO} as deduced from the temperature-dependent intramolecular deformations. Raman and

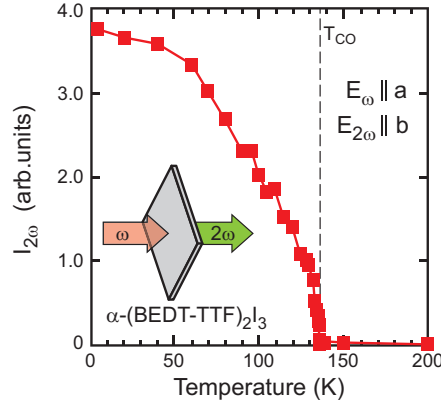


Figure 16. Temperature dependence of the optical second-harmonic-generation (SHG) signal in α -(BEDT-TTF) $_2$ I $_3$. The SHG signal, recognized as a most reliable fingerprint of inversion symmetry breaking, is generated right at the charge-ordering phase transition $T_{CO} = 135$ K, and steadily increases further as the temperature is reduced (after [168]).

infrared vibrational spectroscopy as well as ^{13}C -NMR measurements unanimously confirm these results [154,156–158,163,171–174]. Figure 15 displays the abrupt splitting of the charge-sensitive $\nu_{27}(b_{1u})$ mode at $T_{CO} = 135$ K, resembling a first-order phase transition; further cooling leads to only minor changes. Eventually two pairs of bands are observed: a stronger one around 1425 cm^{-1} and a weaker one slightly above 1500 cm^{-1} , signaling the formation of four different molecular sites in the unit cell. The lower-frequency bands correspond to a charge of approximately $+0.79e$ and $+0.84e$ per molecule, and the upper-frequency bands to $+0.25e$ and $+0.22e$, respectively. The overall results reveal the formation of horizontal stripes of charge-rich and charge-poor molecular sites as illustrated in Figure 17(a). In stack II the molecules are equally spaced, but B and C differ in charge. On the other column, the molecules A and A' are crystallographically equivalent at temperatures above T_{CO} , but possess different charge for $T < T_{CO}$. Now a net-dipole moment is generated as sketched in Figure 14(b). Conversely, the equivalent bonds within stack II result in a cancellation of the electric dipoles between the charge-rich and charge-poor neighboring molecules. Importantly, there are two ways of rearranging stack I below T_{CO} : (A, A')(A, A') and (A', A)(A', A). The two possible valence arrangements along the a -axis lead to twin polar domains, as illustrated in Figure 18.

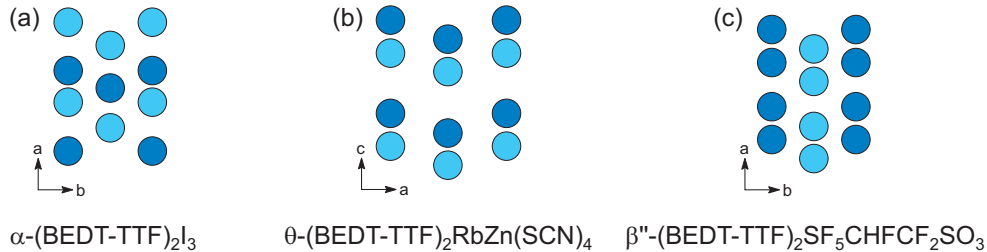


Figure 17. Schematic representation of the horizontal charge stripe arrangement observed in (a) α -(BEDT-TTF) $_2$ I $_3$, (b) θ -(BEDT-TTF) $_2$ RbZn(SCN) $_4$ and in (c) β'' -(BEDT-TTF) $_2$ SF $_5$ CHFCF $_2$ SO $_3$. Dark and light shaded circles denote charge-rich and charge-poor molecules, respectively. Dimerized molecular chains run along the a -axis in α -(BEDT-TTF) $_2$ I $_3$ and β'' -(BEDT-TTF) $_2$ SF $_5$ CHFCF $_2$ SO $_3$, and along the c -axis in θ -(BEDT-TTF) $_2$ RbZn(SCN) $_4$, due to labelling convention. Charge order is accompanied by bond order in α -(BEDT-TTF) $_2$ I $_3$ and in θ -(BEDT-TTF) $_2$ RbZn(SCN) $_4$, while there is no bond order in β'' -(BEDT-TTF) $_2$ -SF $_5$ CHFCF $_2$ SO $_3$.

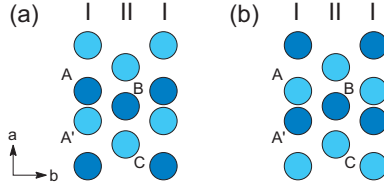


Figure 18. Twin domains in α -(BEDT-TTF) $_2$ I $_3$. The stripes are formed either (a) by the charge-rich molecules A and B or (b) by the charge-rich molecules A' and B.

When θ -(BEDT-TTF) $_2$ RbZn(SCN) $_4$ crystals are slowly cooled, a similar charge order is identified below the metal-insulator transition at $T_{CO} = 190$ K [56,167,175,176]. ^{13}C -NMR, Raman, infrared spectroscopy and x-ray structural studies, all have concordantly revealed the formation of horizontal charge stripes similar as illustrated in Figure 17(b); the stripes are formed in-plane along the a -axis with a charge-rich and charge-poor pattern along the c -axis: $+0.8e : +0.2e$ on two non-equal BEDT-TTF molecules within dimers stacked in two columns in the unit cell [146,153,165,175,177,178]. Therefore, the net-dipole moment is generated by the electric dipoles on the molecular dimers within both BEDT-TTF columns, in contrast to the ferroelectricity established in α -(BEDT-TTF) $_2$ I $_3$. Another distinction concerns the bonds between molecules along the two diagonal directions in the plane: for θ -(BEDT-TTF) $_2$ RbZn(SCN) $_4$ the bonds are identical, yielding an uniform Heisenberg coupling between spins. Consequently, no gap opens in the spin sector at T_{CO} and the system behaves as a paramagnetic insulator down to the spin-Peierls phase transition at $T_{SP} = 30$ K, where it enters into the spin-singlet phase [56,165,179]. Notably, the bonds become inequivalent in the singlet phase, resembling the charge-ordered state of α -(BEDT-TTF) $_2$ I $_3$. Finally, we note that structural changes associated with a loss of inversion centers between the BEDT-TTF molecules and the doubling of unit cell along the in-plane c -axis are much larger than in α -(BEDT-TTF) $_2$ I $_3$ [56,167,180].

3.2.3. Character of the metal-insulator phase transition

A close inspection of the presented results infers that the phase transition between the high-temperature paraelectric and low-temperature ferroelectric states is of first-order: the charge distribution among the BEDT-TTF molecules within the dimerized chains, the SHG signal, as well as the reduced space symmetry evidence a very rapid variation at $T_{CO} = 135$ K (cf. Figures 15 and 16). Similar abrupt changes are also noticed in other quantities. At T_{CO} the dc and ac conductivity suddenly drops by several orders of magnitude along all three crystallographic directions, optical spectroscopy and measurements of the static susceptibility evidence that charge and spin gaps suddenly open, revealing the insulating and diamagnetic nature of the ferroelectric low-temperature state in α -(BEDT-TTF) $_2$ I $_3$ [52,53,133,150,158,181,182].

By applying hydrostatic pressure, the charge-order phase transition shifts to lower temperatures at the rate 80-90 K/GPa and is fully suppressed above 1.5 GPa. The charge disproportionation is concomitantly reduced by 0.17 e /GPa and the optical gap decreases by 470 cm^{-1} /GPa [156,163]. Notably, a rather abrupt change in charge disproportionation at T_{CO} persists at all applied pressures, whereas steepness of the conductivity drop is gradually diminished, as seen from Figure 19. For pressure values above 1.5 GPa and at low temperatures, the BEDT-TTF molecules carry nearly the same amount of charge as they do at ambient conditions in the semi-metallic state. The observed behavior may be ascribed to the pressure-induced enlarged bandwidth and

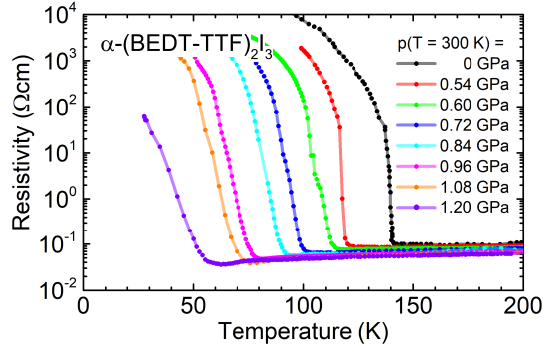


Figure 19. Temperature dependence of the in-plane dc resistivity of α -(BEDT-TTF) $_2$ I $_3$ under different pressure values as determined at room temperature (extracted from [163]). The behavior for higher pressure and lower temperatures is plotted in Figure 29.

the resulting decrease of effective intersite Coulomb repulsion [156,163]. In Section 3.3.2 we come back to the low-temperature behavior when higher pressure is applied, and continue with a detailed discussion of correlation effects and Dirac electrons.

Let us just mention here that in slowly cooled θ -(BEDT-TTF) $_2$ RbZn(SCN) $_4$, unlike the latter compound – the charge-order phase transition rises with hydrostatic pressure, which may be due to the enhancement of electronic correlations caused by an increase of dihedral angle between neighboring BEDT-TTF molecules [56]. Ref. [115,158,160,162] give extensive account on charge-ordering phase transition and charge-sensitive Raman and infrared vibrational modes in the metallic phase of the charge-ordered state in θ -(BEDT-TTF) $_2$ RbZn(SCN) $_4$ as well as in α -(BEDT-TTF) $_2$ I $_3$.

On the one hand, the observations summarized above indicate that only the ferroelectric order parameter, which is associated with the symmetry breaking at T_{CO} and the appearance of charge disproportionation at the dimerized BEDT-TTF molecular sites, are indeed of first-order [183]. On the other hand, the dc conductivity reveals no hysteresis and the temperature behavior of the transport gap indicates a dominantly mean-field character [150,158]. Thus, the situation does not appear simple; we recall similar controversies and dilemmas in numerous strongly correlated electron systems [87].

The recent cryogenic scanning optical near-field microscopy study sheds light on this intriguing issue by revealing the spatial evolution of this phase transition, which evidences its first-order nature [184]. Recorded images around $T_{CO} = 135$ K demonstrate a pronounced phase segregation with a sharp boundary between metallic and insulating regions within a few hundred mK temperature range (Figure 20). The narrow coexistence range explains why the dc conductivity experiments failed to detect any hysteresis. Remarkably, such a sharp transition occurs only in a homogeneous single crystal. Conversely, when the sample is subject to appreciable strain – a situation that may easily arise due to improper mounting – metallic and insulating regions spatially coexist in a wide temperature range. As a consequence of the pressure dependence presented in Figure 19, the phase transition is suppressed to lower temperatures.

3.2.4. Origin of the charge-order phase transition and ferroelectric ground state

In an attempt to explain the metal-insulator phase transition observed in α -(BEDT-TTF) $_2$ I $_3$, Fukuyama and collaborators suggested that electron-electron interactions play a crucial role in this regard [185,186]. Including the intersite Coulomb repulsion V ,

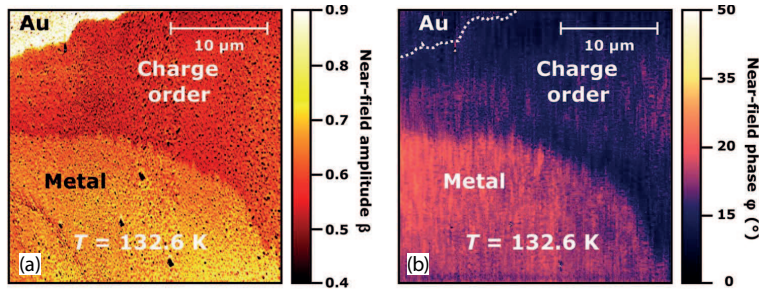


Figure 20. Near-field image of a $28\mu\text{m} \times 28\mu\text{m}$ area recorded with a spatial resolution of 25 nm slightly below the charge ordering phase transition in $\alpha\text{-(BEDT-TTF)}_2\text{I}_3$. The microscopic images are obtained by the (a) amplitude and (b) phase of the scattered CO_2 laser beam ($\lambda = 11\mu\text{m}$) at an oscillating afm tip. There is a well-defined phase boundary between the metallic (light) and insulating (dark) regions proving its first-order character. The evaporated gold layer (upper left corner) serves as a reference (after [184]).

they identified the importance of charge order in low-dimensional quarter-filled compounds [127,187–189], opening a completely new chapter for these molecular quantum materials. Seo *et al.* also worked out a solely electronic mechanism [90,179] including on-site and inter-site Coulomb interactions, U and V in an extended Hubbard model; it results in a Wigner-crystal-type phase with three possible charge-order patterns as depicted in Figure 21. Importantly, in this mean-field approach the horizontal stripe pattern is only found if the dimerization is explicitly included.

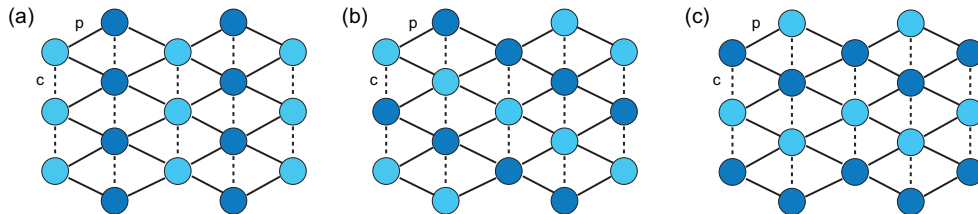


Figure 21. Schematic presentation of charge order patterns: (a) vertical stripe, (b) diagonal stripe, (c) horizontal stripe. All patterns have identical energies within the classical limit, assuming that intersite Coulomb interactions are identical in all three crystallographic directions. According to Clay *et al.* [190] the horizontal stripe is the most stable charge order thanks to the “1010” charge pattern in the direction of weakest intermolecular hopping and the “1100” along the two diagonal directions with strong intermolecular hopping.

The explanation on purely electronic grounds, however, was challenged subsequently; we now understand that a coupling to the lattice cannot be neglected. In a charge transfer crystal electron-electron and electron-phonon coupling are always present simultaneously. Thus, even if the ferroelectric phase transition is primarily an electronic instability, *i.e.* driven by charge ordering, the lattice modifications remain an important side effect due to a finite coupling of electrons to the lattice. The prevailing electronic origin of ferroelectricity is supported by strong non-linear effects and ultra-fast photoresponse; this will be discussed further in Section 3.4.4.

Along this avenue Clay, Mazumdar and collaborators proposed a model beyond the mean-field theory, termed “paired electron crystal” that includes electron-electron and electron-phonon interactions [190–192]. Numerical many-body calculations successfully reproduce the experimentally established charge pattern shown in Figures 15 and 17(a,b). Remarkably, only a relatively weak electron-phonon interaction has to be incorporated for forming horizontal stripes; in addition, the bond dimerization perpendicular to them appears as a consequence of the charge ordering. The authors suggest that the simultaneous formation of the paired electron crystal and the coex-

isting spin-singlet state in a sole phase transition occurs only due to lower symmetry in α -(BEDT-TTF)₂I₃ as compared to θ -(BEDT-TTF)₂RbZn(SCN)₄ where charge ordering and spin-singlet transition take place at different temperatures.

In another approach, Alemany *et al.* argue that electronic interactions between molecular sites are not the driving force of the phase transition; rather it is the interplay between coupled BEDT-TTF molecular and anion subsystems that stabilizes charge order and ferroelectricity [138,193]. Notably, density-functional theory (DFT) calculations yield no significant changes in the wave-vector dispersion of the band structure below T_{CO} , suggesting that only modifications of the local anion-molecular interactions occur at the ordering. In that case even small displacements of anions toward (away) the charge-rich (charge-poor) molecules would increase (decrease) the hydrogen bonding between anions and BEDT-TTF molecules, and thus induce charge redistribution; the resulting striped charge pattern qualitatively corresponds to the experimental findings.

A close look at the phase transition of α -(BEDT-TTF)₂I₃ by Pouget *et al.* provides additional support to the relevance of this mechanism [194]. They also point out that the paradigmatic metal-insulator phase transition at 135 K is actually a semimetal-semiconductor phase transition. The presence of two types of charge carriers, electrons and holes, allow at high temperatures that the electron-hole interaction generates excitonic effects and plays a role in the semimetal-semiconductor phase transition [195]. Finally, the existence of two types of carriers questions the basic assumption of the extended Hubbard model, which considers a quarter-filled system with one type of carriers only. Further work is needed to consistently explain the complex nature and origin of the phase transition in α -(BEDT-TTF)₂I₃.

3.2.5. Charge-ordered states with no ferroelectricity

It is instructive to compare the charge order in α -(BEDT-TTF)₂I₃ and θ -(BEDT-TTF)₂RbZn(SCN)₄, on the one hand, with the one observed in β'' -(BEDT-TTF)₂SF₅CHFCF₂SO₃, on the other hand. In all three systems, the charge density is arranged in horizontal stripes, however, other properties of the charge order in β'' -(BEDT-TTF)₂SF₅CHFCF₂SO₃ are strikingly different [144,145]. In the first two systems, below the metal-insulator phase transition differently charged molecules arrange themselves along dimerized stacks; thus allow the formation of ferroelectricity. Conversely, in β'' -(BEDT-TTF)₂SF₅CHFCF₂SO₃, the BEDT-TTF molecules have equal charge densities within dimerized stacks, while a charge disproportionation of $2\delta_\rho \approx 0.10e$ exists between crystallographically nonequivalent BEDT-TTF molecules belonging to two neighboring stacks [Figure 17(c)]. Thus, charge order is present without bond order; and consequently no net polarization can be established (see Figure 10). Another important distinction lies in the fact that charge order persists at all temperatures without any noticeable temperature dependence of the charge imbalance; hence it is not associated with the metal-insulator phase transition at 190 K, below which the high-temperature non-polar space group $P\bar{1}$ does not change. The origin of the temperature-independent charge order, as well as the metal-insulator phase transition remains to be clarified. The phase transition may be related to the pronounced one-dimensional character of dimer chains running along the interstack direction at low temperatures, or it may be due to anion ordering [144,196]. It is remarkable that the particular structure in β'' -(BEDT-TTF)₂SF₅CHFCF₂SO₃ enables several short hydrogen bonds between the BEDT-TTF molecules and the oxygen and fluorine atoms of the anions; at present, however, it is not established whether these

short hydrogen bonds differ for two non-equivalent BEDT-TTF molecules. In any case, the anions are disordered at room temperature as well as at 150 K, *i.e.* below the metal-insulator phase transition. On the other hand, the ethylene end groups of the BEDT-TTF molecules, which are disordered at room temperature, are ordered below the phase transition at $T = 150$ K. This change may contribute to the mechanism of the phase transition, as it does in θ -(BEDT-TTF)₂RbZn(SCN)₄ [193]. These hypotheses should be verified in the future.

3.3. States nearby charge order

3.3.1. Charge glass

Glassy phases and related phenomena such as metastability and slow relaxation are found in a variety of systems when long-range order is prevented by randomness, rapid cooling or competing interactions [87,197]; these effects are commonly attributed to disorder. A more intriguing case is the disorder-free glassy behavior established in geometrically-frustrated spin systems [198,199], while the influence of geometric frustration in the charge sector is less explored [200]. Glassy phenomena have been demonstrated in the compound θ -(BEDT-TTF)₂RbZn(SCN)₄ with triangular arrangement of molecular units, where a high degree of charge frustration is present [140,141,201]. As discussed in the previous Section 3.2, the material displays a metal-to-insulator transition at $T_{CO} = 190$ K when cooled slowly, leading to a charge-order-driven ferroelectric ground state. The transition can be avoided either by rapid cooling or by replacing the $\text{RbZn}(\text{SCN})_4^-$ anions with $\text{CsZn}(\text{SCN})_4^-$ as shown in Figure 22. In the absence of long-range charge order, the resistivity remains low, the dielectric peak is suppressed [202] and the rapidly-cooled phase bears similarities with the high-temperature phase, e.g. it exhibits slow dynamics of the order of kHz [166].

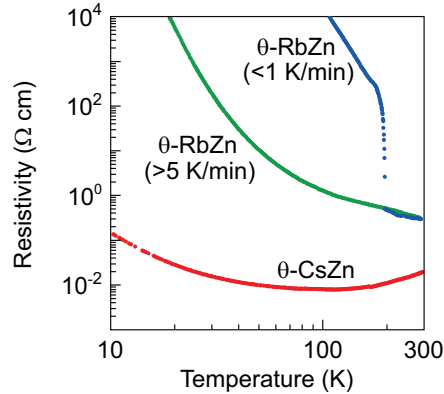


Figure 22. Resistivity behavior $\rho(T)$ of θ -(BEDT-TTF)₂RbZn(SCN)₄ drastically depends on the cooling rate: the charge-order phase transition is suppressed by rapid cooling leaving space to charge-glass formation. The transition is also suppressed by replacing Rb by Cs in θ -(BEDT-TTF)₂CsZn(SCN)₄: the obtained resistivity behavior does not change with cooling rate in the range of 0.1 – 10 K/min (after [141]).

3.3.1.1. Slow charge dynamics. The temperature evolution of the slow charge dynamics in organic charge transfer salts can be revealed by resistance fluctuation spectroscopy [203], as demonstrated in Figure 23. One observes resistance fluctuations with a characteristic frequency superimposed on the background $1/f$ noise for both

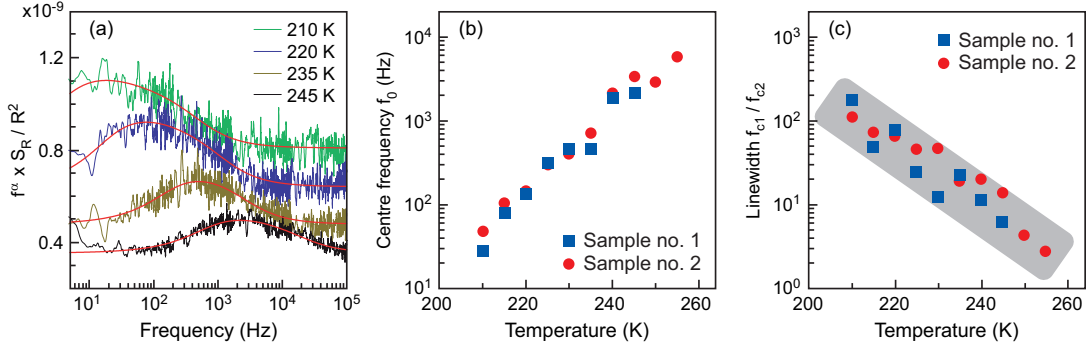


Figure 23. Resistance fluctuations in the rapidly cooled θ -(BEDT-TTF)₂RbZn(SCN)₄. (a) Resistance power spectrum density multiplied by frequency at representative temperatures. Full lines are fits to continuously distributed Lorentzians plus $1/f^\alpha$. (b) Slowing down of the characteristic frequency and (c) growth of the dynamic heterogeneity (after [140]).

compounds: θ -(BEDT-TTF)₂RbZn(SCN)₄ when cooled rapidly [140], and θ -(BEDT-TTF)₂CsZn(SCN)₄ [141]. When plotting $f^\alpha \times S_R$ as a function of frequency, a broad peak is uncovered that rises out of a constant background [Figure 23(a)]. The spectral shape is well described by a superposition of continuously distributed Lorentzians with high-frequency f_1 and low-frequency f_2 cutoffs. When T is reduced, the peak position shifts to lower frequency and its linewidth strongly increases [panels (b) and (c)], indicating that the dynamics becomes slower and more heterogeneous. Both features are fingerprints of glassy freezing in supercooled liquids [204]. It is interesting to note that the growth of slow dynamics is correlated with the evolution of two-dimensional charge clusters, recorded by x-ray diffuse scattering. These charge clusters are present already at high temperatures and their intensities and correlation lengths increase on cooling down to T_{CO} , as illustrated in Figure 24. After rapid cooling, when the charge ordering is suppressed, charge clusters are only recorded at $T = 120$ K. The correlation length $\xi = 140$ Å corresponds to about 25 triangular units and is temperature independent up to $T = 150$ K, indicating a frozen metastable state with no long-range order. With further warming, ξ increases and at $T_g \approx 165$ K attains the value of about 200 Å in accord with data recorded on cooling. The temperature behavior of ξ indicates that T_g can be identified as the glass transition temperature of charge cluster dynamics.

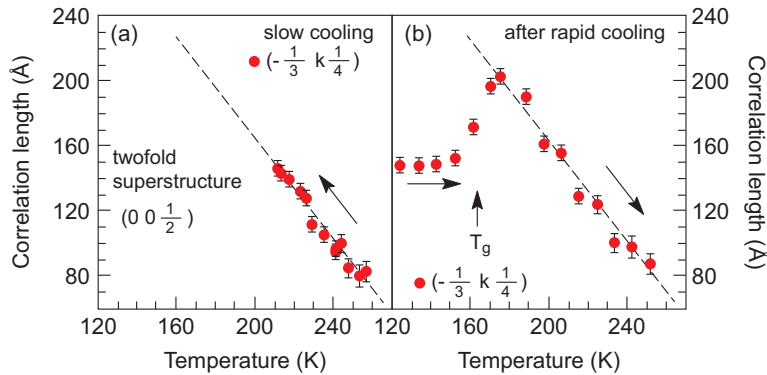


Figure 24. Temperature evolution of the charge cluster correlation length $\xi(T)$ during (a) slow cooling and (b) after rapid cooling of θ -(BEDT-TTF)₂RbZn(SCN)₄ (after [140]).

3.3.1.2. *Evolution of the electronic crystal in time.* Having established the charge glass in rapidly cooled θ -(BEDT-TTF)₂RbZn(SCN)₄ as a metastable state, the time evolution of the electronic crystal state can be followed by monitoring at a fixed temperature $T_q < T_{CO}$ how the resistivity and NMR spectra evolve in time after the crystal was cooled down rapidly. The resistivity is much lower in the glass state compared to the electronic-crystal charge-ordered state and thus characterizes the electronic state macroscopically. In Figure 25, the crystallization time is plotted versus T_q ; the dome-like structure is known as time-temperature-transformation (TTT) curve, commonly observed for crystallization of structural, ionic glasses, or metallic alloys [205]. Analyzing the TTT curve within classical nucleation theory allows the determination of nucleation and growth dominated regimes. Microscopic evidence for the electronic crystal growth from a glass state was obtained by ¹³C-NMR investigations. Figure 26 compares the NMR spectra obtained during the slow cooling process with the time evolution of spectra obtained at $T = 140$ K after rapid cooling. Remarkably, the broad spectrum observed initially at 140 K changes its structure in time and eventually adopts the shape characteristic for a charge-ordered state.

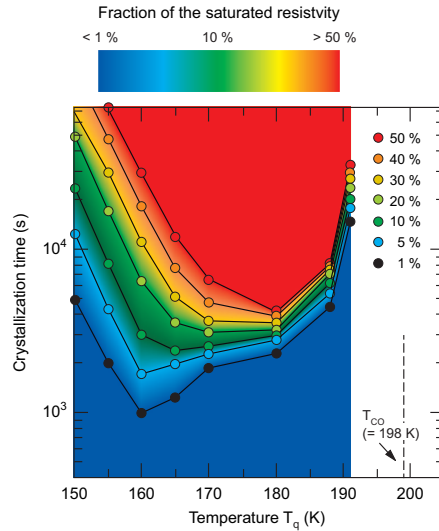


Figure 25. Time-temperature-transformation (TTT) curves of θ -(BEDT-TTF)₂RbZn(SCN)₄ deduced from the time evolution of resistivity after rapid cooling at different temperatures T_q . The color scale denotes the percentage of resistivity recovery (after [201]).

3.3.1.3. *Charge vitrification and aging.* Eventually charge-order prevents further investigations of the glassy phenomena in θ -(BEDT-TTF)₂RbZn(SCN)₄ under slow cooling. This problem can be circumvented by studying θ -(BEDT-TTF)₂CsZn(SCN)₄, where the higher degree of frustration fully prevents long-range charge order. Indeed, additional fingerprints of glassy states such as cooling-rate-dependent charge vitrification and non-equilibrium aging behavior were successfully demonstrated in θ -(BEDT-TTF)₂CsZn(SCN)₄ [141].

(i) From the resistivity *vs.* temperature curves under different sweeping rates, we can conclude that faster cooling leads to a higher glass transition temperature T_g , as expected in glass phenomenology. (ii) The charge-fluctuation broad peak exhibits a strong decrease in characteristic frequency f_0 around 100 K. This indicates that the glass transition temperature $T_g \approx 100$ K. (iii) At $T < T_g$, aging behavior can be observed in the resistivity, as shown in Figure 27. It can be well described by the

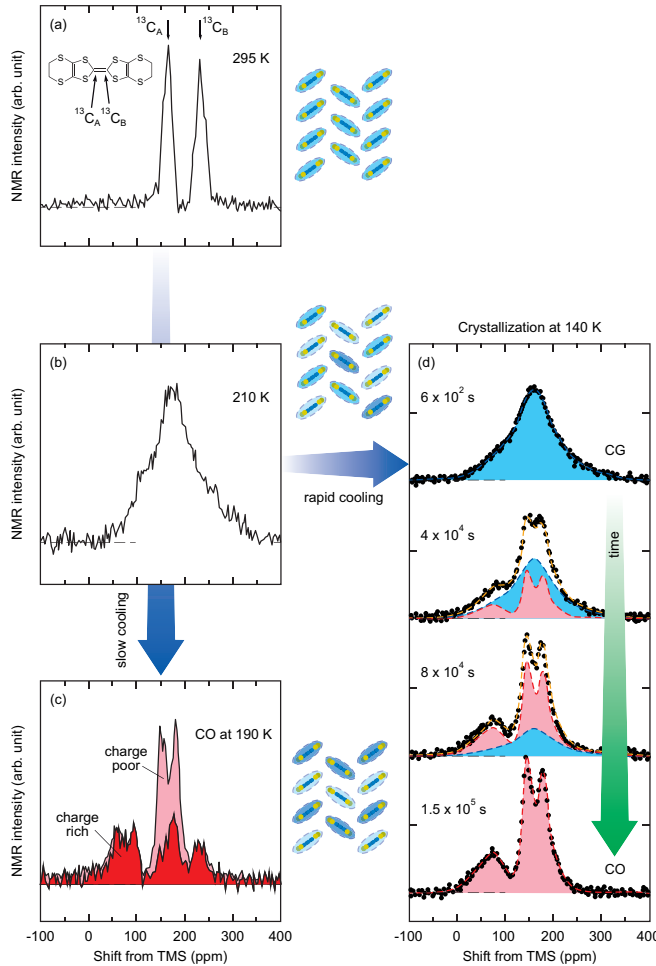


Figure 26. Temperature and time evolution of the ^{13}C -NMR spectra of θ -(BEDT-TTF) $_2\text{RbZn}(\text{SCN})_4$. Slow cooling results in the charge-ordered electronic crystal, while after rapid cooling the charge glass is established. (a) At room temperature the spectrum consists of two narrow lines due to two non-equivalent ^{13}C sites in the BEDT-TTF molecule indicating homogeneous charge density. (b) Upon cooling the spectrum broadens due to the slowing down of charge dynamics. (c) The spectrum indicates that charge poor and charge rich sites are formed in the charge ordered state at $T = 190$ K. (d) Time evolution of ^{13}C -NMR spectra after rapid cooling during the crystallization process at $T = 140$ K. The blue and red components are attributed to the charge glass and charge order state (after [201]).

Kohlrausch-Williams-Watts-law based on stretched exponential function [204,206]. Its relaxation time τ_{aging} obeys the Arrhenius law reaching 100 – 1000 s in the vicinity of T_g ; again consistent with the conventional definition of glass transition. Most significantly, $\tau_{\text{noise}} = 1/f_0$ at $T > T_g$ follows the same behavior uncovering common dynamics of the equilibrium states at high temperatures and of the non-equilibrium states below T_g . The observed Arrhenius behavior indicates strong-liquid nature meaning that the glassy dynamics on approaching T_g can be described as a gradual slowing down probably reflecting an increasing number of dynamically correlated charge clusters. (iv) Consistently, x-ray diffuse scattering data reveal that the spatial growth of the charge clusters is closely associated with the glassy charge dynamics.

Having in mind that these organic materials are rather clean systems with no significant amount of impurities, and that θ -(BEDT-TTF) $_2\text{CsZn}(\text{SCN})_4$, in contrast to θ -(BEDT-TTF) $_2\text{RbZn}(\text{SCN})_4$, possess nearly equilateral triangular lattice, Kanoda

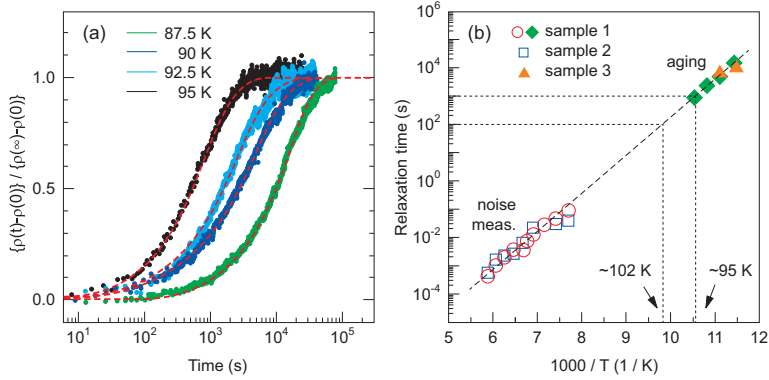


Figure 27. Aging behavior of θ -(BEDT-TTF) $_2$ CsZn(SCN) $_4$. (a) Evolution of the resistivity in time at representative temperatures below the glass transition T_g . The lines are fits to the Kohlrausch-Willimas-Watts (KWW) relaxation law. (b) Aging relaxation time extracted from the Kohlrausch-Willimas-Watts behavior τ_{aging} and $\tau_{\text{noise}} = 1/f_0$ extracted from the resistance fluctuations peak as a function of inverse temperature. The line is a fit to Arrhenius law giving the activation energy of about 2600 K. The dotted lines denote the temperature range where τ_{aging} reaches values 100-1000 s widely recognized to define T_g (after [141]).

and collaborators suggested that the charge frustration works against long-range electronic crystallization and thus plays the primary role in the formation of charge glass in these two-dimensional strongly correlated systems [140,201]. In other words, the competition between the charge-ordered phase and a charge glass may be governed by geometrical frustration. Indeed, Dobrosavljević and collaborators demonstrated theoretically that the interplay of long-range interactions and geometric frustration in disorder-free Coulomb liquids consists in lifting the ground state degeneracy produced by frustration and in generating a manifold of low-lying metastable states together with characteristic features of glassy dynamics, as observed experimentally. Their results suggest that θ -(BEDT-TTF) $_2$ RbZn(SCN) $_4$ and θ -(BEDT-TTF) $_2$ CsZn(SCN) $_4$ constitute prominent examples of a self-generated Coulomb glass [207]. Still, we should recall that the lattice degrees of freedom are involved in the creation of the electronic-crystals states, both the charge glass as well as the charge order; the extent to which they influence the crystallization mechanism remains to be clarified.

3.3.2. Dirac electrons

For more than three decades the charge-transfer salt α -(BEDT-TTF) $_2$ I $_3$ is one of the most fascinating members of the BEDT-TTF family [52,53,133]. Besides serving as the prime model for charge-order, the compound attracts enormous attention for the formation of a Dirac electronic state when pressure is applied (Figure 19). Dirac materials are a novel class of solid state systems in which the low-energy electronic properties are not described in terms of a Schrödinger wave equation, but by a relativistic Dirac equation resulting in a linear energy dispersion around the Fermi energy, where valence and conduction bands touch each other [208,209]. While three-dimensional Dirac and Weyl semimetals are subject to intense research nowadays [210], the underlying physics was first explored in the two-dimensional case of mono-layered graphite, *i.e.* graphene [208]. Whereas in graphene the Dirac cones are isotropic, less symmetric Dirac materials such as two-dimensional organic solid α -(BEDT-TTF) $_2$ I $_3$ possess anisotropic cones with tilted axes and in presence of long-range and short-range Coulomb interaction provide novel exotic phenomena.

Experimentally this topic was pioneered by the magnetotransport studies of Tajima

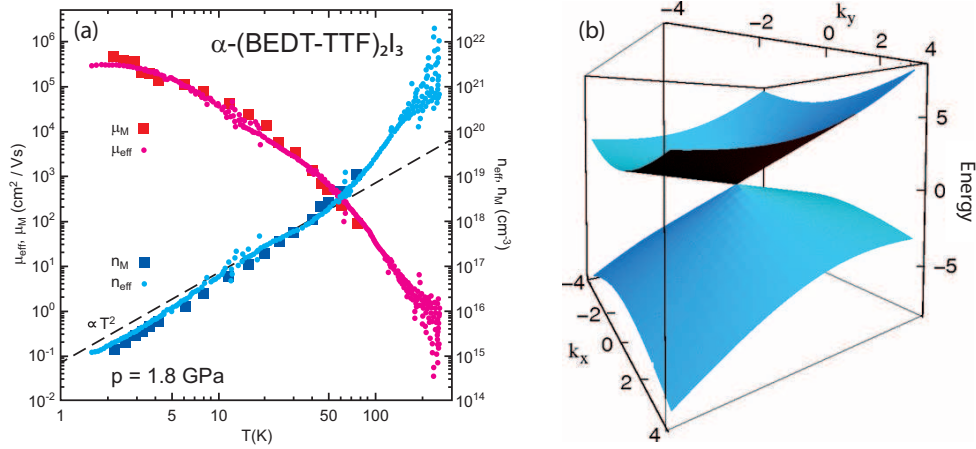


Figure 28. (a) The carrier density $n(T)$ and the mobility $\mu(T)$ under the pressure of $p = 1.8$ GPa plotted as a function of temperature in double logarithmic manner. The cyan dots show the effective carrier density n_{eff} and the magenta dots the mobility μ_{eff} estimated from the Hall coefficient ($R_H = 1/ne$) and the conductivity ($\mu = \sigma_1/ne$). The magnetoresistance mobility μ_M and the density n_M , on the other hand, is shown as red and blue squares, respectively. The carrier density obeys $n(T) \propto T^2$ from $T = 10$ K to 50 K (indicated by the dashed line) (data from [134]). (b) Band structure of α -(BEDT-TTF) $_2$ I $_3$ near the Dirac point. The energy dispersion $E_\lambda(q) = w_0 + \lambda\sqrt{w_x^2q_x^2 + w_y^2q_y^2}$ for the special choice of $w_x = w_y = 1$ and $w_0 = (0, 0.6)$ is given in natural units. The Dirac cone is tilted in the y -direction (reproduced from [219] with permission).

and collaborators [134,211–215], quickly explained by bandstructure calculations [215–220]. Here the challenge is that the atomic coordinates are not really known with high precision in the required parameter range of high-pressure and low-temperature; and that the influence of the I_3^- anions cannot be neglected [138,221,222]. Although the electrical conductivity is basically temperature independent, the carrier density drops quadratically with temperature while the mobility increases approximately by $\mu(T) \propto T^{-2}$, as shown in Figure 28(a). Subsequent measurements of specific heat [223], nuclear magnetic resonance (NMR) [135,224] and optical spectroscopy [132,163] provide further evidence of massless Dirac Fermions.

Using an extended Hubbard model within the Hartree mean-field theory, Kobayashi *et al.* examined the band structure of the stripe charge-ordered state of α -(BEDT-TTF) $_2$ I $_3$ under pressure and found that with increasing pressure a topological transition occurs from a conventional insulator with a single-minimum in the dispersion relation at the M point in the Brillouin zone, toward a new phase, which exhibits a double minimum [225,226]. The transition is characterized by the appearance of a pair of Dirac electrons with a finite mass. Due to the topological nature of this transition, the Berry curvature vanishes in the conventional phase and has a double peak structure with opposite signs in the new phase [227]. Osada considered the possibility that α -(BEDT-TTF) $_2$ I $_3$ becomes a Chern insulator due to additional transfers, potentials and magnetic modulations [228–230].

An interesting approach should be mentioned at this point; instead of applying hydrostatic pressure, two and four sulfur atoms in the BEDT-TTF molecule can be replaced by selenium in order to increase the orbital overlap and bandwidth [231]. The resulting α -(BEDT-STF) $_2$ I $_3$ and α -(BEDT-TSF) $_2$ I $_3$ [better known as α -(BETS) $_2$ I $_3$] stay metallic down to $T_{\text{CO}} = 80$ K and 50 K, respectively. There have been suggestions that exotic Dirac cones can be achieved even under ambient pressure and temperature [232,233], unfortunately heavy disorder makes the experimental realization challenging at present[234–236].

3.3.2.1. Effect of correlations. In contrast to graphene, the Dirac cones in α -(BEDT-TTF)₂I₃ are strongly tilted [216,219], as shown in Figure 28(b). The position of the bands can be tuned by pressure; also temperature is an important parameter. The real situation in α -(BEDT-TTF)₂I₃, however, is not as clean as in the case of graphene, due to the existence of additional electronic bands and the effect of the anion sheets [47,138]. Pressure-dependent optical studies [132,163] reveal the presence of additional charge excitations, also inferred from magnetotransport [237]. The effect of interlayer magnetoresistance in the case of tilted Dirac cones was subsequently discussed [214,238,239] and suggested that angular-dependent measurements could reveal the in-plane anisotropy of electronic structure.

Liu *et al.* [139] observe an increase of $\rho(T)$ at low temperatures [139] that cannot be completely suppressed and becomes stronger when approaching the charge-ordering transition (Figure 29). They suggest that massless Dirac fermions interact via short-range Coulomb repulsion [240]. A pseudogap forms in the charge channel before opening a real charge gap in the charge-ordered phase; this is in accord with pressure-dependent optical experiments, which infer that the closing of the charge-order gap with pressure comes to a halt around 1 GPa [163]. Recently it was pointed out [241] that in organic materials spin-orbit coupling might play an important role, causing spin-orbit gaps that render impossible the realization of a true zero-gap Dirac state in α -(BEDT-TTF)₂I₃.

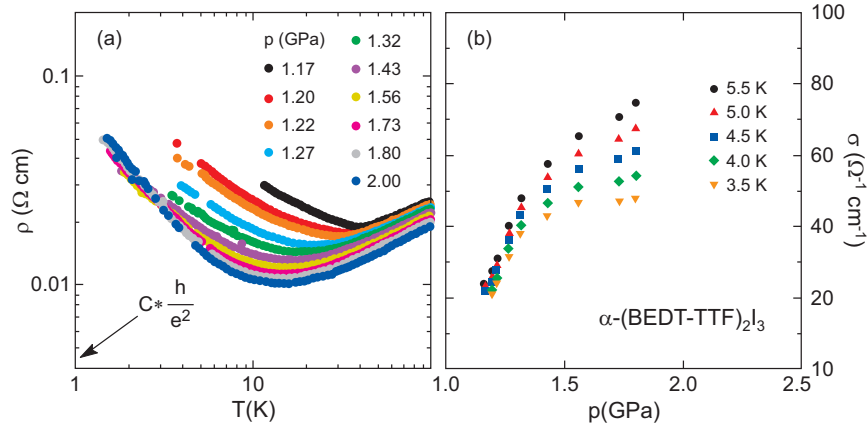


Figure 29. (a) In the massless Dirac fermion state of α -(BEDT-TTF)₂I₃ above 1.1 GPa the resistivity $\rho(T)$ increases at very low temperatures even when the pressure is raised up to 4 GPa. Also indicated is the bulk resistivity corresponding to the quantum sheet resistance, $C \cdot (h/e^2) = 4.5 \times 10^{-3} \Omega\text{cm}$, with the lattice constant along the c -axis under a pressure of around 2 GPa: $C = 1.7 \text{ nm}$. (b) Conductivity versus pressure for fixed temperatures above 1.1 GPa in the low-temperature region, where the resistivity upturn appears (after [139]).

From extensive optical studies under high pressure up to 4.0 GPa, Uykur *et al.* concluded that at low pressure α -(BEDT-TTF)₂I₃ possesses a clear charge-order gap in the optical conductivity; but with rising p these bands approach each other and overlap, leading to a more-or-less narrow Drude contribution. At low temperatures the edge of these two bands develop linear dispersions. As illustrated in Figure 30, $\sigma_1(\omega)$ consists of three components in the range of high-pressure: (i) a low-energy Drude response, (ii) a frequency-independent conductivity due to the Dirac electrons and (iii) a mid-infrared band arising with the incoherent transitions due to on-site and inter-site Coulomb repulsion. Upon cooling, electronic correlations gave in a pseudogap with states piling up at the edges. As a result, the Drude spectral weight is transferred to finite energies. In other words, there are clear fingerprints of the electronic correlations

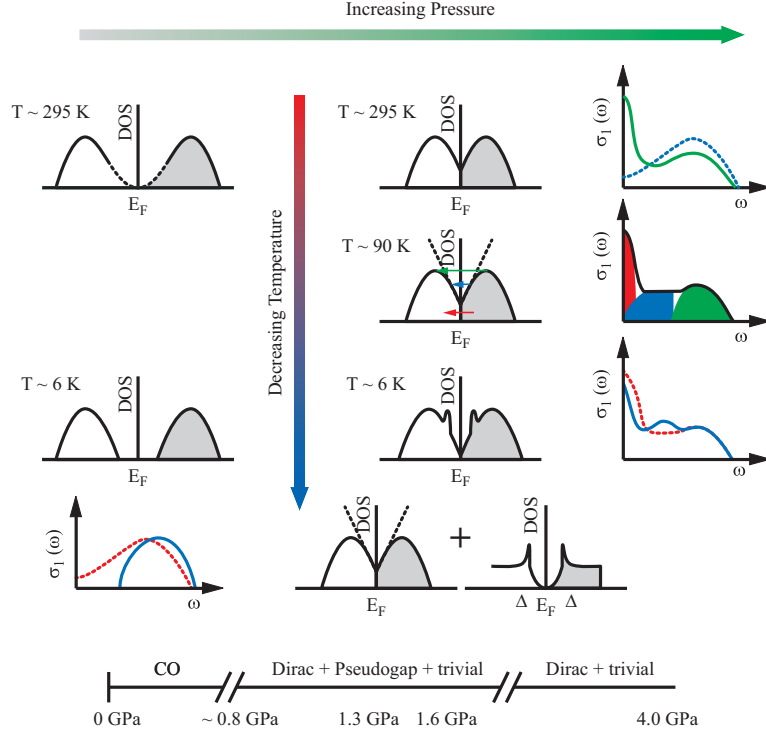


Figure 30. Schematic diagrams for the electronic structure and corresponding optical conductivity of α -(BEDT-TTF) $_2$ I $_3$ (reproduced from [132]). The diagrams are given for the low-pressure insulator state and the high-pressure Dirac state at various temperatures. Here, T_{PG} stands for the temperature, where the pseudogap starts to open. At the bottom the pressure evolution of the various electronic phases of α -(BEDT-TTF) $_2$ I $_3$ at low T is summarized: the charge-order insulating state at low pressure; a metallic states in the intermediate pressure regime consisting of massless Dirac electrons, next to carriers in correlation-split and trivial bands; and above 4.0 GPa only the Dirac electronic state and carriers in trivial bands remain.

among the Dirac electrons; the interaction can be tuned by temperature and pressure.

Also NMR investigations lead to the conclusion that the Dirac fermions in α -(BEDT-TTF) $_2$ I $_3$ do interact [135,224]. Using ^{13}C -NMR spectroscopy an unusual temperature dependence of spin-related properties was observed in α -(BEDT-TTF) $_2$ I $_3$, when pressure of 2.3 GPa is applied indicating strong correlations among the linearly dispersing electrons [224]. In regular metals, the electronic density of states is constant in energy, resulting in a constant quantity $1/(T_1TK^2)$ upon cooling, where T_1 is the spin-lattice relaxation rate, T the temperature and K is the Knight shift; this is known as the Korringa law [242,243]. In contrast, in systems with linearly dispersing bands and Dirac cones, both $1/T_1T$ and K^2 rapidly drop upon cooling, reflecting the vanishingly small density of states (DOS) around the Fermi energy E_F . Despite the fact that the charge-order transition is strongly suppressed at a pressure of 2.3 GPa as shown in Figure 19, a crossover from a Korringa-like metal to a gapless state occurs below $T \approx 150$ K, suggesting a density of state profile depicted in the inset of Figure 31(a).

The strength of short-range electronic correlations can be measured by a so-called Korringa ratio

$$\mathcal{K} = \frac{1}{T_1T} \frac{1}{S_0\beta K^2} \quad \text{with} \quad S_0 = \frac{4\pi k_B}{\hbar} \frac{\gamma_n}{\gamma_e}, \quad (2)$$

where γ_n is the nuclear gyromagnetic ratio and γ_e is the electron gyromagnetic ratio;

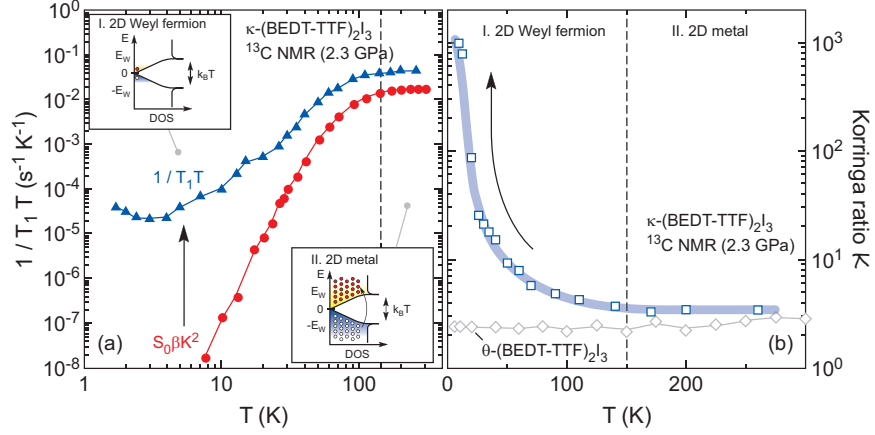


Figure 31. (a) Temperature dependence of the ^{13}C -NMR spin-lattice relaxation rate $1/T_1T$ (triangles) and the squared Knight shift K (circles) [135] measured at a pressure of 2.3 GPa and a magnetic field of 6 T. The insets depict the density of electronic states near E_F with thermally generated electron-hole pairs (circles) indicated for low (I) and high (II) temperatures, respectively. The density of states is linear up to $|E_W - E_F|$ and levels off above it. (b) The Korringa ratio K (squares) dramatically increases as the temperature is lowered. For comparison the results for θ -(BEDT-TTF) $_2\text{I}_3$ (diamonds) are plotted [244] (after [224]).

k_B is the Boltzmann constant and $\hbar = 2\pi\hbar$ the Planck constant; β is a form factor representing the anisotropy of the hyperfine interaction. In weakly correlated electron systems, \mathcal{K} is constant in T and of the order of unity, as demonstrated in Figure 31(b) for the example of θ -(BEDT-TTF) $_2\text{I}_3$. The divergent increase of the Korringa ratio by a factor of 1000 upon cooling evidences that α -(BEDT-TTF) $_2\text{I}_3$ at high pressure is far from behaving like a regular metal. Combining these observations with model calculations, Hirata *et al.* suggest that this divergence stems from an interaction-driven velocity renormalization that almost exclusively suppresses zero-momentum spin fluctuations because the long-range part of the Coulomb interaction remains unscreened around the Dirac points. In addition the bandwidth is reduced by short-range electron correlation. The NMR results also indicate that preexisting excitonic fluctuations in close proximity to the charge order govern the electronic nature in the low-temperature region. The excitonic instability is controlled by a small chemical-potential shift and an in-plane magnetic field. NMR relaxation rate probes these excitonic-spin fluctuations [245].

3.3.2.2. Domain Walls. Dielectric and optical studies of the anisotropic charge response in α -(BEDT-TTF) $_2\text{I}_3$ revealed two low-frequency relaxation modes (Figure 33), as discussed in full detail in Sections 3.4.2 and 3.4.3. Both modes can be attributed to the motion of domain wall pairs between two types of domains which are created due to breaking the inversion symmetry. The first mode is attributed to the motion of charged-domain walls along the a -axis, while the smaller second mode is associated with the motion of neutral 180° domain-wall pairs along the b -axis (cf. Figure 35).

Ohki *et al.* examined the detailed temperature dependence of the electronic states of interacting two-dimensional Dirac electrons in pressurized α -(BEDT-TTF) $_2\text{I}_3$ by using a semi-infinite two-dimensional lattice model [246]. Above the charge-order gap, a peak structure emerges due to the two-dimensional Dirac cones, which drastically changes in the vicinity of T_{CO} when they merge with the massive Dirac electrons [247]; a behavior not uncommon in indirect semiconductors. They also address the problem of domain wall conductivity in a charge-ordered insulating phase and can explain the

discrepancy of a small energy gap extracted from resistivity data [139] compared to the optical gap [163] by metallic conduction along a one-dimensional domain wall emerging at the border of two charge-ordered ferroelectric regions with opposite polarizations. With increasing intersite interaction V , a transition from the massless Dirac phase to the massive Dirac phase occurs simultaneously with the charge ordering [248–250]. Upon further increasing V , the system changes from the charge-ordered massive Dirac state to the charge-ordered state with no Dirac cones.

3.4. *Electrodynamics of weakly dimerized ferroelectrics*

Electronic ferroelectricity describes an ordering phenomenon that involves mainly electrons [102,110,115,124,251,252], in contrast to conventional ferroelectricity, for instance in BaTiO_3 or other titanates, where the ferroelectric properties are determined by the ions [86] (see the introductory part of this Chapter 3 and references therein for more information). In the above Section 3.2 we have discussed basic features characteristic for electronic ferroelectricity which have been observed in two-dimensional organic solids: the optical second harmonic generation, the development of charge disproportionation and the formation of ferroelectric domains. Here we continue by exploring dynamical features: hysteresis effect, specific dielectric response, and strong non-linear effects and ultrafast response.

3.4.1. *Polarization switching*

Polarization reversal or switching induced by an electric field is commonly considered as the most important property of ferroelectrics. The occurrence of a ferroelectric hysteresis loop is a direct consequence of the motion of domain walls which is microscopically explained by the switching of polarization. In the case of $\alpha\text{-(BEDT-TTF)}_2\text{I}_3$, Lunkenheimer *et al.* could proof ferroelectricity by conducting the respective polarization experiments [182]. In Figure 32 the polarization-induced current response is plotted as a function of time while the electric field is switched as shown in the upper inset. The polarization shows a hysteresis loop that closes around 20 kV/cm and

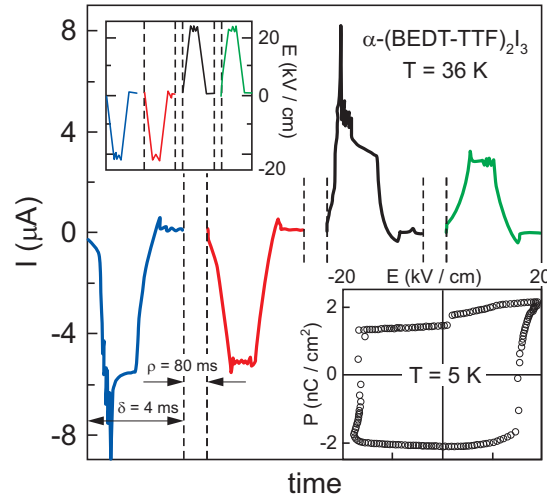


Figure 32. Time-dependent current of $\alpha\text{-(BEDT-TTF)}_2\text{I}_3$ at $T = 36\text{ K}$ (main frame) generated by the sequence of excitation signals plotted in the upper inset. The lower inset shows the polarization as a function of the electric field at $T = 5\text{ K}$ (after [182]).

exhibits the form typically observed in true ferroelectrics (lower inset of Figure 32). The latter result is obtained only at $T = 5$ K, probably because the conductivity at elevated temperatures is still too high and the remaining Ohmic losses prevent switchability [253]. Surprisingly, the saturation polarization of 2 nC/cm^2 is several orders of magnitude smaller than the values typically found in one-dimensional organic ferroelectrics such as TTF-CA [115]. This suggests that at $T = 5$ K only a tiny fraction of polar domains can be switched by the applied electric fields, indicating a high degree of cooperative freezing of the domain wall motion; for further discussion see Section 3.4.2. Finally, we note that in θ -(BEDT-TTF) $_2$ RbZn(SCN) $_4$ polarization switching has not been reported by now, which may be due to either relatively high conductivity or due to a low breakdown field.

3.4.2. Dielectric response

For α -(BEDT-TTF) $_2$ I $_3$ a rather complex and anisotropic dielectric response is observed in the Hz to MHz frequency range below T_{CO} [133,150,158,182,254,255]. To disentangle the different contributions, simultaneous fits of real and imaginary parts of the dielectric function by a generalized Debye form, known as Cole-Cole function [256,257], are performed as plotted in Figure 33. The results reveal that within the molecular planes the dielectric spectra exhibit substantial dispersion with two discernible contributions:

$$\varepsilon(\omega) - \varepsilon_\infty = \frac{\Delta\varepsilon_{\text{LD}}}{1 + (i\omega\tau_{0,\text{LD}})^{1-\alpha_{\text{LD}}}} + \frac{\Delta\varepsilon_{\text{SD}}}{1 + (i\omega\tau_{0,\text{SD}})^{1-\alpha_{\text{SD}}}} \quad , \quad (3)$$

where ε_∞ is the high-frequency dielectric constant, $\Delta\varepsilon$ is the dielectric strength, τ_0 the mean relaxation time and $(1 - \alpha)$ the symmetric broadening of the relaxation time distribution function of the large (LD) and small (SD) dielectric modes, respectively. The broadening parameter $(1 - \alpha)$ of both modes is about 0.70 ± 0.05 , and the dielectric strength does not change significantly with temperature. Importantly, $\tau_{0,\text{LD}}$ changes with temperature in a thermally activated manner, whereas $\tau_{0,\text{SD}}$ is temperature-independent and reminiscent of a domain-wall-like behavior.

These features of the dielectric response are strikingly different from the ones found

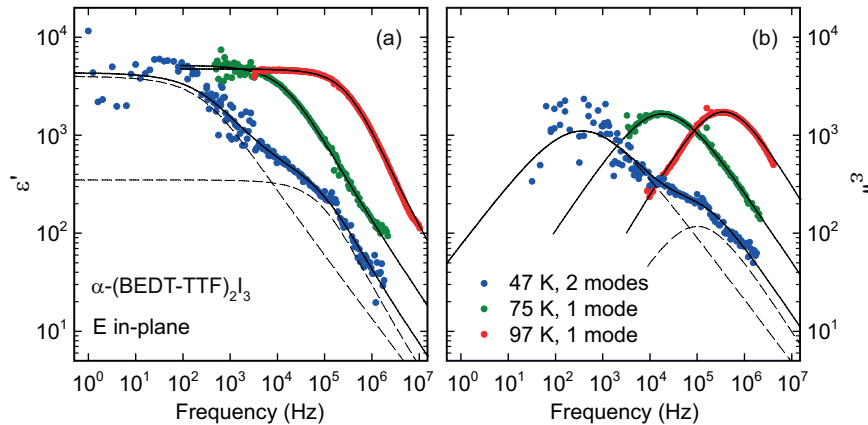


Figure 33. Double logarithmic plot of the real part (a) and imaginary part (b) of the in-plane dielectric function of α -(BEDT-TTF) $_2$ I $_3$ for three representative temperatures. For $T = 47$ K the full lines correspond to the fit to a sum of two generalized Debye functions; the dashed lines represent contributions of the two single modes. Above $T = 75$ K, only one mode is identified, and the full lines represent fits to single generalized Debye function (after [158]).

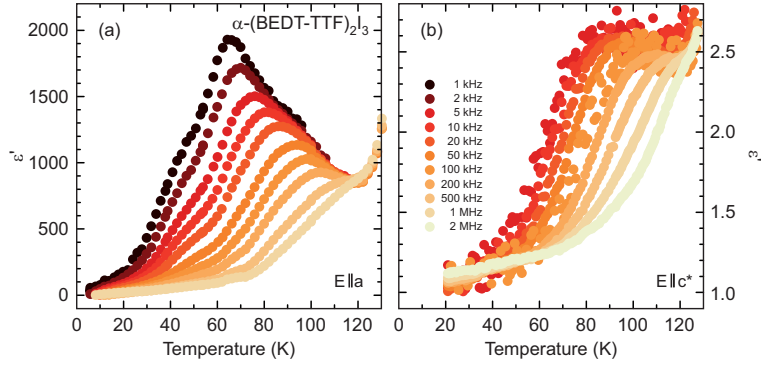


Figure 34. Temperature dependence of the real part of dielectric function of α -(BEDT-TTF) $_2$ I $_3$ measured (a) in plane and (b) out of plane for various frequencies as indicated (after [150]). For the in-plane direction a second, smaller peak is resolved in the temperature sweep of $\epsilon'(T)$ that corresponds to the complex two-mode response detected in frequency space, plotted in Figure 33.

in one-dimensional organic ferroelectrics, such as TMTTF $_2$ X and TTF-CA compounds (see [115] and references therein) and also reported in θ -(BEDT-TTF) $_2$ RbZn(SCN) $_4$ [258]. In those ferroelectrics a clear Curie peak is observed at T_{CO} , as expected for a regular ferroelectric phase transition. In contrast, α -(BEDT-TTF) $_2$ I $_3$ shows no sign of a non-dispersive Curie-like peak in $\epsilon'(T)$ at T_{CO} , where a clear-cut charge order occurs, as discussed in Section 3.2. Instead, when recording the dielectric response as a function of temperature as displayed in Figure 34, one finds a strongly dispersive peak in $\epsilon'(T)$ well below T_{CO} . It is more pronounced within the plane compared to the perpendicular direction. A finite out-of-plane component of polarization is expected due to an asymmetric charge distribution along the molecular axis oriented almost parallel to the c^* -axis, the direction perpendicular to molecular ab -planes (cf. Figure 3). For the in-plane orientation a second, smaller peak can be resolved; this particular detailed structure is due to the complex two-mode response as revealed by the data recorded in the frequency space. Distinct interpretations have been suggested to explain these observations ranging from two-dimensional cooperative bond-charge-density wave with ferroelectric nature [115,158,254], over relaxor-based picture [116,182] to disorder-induced scenario [150,158].

In the following we have to answer conclusively the fundamental question: what is the origin of the complex dielectric response in α -(BEDT-TTF) $_2$ I $_3$? The aim is to adequately describe both the large dispersive and small non-dispersive mode in the charge ordered state developed at long-range scale as testified by optical second harmonic generation (Figure 16) [168].

3.4.3. Domain walls

According to this interpretation, the long-range ferroelectric order remains in place. The failure in detection of the Curie peak is likely due to experimental problems related to the high conductivity at $T > T_{CO}$ and/or restricted frequency range of the dielectric measurements. The dielectric response in the charge order state of α -(BEDT-TTF) $_2$ I $_3$ is then naturally attributed to domain wall motion. This motion commonly depends on the interaction with randomly located defects, resulting in a distribution of relaxation times, just as observed. It indicates that the dielectric relaxation takes place between different metastable states, which correspond to local changes of the charge distribution across the length scale of the domain-wall thickness. In α -(BEDT-

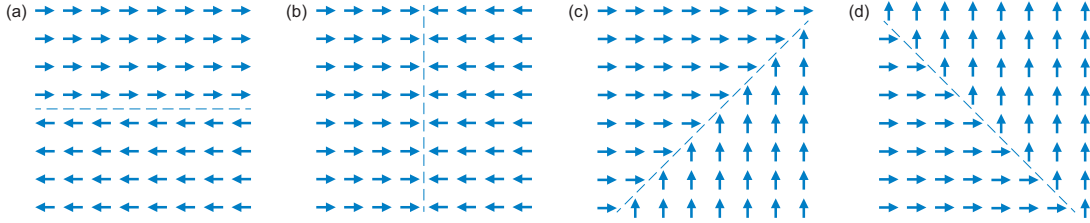


Figure 35. Different configurations of domain wall denoted by the dashed lines: (a) Sketch of 180° domain wall with dipoles oriented antiparallel next to each other. (b) Also a head-to-head arrangement is possible, leading to a charged domain wall. Panels (c) and (d) depict 90° domain walls.

$-\text{TTF})_2\text{I}_3$, disorder originates in the anions [133] and due to many short hydrogen bonds between anions and ethylene groups of BEDT-TTF molecules on A, A', and B sites [138] directly influence the charge response in the BEDT-TTF conducting layers [150,158].

Domain walls in ferroelectric crystals separate the symmetry-equivalent directions of the polarization; their creation minimizes the electrostatic and elastic energies [259]. They are commonly classified in two types according to the relative angle between the domain-wall plane and the polarization vector: electrically neutral domain walls and charged domain walls. Figure 35 illustrates that in two dimensions the neutral domain wall orientation is restricted to 180° and 90° walls; the former one segregate domains with antiparallel polarization, while the 90° walls separate regions with mutually perpendicular polarization. On the other hand, domain configurations with a jump of the normal component of polarization can be separated only by domain walls that carry bound charge. The creation of this type of walls require almost a perfect compensation by free charge carriers [260].

As mentioned in Section 3.2.2, x-ray diffraction and optical second-harmonic interferometry provide experimental evidence of domain walls in $\alpha\text{-(BEDT-TTF)}_2\text{I}_3$. Yamamoto *et al.* took images of large polar domains with opposite polarizations that are reproduced in Figure 36. They clearly resolved the formation of the boundary along the a -axis indicating 180° domains [170]. The mobility of these walls was determined by recording images of the same crystal area after rapid (panel c) and slow cooling (panel d) through the charge-ordering phase transition at $T_{\text{CO}} = 135$ K. The image of the domain structure in the annealed state demonstrates a lateral shift of the neutral 180° -wall and growth of the bright domain. Furthermore, the domain boundaries are rugged and a closer inspection reveals that they consist of both neutral and charged domain walls. Evidently, the latter are strongly pinned and thus much less mobile. A low degree of switchable polarization at $T = 5$ K, shown in Figure 32, may be a result of mobility difference between neutral and charged domain walls: only the domain states that contain neutral 180° -domain walls exhibit polarization switching.

On this basis, the complex dielectric response in $\alpha\text{-(BEDT-TTF)}_2\text{I}_3$ can be understood. Ivek *et al.* [158] suggested two possible types of domain-wall pairs with the constraint of charge neutrality implying that a change of stripes is equivalent to strictly replacing the unit cells of one twin type [(A,B)-rich unit cells] by another [(A',B)-rich unit cells], as depicted in Figure 18. In Figure 35(a) we illustrate that the first type is a pair of neutral 180° domain walls, *i.e.* a domain wall and the corresponding anti-domain wall between the charge-rich and charge-poor stripes along the b -axis. A second type of charged domain walls that develops along the a -axis is shown in Figure 35(b): here a jump of the normal component of the polarization is equal to the polarization itself. Importantly, in contrast to neutral 180° domain walls, the stability of charged

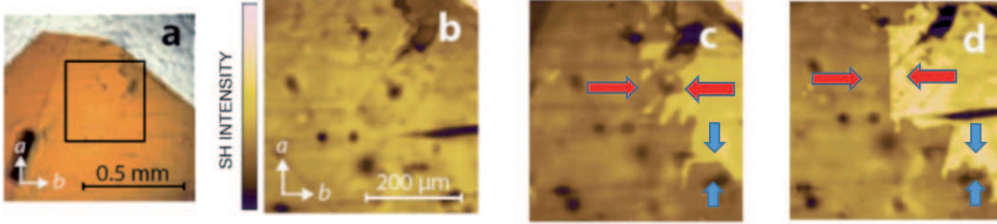


Figure 36. (a) Transmission image of a single crystal of α -(BEDT-TTF) $_2$ I $_3$. Square denotes the area of sample used in second harmonic generation (SHG) interferometry measurements; (b) SHG image taken at $T=140$ K (above T_{CO}) (c) SHG image taken at $T=50$ K (below T_{CO}) after rapid cooling. Bright and dark regions are split dominantly along the a -axis indicating 180° domain wall; (d) SHG image taken at 50 K after high-temperature annealing; the image reveals that the domains were displaced from the original positions before annealing dominantly along the b -axis. Red and blue arrows in (c) and (d) denote neutral and charged domain walls, respectively (reproduced from Yamamoto *et al.* [170] with the permission of AIP Publishing).

domain walls depends on the compensation by free charge carriers.

The nearly temperature-independent mean relaxation time of the small dielectric relaxation observed in α -(BEDT-TTF) $_2$ I $_3$ evidences that resistive dissipation is not dominant; thus it is described appropriately by 180° domain walls. Let's now return to the large dispersive dielectric mode observed in α -(BEDT-TTF) $_2$ I $_3$ (Figure 34). We propose that this dispersive mode is caused by the motion of charged-domain walls, whose formation should be promoted by screening since the charge-ordered state is characterized by a relatively high conductivity. They will remain stable as long as the free-charge-carrier screening effectively compensates their charges. Since dispersion is determined by the free carrier screening, the mode should follow a thermally activated behavior similar to the dc resistivity, exactly as observed.

There still remain some open questions concerning the dielectric response in α -(BEDT-TTF) $_2$ I $_3$. In order to reveal its microscopic origin, as well as to clarify the low degree of switchable polarization, further investigations of the topology of domain structure are highly desirable. A first approach was recently reported utilizing scanning near-field infrared nanoscopy in the vicinity of T_{CO} [184].

3.4.4. Non-linear effects and ultra-fast response

Domain wall motion may also be responsible for the huge negative differential resistance above very high threshold fields and in reversible switching to transient high-

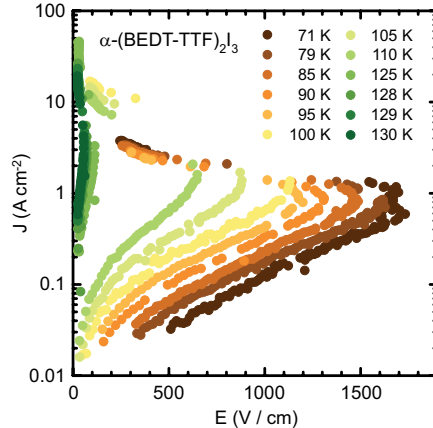


Figure 37. Current density J as a function of the applied electric field E measured in α -(BEDT-TTF) $_2$ I $_3$ at different temperatures below T_{CO} . A negative differential resistance behavior is observed above the threshold field, which increases with decreasing temperature (after [263]).

conducting states, plotted in Figure 37. Time- and field-dependent transport measurements on α -(BEDT-TTF) $_2$ I $_3$ provide evidence [261–263] that the rate of domain wall formation strongly increases when the dc electric fields is high enough to overcome their formation due to thermal excitations. Under these conditions, the motion of domain wall pairs becomes increasingly correlated and creates growing conduction regions until percolation promotes negative differential resistance. The time-dependent effects are due to changes in the coupling between molecular and anion sublattices induced by the applied electric field, otherwise involved in the charge-ordering phase transition [138].

Alternatively, the overall behavior can be explained within a two-state model of non-equilibrium electrons by excitation of charge carriers with the high mobility [263]. Especially optical studies show that transient optical properties of electric field-induced metallic state at about 125 K, *i.e.* close to T_{CO} , differ from the state induced deep in the insulating state at around 80 K. From Figure 38, we can see that the spectral signatures of the former are similar to the optical properties found for $T > T_{CO}$, while the spectral response of the latter evidences a novel electronically induced metallic-like state. Peterseim *et al.* suggest that the novel state is characterized by excitations of charge carriers with an extremely high mobility, which resemble massless Dirac-like carriers with linear dispersion found in α -(BEDT-TTF) $_2$ I $_3$ at high pressure [263] (cf. Section 3.3.2).

Another non-linear study performed at temperatures lower below $T = 60$ K revealed a power-law behavior in the current-voltage characteristics that is explained by assuming an electric field dependent potential barrier of the thermally excited topological defects such as electron-hole pairs and/or domain walls from the charged-ordered state [264]. On reducing the temperature, the power-law exponent increases from 1 to 3 around $30 \text{ K} < T_{KT} < 40 \text{ K}$, which is interpreted as a fingerprint of the Kosterlitz-Thouless type of transition. This interpretation implies that many topological defects exist above T_{KT} , while there remain only few below T_{KT} . Uji *et al.* [264] suggest that these very excitations, when polarized by an ac electric fields, also contribute to the in-plane dielectric function ϵ' . Finally, Okamoto and collaborators reported nonlinear electric transport measurements at 30 K conducted simultaneously with a terahertz-radiation imaging method. The results showed that in the negative differential resistance state the ferroelectric order melts in the elongated region forming

a nonlinear conducting path [265].

Electrical conductivity switching and negative differential resistance can also be induced by strong light pulses. Usually, photoexcited states undergo a rapid decay to the ground electronic state and most changes induced by photoexcitation occur transiently. Time-resolved measurements of the electrical conductivity are therefore required to detect a transient photo response. By irradiating the crystal with a pulsed laser, it is switched to a high conductivity state; then the current response to an applied voltage pulses is measured. Notably, the conductivity switching can be repeatedly retrieved by applied pulsed voltage without further irradiation, thus indicating a memory effect. The memory effect can be controlled by the temporal width and height of voltage pulses; it is understood in terms of a high current filament formation in the high conductivity state [266,267].

As the last point in this Section, we briefly address the photo-induced phase transition phenomena observed by time-resolved femtosecond pump-probe spectroscopy on these charge-ordered systems [168,268–273]. The findings strongly support a purely electronic mechanism of ferroelectricity, while the electron-phonon interaction resulting in the molecular rearrangements contribute to the decay processes. Iwai *et al.* found that charge order is destroyed by an initial femtosecond laser pulse; the charge-ordered state melts extremely fast on a sub-picosecond time scale, indicating that the initial process is purely electronic and no structural instability is associated with it. Microscopic metallic domains form within 15 fs; while in α -(BEDT-TTF)₂I₃ they condense further to a macroscopic metallic region on a timescale of about 200 fs, in θ -(BEDT-TTF)₂RbZn(SCN)₄ a large potential barrier against molecular displacement prevents the evolution of macroscopic metallic islands; this is sketched in Figure 39(a). Eventually, both systems relax back to the charge-ordered state within several picoseconds or nanoseconds. This fast relaxation is clearly different from the one at the millisecond time scale observed when a high dc electric field is applied, as shown in Figure 38. The decay processes strongly depend on temperature and light intensity: a significant slowing-down is found when the temperature rises close to T_{CO} suggesting an inhomogeneous character of the photo-induced metallic state. While for low intensities these microscopic metallic domains relax rapidly to the charge-ordered insulating state, for high laser intensities the decay time of metallic state gets markedly longer, enabling formation of macroscopic domains associated with some molecular rearrangement. The

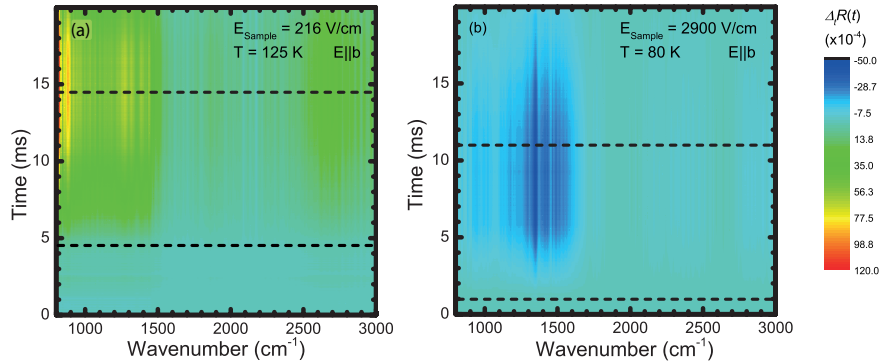


Figure 38. Contour plot of the reflectivity change $\Delta R(\nu, t)$ along the b -direction of α -(BEDT-TTF)₂I₃ at different temperatures: (a) At $T = 125$ K an electric field of $E_{\text{sample}} = 216$ V/cm is applied along the a -axis lasting for 10 ms. (b) At lower temperatures, $T = 80$ K, $E_{\text{sample}} = 2900$ V/cm have to be applied. The dashed horizontal lines mark the onset and end of the voltage pulse. The vertical stripes in the spectrum are due to instabilities of the interferometer mirror during the step-scan run (after [263]).

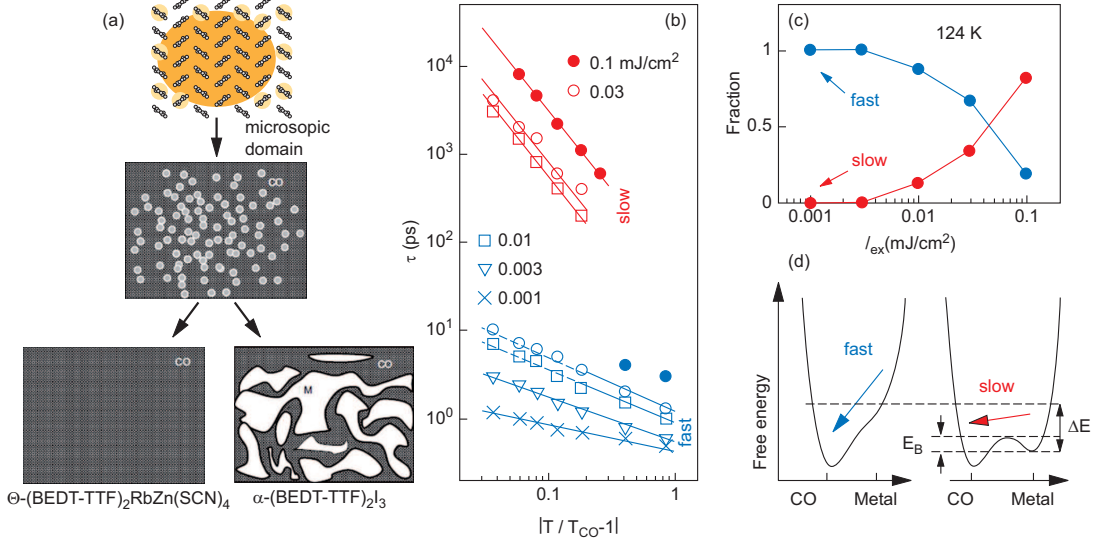


Figure 39. (a) Schematic representation of the primary processes of the photo-induced phase transition: initially the microscopic metallic domains are generated; they can quickly recover the charge ordered state as in θ -(BEDT-TTF) $_2$ RbZn(SCN) $_4$, or they can evolve in macroscopic metallic domains as in α -(BEDT-TTF) $_2$ I $_3$. (b) Relaxation times of the photoinduced metallic state in α -(BEDT-TTF) $_2$ I $_3$, τ_{fast} and τ_{slow} versus reduced temperature for several excitation intensities. (c) Fraction of the fast (blue dots: $\tau_{\text{fast}} \approx 1$ ps) and slow (red dots: $\tau_{\text{slow}} \approx 1$ ns) decay components as a function of I_{ex} at $T = 124$ K. (d) Schematic illustrations of free energy surface for $T \ll T_{\text{CO}}$ (fast relaxation) and $T \approx T_{\text{CO}}$ (slow relaxation). The energy barrier E_B is much smaller than the thermal energy $k_B T \approx 10$ meV (after [273]).

decay process consists of two components; the two relaxation times of the metallic state follow a critical slowing down behavior. Slower recovery takes place at the temperatures close to T_{CO} , while fast recovery occurs at the temperatures deep below T_{CO} . The corresponding relaxation times, slow and fast, are associated with the relaxation of macroscopic and microscopic metallic islands, respectively [Figure 39(b-d)].

Very recently an ultrafast response of the THz-wave generation was discovered in α -(BEDT-TTF) $_2$ I $_3$ upon photoexcitation [274,275]. The THz-wave generation by means of optical rectification is a second-order nonlinear optical process – the same way the generation of a second-harmonic signal (SHG) is. Remarkably, the electric field amplitude of THz-wave sets in at T_{CO} , as SHG does (Figure 16), indicating that it originates in charge ordering driven ferroelectric polarization.

The difference in the photo-induced dynamics found in α -(BEDT-TTF) $_2$ I $_3$ and θ -(BEDT-TTF) $_2$ RbZn(SCN) $_4$ are only quantitative. Numerical studies using the extended Peierls-Hubbard model on an anisotropic triangular lattice show [271] that this difference arises from the distinct crystallographic symmetry and different degree of structural modification associated with the thermally-driven charge order phase transition: in the former low-symmetry system it is very small [154,276], while in the latter high-symmetry compound it is rather substantial [50,56,167,277]. A detailed account of this topic is given by Iwai in [273].

3.5. Ferroelectricity driven by charge order in dimerized solids

Charge ordering phenomena are rare in dimerized two-dimensional BEDT-TTF compounds because the organic layers consist of face-to-face pairs of BEDT-TTF $^{0.5+}$ molecules, *i.e.* dimers, resulting in an effectively half-filled band. In that case the

onsite Coulomb repulsion U is much more important compared to the nearest neighbor interaction V . For a long time, there were only a few compounds reported to exhibit appreciable charge order, such as κ -(BEDT-TTF)₄PtCl₆·C₆H₅CN, the triclinic κ -(BEDT-TTF)₄[M(CN)₆][N(C₂H₅)₄]·3H₂O and the monoclinic κ -(BEDT-TTF)₄[M(CN)₆][N(C₂H₅)₄]·2H₂O (with $M = \text{Co}^{\text{III}}, \text{Fe}^{\text{III}}, \text{and Cr}^{\text{III}}$) salts. However, all of them are challenging to grow and limited in crystal size; hence details of their physical properties and electronic states are lacking at the moment [278–280].

Due to the lack of appreciable charge disproportionation in most of the commonly studied Mott insulators and quantum spin liquid compounds, a family of dimerized BEDT-TTF compounds has drawn particular attention, the κ -(BEDT-TTF)₂Hg(SCN)₂ X series, where $X = \text{Cl}^-, \text{Br}^-, \text{I}^-$, that was introduced almost twenty years ago by Lyubovskaya *et al.* [77,281–284]. In contrast to the κ -salts containing Cu-ion in the polymeric anion sheet, the BEDT-TTF molecules of the Hg-compounds are slightly displaced with respect to each other within a dimer, as shown in Figure 7(a). This results in a smaller intra-dimer transfer integral $t_d = 129$ meV and correspondingly a weaker on-site Coulomb repulsion $U \approx 250$ meV [75]. For the case of κ -(BEDT-TTF)₂Hg(SCN)₂Cl, *ab initio* density functional theory calculations were performed using the full potential local orbital basis, generalized gradient approximation and the room-temperature crystal structure [76]. With interdimer transfer integrals $t' = 51.0$ meV and $t = 40.4$ meV, as defined in Figure 7(b), the frustration is rather strong $t/t' \approx 0.8$, although not as close to unity as the canonical spin liquid systems listed in Table 1, Section 5.1.

κ -(BEDT-TTF)₂Hg(SCN)₂Cl is characterized by a moderate strength of dimerization, thus bridging the space between weakly dimerized, quarter-filled systems on one side (Chapter 3) and strongly dimerized, half filled dimer-Mott systems (Chapters 4 and 5) on the other side (cf. Hotta’s classification in Figure 69). At this point, it stands as a sole example of a dimerized solid that undergoes a pronounced metal-insulator phase transition due to charge ordering when cooled through $T_{\text{CO}} = 30$ K [75,285]. In the metallic state, at temperatures above T_{CO} , optical and dc resistivity properties are characteristic of a metal with half-filled band and strong electronic correlations. A broad band of the C=C vibration $\nu_{27}(\text{b}_{1u})$ peaks around 1455 cm^{-1} at room temperature and narrows on cooling down. Below about 100 K, it becomes obvious that the band consists of two peaks, which are assigned to the different environment of the BEDT-TTF molecules in the unit cell. Charge ordering is evidenced by a clear splitting of the ν_{27} mode below T_{CO} into two well-separated bands at 1441 and 1470 cm^{-1} , plotted in Figure 40. The splitting takes place as abruptly as in α -(BEDT-TTF)₂I₃ and θ -(BEDT-TTF)₂RbZn(SCN)₄ that exhibit charge ordering and ferroelectricity (see Section 3.2). Fitting the optical bands by two Fano resonances for temperatures above $T_{\text{CO}} = 30$ K and by four modes below T_{CO} reveals a charge imbalance of $2\delta_\rho \approx 0.2e$ between two different molecular sites, which are most likely located within the BEDT-TTF dimer. This value is certainly smaller than the charge disproportionation $2\delta_\rho \approx 0.6e$ found in α -(BEDT-TTF)₂I₃ and θ -(BEDT-TTF)₂RbZn(SCN)₄, but significantly larger than the charge disproportionation in other dimerized salts, such as κ -(BEDT-TTF)₂Cu[N(CN)₂]Cl or κ -(BEDT-TTF)₂Cu₂(CN)₃, that does not exceed the limit of $2\delta_\rho \approx \pm 0.01e$ (see Section 6.1).

The charge ordering transition in κ -(BEDT-TTF)₂Hg(SCN)₂Cl is of first order as testified by a strong change of the magnitude of low-frequency resistance fluctuations [286], and by jump-like anomalies of the relative length change, implying a divergent thermal expansion coefficient, and by thermal hysteresis between cooling and warming cycles [76]. The dominant lattice change takes place along the out-of-plane a -axis,

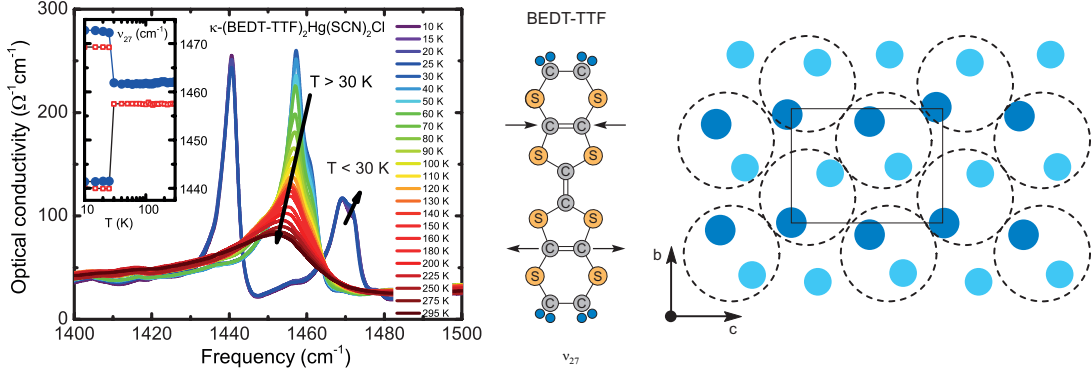


Figure 40. Molecular vibration $\nu_{27}(b_{1u})$ as a function of temperature of κ -(BEDT-TTF) $_2$ Hg(SCN) $_2$ Cl showing clear splitting when the charge ordering is established at $T_{CO} = 30$ K. A shoulder in the mode above T_{CO} indicating two crystallographically different sites per unit cell; below T_{CO} this becomes even more pronounced in two doubled components. The results of fits with two, respectively four components are indicated by red and blue dots in the inset (after [285]). On the right we show a schematic representation of the horizontal charge stripe arrangement within the bc dimer layer proposed for κ -(BEDT-TTF) $_2$ Hg(SCN) $_2$ Cl [75]. The dark and light blue circles denote charge-rich and charge-poor molecules, respectively.

indicating that the coupling between anions and molecular cations plays an important role in the formation of charge order. Lang and collaborators argue that the interplay between charge ordering and cation-anion coupling results in the charge stripes running along the c -axis (Figure 40), as previously proposed by Drichko *et al.* based on the large anisotropy of the optical spectra [75]. Unfortunately, an experimental evidence for the charge pattern shown in Figure 40 is still missing: x-ray diffraction measurements performed down to $T = 10$ K could not resolve any symmetry change [75].

The problem might be due to melting of charge order at low temperatures. Results from a recent Raman scattering study suggest that the charge-ordered state formed at $T_{CO} = 30$ K is not the ground state; rather it persists only down to $T = 15$ K and gradually melts below [287]. In Figure 41 the temperature evolution of the Raman spectra is plotted in the frequency range of the charge-sensitive $\nu_2(a_g)$ stretching vibration that involves the central C=C bond of the BEDT-TTF molecules. The single ν_2 mode at 1490 cm^{-1} corresponding to BEDT-TTF $^{0.5+}$ observed above T_{CO} , splits into two bands at 1475 cm^{-1} and 1507 cm^{-1} at $T = 20$ K, corresponding to BEDT-TTF $^{0.4+}$ and BEDT-TTF $^{0.6+}$ below T_{CO} . On cooling below 15 K, these bands gradually broaden, move closer in frequency and lose spectral weight concomitantly as the band corresponding to BEDT-TTF $^{0.5+}$ gains it. At $T = 2$ K the distribution of differently charged BEDT-TTF molecules $+0.4e : +0.5e : +0.6e$ is approximately equal to 0.3. The question remains whether this charge distribution is the final state or whether it changes on further cooling.

The charge-order phase transition in κ -(BEDT-TTF) $_2$ Hg(SCN) $_2$ Cl is extremely sensitive to external pressure: once the charge order is suppressed the compound remains metallic without indications of superconductivity [76,130,131]. This behavior is distinct from the linear pressure dependence of charge imbalance observed in α -(BEDT-TTF) $_2$ I $_3$ [163]. It is very surprising that such small pressure variations lead to so substantial changes in the electronic properties; it is only comparable to κ -(BEDT-TTF) $_2$ Cu[N(CN) $_2$]Cl, which is located next to the Mott insulator-metal transition, discussed in Section 4.1. In the case of the charge-ordered κ -(BEDT-TTF) $_2$ Hg(SCN) $_2$ Cl one does not expect that reducing the effective Coulomb repulsion V/W or U/W , where V , U and W are inter-site and on-site Coulomb interaction, and bandwidth,

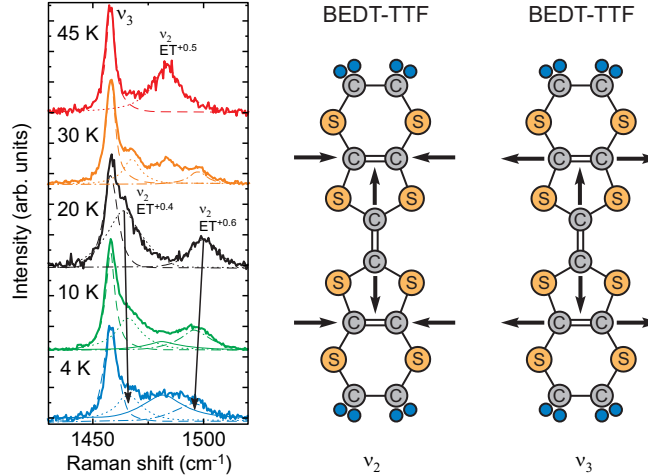


Figure 41. The fully symmetric molecular vibrations $\nu_2(a_g)$ and $\nu_3(a_g)$ are very sensitive to the local charge per molecule; the corresponding motion of the C=C bonds are indicated to the right. The Raman shift measured for κ -(BEDT-TTF) $_2$ Hg(SCN) $_2$ Cl at several representative temperatures above and below $T_{CO} = 30$ K evidences that the ν_3 remains unaffected. Significant changes, however, are observed for the ν_2 mode. $ET^{0.5+}$, $ET^{0.4+}$ and $ET^{0.6+}$ denote ν_2 bands corresponding to $+0.5e$, $+0.4e$ and $+0.6e$ charge per BEDT-TTF molecule. In the metallic state at $T = 45$ K BEDT-TTF $^{0.5+}$ band is observed, while in the charged ordered state at 20 K two bands BEDT-TTF $^{0.4+}$ and BEDT-TTF $^{0.6+}$ are clearly resolved. On further cooling at $T = 10$ K and 4 K signatures of charge order melting are detected: the two bands BEDT-TTF $^{0.4+}$ and BEDT-TTF $^{0.6+}$ broaden and a BEDT-TTF $^{0.5+}$ band emerges (after [287]).

respectively, is responsible for the pronounced effect. Löhle *et al.* suggested that the lattice plays an important role in the phase transition [130]. However, from Raman spectroscopy no major changes of lattice phonons are observed at T_{CO} implying that the coupling of the charge order to the lattice is weak.

Finally, indications for ferroelectricity driven by charge-order in κ -(BEDT-TTF) $_2$ -Hg(SCN) $_2$ Cl, were provided by dielectric spectroscopy, albeit no polarization switching could be recorded so far, probably due its rather high in-plane conductivity [76]. For that reason, the dielectric measurements were performed with the ac electric field applied along the out-of-plane a -axis only. The dielectric response observed in the MHz frequency range exhibits some features expected for conventional ferroelectrics: Curie-like peak occurs in the real part of dielectric function $\epsilon'(T) \approx 400$ right at $T_{CO} = 30$ K with negligible dispersion. Also, the two branches of $1/\epsilon'(T)$ above and below T_{CO} are close to linear; the slope in the ordered state is much larger than the one above T_{CO} . It was suggested that the ferroelectric order formed below the metal-insulator transition is of order-disorder type [76]. However, a pronounced frequency dependence of $\epsilon'(T)$ is expected in this case [288], just in contrast to what is observed. Order-disorder type implies that disordered electric dipoles exist already in the metallic phase above T_{CO} , but compelling experimental evidence for this proposal is lacking. Another important issue in this regard is the anionic contribution to the measured dielectric response. As pointed out [76], the anions are mobile in some way and shift towards charge-rich molecular sites in the vicinity of T_{CO} in order to minimize overall Coulomb energy; this arrangement stabilizes the long-range charge order. This implies that the dielectric measurements along the a -axis probe not only the electronic but also the anionic contribution to the dielectric response, because this is exactly the direction the cationic BEDT-TTF molecules and the anion layers alternate. Recently it was shown [289] that similar effects happen in the quasi-one-dimensional organic ferroelectrics (TMTTF) $_2X$.

We close by noting that the subject of ferroelectricity driven by charge order in dimerized solids deserves more attention in future. Specifically, efforts should be invested to unravel conclusive experimental evidences for the charge stripe pattern in the ground state, the role of electron-phonon coupling and the intrinsic dielectric response.

4. Mott Metal-Insulator Phase Transition

The properties of materials are only understood when their ground states and phase transitions can be described and predicted. In the case of correlated electron systems, the Mott metal-insulator transition (MIT) serves as the litmus test: no structural modification drives the phase transition but the increasing influence of electronic repulsion [290–293]. Tremendous efforts have been devoted to this fundamental problem, nevertheless there is still no general agreement on all detail how the Mott transition actually takes place. The validation of theoretical advances by meaningful experiments on suitable model systems turns out to be the real challenge. Research was boosted on the experimental and theoretical frontier by the discovery of high-temperature superconductivity in cuprates, which are doped Mott insulators [38]. But one should keep in mind that raising the carrier concentration yields a rather different scenario than varying correlations at constant half band filling. In this regard the bandwidth-tuned metal-insulator transition in vanadium oxides has been intensely studied for decades [294–297], however, there is still no unanimous conclusion to what extent it is affected by corresponding structural transitions or solely driven by strong electron–electron correlations [298–301]. Unfortunately, the majority of transition-metal oxides undergoes antiferromagnetic (afm) order in the insulating state at low temperatures preventing the exploration of the genuine Mott state and metal-insulator transition [38]. At the phase transition not only the electronic properties change but also the magnetic degrees of freedom.

Having said that, organic charge-transfer salts are realized by now as superior model systems for studying Mott physics:

- The energy scales are much smaller compared to transition metal compounds, allowing the coverage of a significantly wider range in effective temperature T/W and correlations U/W . The investigations are also carried out at lower temperatures – but still accessible for regular helium cryostats – where thermal fluctuations are of minor importance and quantum effects may become decisive.
- Since the compounds are rather soft, external pressure is a powerful tool to substantially increase the orbital overlap t and hence the bandwidth W . Alternatively, isovalent substitution of anions with different size acts as chemical pressure. Furthermore, the bandwidth can be readily varied by chemical substitution in the organic donor molecules, for instance, when replacing S by Se.
- For comparison with theory it is advantageous that most organic systems under study, contain only a single band of relevance.
- In analogy to transition metal oxides, the simple or extended Hubbard model can be applied to these strongly correlated molecular compounds. The Mott transition results in splitting the conduction band into lower and upper Hubbard bands with a gap at the Fermi energy of typically 0.2 to 1 eV. No charge-transfer band disturbs this ideal scenario.

In a first approach, we assume that the Mott gap gradually closes by reducing the electron-electron interaction U or increasing the bandwidth W , implying that the Mott

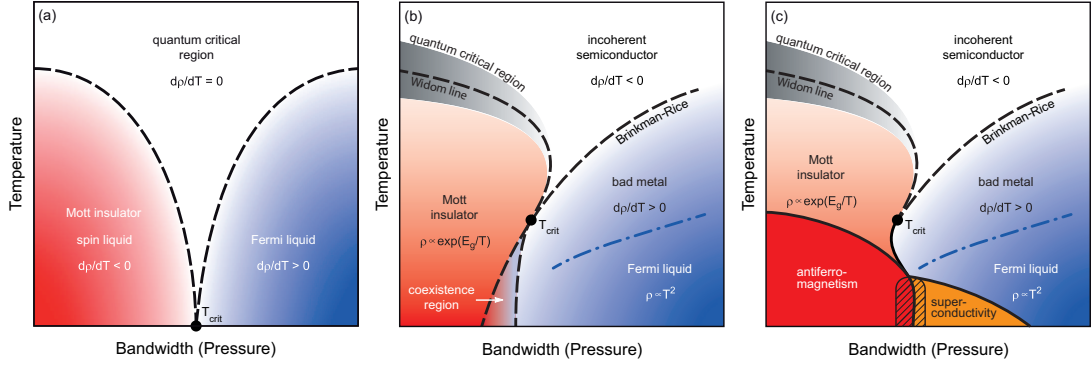


Figure 42. Upon tuning the bandwidth by chemical or physical pressure, for instance, a paramagnetic Mott insulator transforms to a correlated metal. Different theoretical scenarios of the Mott insulator-metal transition are considered. (a) Based on mean-field theory, a quasi-continuous transition from a Mott insulator to the Fermi liquid through a quantum critical point at $T_{\text{crit}} = 0$ is suggested for quantum spin liquids with spinon quasiparticles on the Mott insulating side [302,303]. (b) For a fully frustrated system with no magnetic order, dynamical mean-field theory predicts a first-order transition with phase coexistence up to the critical endpoint T_{crit} [304], and a fan-shaped quantum-critical regime associated with the quantum Widom line at higher temperatures [305,306], in excellent agreement with experiment [307–309,309]. The metallic state is confined by the Brinkman-Rice temperature [310,311], identified by a maximum in $\rho(T)$; the coherent Fermi-liquid regime occurs at lower temperatures. When thermal fluctuations exceed the bandwidth W and interaction strength U , semiconducting behavior prevails; neither a gap nor a quasiparticle peak are stabilized. (c) Strong magnetic interactions commonly leads to antiferromagnetic order of the Mott insulator at low temperatures with significant impact on the phase boundary. A spatial coexistence of antiferromagnetic order and superconductivity is observed in the vicinity of the first-order phase transition.

transition is of second order [302,303,312]. For the particular case of two-dimensional systems with no long-range magnetic order, one expects a direct and continuous transition between a paramagnetic metal and a paramagnetic Mott insulator as sketched in Figure 42(a). This would be a particular example of a quantum critical point at $T = 0$ unrelated to any mechanism of spontaneous symmetry breaking. As correlations become more effective, the weakly-correlated Fermi liquid with Landau quasiparticles vanishes at the Mott critical point. However, there remain gapless spin excitations (spinons) on the insulating side, *i.e.* a Mott insulating spin liquid with a spinon Fermi surface. Both the gap in the spectral function and the quasiparticle weight vanish at the critical point. At finite temperatures there is a crossover to a marginal spinon liquid and a marginal Fermi liquid, respectively. Above the Mott critical point a quantum critical regime develops with non-Fermi-liquid properties [303].

In contrast to this scenario, already Mott predicted that the transition between the insulating and metallic states should be discontinuous, implying a regime of coexistence, as depicted in Figure 42(b). Calculations based on dynamical mean field theory (DMFT) [304,313–317] confirm the picture of a first-order phase transition with a coexistence region on both sides limited by spinodal lines that end at the critical endpoint T_{crit} , which now has moved to finite temperatures. In the high-temperature crossover region ($T > T_{\text{crit}}$) paramagnetic DMFT calculations on a single-band Hubbard model at half filling yield quantum critical transport [305,306,318] that spreads out following the quantum Widom line. For experimental verification of this behavior, it is decisive that the critical endpoint is only around 20 to 40 K for κ -(BEDT-TTF) $_2X$ salts, while $T_{\text{crit}} \approx 450$ K is an order of magnitude larger for $(V_{1-x}Cr_x)_2O_3$ [296].

The electronic phase diagram resembles the thermodynamic phases of classical gases and liquids. The phase boundary in the p - T -diagram is well defined only up to the critical endpoint T_{crit} ; in the supercritical regime above, there is no way to strictly

distinguish gas from liquid [312,319]. The Widom line is the crossover between liquid-like and gas-like behavior [320,321] and can be identified by changes in the derivative, as illustrated in Figure 48 for the case of electronic analogues of interest here.

Except for a few quantum spin liquid candidates, organic Mott insulators are also prone to antiferromagnetic order at low-enough temperatures [322], which gives an additional twist to the insulator-metal boundary [Figure 42(c)] rendering the common negative slope $dT/dp < 0$ due to the magnetic contribution to the entropy [323]. The common border of antiferromagnetism and superconductivity implies important contributions of spin fluctuations to the superconducting glue, similar to transition metal oxides. Let us consider this case first before we discuss the fully-frustrated paramagnetic insulators.

4.1. Antiferromagnetic Mott insulator

Here the antiferromagnetic Mott insulator κ -(BEDT-TTF)₂Cu[N(CN)₂]Cl certainly is of superior importance because a tiny pressure of 30 MPa suffices for entering the metallic or superconducting phase with the record high $T_c \approx 13$ K. At elevated temperatures, the overall charge transport is incoherent; but upon cooling the behavior bifurcates. At ambient pressure, the system becomes a pronounced insulator: a maximum of the transport gap derived from the logarithmic derivative of $\rho(T)$ indicates the so-called quantum Widom line [308,324]. This crossover from a more insulating to a more metallic regime is best seen in electrical transport studies using pressure sweeps at fixed temperatures [325]. Furukawa *et al.* investigated several organic Mott insulators and could extract extended crossover regimes as plotted in Figure 43. The observed behavior collapses into a genuine phase diagram for all compounds, displayed in Figure 48, if the temperature T and the electronic correlations U are normalized by the respective bandwidth W [308]. Using advanced temperature-dependent scaling, a mirror-symmetric behavior on the insulating and metallic sides can be obtained, leading to a fan-shaped quantum critical region in the pressure-temperature phase diagram. A material-independent quantum-critical scaling relation was identified with a clear distinction into a Fermi liquid or a Mott insulator, irrespective of the ground states of the organic compounds [325]. The observed Mott quantum criticality confirms the predictions of Dobrosavljević and collaborators [305], who calculated the incoherent charge transport in the high-temperature crossover region.

4.1.1. Mott quantum criticality

The critical point $T_{\text{crit}} \approx 40$ K has drawn particular interest as it ends the first-order phase boundary, and might act as the starting point for quantum critical behavior. In the seminal work on Cr-substituted V₂O₃, Limelette *et al.* analyzed the critical exponents and scaling functions close to the critical endpoint of the Mott metal-insulator transition [Figure 43(f)]

$$\sigma - \sigma_c \propto (T_{\text{crit}} - T)^\beta, \quad \sigma - \sigma_c \propto (p - p_{\text{crit}})^{1/\delta}, \quad (d\sigma/dp)|_{p_c(T)} \propto (T - T_{\text{crit}})^\gamma, \quad (4)$$

and found the universal properties of a liquid-gas transition [296]; *i.e.* $\beta = 0.5$, $\delta \approx 3$, and $\gamma = 1$ as predicted by mean-field theory [327,328]. These critical exponents are believed to be universal, *i.e.* independent on the microscopic details of the system [312,319]. Along these lines, Kagawa *et al.* investigated κ -(BEDT-TTF)₂Cu[N(CN)₂]Cl using a variable gas pressure cell down to $T = 33$ K [329,330]; the critical exponents

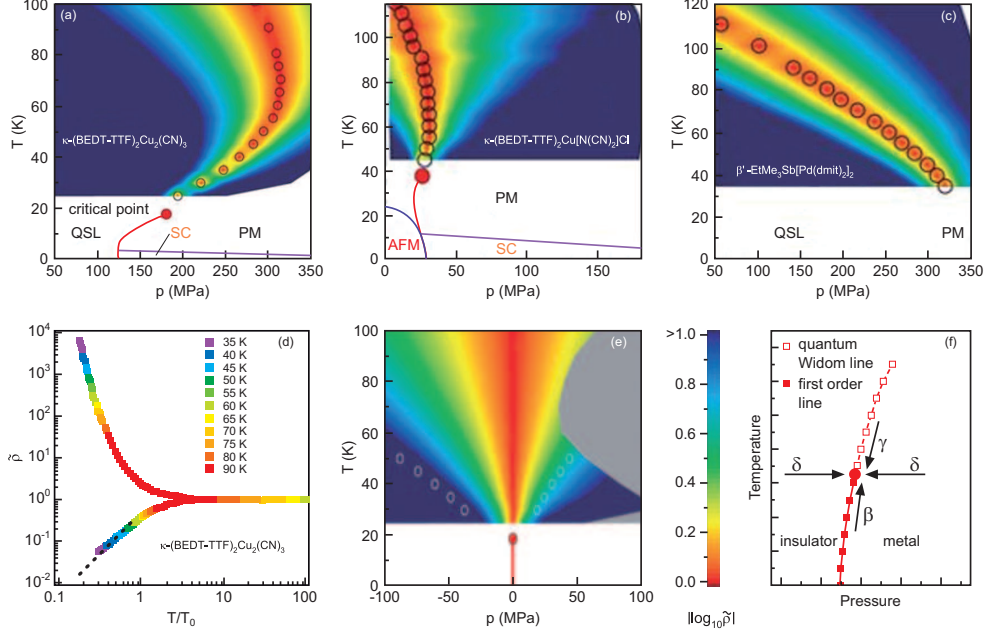


Figure 43. Pressure–temperature phase diagram of (a) κ -(BEDT-TTF)₂Cu₂(CN)₃, (b) κ -(BEDT-TTF)₂Cu-[N(CN)₂]Cl and (c) β' -EtMe₃Sb[Pd(dmit)₂]₂ obtained from resistivity measurements in a gas-pressure cell. QSL stands for quantum spin liquid, SC for superconductor, AFM for antiferromagnet and PM for paramagnetic metal. The red line represents the first-order Mott transition line terminating at a critical end point. The open circles indicate the metal–insulator crossover pressure $p_c(T)$. The color represents the magnitude of $|\log_{10} \tilde{\rho}|$, where $\tilde{\rho}$ is the normalized resistivity. (d) The scaling plot of the normalized resistivity $\tilde{\rho}(\delta p, T)$ versus $T/T_0 = T/|c \delta p|^{z\nu}$ with the present values, $z\nu = 0.62$ and $c = 20.9$ for κ -(BEDT-TTF)₂Cu₂(CN)₃. (e) A symmetric quantum critical region can be obtained by renormalizing the axes. A range of colour represents the magnitude of $|\log_{10} \tilde{\rho}|$ for κ -(BEDT-TTF)₂Cu₂(CN)₃, where $\tilde{\rho}$ is the normalized resistivity. The grey-colored region is experimentally inaccessible. The bold red line represents the first-order Mott transition line terminating at a critical endpoint. The insulating and metallic states form at $\delta p < 0$ and $\delta p > 0$, respectively. The open circles indicate the characteristic temperatures for the entrance to the low-temperature regimes of the gapped Mott insulator or the Fermi liquid, T^* , defined by the value of T/T_0 at which $\tilde{\rho}(\delta p, T)$ starts to deviate from the critical behavior $\tilde{\rho} = \exp\{\pm(T/T_0)^{-1/z\nu}\}$ ($z\nu = 0.62$). Below these circles, the system departs from the quantum critical regime toward the Mott insulator ($\delta p < 0$) or Fermi liquid ($\delta p > 0$) (data from [325]). (f) Scheme how the different critical exponents β , γ and δ are determined from scans in the phase diagram as a function of temperature and pressure (suggested in [326]).

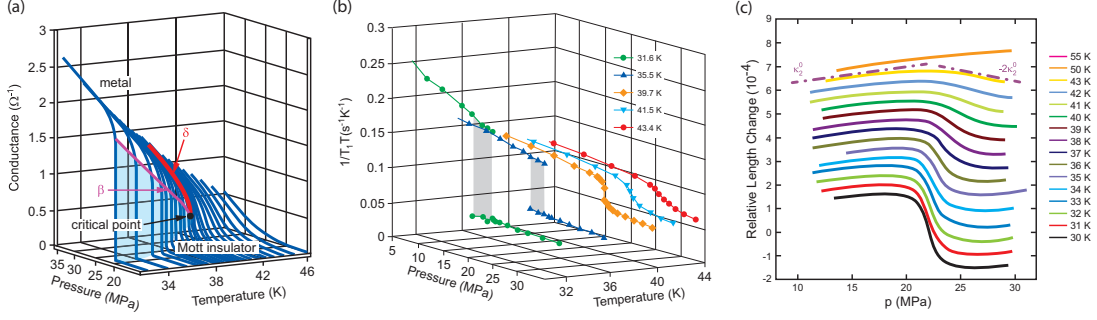


Figure 44. The critical behavior is observed in the electrical, magnetic and lattice degrees of freedom. (a) Pressure-dependent conductance $G_T(p)$ of κ -(BEDT-TTF) $_2$ Cu[N(CN) $_2$]Cl measured at various temperatures around the critical endpoint (filled circle). The shaded area indicates the conductance jump. The red and green curves represent the critical behaviour at $T = T_{\text{crit}} \approx 39.7$ K and $T < T_{\text{crit}}$, which give the critical exponents δ and β , respectively. The hysteresis of the conductance jump (for example, ~ 0.2 MPa at ~ 32 K) is not appreciable at this scale. (reproduced from [329] with permission). (b) ^{13}C -NMR relaxation rate around the Mott critical endpoint T_{crit} . The pressure dependence of $1/T_1T$ at various fixed temperatures; note the reversed pressure scale, compared to panel (a). The gray shaded areas represent the coexistence of insulating and bad metallic phases (taken from [331]). (c) Relative length changes, $\Delta L/L$, as a function of applied pressure at constant temperatures between 30 and 55 K measured on κ -(BEDT-TTF) $_2$ Cu[N(CN) $_2$]Cl along a -axis. The data have been offset for clarity. The broken lines close to the data at $T = 43$ K, that is, distinctly above $T_{\text{crit}} \approx 36.5$ K of the critical endpoint, are guides to the eyes and serve to estimate the pressure-induced changes in compressibility. The strong non-linearities, which are observed here, reflecting nonlinear strain-stress relations, highlight a breakdown of Hooke's law of elasticity (data from [326]).

extracted ($\beta = 1$, $\delta = 2$, and $\gamma = 1$) did not correspond to any known universality class [Figure 44(a)]. The analysis extended up to $|T - T_{\text{crit}}|/T_{\text{crit}} < 0.2$ with significant deviations close to the critical endpoint.

Although the Mott transition takes place in the charge sector, it is interesting to consider also the spin degrees of freedom in these strongly correlated electron systems. The spin-lattice relaxation rate $1/T_1$ measured by ^{13}C -NMR is a probe of spin fluctuations. A clear jump in $1/T_1T$ is observed at the Mott transition at low temperatures when the system is isothermally tuned across the transition by He-gas pressure [331], as depicted in Figure 44(b). The jump vanishes at the critical point and only a smooth cross-over remains at higher temperatures. As seen in Figure 44(a) and (b), the conductance is enhanced when the Mott transition is crossed to a metal with increasing pressure; the paramagnetic spin fluctuations are strongly suppressed. $[1/T_1(p)T - 1/T_1(p_c)T]$ follows a power law $|p - p_c|^{1/\delta}$ with $\delta = 2$, again. Any deviation from the average value of one electron per site obviously makes charge carriers contribute to the conductivity, but in addition spin fluctuations are suppressed [332]. The subject remains open for future investigations.

Commonly neglected by theory, the electronic system couples to the underlying compressible crystal lattice. Lang and collaborators thoroughly measured the temperature and pressure dependence of the thermal expansion in order to study the lattice response near the Mott transition. Fully deuterated κ -(d8-BEDT-TTF) $_2$ Cu[N(CN) $_2$]Br falls extremely close to the critical point already at ambient pressure [333]; it was found that near the critical endpoint the Grüneisen scaling breaks down [334–338]. In a next step κ -(BEDT-TTF) $_2$ Cu[N(CN) $_2$]Cl could be deliberately tuned across the Mott transition using a continuously controlled helium-gas pressure. The relative length change $\Delta L/L$ with pressure exhibits a strong nonlinear variation around T_{crit} ; here Hooke's law of elasticity breaks down [326]. Figure 44(c) displays $\Delta L/L$ as a function of pressure measured within the plane at various temperatures; similar re-

sults are recorded perpendicular to the ac -plane. At $T = 30$ K an abrupt jump is observed, reflecting the first-order character of the phase transition. As the temperature rises, the discontinuity gradually decreases until it becomes a continuous crossover for $T > T_{\text{crit}}$. Slightly above the critical endpoint the relative length change is rather nonlinear, which is explained by a critical elasticity as a result of the coupling of the critical electronic background to the lattice; in other words Hooke's law does not hold in the temperature-pressure regime close the critical endpoint. The critical exponents [Eq. (4)] extracted from the experimental data, $\beta = 0.52$, $\delta = 3.2$, and $\gamma = 1.0$, are in good consistence with the values for the mean-field universality class. There are valid arguments that this behavior at the Mott transition holds for all systems that are amenable to pressure tuning [326].

While κ -(BEDT-TTF)₂Cu[N(CN)₂]Br is well on the metallic side of the phase boundary, the successive substitution of deuterated (d8-BEDT-TTF) molecules effectively increases correlations and eventually shifts the alloy across the Mott transition. Magnetotransport measurements by Sasaki *et al.* [339] found that a suppression of T_c in magnetic fields; for $H > H_{c2} \approx 12$ T the superconducting phase has completely vanished. The critical endpoint T_{crit} , however, seems not to be affected. An alternative approach utilizes x-ray irradiation to systematically influence the critical behavior in κ -(BEDT-TTF)₂Cu[N(CN)₂]Cl [340]. The introduced disorder reduces the superconducting transition temperature T_c only slightly but strongly affects the resistivity around the critical endpoint. Pressure-sweeps at fixed temperatures down to 15 K yield a broadening of the phase transition and a corresponding shift of T_{crit} . Analyzing their data according to Figure 43, Urai *et al.* found that the exponent $z\nu \approx 0.46$ basically does not change upon irradiation up to 70 h. The drastic suppression of the critical end point T_{crit}^* is interpreted as disorder-enhanced critical fluctuations of the metal-insulator transition. They speculate that the Mott quantum critical fluctuations are hidden behind the first-order transition and can be revealed by disorder. However, this implies that the system is spatially homogeneous for $T > T_{\text{crit}}^* \rightarrow 0$ due to disorder, which is in contrast to the coexistence regime. As discussed in more detail in Sec. 4.4, extended irradiation blurs any clear signatures of a discontinuous metal-insulator transition [76]; *i.e.* above a certain disorder level, the Mott transition becomes a smeared first-order transition with some residual hysteresis.

4.1.2. Coexistence regime

The Mott transition is supposed to be of first order below the critical endpoint T_{crit} , implying a pressure region in which correlated metal and insulator coexist [304,317, 341]. Limelette *et al.* measured the in-plane electrical transport of κ -(BEDT-TTF)₂-Cu[N(CN)₂]Cl at fixed temperatures below $T_{\text{crit}} \approx 40$ K in a gas pressure cell [342] and observed a marked hysteresis around the metal-insulator transition that was attributed to spatial inhomogeneities. As depicted in Figure 45(a), the coexistence regime extends over a pressure range of approximately 20 MPa, as determined from the inflection in the conductivity data $\sigma(p)$ upon increasing and decreasing pressure.

Below $T_N \approx 25$ K, antiferromagnetic ordering occurs that was investigated by magnetic resonance spectroscopy and other methods [343,344]. Extended ac susceptibility measurements as a function of pressure for selected temperatures as well as by taking cooling and heating curves at fixed pressure values were used by Lefebvre *et al.* to map the coexistence regime between the antiferromagnetic Mott insulator and superconducting states [344] as plotted in Figure 45(b). Below a characteristic temperature $T^* \approx 20$ K the NMR lines split into two groups corresponding to a metallic (super-

conducting) and an insulating (antiferromagnetic) phase that spatially coexist. These remarkable findings evidence percolative superconductivity [345–347]. The results indicate the absence of itinerant antiferromagnetism in κ -(BEDT-TTF)₂Cu[N(CN)₂]Cl,

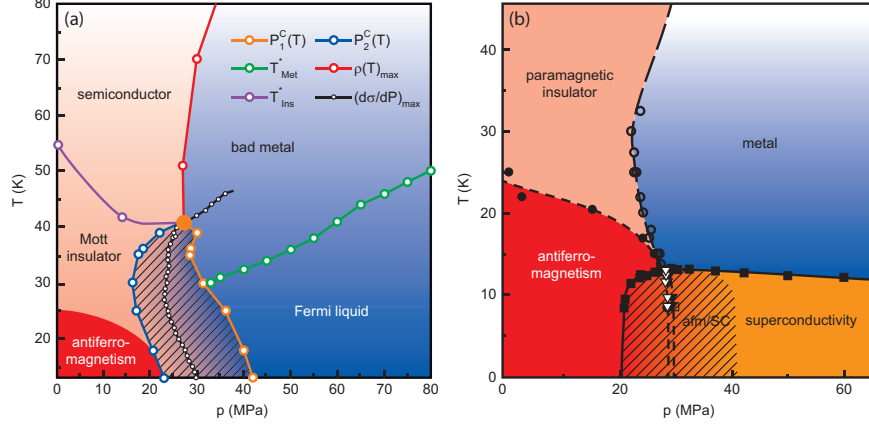


Figure 45. Pressure-temperature phase diagram of the κ -(BEDT-TTF)₂Cu[N(CN)₂]Cl salt. (a) Four regions can be identified from transport measurements [342]: bad metal, Fermi liquid, semiconductor and insulator, which orders antiferromagnetically below $T_N \approx 25$ K [343,344]. The spinodal lines define the region of coexistence of insulating and metallic phases, which is indicated by the hatched area. The first-order transition line is identified by the maximum slope $d\sigma/dP$ and terminates at the critical end point. (b) The antiferromagnetic critical line $T_N(P)$ (dark circles) was determined from NMR relaxation rate while $T_c(P)$ for unconventional superconductivity and the metal-insulator $T_{\text{MI}}(P)$ (open circles) lines were obtained from the ac susceptibility. The afm/SC boundary (double-dashed line) is determined from the inflection point of $\chi'(P)$ and, for 8.5 K, from sublattice magnetization. This boundary line separates two regions of inhomogeneous phase coexistence (shaded area) (adopted from [342,344]).

confirming previous suggestions [348]; the interacting spins are localized on the dimers. This scenario is in contrast to (TMTSF)₂PF₆, where superconductivity coexists with the itinerant antiferromagnetism of the spin-density-wave phase [349]. In the present case superconductivity can be directly stabilized from the antiferromagnetic Mott insulator.

These findings were confirmed by ultrasonic velocity and attenuation measurements on κ -(BEDT-TTF)₂Cu[N(CN)₂]Br [350] where the coexistence zone of the antiferromagnetic and superconducting phases was observed deep in the metallic part of the pressure-temperature phase diagram. The system was tuned by varying the cooling cycle, *i.e.* fast, slow cooling, low-temperature annealing. The two phases are found to compete, whereas superconducting fluctuations begin to contribute to the attenuation at 15 K, namely, at the onset of magnetic order that is well above the superconducting transition temperature $T_c = 11.9$ K.

In order to demonstrate the spatial phase separation Kimura and collaborators [352,353] studied the properties of partially deuterated κ -(BEDT-TTF)₂Cu[N(CN)₂]Br using spatially resolved magneto-optical spectroscopy. While they can conclude a coexistence of the metallic or superconducting phases with the insulating phase, the present resolution of approximately 10 μm constitutes only an upper limit. Interestingly, with increasing magnetic field, the insulator-metal phase boundary shifts towards smaller U/W , in accord with transport experiments [339]; above H_{c2} , however, they suggest an enlargement of the metallic regime. Concomitantly, Sasaki *et al.* focussed on the vibrational features of κ -(BEDT-TTF)₂Cu[N(CN)₂]Br to obtain

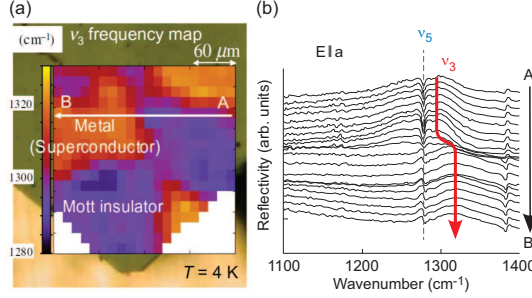


Figure 46. (a) Peak frequency contour map of the ν_3 mode ($E \parallel a$ -axis) of κ -[(h8-BEDT-TTF) $_{0.4}$ (d8-BEDT-TTF) $_{0.6}$] $_2$ Cu[N(CN) $_2$]Br at $T = 4$ K. Bright orange colors (higher frequency) indicate a metallic nature and dark violet colors (lower frequency) indicate an insulating nature. The metal–insulator phase separation can be observed as a spatial image. (b) Reflectivity spectra along the arrow A–B in panel (a) with a $12 \mu\text{m}$ steps (reproduced from [351]).

the crucial contrast between metallic and insulating regions when tuning through the phase transition by different amount of deuteration [351,354,355]. The fully symmetric $\nu_3(a_g)$ mode around 1300 cm^{-1} is strongly electron-molecular vibrational (emv) coupled [41,159,160] and provides a local probe for detecting changes in the electronic state. Figure 46 displays a contour map of metallic and insulating regions having micrometer sizes and irregular shapes. The boundary between the insulating and metallic regions is within the instrumental resolution, and hence no intermediate state appears at the frontier. This observation indicates a macroscopic phase separation between the metal/superconductor and Mott insulator. Since the system falls right at the characteristic S-shape phase boundary, the sample crosses the first-order transition when cooled from room temperature. The phase separation occurs after intersection with the first-order transition line.

Müller *et al.* [356,357] established fluctuation spectroscopy as a powerful method for investigating the dynamics of correlated charge carriers in the vicinity of the Mott transition in the quasi-two-dimensional charge-transfer salts, looking in particular at κ -(d8-BEDT-TTF) $_2$ Cu[N(CN) $_2$]Br. The observed $1/f$ -type fluctuations are quantitatively very well described by a phenomenological model based on the concept of non-exponential kinetics. The main result is a correlation-induced enhancement of the fluctuations accompanied by a substantial shift of spectral weight to low frequencies in the vicinity of the Mott critical end point. This sudden slowing down of the electron dynamics is considered as a universal feature of metal-insulator transitions. The findings support the idea of electronic phase separation in the critical region of the phase diagram [356,357].

4.2. Frustrated Mott insulator

In order to target investigations of the genuine Mott transitions without being affected by magnetic order, quantum spin liquids are the systems of choice. As illustrated in Figure 42(b), the phase boundary is solely determined by the electronic degrees of freedom; hence magnetic contributions to the entropy are absent. In this case, Clausius-Clapeyron relation implies that the phase boundary acquires a positive slope

$dT_{\text{IM}}/dp > 0$: the thermodynamic ground state is metallic. In other words, the mobile electrons in the Fermi liquid state have less entropy than those localized in the Mott state.

Pustogow *et al.* succeeded to compose a genuine phase diagram of Mott insulators by combining optical and transport experiments on three representative spin liquid compounds β' -EtMe₃Sb[Pd(dmit)₂]₂, κ -(BEDT-TTF)₂Ag₂(CN)₃ and κ -(BEDT-TTF)₂Cu₂(CN)₃ [308]. Figure 47 presents the temperature changes of the frequency-

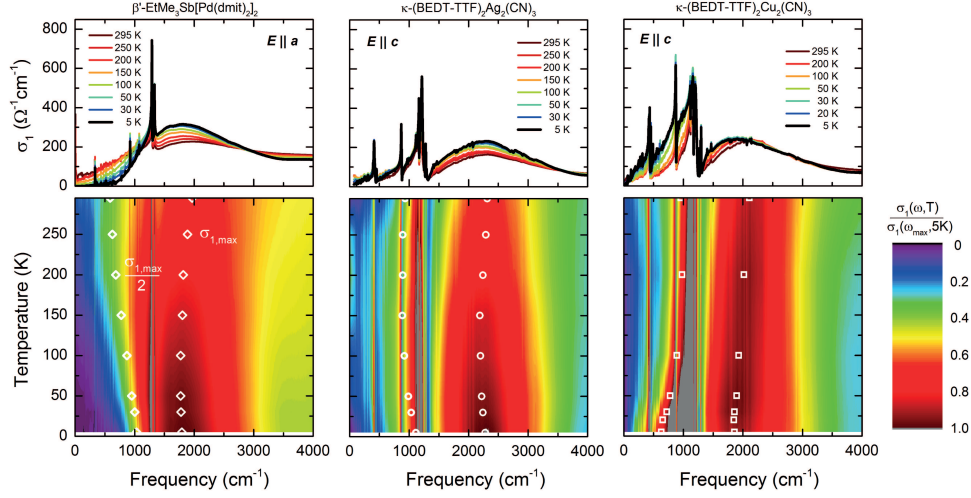


Figure 47. Temperature evolution of the optical conductivity of the three quantum-spin-liquid compounds β' -EtMe₃Sb[Pd(dmit)₂]₂, κ -(BEDT-TTF)₂Ag₂(CN)₃ and κ -(BEDT-TTF)₂Cu₂(CN)₃. The dominant feature that contains all information of the intrinsic Mott physics is the Mott-Hubbard band centered around 2000 cm⁻¹. At low frequencies narrow phonon modes appear on top. The contour plots illustrate the temperature-dependent changes of the Mott-Hubbard band, where the open white symbols denote the maximum and half-maximum positions (cf. Figure 48 upper right). Note that the band shape and the low-frequency conductivity show distinct behavior for each compound which is related to the respective position in the phase diagram (following [308]).

dependent conductivity measured along one representative orientation. While in β' -EtMe₃Sb[Pd(dmit)₂]₂ the low-frequency Mott-gap opens upon cooling, and spectral weight shifts toward the Mott-Hubbard band, for κ -(BEDT-TTF)₂Ag₂(CN)₃ only little variation is observed below 1000 cm⁻¹. Most surprising, however, is the increase of the in-gap absorption in κ -(BEDT-TTF)₂Cu₂(CN)₃ [358,359] that could be assigned to metallic fluctuations. One can imagine that upon approaching the metal-insulator-phase boundary, the number and effect of metallic puddles increases, reflecting the phase coexistence close to the first-order phase boundary, as depicted in Figure 42(b). When normalizing the temperature T and the correlation strength U by the respective bandwidth W as determined from optical experiments, the materials behavior collapses on a quantitative level as displayed in Figure 48. The quantum Widom line is clearly seen as well as the back-bending towards the critical endpoint. Below T_{crit} , it becomes a first-order phase boundary with a range of coexisting phases, which have been subject of subsequent studies.

Tuning the bandwidth enables us to follow the electron system from the strongly correlated Mott insulator through the range of phase coexistence into the metallic regime even at lowest temperatures. Unfortunately, for the paradigmatic quantum spin liquids, like κ -(BEDT-TTF)₂Cu₂(CN)₃, T_{crit} is around 20 K, *i.e.* below the temperature range accessible for continuously-tunable helium gas pressure cells due to solidification of the pressure medium [361]; preventing a continuous pressure sweep at

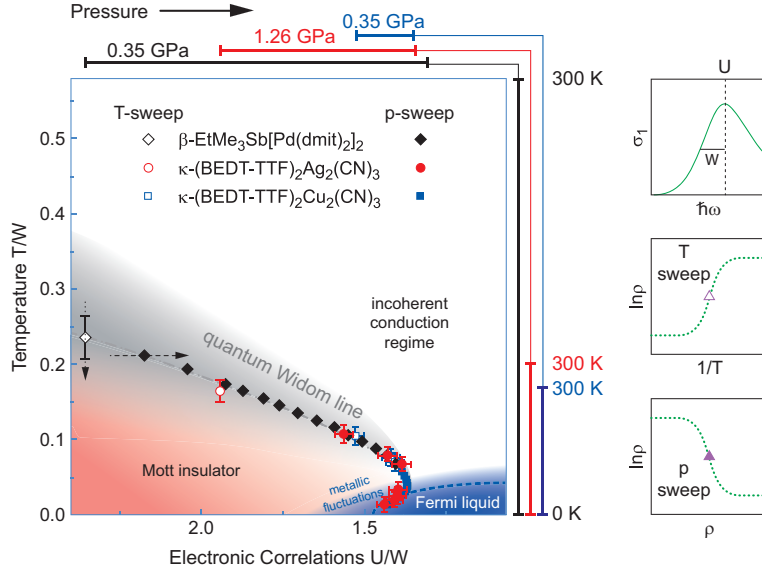


Figure 48. Quantitative phase diagram of pristine Mott insulators. The temperature $k_B T$ and Coulomb repulsion U are normalized to the bandwidth W extracted from optical spectroscopy; note that the direction of the bottom axis is reversed in order to mimic pressure. Since in these quantum spin liquids magnetic order is suppressed, the large residual entropy causes a pronounced back-bending of the quantum Widom line at low temperatures leading to metallic fluctuations (semi-transparent blue area) in the Mott state close to the phase boundary. As the effective correlations decrease further, a metallic phase forms (blue area) with Fermi liquid properties [343]. The universal phase diagram guided by the quantum Widom line is constructed on basis of optical and transport data [308] as well as the pressure-dependent transport studies [325,360] on β' -EtMe₃-Sb[Pd(dmit)₂]₂ (black diamonds), κ -(BEDT-TTF)₂Ag₂(CN)₃ (red circles), and κ -(BEDT-TTF)₂Cu₂(CN)₃ (blue squares). Upon rescaling temperature (right bars) and pressure (top bars), the quantum Widom line is found to be universal for all compounds. The curvature, as well as the $T = W$ and $U = W$ values match well with theoretical calculations [306]. On the right we illustrate how U and W are determined from the optical spectra and the quantum Widom line from the electrical resistivity $\rho(T; p)$ measured as a function of temperature (open symbols) and pressure (solid symbols), indicated by arrows in the main graph.

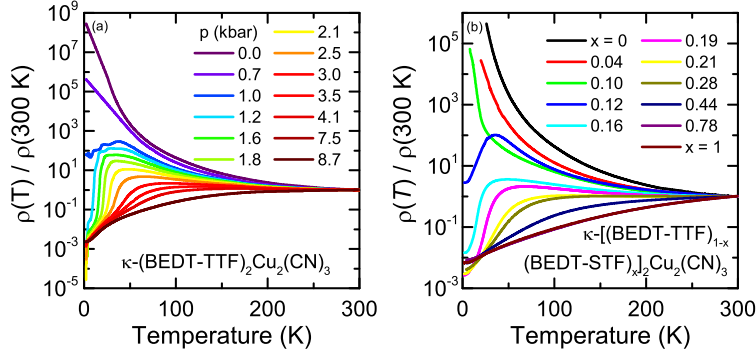


Figure 49. (a) Temperature dependence of the dc resistivity of κ -(BEDT-TTF) $_2$ Cu $_2$ (CN) $_3$ measured within the highly conducting bc -plane when applying different values of hydrostatic pressure as indicated [131]. (b) Temperature dependent resistivity of κ -[(BEDT-TTF) $_{1-x}$ (BEDT-STF) $_x$] $_2$ Cu $_2$ (CN) $_3$ where in the inner BEDT-TTF rings sulfur was partially substituted by selenium. The data are normalized to room temperature [364].

fixed temperatures that could be applied in the case of V $_2$ O $_3$ and κ -(BEDT-TTF) $_2$ -Cu[N(CN) $_2$]Cl. Nevertheless, temperature-dependent experiments at a large number of pressure values or chemical substitutions make it possible to densely map the region around the phase transition.

Figure 49 demonstrates the evolution of temperature-dependent dc transport of the highly-frustrated Mott insulator κ -(BEDT-TTF) $_2$ Cu $_2$ (CN) $_3$ as the bandwidth is enlarged in two alternative ways: hydrostatic pressure and chemical substitution. The strongly insulating behavior turns into a metallic, first at low temperatures, eventually in the entire temperature range. The data provide a wealth of information on the insulating as well as on the conducting regime that is discussed in Section 5.5. Concerning the insulator-metal transition, however, the temperature sweeps do not really cross the first-order phase boundary because the critical pressure changes only weakly with temperature [69,362,363]; hence no hysteresis is observed.

The hallmark of a first-order phase transition is the involvement of latent heat, often seen as a hysteric behavior in various physical quantities. Maybe more compelling is the real-space phase coexistence in a sizeable tuning range. In Sec. 4.1 we discussed how optical methods allow a mapping of the phase segregation at low temperatures, but common infrared spectroscopy is limited to a resolution of approximately 10 μ m, as illustrated in Figure 46(a). Utilizing scanning near-field microscopy in the infrared spectral range [365–367], spatial inhomogeneities on the nanometer scale can be visualized, as first demonstrated by Basov and collaborators on vanadium oxides [368–372]. In Figure 20 the example of α -(BEDT-TTF) $_2$ I $_3$ is presented where cryogenic near-field nanoscopy was first applied to the charge-order phase transition at $T_{CO} = 135$ K [184]. At present, however, temperatures below 20 K are not routinely accessible for this method, and only first attempts have been made so far to apply it to the problem under discussion here [373].

Nevertheless, indirect methods have been employed in order to prove that at this first-order phase transition, metallic regions coexist in the insulating matrix. As a matter of fact, the transformation from an insulator to a metal resembles classical percolation phenomena, where a conduction threshold is hit when the metallic filling fraction rises. The statistical problem of percolation has been subject to numerous theoretical and numerical treatments [374–376]; the behavior depends on the dimension and particular type of percolation (bond, site). The electrodynamic properties of

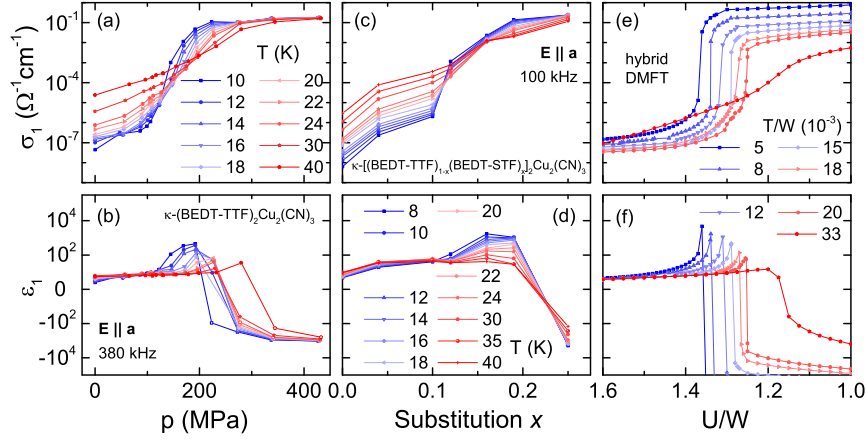


Figure 50. (a) The Mott insulator-to-metal transition of κ -(BEDT-TTF) $_2$ Cu $_2$ (CN) $_3$ appears as a rapid increase of $\sigma_1(p)$ that smoothens at higher temperatures; above T_{crit} a gradual crossover remains. (b) $\epsilon_1(p)$ exhibits a sharp peak below T_{crit} . The results are taken at $f = 380$ kHz and plotted on a logarithmic scale. (c,d) Similar behavior is observed for chemical BEDT-STF substitution. (e,f) Fixed-temperature line cuts of hybrid DMFT simulations (see text) as a function of correlation strength U/W and T/W [306,308] resemble the experimental situation in minute detail, including the shift of the transition with temperature. The lack of saturation of σ_1 as temperature is lowered, which is seen in DMFT modeling, simply reflects the neglect of elastic (impurity) scattering within the metallic phase (outside the phase coexistence region) (from [383]).

mixed media can be well described by effective-medium approximations suggested by Garnett, Bruggeman and others [377,378]. A characteristic of the percolation regime is the pronounced divergence of the dielectric constant [379–382] shortly before the percolation threshold is reached. In order to look at the coexistence regime of the first-order Mott transition from this perspective, comprehensive dielectric measurements have been conducted on κ -(BEDT-TTF) $_2$ Cu $_2$ (CN) $_3$ as a function of temperature and frequency, when the bandwidth is increased via hydrostatic pressure as well as chemical substitution of the organic molecules [309,364,383] (cf. Figure 49).

Figure 50(a) demonstrates the temperature evolution of the conductivity step as the pressure increases across the insulator-metal transition. The rapid enhancement of six orders of magnitude within a narrow range of less than 100 MPa at $T = 10$ K becomes smoother and more gradual as the temperature rises towards and across T_{crit} . A rather similar behavior is seen in Figure 50(c) where the substitutional-dependence of $\sigma_1(T, x)$ is plotted for various T . Although the density of p - and x -dependent data points do not allow to extract critical exponents, the overall behavior resembles well the case of the antiferromagnetic Mott insulator κ -(BEDT-TTF) $_2$ Cu[N(CN) $_2$]Cl discussed in Sec. 4.1, in particular Figure 44(a). In the corresponding lower panels of Figure 50, the permittivity ϵ_1 is plotted for fixed temperatures as a function of pressure and BEDT-STF substitution, respectively. Around the critical pressure $p \approx 150$ MPa and critical concentration of $x \approx 0.15$, ϵ_1 reaches a maximum that shifts to higher p - and x -values as T increases, corresponding to the positive slope predicted in Figure 42(b). Well above the critical temperature T_{crit} , the increase in ϵ_1 is minuscule. The experimental observations are well reproduced by DMFT calculations for a single-band Hubbard model [Figure 50(e,f)], which are supplemented by an appropriate electrical-network model representing such spatial inhomogeneity utilizing the standard effective-medium approximation [309,383].

Rösslhuber *et al.* mapped the dielectric catastrophe as a function of T and effective correlations [309,364,383], displayed in Figure 51. The two alternative methods of tuning the bandwidth in the highly frustrated spin-liquid compound κ -(BEDT-TTF) $_2$ -

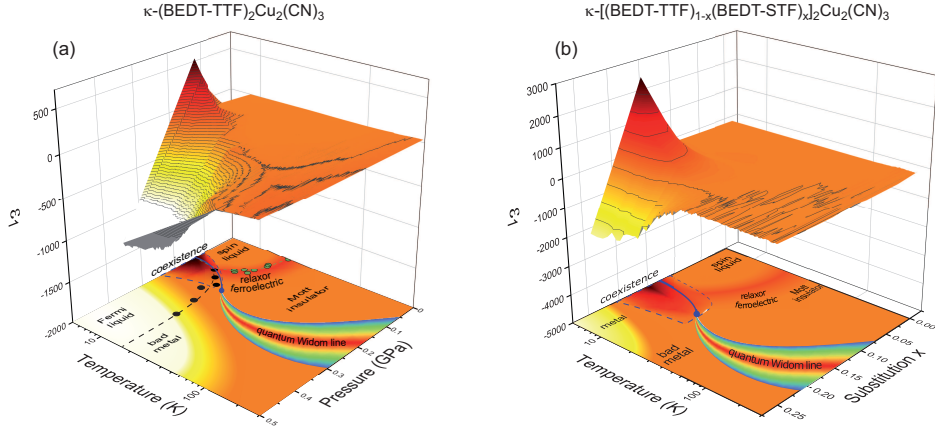


Figure 51. (a) Temperature-pressure contour plot of the dielectric permittivity of κ -(BEDT-TTF) $_2$ Cu $_2$ (CN) $_3$. The permittivity of $\epsilon_1(T, p)$ probed at $f = 380$ kHz increases up to 600 centered around $p = 180$ MPa and below $T = 20$ K, close to the first-order Mott transition. (b) The temperature-substitution plot of the permittivity for κ -[(BEDT-TTF) $_{1-x}$ (BEDT-STF) $_x$] $_2$ Cu $_2$ (CN) $_3$ exhibits its maximum of $\epsilon_1 \approx 2500$ around $x = 0.15$. This is ascribed to a range of spatially separated metallic and insulating regions. Projected phase diagram also includes $\rho(T, p)$ data: at T^* , the resistivity deviates from the Fermi-liquid behavior (after [309,364]).

Cu $_2$ (CN) $_3$ yield rather similar features as far as the overall behavior is concerned as well as most of the details. This provides compelling evidence that in fact the intrinsic physics is probed consisting of correlation effects and spatial percolation.

Note, the dielectric catastrophe at the Mott transition was first observed and discussed in the context of critically doped semiconductors, such as Si:P [290,384–389], which is a particular blend of percolation, correlations and disorder. It was suggested [305] that the transition from a quantum spin liquid as the fully frustrated Mott insulator to a Fermi-liquid metal is a much cleaner and well defined situation. Although disorder might be an issue for the substitutional series, the agreement between both approaches infer that the overall behavior is not severely affected. It would be of interest to apply this dielectric method to intentionally disordered systems using progressive irradiation.

4.3. Coherent transport

In a seminal paper, Merino and McKenzie [390] demonstrated that the transport properties of κ -BEDT-TTF salts can be described even on a quantitative level within dynamical mean-field theory (DMFT) [314,342,391,392]. At low temperatures, κ -(BEDT-TTF) $_2$ Cu[N(CN) $_2$]Br, κ -(BEDT-TTF) $_2$ Cu(SCN) $_2$ and similar organic conductors constitute prime examples of Fermi-liquids: The resistance exhibits a quadratic temperature dependence

$$\rho(T) = \rho_0 + AT^2 \quad , \quad (5)$$

obeying the Kadowaki-Woods rule [393]

$$A \propto \gamma_e^2 \quad , \quad (6)$$

with γ_e the Sommerfeld coefficient, characterizing the electronic contribution to the specific heat, *i.e.* the electronic density of states at the Fermi level E_F . This coherent state extends up to the Fermi-liquid temperature T_{FL} , where the parabolic increase in $\rho(T)$ is lost. Metallic transport, defined by $d\rho(T)/dT > 0$, prevails up to the so-called Brinkman-Rice temperature T_{BR} , well above the Ioffe-Regel-Mott limit where metallic transport is supposed to break down [383], see Figure 42(b). Above this maximum in $\rho(T)$ around 80 to 100 K, the systems exhibit some incoherent behavior resulting in a semiconducting temperature dependence. The smooth crossover from coherent Fermi-liquid to more incoherent excitations leads to a non-monotonic T -dependence not only in the electrical resistance, but also in thermopower and Hall coefficient. While the overall behavior is quite generic, details are sample dependent and due to intrinsic remnant disorder caused by an incomplete ordering of the ethylene-end-groups of BEDT-TTF molecule at about 75 K [40,394]; cf. Figure 1 in Chapter 2.

Among the molecular quantum materials, the κ -phase BEDT-TTF family serves as the primary testfield for the correlation dependence of their electronic properties. The starting point is either the antiferromagnetic Mott insulator κ -(BEDT-TTF)₂Cu[N(CN)₂]Cl or the highly-frustrated sister compound κ -(BEDT-TTF)₂Cu₂(CN)₃. The systems can be tuned into the metallic or even superconducting Fermi-liquid state by increasing the bandwidth via external pressure or chemical modification, as depicted in Figure 42(b) and (c).

Limelette *et al.* investigated κ -(BEDT-TTF)₂Cu[N(CN)₂]Cl under pressure $p > 30$ MPa in order to explore the emerging Fermi-liquid regime [342]: they could characterize the dc resistivity according to Eq. (5) up to T_{FL} , which is of the order of 35 K at 50 MPa. The prefactor $A(p)$ strongly increases as the pressure is reduced and diverges with a critical pressure of approximately 20 MPa (see Figure 45).

Replacing Cl by Br in κ -(BEDT-TTF)₂Cu[N(CN)₂]Br_{*x*}Cl_{1-*x*} provides an alternative route to shift the compound across the metal-insulator transition. Despite the larger ions, the orbital overlap increases and the effective Coulomb repulsion U/W decreases, as depicted in the phase diagram of Figure 52(b). Comprehensive optical, transport and magnetic investigations on κ -(BEDT-TTF)₂Cu[N(CN)₂]Br_{*x*}Cl_{1-*x*} yield the charge and spin dynamics as the metallic state evolves, when moving across the phase boundary or reducing the temperature [343,392,397–399]. As shown in Figure 52(a), the pristine and weakly substituted compounds behave strongly insulating; but for $x = 0.4$ metallic fluctuations become obvious at low temperatures. Above $x = 0.7$, metallic and superconducting properties are present. It is important to note, however, that in these cases the coherent charge carrier response develops only below approximately 50 K, in accord with theory [390]. In Figure 53(d)-(f), $\rho(T)$ is presented on a quadratic temperature scale in order to better visualize the Fermi liquid behavior. The $[\rho(T) - \rho_0] \propto T^2$ dependence holds up to the Fermi-liquid temperature $T_{\text{FL}} \approx 30$ K basically independent on x . Pressure-dependent studies [342] shown in Figure 45(a) reveal a somewhat stronger increase with p .

4.3.1. Fermi-liquid behavior

The obtained prefactor $A(x)$ in Eq. (5) increases, when going from the pristine Br compound to $x = 0.7$. Within Landau's Fermi-liquid theory, the factor A characterizes

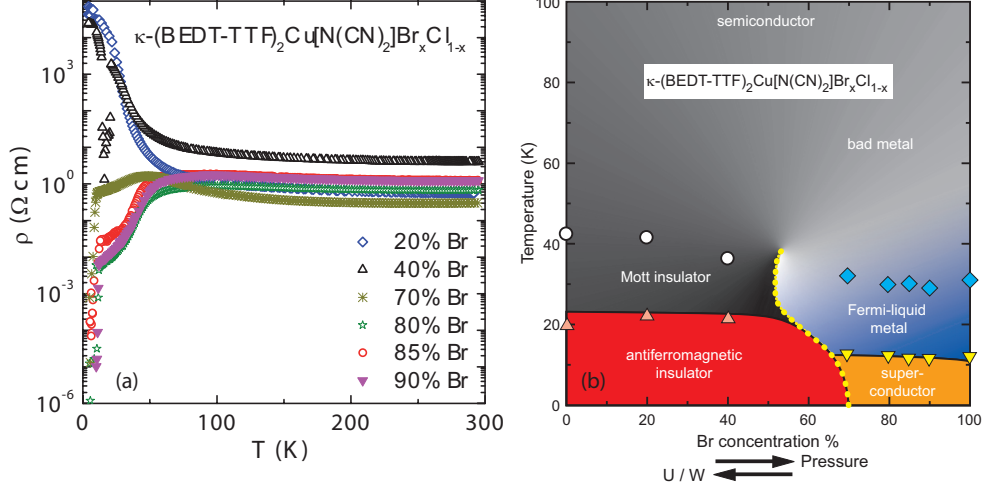


Figure 52. (a) Temperature dependence of the in-plane dc resistivity $\rho(T)$ of $\kappa\text{-(BEDT-TTF)}_2\text{Cu[N(CN)}_2\text{]Br}_x\text{Cl}_{1-x}$ with different Br substitution as indicated. For $x = 40\%$ metallic fluctuations indicate the closeness to the metallic phase. (b) Schematic phase diagram of $\kappa\text{-(BEDT-TTF)}_2X$. The on-site Coulomb repulsion with respect to the bandwidth U/W can be tuned either by external pressure or modifying the anions X . The bandwidth controlled phase transition between the insulator and the Fermi liquid/superconductor can be explored by gradually replacing Cl by Br in $\kappa\text{-(BEDT-TTF)}_2\text{Cu[N(CN)}_2\text{]Br}_x\text{Cl}_{1-x}$. The first-order insulator-to-metal transition line is sketched after the generic diagram for $\kappa\text{-(BEDT-TTF)}_2X$ [342,395,396]. The data points are obtained from transport measurements (a) and magnetic susceptibility (from [343]).

the strength of the electron-electron interaction and is related to the effective carrier mass m^* or the effective Fermi temperature T_F^* , like

$$A \propto (m^*)^2 \propto (T_F^*)^{-2} \quad , \quad (7)$$

in accord with the Kadowaki-Woods relation (6), that is well established for heavy fermions or transition-metal compounds, and was also seen in organics [393,395,400–402]. The product $A \times (T_{FL})^2$ was suggested to remain constant when going through the phase diagram either by chemical or physical pressure [342,343]; more detailed studies are required to confirm this point. We should note that results on $\kappa\text{-(BEDT-TTF)}_2\text{Cu[N(CN)}_2\text{]Br}$ have been reported, which deviate from this behavior [40], likely caused by a remnant disorder [394].

In addition to the temperature dependence, optical spectroscopy provides the possibility to extract the frequency dependence of the scattering rate and of the effective mass, when performing an extended Drude analysis of the conductivity spectra [403,404]. Eventually we can consider a ω - T scaling of the scattering and interaction processes with respect to these two energies. For $\kappa\text{-(BEDT-TTF)}_2\text{Cu[N(CN)}_2\text{]Br}_x\text{Cl}_{1-x}$ single crystals with $x = 0.9$ and 0.85 and 0.73 one obtains a gradual increase in the effective mass from 2 to $m^*/m_b \approx 6$ [398,405]. This agrees with the general prediction by Brinkman-Rice theory [38] and DMFT calculations [304] that the electronic correlations become stronger on approaching the Mott transition from the metallic side. More recent calculations by resonating-valence-bond theory of the Hubbard-Heisenberg model also predict a gradual increase in m^* for values of effective repulsion U/W not too close to the first-order Mott transition and a strong increase very close to the transition [406]. Kagawa *et al.* [331] noted that m^* is well defined only in the Fermi-liquid regime at low temperatures; in the ‘bad metallic’ regime of

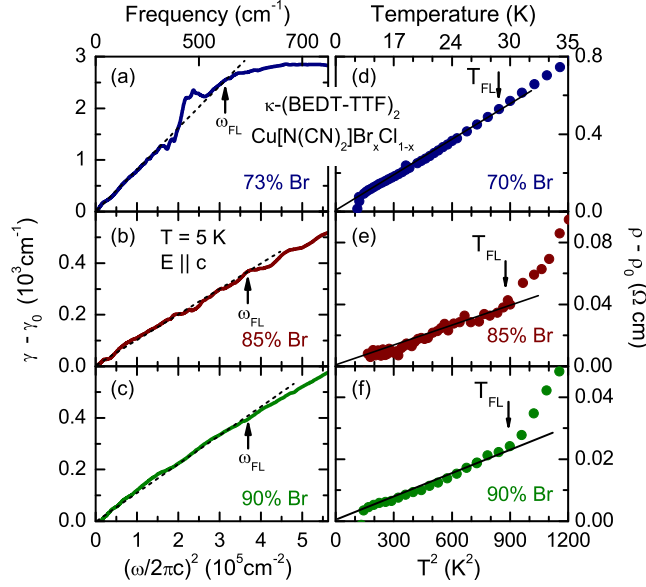


Figure 53. Temperature and frequency dependence of the scattering rate for κ -(BEDT-TTF) $_2$ Cu[N(CN) $_2$] $\text{Br}_x\text{Cl}_{1-x}$ with different substitution values x . (a) - (c) The frequency-dependent part of the scattering rate $\gamma(\omega) - \gamma_0$ at $T = 5$ K of κ -(BEDT-TTF) $_2$ Cu[N(CN) $_2$] $\text{Br}_x\text{Cl}_{1-x}$ as function of the squared frequency. We determined for the frequency-independent dc limit of the scattering rate γ_0 the following values: 315 cm^{-1} ($x = 0.73$), 48 cm^{-1} ($x = 0.85$), and 280 cm^{-1} ($x = 0.9$). Note the different vertical scales for the frames. (d) - (f) The temperature-dependent scattering rate $\tau^{-1}(T) = \gamma(T)$ is obtained from the in-plane dc resistivity $(\rho(T) - \rho_0) \propto 1/\tau(T)$. The plots as a function of T^2 in the low-temperature region yield a quadratic behavior up to T_0 . Below $T_c \approx 12$ K the systems become superconducting (data from [343,398]).

the phase diagram [Figure 52(b)], however, m^* is probably not an adequate physical parameter to feature the Mott criticality at the critical end point.

Fermi-liquid theory makes predictions about the temperature dependence of the scattering rate as well as about its frequency dependence [407–410]:

$$\gamma(T, \omega) = \tau^{-1} = \gamma_0 + B [(p\pi k_B T/\hbar)^2 + \omega^2] \quad , \quad (8)$$

where the constant γ_0 describes the residual scattering processes at zero energy due to impurities, surface etc. corresponding to the residual resistivity ρ_0 in Eq. (5). The parameter B is related to the density of electronic states at the Fermi level E_F . For purely inelastic scattering, $p = 2$ is predicted [411–414] but experimental verification is scarce [343,415–418]. As seen from Figure 53(a)-(c), a quadratic frequency dependence of the low-temperature scattering rate was obtained in the case of κ -(BEDT-TTF) $_2$ -Cu[N(CN) $_2$] $\text{Br}_x\text{Cl}_{1-x}$ up to approximately 600 cm^{-1} where unconventional non-Fermi-liquid behavior prevails even at $T = 5$ K [398,405]. The corresponding temperature-dependent dc resistivity is plotted in panels (d) to (f). Consistently, the slope rises as the Mott transition is approached: the effective correlations U/W increase due to the reduction of bandwidth. From the optical data taken at different temperatures, $p = 2.3$ is extracted close to the expectation. As seen in Figure 53, the upper limit of the Fermi-liquid regime is determined by deviations from the T^2 and ω^2 line. It is interesting to note that in all cases the rise in temperature has a much stronger effect than the increase in frequency.

An indirect method of probing the metallic phase boundary was suggested by Sasaki *et al.* [419] similar to the spatially resolved study presented in Figure 46: by carefully

following the $\nu_3(a_g)$ mode of several κ -(BEDT-TTF) $_2X$ salts when the temperature is reduced, they can identify the border T^* between the bad metallic behavior at elevated temperature and the Fermi-liquid behavior of a correlated good metal at low temperatures. Variations of the electronic properties affect the emv coupling of the molecular vibrations. They also found a shift in the $\nu_3(a_g)$ mode when the boundary to the Mott insulator is crossed by cooling κ -(BEDT-TTF) $_2\text{Cu}[\text{N}(\text{CN})_2]\text{Cl}$.

4.3.2. ω - T scaling

A comprehensive investigation of the Fermi-liquid regime in the two-dimensional organic compounds was conducted by Pustogow *et al.* [420], who compared the transport and optical properties of the substitutional series κ -[(BEDT-TTF) $_{1-x}$ (BEDT-STF) $_x$] $_2\text{Cu}_2(\text{CN})_3$ with $0 \leq x \leq 1$. Due to the extended selenium orbitals, the bandwidth W is enlarged as the BEDT-STF content increases; the Mott transition takes place around $x = 0.12$ as shown in Figure 49(a). The optical conductivity displayed in the inset of Figure 54(b) resembles an insulator [$\sigma_1(\omega \rightarrow 0) = 0$] for low x with a pronounced mid-infrared absorption band ($U \approx 2000 \text{ cm}^{-1}$) that corresponds to excitations across the Mott-Hubbard gap. With increasing x , spectral weight shifts to lower energies and eventually a Drude-like term appears as the metallic phase is entered [364]. The contour plot illustrates the evolution of the conductivity as x rises. Fueled by the vanishing Mott-Hubbard excitations, the coherent quasiparticle response appears above $x \approx 0.2$. In that range, an extended Drude analysis of the optical conductivity [403] yields the energy dependence of the scattering rate and effective mass, presented in Figure 54(b) and (c). When plotting $\gamma(\omega)$ as a function of ω^2 , a straight-line behavior can be observed up to ω_{FL} , which corresponds to the upper limit of the Fermi liquid regime. With increasing x the boundary considerably shifts to higher energies, in accord with the observations made on κ -(BEDT-TTF) $_2\text{Cu}[\text{N}(\text{CN})_2]\text{Br}_x\text{Cl}_{1-x}$ (Figure 53). It is worth to note that the Fermi-liquid behavior is observed over an extremely large temperature and frequency range because of the narrow bands compared to transition metal oxides, for instance. The slope determined by the prefactor B decreases with rising x , *i.e.* as we move away from the insulator-metal transition. Correspondingly, from the frequency dependence of the renormalized mass, a strong increase of m^* is observed as x is reduced towards the Mott transition at 0.12. The low-frequency limit is taken as a measure of the correlation strength that is related as $B \propto (m^*/m_b)^2$ in analogy to Eq. (6).

The crucial point is the ω - T scaling expressed in Eq. (8): The quadratic dependence of the scattering rate on frequency, plotted in Figure 54(b), is observed at different temperatures; they can be unified by scaling the curves with a temperature independent factor p . This is taken as compelling evidence for the universality of Landau's Fermi-liquid concept upon varying the correlation strength and do not leave much space for theories of a quasi-continuous Mott transition that involve a divergent Kadowaki-Woods ratio [303]. Interestingly, the proportionality between the T^2 and ω^2 dependence of $\gamma(T, \omega)$ exceeds the inelastic limit $p = 2$ and exhibits a pronounced enhancement towards the Mott metal-insulator transition [420,421]. This behavior is in contrast to the observations in various strongly correlated electron systems [410], and can be explained by the fact that in κ -[(BEDT-TTF) $_{1-x}$ (BEDT-STF) $_x$] $_2\text{Cu}_2(\text{CN})_3$ the narrow quasiparticle peak centred at $\omega = 0$ coexists and considerably overlaps with the broad, non-metallic Hubbard bands at $\pm U/2$ (with a width W) as we are close to the Mott transition. In other words, the strongly correlated charge carriers are not as freely moving as expected for a good metal; in part they are localized due strong

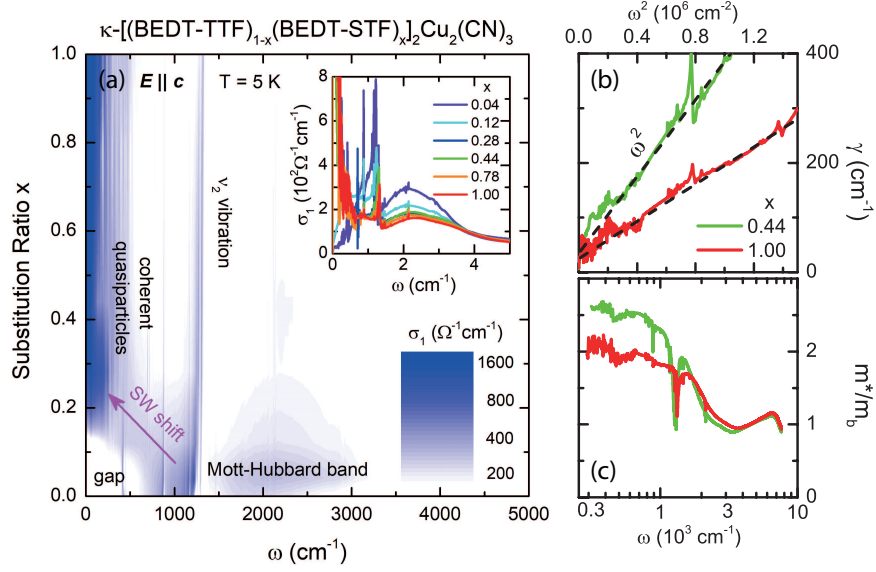


Figure 54. Optical properties of the series $\kappa\text{-}[(\text{BEDT-TTF})_{1-x}(\text{BEDT-STF})_x]_2\text{Cu}_2(\text{CN})_3$. The inset in panel (a) displays the optical conductivity for several crystals with different substitution x as indicated. The data are recorded at $T = 5$ K for the polarization $E \parallel c$. The most prominent feature is the Mott-Hubbard band around 2000 cm^{-1} . Upon increasing x , this peak shifts towards higher energies. At the same time, a strong Drude-type zero-frequency conductivity emerges indicating the transition from a gapped Mott insulator to a strongly correlated metallic state with renormalized quasiparticles. The main frame contains the contour plot of the conductivity spectra at different substitutional values x (σ_1 is plotted on a logarithmic blue-white scale) illustrating the spectral-weight shift from high to low energies as the BEDT-STF content increases. As correlations become less pronounced, the Mott gap closes and coherent quasiparticles are stabilized at low frequencies. The strong but substitution-independent vibrational feature at 1250 cm^{-1} corresponds to the emv coupled $\nu_2(a_g)$ mode. (b) From the extended Drude analysis, the energy-dependent scattering rate γ and effective mass m^* is obtained. For the metallic compounds $x \geq 0.28$, $\gamma(\omega)$ increases quadratically with frequency, providing strong evidence for a Fermi liquid response. With increasing x , the slope B is reduced and the $\gamma(\omega) \propto \omega^2$ range expands to higher frequency, shown for the two examples $x = 0.44$ and 1.00 . (c) Effective mass as a function of frequency for different BEDT-STF substitutions. The mass enhancement becomes more pronounced as the Mott transition is approached; for $x = 0.44$ one finds $m^*/m_b = 2.6$ (taken from [420,421]).

Coulomb repulsion. Further theoretical studies are required in order to elucidate these issues in more depth.

4.3.3. Bad-metal regime and Ioffe-Regel-Mott limit

The Fermi-liquid transport at low temperatures ($T < 50$ K or so) is followed by a vaguely-defined ‘bad metal’ regime [422]. Although quasiparticles are still present, their lifetime is significantly limited [311]. This regime – often identified with a linear-in- T resistivity – is not well understood, although continuously subject to theoretical treatises [423]. At even high temperatures, when transport becomes incoherent and dominated by the large scattering rate, metallic conduction breaks down. The so-called Ioffe-Regel-Mott limit is the maximal resistivity that can be reached in a metal according to the Boltzmann semiclassical theory [424,425]. As first realized by Ioffe and Regel [426], the metallic conductivity is restricted as the mean free path ℓ cannot get smaller than the lattice spacing d [427]; in other words, the linear-in-temperature increase of the resistivity should saturate at one point. There are numerous examples of strongly correlated systems, however, for which $\rho(T)$ does not show a sign of saturation up to fairly elevated temperatures.

For that reason, it is rather illuminative to look at the optical response, where the

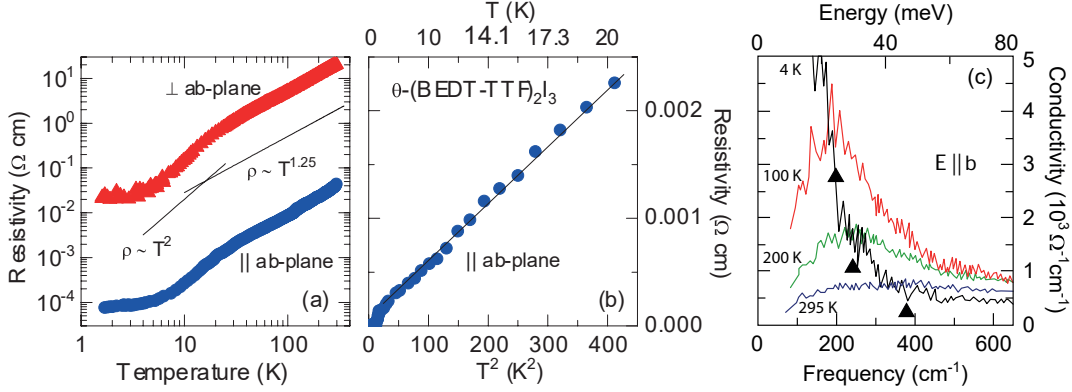


Figure 55. Temperature-dependent electronic properties of θ -(BEDT-TTF) $_2$ I $_3$. (a) Parallel and perpendicular to the ab -planes, the resistivity exhibits a $\rho(T) \propto T^{1.25}$ power-law behavior at elevated temperatures. (b) Below $T_0 \approx 20$ K a quadratic dependence reveals a Fermi-liquid (after [405]). (c) In-plane conductivity spectra of θ -(BEDT-TTF) $_2$ I $_3$ at different temperatures. The Drude component at low temperatures diminishes and shifts to a finite energy peak (indicated by black triangles) with increasing T (after [429]).

low-frequency spectral weight becomes reduced and the simple Drude-like behavior modified well before $\rho(T)$ saturates. We can define ‘bad metals’ by the loss of coherence. Dynamical mean field calculations [311,342,390,391] predict the modification of the Drude peak that extends well above the Ioffe-Regel-Mott limit, in full agreement with experiments on several κ -(BEDT-TTF) $_2$ X salts [364,392,398,420,428], as shown in Figure 54(a), but also θ -(BEDT-TTF) $_2$ I $_3$.

The two-dimensional organic conductor θ -(BEDT-TTF) $_2$ I $_3$ draws attention for numerous reasons. In contrast to other θ -phase salts that undergo charge-ordering transitions into an insulating ground state [21,50,193], the dc resistivity of θ -(BEDT-TTF) $_2$ I $_3$ remains metallic down to $T_c = 3.6$ K. The transition temperature can be raised above 5 K, when the specimens are tempered at 70 °C [430]. Quantum oscillations prove the presence of a Fermi surface with two-dimensional orbits and one-dimensional trajectories [430–433]. The presence of a Fermi-liquid state is also seen from a quadratic temperature increase in the resistivity observed at low temperatures. As displayed in Figure 55(a,b), it turns into a $T^{1.25}$ dependence above $T_{FL} \approx 20$ K or so. A closer inspection reveals a slight kink around 120 K where also the anisotropy $\rho_{\parallel}/\rho_{\perp}$ changes [430].

As pointed out by Takenaka *et al.* [429], above $T \approx 50$ K the in-plane resistivity exceeds the Ioffe-Regel-Mott limit $\rho_{IRM} = (h/e^2)d = 4.4 \times 10^3 \Omega \text{ cm}$ for an interlayer distance of $d = 17 \text{ \AA}$ [434], implying incoherent transport above. The transition from a coherent quasiparticle state to an incoherent state was addressed by temperature-dependent optical spectroscopy on θ -(BEDT-TTF) $_2$ I $_3$. Despite the metallic behavior of $\rho(T)$, a well defined Drude peak is present only at low-temperatures. Upon warming to $T = 100$ K, the peak moves to finite frequencies in the far infrared spectral range. The origin of the finite energy peak seen in Figure 55(c) is not clear. For both directions ($E \parallel a$ and b) the maximum moves to approximately 250 – 400 cm^{-1} when going up to room temperature. It is discussed whether this spectral behavior represents a ‘dynamical localization’ theoretically explored for other organic semiconductors in more detail [435], or can be treated like fluctuating density waves [436].

The disappearance of the Drude peak is accompanied by a shift of spectral weight to energies above 1 eV. The loss of coherence and the redistribution of a substantial

amount of spectral weight is explained by strong electronic correlations, as has been observed in a large variety of correlated bad metals [437]. The disappearance of the Drude peak indicates a strong suppression of kinetic energy with increasing T : the charge carriers transport becomes incoherent. The spectral weight shifts to energies higher than the bandwidth. Gunnarsson and collaborators pointed out [438] that the reason for this violation of the Ioffe-Regel-Mott limit is not simply due to interactions, like in some transition metal oxides, or due to the small bandwidth compared to the temperatures.

$$\sigma_1(0) = \frac{\varphi}{W} \int_0^\infty \sigma_1(\omega) d\omega \approx \frac{|E_k|}{W} \quad , \quad (9)$$

where $\varphi = 1-2$ and W is the bandwidth of the order of 500 meV. In the case of κ -(BEDT-TTF)₂ X salts [397,398], $\sigma_1(\omega)/\rho_{\text{IRM}}$ is suppressed due to correlations reducing $|E_k|$ and expanding the energy scale [438].

It is interesting to note that the behavior of the optical conductivity $\sigma_1(\omega)$ in the bad metallic regime at high temperatures is rather similar to that seen in disordered materials at low T [425]. Radonjić *et al.* [439] showed that with increasing disorder the bandwidth W increases, but disorder does not lead to qualitative differences. The large bandwidth makes the compounds more metallic, in accord with experiments [440] as discussed in Sec. 4.4. With proper scaling, the optical conductivity remains even quantitatively very similar. No question, the ‘bad metallic’ regime remains a desideratum for future research.

Using numerical methods Wessel and collaborators considered the Mott metal-insulator transition while varying the degree of frustration [323]. Most interesting, the slope of the phase boundary changes sign, from positive slope of dT/dp at $t' = t$ to negative slope for the unfrustrated case $t' = 0$. This basically reflects the difference in entropy of the insulating ground state. Similar results have been received earlier by Tremblay and collaborators. They also provided a detailed thermodynamic description of the correlation-driven Mott transition [441–443], where they can trace the quantum Widom line above T_{crit} and the spinodal lines U_{c1} and U_{c2} below. Particular attention was paid to the local entropy.

4.4. *Effects of disorder on the Mott transition*

The electronic properties of real materials are strongly affected by electronic interaction and randomness [293,444,445]. Localization of particles can be caused by Coulomb repulsion and disorder. While electronic correlations are the driving force behind the Mott transition, the Anderson transition is due to coherent backscattering of non-interacting particles from randomly distributed impurities. The challenge for a theoretical understanding is that disorder and interaction effects are known to compete in subtle ways [388,446–451].

In Figure 56 the ground state phase diagram of the Anderson-Hubbard model is displayed, based on dynamical mean field theory (DMFT) calculations of the disordered Hubbard model at half filling with the typical local density of states [446]. The interaction strength is given by U/W , the disorder strength by Δ . Two different phase transitions are found: a Mott insulator-metal transition for weak disorder Δ and an Anderson transition for weak interaction U . Two insulating phases surround the correlated, disordered metallic phase.

Dobrosavljević and collaborators also considered the temperature evolution when

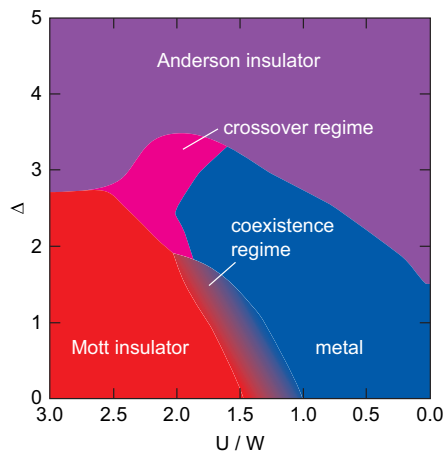


Figure 56. Phase diagram of the non-magnetic Anderson-Hubbard model as calculated by dynamical mean field theory with the typical local density of states (based on [446]). Note the reversed scale for U/W .

investigating the effect of disorder on the Mott transition by DMFT combined with typical medium theory [452–455]; in particular they looked at the coexistence regime of insulating and metallic solutions. While for weak disorder the coexistence region is found to be similar to that in the clean case, with increasing disorder Anderson localization effects are responsible for shrinking the coexistence region, as depicted in Figure 57. Both the U_{c1} and U_{c2} lines move toward larger interaction potential and become closer to each other when disorder increases. As disorder becomes even stronger and exceeds twice the bandwidth, the region drastically narrows and the critical temperature T_{crit} abruptly goes to zero. Here the transition occurs at $U \approx W$ and Anderson and Mott routes to localization become equally important; in other words the effects of interaction and disorder are of comparable relevance for charge localization. The observation of a metal-insulator transition without a coexistence region suggests that the nature of the transition has changed from first to second order as disorder increases. This is in accord with the idea of a quantum-critical regime for $T > T_{\text{crit}}$, that was suggested by theory [305] and experiments [325] on various dimerized organic Mott insulators, as shown in Figure 43 and discussed in Sec. 4.1.1.

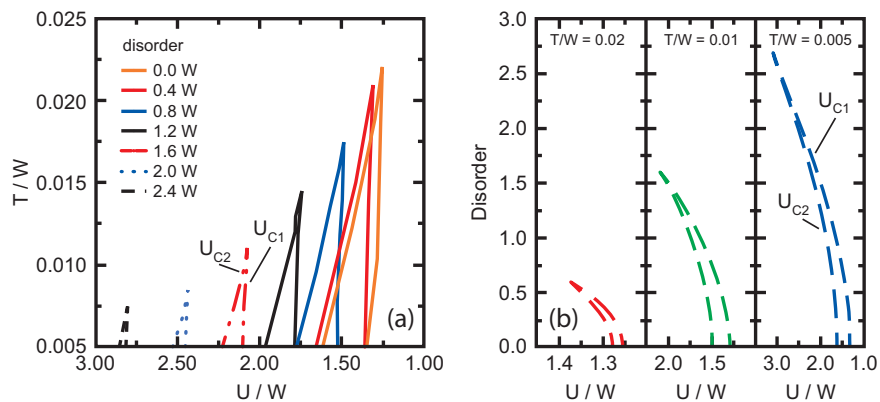


Figure 57. Phase diagram for the disordered Hubbard model at nonzero temperature (a) for different degrees of disorder and (b) for different temperatures T given in units of the bandwidth W (after [454]); note the axis U/W goes from right to left in order to mimic the pressure dependence. The spinodal lines U_{c1} and U_{c2} indicate the boundaries to the insulating and metallic solutions.

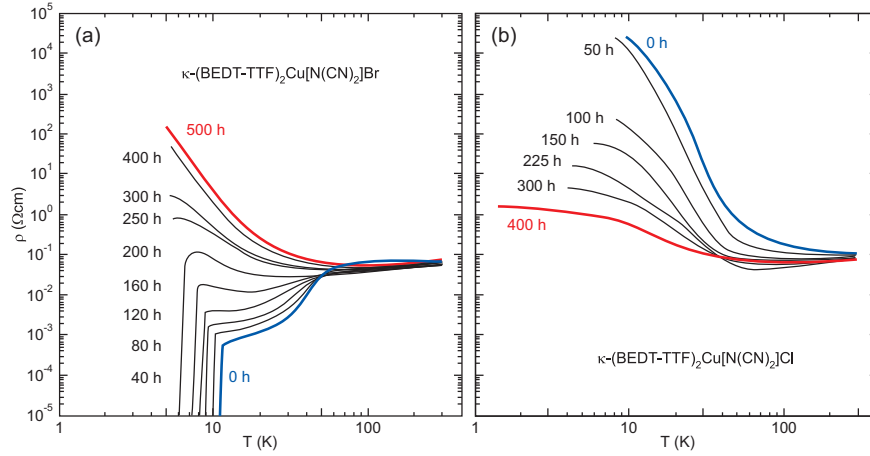


Figure 58. Temperature dependence of the dc resistivity of (a) κ -(BEDT-TTF) $_2$ Cu[N(CN) $_2$]Br und (b) κ -(BEDT-TTF) $_2$ Cu[N(CN) $_2$]Cl irradiated by x-ray. The time indicated is the total x-ray exposure time at room temperature (data from [440,477,480]).

Single crystals from organic charge transfer salts are renowned for their superior quality, mainly because they are grown by electrochemical methods [26,456]. Occasionally some effect of the starting molecules, solvent, or atmospheric environment has been reported [40,457,458], but the crystal structure and overall behavior is barely affected. An intrinsic and reversible way of introducing disorder in BEDT-TTF salts is the adjustment of the cooling rate [459,460], which affects the freezing of the terminal ethylene-group disorder (Figure 1) at around 70 to 80 K and thereby the resistivity profiles [461–464] and the pairing symmetry of the superconducting ground state [394,465–473].

This provides the possibility to study the disorder dependence of physical properties by targeted artificial defects. X-ray irradiation is commonly utilized to create disorder in molecular solids in a controlled way. Sasaki and collaborators could show [440,474–476] that the defects are introduced mainly in the anion layers separating the organic molecules leading to a modulation of the potential rather than a creation of electronic charges [477,478]. In general, the room-temperature resistivity substantially decreases with irradiation dose. Also the characteristic hump around $T = 100$ K quickly disappears [440,479,480], in good agreement with DMFT calculations [439]. The low-temperature properties are even more sensitive to irradiation as revealed by extensive studies of the normal and the superconducting state of κ -(BEDT-TTF) $_2$ -Cu(SCN) $_2$ and κ -(BEDT-TTF) $_2$ Cu[N(CN) $_2$]Br, as well as of β -(BEDT-TTF) $_2$ AuI $_2$. Already small doses increase the residual resistance ρ_0 and reduce the transition temperature T_c [479,481]; however it takes rather extensive irradiation to completely kill the superconducting state [474,480]. The metallic compound κ -(BEDT-TTF) $_2$ Cu[N(CN) $_2$]Br, displayed in Figure 58(a) as an example, turns insulating when the electrons become localized due to the randomness of the potential: the charge transport takes place via hopping between sites [480].

The Mott insulators, on the other hand, such as κ -(BEDT-TTF) $_2$ Cu[N(CN) $_2$]Cl or κ -(BEDT-TTF) $_2$ Cu $_2$ (CN) $_3$, loose their high-resistivity state upon irradiation: the resistivity decreases in the whole temperature range. For κ -(BEDT-TTF) $_2$ Cu[N(CN) $_2$]Cl a metallic-like temperature dependence down to about 50 K is reached at a rather low dose [340,440], as shown in Figure 58(b). With increasing defect concentration, the Mott gap is filled, resulting in a shift of spectral weight from the interband transition

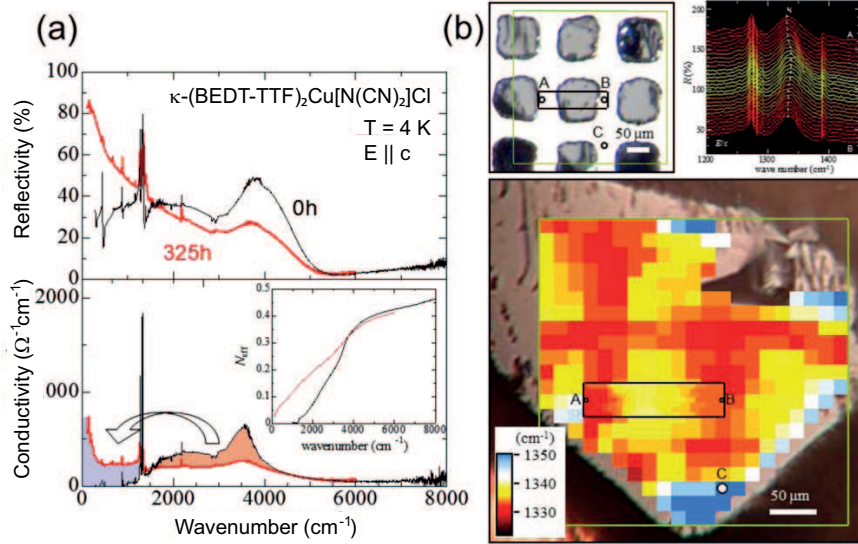


Figure 59. (a) Infrared optical reflectivity and conductivity of κ -(BEDT-TTF) $_2$ Cu[N(CN) $_2$]Cl before and after x-ray irradiation. The inset of the lower panel indicates the effective number of carriers; (b) Scanning micro-region infrared reflectance spectroscopy map of the partly x-ray irradiated κ -(BEDT-TTF) $_2$ -Cu[N(CN) $_2$]Cl. The sample is irradiated through the molybdenum mesh mask (reproduced from [440]).

to low energies: optical measurements [482] show a Drude-like behavior at low temperatures, shown in Figure 59(a). DMFT calculations by Radonjić *et al.* explain this behavior by an increase of the bandwidth [439]. By using an x-ray microbeam, the spatial dependence can be investigated. To that end a κ -(BEDT-TTF) $_2$ Cu[N(CN) $_2$]Cl crystal is irradiated through a molybdenum mesh ($90 \mu\text{m} \times 90 \mu\text{m}$) [354,355] and the fabricated pattern studied by scanning micro-region infrared reflectance spectroscopy with a spatial resolution of 5 to $15 \mu\text{m}$ as already introduced in Sections 4.1.2 and 4.3.1. Mapping the emv coupled molecular vibration $\nu_3(a_g)$ provides local information on the electronic states (Figure 59) because the frequency of the mode reflects the electronic state via electron molecular vibration coupling [419,440].

Spatial inhomogeneities in the two-dimensional electron and magnetic system may give rise to a Griffiths phase at the metal-insulator transition [87,483,484]. Following theoretical studies [485,486] recent ^{13}C -NMR investigations on strongly irradiated (500 h x-ray exposure) κ -(BEDT-TTF) $_2$ Cu[N(CN) $_2$]Cl found a slow dynamics that was interpreted in this regard [487]. The electronic system exhibits long-length self-organization without long-range order. A temperature-pressure-randomness phase diagram with an electronic Griffiths phase is proposed as displayed in Figure 60.

The quantum-spin-liquid Mott insulator κ -(BEDT-TTF) $_2$ Cu $_2$ (CN) $_3$ seems to be less susceptible to x-ray irradiation. The resistivity varies only little [440,477,488] even for large doses and also the magnetic properties remain unchanged by chemical substitution [489]. The Mott gap does not collapse due to irradiation, but hopping conduction, present even in the pristine crystals [359,488,490], becomes dominant.

Čulo *et al.* measured the dc resistivity and Hall effect of several quantum-spin disordered Mott insulators with rather similar chemical compositions and crystal structures: κ -(BEDT-TTF) $_2$ Cu $_2$ (CN) $_3$, κ -(BEDT-TTF) $_2$ Ag $_2$ (CN) $_3$, and κ -(BEDT-TTF) $_2$ B(CN) $_4$ [458,491,492]. While around room temperature the transport properties are mainly determined by the strength of the electron correlations, upon reducing T , hopping transport takes over due to inherent disorder. The most disordered compound

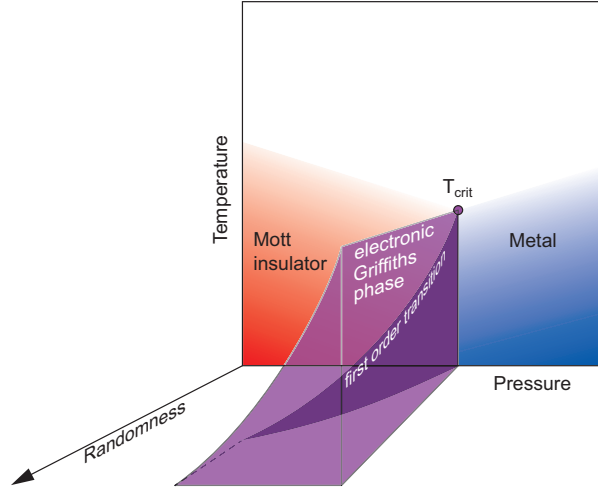


Figure 60. Schematic phase diagram how the Mott transition develops with increasing randomness, as suggested from NMR experiments on κ -(BEDT-TTF) $_2$ Cu[N(CN) $_2$]Cl subject to x-ray irradiation [487]. The co-existence regime at the first-order phase transition gradually diminishes as shown in Figure 57. Above that spatial inhomogeneities give rise to an electronic Griffiths phase.

κ -(BEDT-TTF) $_2$ Cu $_2$ (CN) $_3$ exhibits the lowest dc resistivity and the highest charge carrier density, *i.e.*, in the phase diagram it is located closest to the metal-insulator transition. The least disordered compound κ -(BEDT-TTF) $_2$ B(CN) $_4$ shows the highest resistivity and the lowest carrier density, *i.e.*, lies farthest from the phase transition. The observations are explained within the theory of Mott-Anderson localization as a consequence of disorder-induced localized states within the correlation gap [458,492].

5. Frustration in Two Dimensions: Quantum Spin Liquid versus Magnetic Order

Stimulated by the pioneering work of L. Pauling on geometrical frustration of electric dipoles [493], P.W. Anderson considered spin models possessing an extensive degeneracy of states that prevent long-range magnetic order even at $T = 0$ K [198,494,495]. The idea is that Heisenberg spins form pairs, *i.e.* quantum mechanical singlets, called valence bonds. A resonating valence-bond state can be obtained by superposition of different valence-bond solids, where the singlet pairs are not necessarily restricted to nearest neighbors. These systems do not develop long-range magnetic order despite the strong interactions, hence they are called quantum spin liquids. In contrast to spin glasses, which eventually become static [496–499], spin liquids keep some dynamics down to zero temperature. Although the singlet bonds can be randomly oriented on the triangular lattice, the valence-bond solid involves some symmetry breaking that becomes even more tangible in real materials where the valence-bond solid states are intertwined with lattice distortions that stabilize singlet pairs on bonds with stronger interaction [322,500–506]. In contrast to bosonic ($S = 1$) magnon excitations in long-range-ordered antiferromagnets, these quantum spin liquids exhibit fractional, fermionic ($S = \frac{1}{2}$) magnetic excitations, called spinons, that can propagate independently without involving charge. The absence of an energy gap in the excitation spectrum implies the existence of a spinon Fermi surface.

After searching numerous compounds for experimental realization, molecule-based

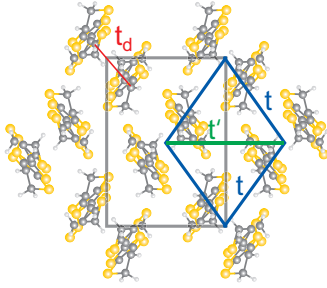


Figure 61. For κ -(BEDT-TTF) $_2$ X the molecules are arranged in dimers that constitute an anisotropic triangular lattice within the conduction layer. The nearest-neighbor and the second-nearest-neighbor inter-dimer transfer integrals are labeled by t and t' , respectively; the inter-dimer transfer integral is marked by t_d .

systems were finally identified as the best suited models for exploring the physics of quantum spin liquids on a triangular lattice [322,501,502,507–509], since alternative systems, such as YbMgGaO $_4$ or 1T-TaS $_2$, have much smaller energy scales [510–512]. Despite enormous theoretical efforts, the origin of the spin-liquid phase in two dimensions is not completely solved because pure geometrical frustration should not suffice to stabilize the quantum spin-liquid state [513–516] and disorder might play an important role, too [517–520]. As a matter of fact, numerous questions remain unanswered concerning the ground state and magnetic excitations spectrum of these materials.

Owing to several reviews on the organic spin liquid compounds κ -(BEDT-TTF) $_2$ -Cu $_2$ (CN) $_3$ and β' -EtMe $_3$ Sb[Pd(dmit) $_2$] $_2$ [322,501,502,507,508], in Section 5.1 we give only a brief summary of their properties, with the focus on κ -H $_3$ (Cat-EDT-TTF) $_2$ as the latest example. In Section 5.2 we start with the question, whether the quantum spin liquid state exhibits a gapped excitation spectrum [521]. In the following sections, open issues and hot topics of current research will be discussed, such as the 6 K-anomaly and charge-spin coupling in κ -(BEDT-TTF) $_2$ Cu $_2$ (CN) $_3$ (Section 5.3), or the influence of magnetic field and disorder on the spin liquid state as well as the formation of a valence-bond solid (Sections 5.4 and 5.5).

5.1. Properties

For the most prominent examples κ -(BEDT-TTF) $_2$ Cu $_2$ (CN) $_3$ [362,522], κ -(BEDT-TTF) $_2$ Ag $_2$ (CN) $_3$ [360,523], β' -EtMe $_3$ Sb[Pd(dmit) $_2$] $_2$ [524,525] and κ -H $_3$ (Cat-EDT-TTF) $_2$ [80,526,527] the starting point is rather similar: here molecular dimers each hosting $S = \frac{1}{2}$ form a highly frustrated triangular lattice [66,67,528]. Defining the frustration as the ratio of transfer integrals t' and t by the sketches in Figures 61 and 75, the compounds are close to a perfect triangular arrangement as summarized in Table 1. The intra-dimer transfer integral of κ -(BEDT-TTF) $_2$ Cu $_2$ (CN) $_3$ and κ -(BEDT-TTF) $_2$ Ag $_2$ (CN) $_3$ is $t_d \approx 200$ meV and 264 meV, respectively. When estimating the onsite Coulomb repulsion $U \approx 2t_d$ [58], at ambient conditions one obtains $U/t = 7.3$ and 10.5 with the ratio of the two inter-dimer transfer integrals $t'/t \approx 0.83$ and 0.90 very close to unity. For comparison, the related compounds κ -(BEDT-TTF) $_2$ Cu[N(CN) $_2$]Br and κ -(BEDT-TTF) $_2$ Cu[N(CN) $_2$]Cl possess a frustration $t'/t \approx 0.42$ and 0.44, respectively [67,537]. Theoretical considerations suggest a frustration t'/t slightly off perfect triangle [323,538–541]

At ambient pressure, no indication of Néel order is observed for temperatures as low as 20 mK, despite the considerable antiferromagnetic exchange of $J \approx 220 - 250$ K for the dimerized κ - and β' -salts [360,522,524] and slightly less in the case of the hydrogen

Table 1. Four different molecular-based quantum spin-liquids compounds on a triangular lattice with antiferromagnetic coupling J ; the degree of frustration t'/t is calculated by tight-binding approximation based on extended Hückel (EH) studies of molecular orbitals or on *ab-initio* density-functional-theory (DFT) calculations [66,67,70,360,529–531]. The effective correlations defined as the ratio of inter-dimer Coulomb repulsion U and bandwidth W are listed as extracted from the optical conductivity; the electronic contribution to the specific heat is also shown γ_e [79,308,360,524,526,527,529,532–536].

Compound	J (meV; K)	t'/t (DFT; EH)	U/W	γ_e (mJ K ⁻² mol ⁻¹)
κ -(BEDT-TTF) ₂ Cu ₂ (CN) ₃	19; 220	0.83; 1.1	1.52	12-15
κ -(BEDT-TTF) ₂ Ag ₂ (CN) ₃	19; 220	– ; 0.90	1.96	10
β' -EtMe ₃ Sb[Pd(dmit) ₂] ₂	22; 250	0.77; 0.90	2.35	19.9
κ -H ₃ (Cat-EDT-TTF) ₂	7-8; 80-90	1.25; 1.48		58.8

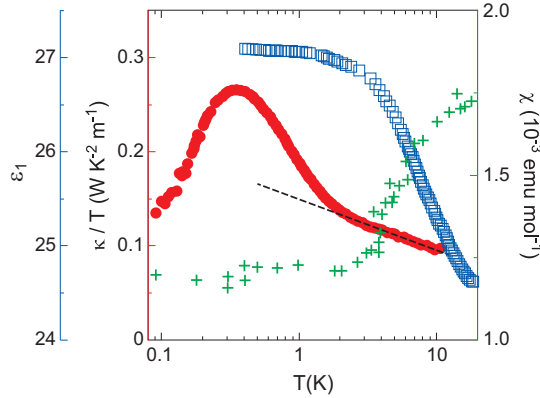


Figure 62. Low-temperature physical properties of κ -H₃(Cat-EDT-TTF)₂ illustrating the spin-liquid and paraelectric states. The temperature dependence of the dielectric constant $\epsilon_1(T)$ corresponds to the blue open squares and left axis, the thermal conductivity divided by temperature κ/T is shown by the red dots on the red left axis, and the magnetic susceptibility $\chi(T)$ refers to the green symbols and right axis. The dashed line is an eye guide. The concurrent occurrence of quantum paraelectric and quantum-spin-liquid phases below $T \approx 2$ K is inferred from the saturation of $\epsilon_1(T)$ and $\chi(T)$ (after [526,527]).

bonded κ -H₃(Cat-EDT-TTF)₂. As an example, the low-temperature physical properties of κ -H₃(Cat-EDT-TTF)₂ are displayed in Figure 62. Below a maximum around 20 K, the spin susceptibility $\chi(T)$ drops upon cooling, but no magnetic transition can be identified down to $T = 50$ mK using SQUID and torque magnetometry [526]. The behavior is reasonably well fitted by the $S = \frac{1}{2}$ antiferromagnetic Heisenberg model on an isotropic triangular lattice. The thermal conductivity shows a maximum around $T = 0.4$ K and then decreases in a linear fashion with a finite intercept as $T \rightarrow 0$. The dielectric permittivity rises as the temperatures is lowered but $\epsilon_1(T)$ saturates below 2 K; this behavior is associated with quantum fluctuations and described by the Barrett formula (12) developed for perovskites [542] (see Section 6.3).

5.2. Gapless quantum spin liquid?

Thermodynamic measurements on κ -(BEDT-TTF)₂Cu₂(CN)₃ reveal a linear term in the heat capacity

$$C_p(T) = \gamma_e T + \beta T^3 \quad (10)$$

that provides evidence for gapless spinon excitations [543–545]; the second term contains the typical phonon contributions. This is in stark contrast to thermal transport data, which exhibit a vanishing κ/T at $T = 0$ K; the result implies the presence of a small gap of $\Delta \approx 0.5$ K *i.e.* the absence of gapless fermionic excitations [546]. The presence of a spinon Fermi surface is of crucial importance for the low-energy excitations in these Mott insulators. While in inorganic compounds the dispersion of the excitation spectrum is directly mapped by inelastic neutron scattering, molecular quantum magnets evade these investigations by the abundance of hydrogen and their limited crystal size. Since most methods applied are indirect, the dispute is not resolved easily one should carefully consider what they are sensitive to. The results of complementary approaches have to be included eventually forming a consistent story; although the peculiarities of certain compounds might stain the unified picture.

In Figure 63(a) the temperature dependence of $C_p(T)$ is plotted for $\kappa\text{-H}_3(\text{Cat-EDT-TTF})_2$ together with the results of other spin-liquid compounds. The extrapolation to $T = 0$ yields a rather large offset of $\gamma_e = 58.8$ mJ K⁻²mol⁻¹, three to four times bigger than observed for $\kappa\text{-(BEDT-TTF)}_2\text{Cu}_2(\text{CN})_3$ and $\beta'\text{-EtMe}_3\text{Sb}[\text{Pd}(\text{dmit})_2]_2$, in accord with $J = 80$ K compared to 220 - 250 K of the other materials listed in Table 1. The large electronic density of states has been related to spinon excitations in the gapless spin liquid. The thermodynamic observations are confirmed by susceptibility measurements ($\chi_0 = 1.2 \times 10^{-3}$ emu/mol). It is instructive to consider the Wilson ratio

$$R_W = \frac{4\pi^2 k_B^2 \chi_0}{3(g\mu_B)^2 \gamma_e} \quad , \quad (11)$$

where $g \approx 2.002$ is the g -value of non-interacting electrons, μ_B is the Bohr magneton and k_B the Boltzmann constant. The Wilson ratio is also seen as an empirical indicator for the importance of spin-orbit coupling, which is commonly taken as a minor issue in organics; albeit this aspect has come under scrutiny in some systems recently [241, 547,548]. Most theories on quantum spin liquids predict that $R_W \ll 1$, in contrast to measured ratios [500,549]. For all organic compounds, we find a slightly enhanced Wilson ratio compared to a free electron gas: $R_W = 1.4\text{--}1.6$ [536], but significantly less than the anomalously large Wilson ratio ($R_W = 70$) reported for the three-dimensional quantum spin liquid $\text{Na}_4\text{Ir}_3\text{O}_8$ [550,551].

According to Ng and Lee [552], optical studies may provide important information; if spinon excitations exhibit a Fermi surface, they should show up not only in the thermal conductivity but also contribute to the optical conductivity [552–554]. A power-law behavior $\sigma_1(\omega) \propto \omega^2$ is expected for low-temperatures and frequencies that becomes $\sigma_1(\omega) \propto \omega^{3.3}$ above the exchange coupling J if impurity scattering is negligible. In the case of $\kappa\text{-(BEDT-TTF)}_2\text{Cu}_2(\text{CN})_3$ the challenge is that close to the Mott transition, inadvertent effects of metallic fluctuations and regions dominate at finite temperatures, hampering the extraction of spinon contributions [308,358,359]. Hence, only strongly correlated systems deep in the Mott insulating phase are suitable candidates. By preparing several extremely thin single crystals of the strongly correlated spin-liquid compound $\beta'\text{-EtMe}_3\text{Sb}[\text{Pd}(\text{dmit})_2]_2$ the optical transmission could be measured down to the THz range of frequency. Figure 64 shows that clear indications of spinon contributions to the optical conductivity can be identified. They become pronounced only at rather low temperatures ($T = 3$ K) and low frequencies $\hbar\omega < J = 22$ meV, corresponding to 250 K. For $\hbar\omega < k_B T$ one expects a drop according to $\sigma_1(\omega) \propto \omega^2$ [552] until hopping transport dominates at lowest frequencies

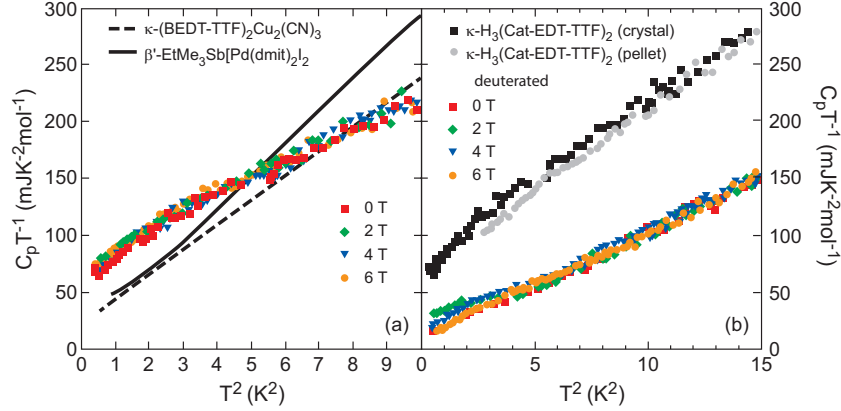


Figure 63. (a) The $C_p T^{-1}$ versus T^2 plot of the specific heat capacity of κ -H₃(Cat-EDT-TTF)₂ in the low temperature region that allows the separation of the contributions according to $C_p(T) = \gamma_e T + \beta T^3$. No dependence on magnetic field is observed up to 6 T. The dashed and solid lines represent the data of other two spin-liquid compounds, κ -(BEDT-TTF)₂Cu₂(CN)₃ and β' -EtMe₃Sb[Pd(dmit)₂]₂. (b) Comparison of $C_p T^{-1}$ vs. T^2 plots of several single crystals of κ -H₃(Cat-EDT-TTF)₂ with a pressed pellet. The data of κ -D₃(Cat-EDT-TTF)₂ obtained under fields up to 6 T are also plotted (after [536]).

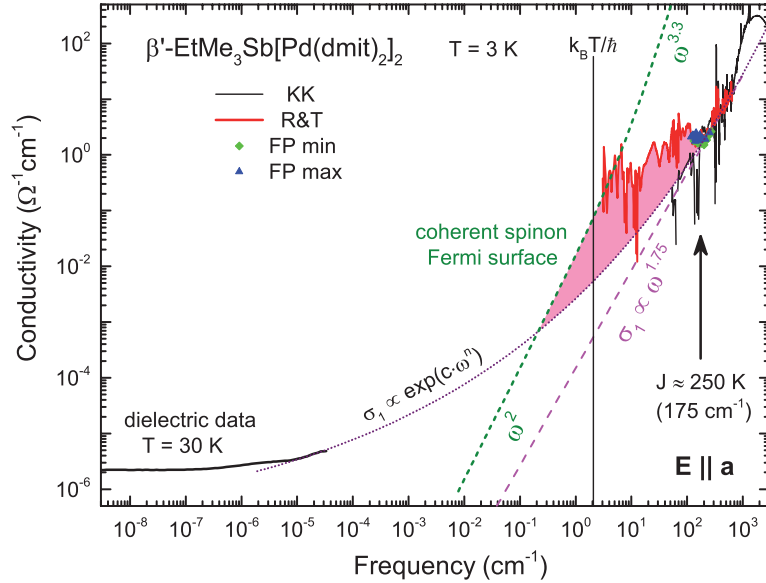


Figure 64. Dielectric and optical conductivity of β' -EtMe₃Sb[Pd(dmit)₂]₂ measured along the a -direction at low temperatures ($T = 3$ K) in a broad range from radio frequencies up to the infrared. Infrared reflectivity measurements yield $\sigma_1(\omega)$ via the Kramers-Kronig analysis (KK), while in the THz range reflectivity and transmission data (R & T) allow a direct evaluation of $\sigma_1(\omega)$. Minima and maxima of Fabry-Perot oscillations (FP) are also used in this regard. The optical data in the THz and far-infrared ranges ($2 \text{ cm}^{-1} < (\omega/2\pi c) < 200 \text{ cm}^{-1}$) is much larger than the background, which was approximated by a power law $\sigma_1 \propto \omega^{1.75}$ from the optical region down to lower frequencies; and by a stretched exponential $\exp\{\omega^{0.1}\}$ that smoothly connects the dielectric range with the optical data. The dashed green line represents the theoretically predicted frequency-dependence of a coherent spinon Fermi surface coupled to the optical conductivity via an emergent gauge field [552]. The effective range of spinons (shaded in red) extends from the crossing of the ω^2 line with the electronic background conductivity up to the antiferromagnetic exchange coupling $\hbar\omega/k_B \approx J \approx 250$ K (data taken from [508,555]).

[458,508,556]. This is a confirmation of gapless excitations and the presence of a spin Fermi surface [555]. Unfortunately, comparable experiments on $\kappa\text{-H}_3(\text{Cat-EDT-TTF})_2$ have not been performed yet.

Measurements of the magnetocaloric effect of $\kappa\text{-(BEDT-TTF)}_2\text{Cu}_2(\text{CN})_3$ down to mK temperatures reveal a decoupling of the electron spins from the lattice in the quantum-spin-liquid state, which is seen as indication for gapless spinon excitations [545]. Isono *et al.* then apply a magnetic field in order to move the system away from a quantum critical point, and they find the number of spin states that interact with the lattice vibrations strongly reduced; in other words, there exists only a weak spin–lattice coupling. The picture of a quantum critical behavior in the quantum-spin-liquid compound $\kappa\text{-(BEDT-TTF)}_2\text{Cu}_2(\text{CN})_3$ was previously suggested on the basis of magnetic torque measurements [557], where a universal critical scaling was observed. Winter and collaborators [548], however, challenged this interpretation and proposed that disorder-induced spin defects (Figure 67) better explain the low-temperature properties. These spins are attributed to valence-bond defects that emerge spontaneously as the quantum spin liquid enters a valence-bond glass phase. This suggestion is strongly supported by recent ESR experiments [558], presented in Section 5.4. Disorder effects may also resolve the dispute on the existence or non-existence of a spin gap, since they make the spinons localized and thus not conduct heat. Indeed, two independent recent studies of $\beta'\text{-EtMe}_3\text{Sb}[\text{Pd}(\text{dmit})_2]_2$ – in contrast to [559] but similar to previous studies of $\kappa\text{-(BEDT-TTF)}_2\text{Cu}_2(\text{CN})_3$ [546] – do not find a finite residual term in the thermal conductivity suggesting an absence of mobile gapless fermionic excitations. They conclude that the low-energy excitations responsible for the sizeable γ_e are localized; the heat transport is entirely due to phonons scattered by low-energy spinon excitations of the spin liquid state [560,561]. We will come back to this topic in Section 5.5 shortly.

5.3. 6 *K-anomaly*

Although the spin-liquid state is supposed to be homogeneous down to lowest temperatures, for $\kappa\text{-(BEDT-TTF)}_2\text{Cu}_2(\text{CN})_3$ a remarkable anomaly was observed around $T^* = 6$ K in a large number of different physical quantities: it is seen in NMR [543], ESR [529,558,562], and magnetic susceptibility measurements [563], in heat capacity and thermal conductivity [522,544,546], by anisotropic lattice effects [563], and as an anomaly in the out-of-plane phonon velocity and ultrasound attenuation [564]. There is no doubt that the 6 K-anomaly in $\kappa\text{-(BEDT-TTF)}_2\text{Cu}_2(\text{CN})_3$ is omnipresent and robust; a broadly accepted explanation, however, remains elusive to date. It was suggested that the second-order phase transition reflects some instability of the quantum-spin-liquid phase. This may be related to a change in the spin chirality with local Z_2 formation [503,565–567], or Amperean pairing of spinons [568–571] or the formation of an excitonic condensate by charge neutral pairs of charge $+e$ and charge $-e$ fermions [572].

Several results evidence that the lattice is involved via spin-phonon coupling. In Figure 65(a) the thermal expansion coefficient $\alpha_i = l_i^{-1}\partial l_i/\partial T$ of $\kappa\text{-(BEDT-TTF)}_2\text{Cu}_2(\text{CN})_3$ is plotted for different crystal direction i . The distinct α_b versus α_c anisotropy implies in-plane lattice distortions. They are temperature dependent and most pronounced for $T < 50$ K, where upon cooling the b -axis lattice parameter strongly contracts (large positive α_b) while the c -axis lattice constant expands ($\alpha_c < 0$). Since the hopping amplitudes t' and t among the dimers depend sensitively on the lattice parameters (cf. Figure 61), the degree of frustration t'/t increases in this

temperature range. Around 10 K the behavior reverses sign. The distinct peak around

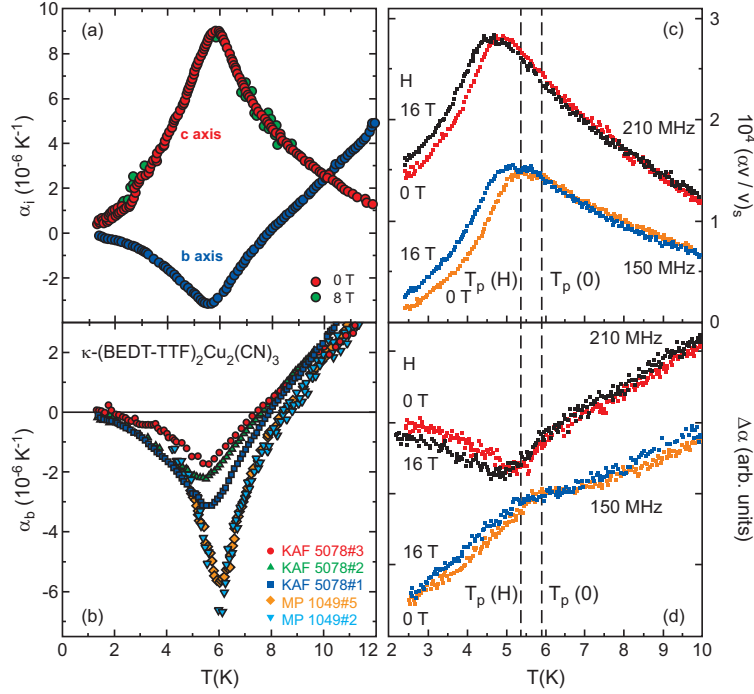


Figure 65. (a) Thermal expansion coefficients $\alpha_i(T)$ for κ -(BEDT-TTF) $_2$ Cu $_2$ (CN) $_3$ measured along the in-plane b - and c -axes around the 6 K phase transition at $H = 0$ and 8 T (green dots) (after [563,573]). (b) When results of different crystals are compared, a large sample-to-sample variation becomes obvious as far as the size of the transition is concerned while the temperature shifts less than 0.5 K (after [574]). (c) Softening peaks $(\Delta V/V)_S$ and (d) variation of the attenuation $\Delta\alpha$ for κ -(BEDT-TTF) $_2$ Cu $_2$ (CN) $_3$ as a function of temperature below 10 K: $H = 0$ T, 150 MHz (red dots) and 210 MHz (blue dots); $H = 16$ T (black symbols). The vertical dashed lines indicate the transition temperatures $T_p(0)$ and $T_p(H)$ (data from [564]).

$T^* = 6$ K clearly indicates a phase transition. While the overall feature is robust, there is a sizeable variation among crystals from the same and different batches, as illustrated in Figure 65(b). Surprisingly, no dependence on magnetic field is observed up to 8 T. The absence of any hysteresis is consistent with a second order phase transition. The entropy release found experimentally [563] exceeds the residual spin entropy considerably, providing strong arguments that spin degrees of freedom alone are insufficient to account for the phase transition. Charge degrees of freedom are a possible candidate to account for this mismatch. In fact, according to optical conductivity measurements [358,359], the charge gap in κ -(BEDT-TTF) $_2$ Cu $_2$ (CN) $_3$ is strongly suppressed because the material is next to the insulator-metal transition where metallic quantum fluctuations are present [308,508] due the vicinity of the coexistence regime.

Ultrasound measurement of κ -(BEDT-TTF) $_2$ Cu $_2$ (CN) $_3$ by Poirier *et al.* [564] reveal a softening of the longitudinal velocity along the direction perpendicular to the bc -plane for temperatures below 20 K. As shown in Figure 65(c), the maximum value is found around 5 K and it slightly depends on a frequency. The behavior below the peak is affected by an applied magnetic field. Although more susceptible to extrinsic effects, the corresponding attenuation displayed in Figure 65(d) is in accord with the sound velocity. Neither a charge-lattice coupling nor a classical magnetoelastic coupling appear appropriate to render an account of these elastic anomalies. On the one hand, vibrational spectroscopy could prove the absence of charge order and any variation around $T^* \approx 6$ K [490]. On the other hand, classical model of the magnetoelastic

coupling cannot predict a softening peak located near 6 K, when the exchange interaction J is 40 times larger at 250 K. Relaxation effects were also discarded because of inconsistencies with the frequency dependence. There are attempts to explain the frequency-dependent velocity softening observed in ultrasound at low temperatures to a spinon-phonon coupling; this effect is reduced below T^* due to a pairing instability transition of the spinons [564].

Below $T \approx 100$ K, numerous physical properties in both the spin and charge sectors evidence some anomalous behavior that infers an exotic charge-spin coupling and the possibility that it may play a pertinent role in the formation of the quantum spin liquid at low temperatures. Microwave investigations reveal an anomaly of the dielectric function around $T^* = 6$ K that depends on frequency and power as well as on external magnetic field [575]. Even more surprising is the Curie-Weiss behavior observed in the audio- and radio-frequency dielectric constant below 60 K; $\epsilon_1(T) \propto C/(T - T_C)^{-1}$, where C is the Curie constant and T_C was fixed to 6 K in line with previous observations [576]; see Figure 73 for illustration. In order to verify this assumption, Pinteric *et al.* worked with both C and T_C as free fit parameters and found that the Curie-Weiss parameters differ for the in-plane and out-of-plane crystallographic directions and for single crystals of different syntheses [458]. This stresses the involvement of the lattice with anionic-cationic layers and the effect of disorder.

Abdel-Jawad *et al.* claimed that the permittivity of κ -(BEDT-TTF)₂Cu₂(CN)₃ exhibits a tiny anomaly around $T_C \approx 6$ K that is almost independent on frequency; the absence of any remnant polarization was interpreted as an indication of antiferroelectric ordering of electric dipoles on dimers. Recent dielectric measurements by Rösslhuber *et al.*, however, cast doubt on this interpretation, as with increasing hydrostatic pressure as well as by chemical substitution, a low-temperature feature evolves and grows rapidly that could be related to percolative effects due to spatial inhomogeneities when the first order phase transition is approached [309,364,383], as discussed in Sec. 4.2. Here no anomaly is found around 6 K. We should also note that the relaxor dielectric anomaly observed in all quantum-spin liquid candidates at temperatures below about 50 K cannot simply be assigned to electric dipoles; the absence of sizeable static electric dipoles has been demonstrated by overall vibrational, dielectric and structural studies thereby eliminating also any connection to the spin-liquid state. However, this conclusion may not discard fluctuating dipoles and the charge-spin coupling in the quantum-spin-liquid formation since fast charge oscillations are observed. We come back to this topic in Section 5.5 and discuss it at length in Sections 6.1 and 6.2.

5.4. Valence-bond solid

Since magnetic field is expected to affect the spin-arrangement in a quantum spin liquid [502], the application of an external H -field was considered for most experiments on κ -(BEDT-TTF)₂Cu₂(CN)₃. Hence it is surprising that the influence reported for common laboratory scale magnetic fields up to 8 - 14 T is negligible, e.g. Figure 65. Low-temperature NMR measurements reveal an anomalous field-dependent spectral broadening of the ¹³C line for fields along the a^* -axis (*i.e.* perpendicular to the planes) that is attributable to spatially nonuniform staggered magnetization induced in the spin liquid under magnetic fields. Nonmagnetic impurities also cause a broadening of the NMR-line [577]. The thermal conductivity κ in the low-temperature regime is slightly enhanced for fields above 4 T in the a -direction, which Yamashita *et al.*

interpreted as the closing of a small spin gap in the quantum-spin-liquid state [546,578]. A negligible field effect in β' -EtMe₃Sb[Pd(dmit)₂]₂ quantum spin liquid was recently reported by two independent groups [428,560], in contrast to previous measurements [559]. The absence of reproducible experimental data on the thermal conductivity $\kappa(T)$ represents a challenge to understanding quantum-spin-liquid nature in organic solids.

Based on muon spin relaxation (μ SR) measurements, a macroscopic phase separation was claimed in the quantum spin liquid κ -(BEDT-TTF)₂Cu₂(CN)₃ below $T = 0.3$ K [579]. Already at zero field two phases are identified by different spin dynamics; but with increasing magnetic field the difference stabilizes and observed as static inhomogeneity. Similar investigations have been conducted by Pratt *et al.* down to mK temperatures [580]. They report that applying a small magnetic field of 5 mT to κ -(BEDT-TTF)₂Cu₂(CN)₃ at very low temperatures produces a quantum phase transition between the spin-liquid phase and an antiferromagnetic phase with a strongly suppressed moment. This is described as Bose–Einstein condensation of spinon excitations with an extremely small spin gap of 3.5 mK. A weak-moment antiferromagnetic phase dominates the low-temperature phase diagram, with several subphases depending on magnetic field and temperature. At higher fields, a second transition is found that suggests a threshold for deconfinement of the spinon excitations. Several of these sub-phases also show up in temperature and field-dependent ESR experiments [558].

Electron spin resonance (ESR) has the advantage to most other spectroscopic methods that it actually uses the electron spins to directly probe the magnetic properties of the quantum-spin-liquid state. In line with first indications observed previously [529,562], comprehensive ESR experiments conducted in a large frequency and temperature range recently [558] give compelling evidence that the spin-liquid state of κ -(BEDT-TTF)₂Cu₂(CN)₃ is modified or even vanishes at $T^* \approx 6$ K. In the high-temperature region, the magnetic properties can be described by an antiferromagnetic Heisenberg model on a triangular lattice, yielding a coupling of $J = 250$ K in accord with previous estimates [522] listed in Table 1. Figure 66(b) shows that the g -values do not depend on temperature and frequency. Below T^* the signal becomes very narrow, and an additional component appears. Most important, the main signal completely vanishes upon further cooling, as plotted in Figure 66(a). In other words, the spin susceptibility $\chi_S(T)$ drops in an exponential way due to opening of a spin gap $\Delta \approx 12$ K in the excitation spectrum. This is explained by the formation of valence bonds (sketched in Figure 67) causing a singlet state; by spin-phonon coupling the lattice is affected like in spin-Peierls systems [581], comprising the observations by lattice expansion and ultrasound, depicted in Figure 65. Similar conclusions can be drawn from the NMR spin-lattice relaxation rate $(T_1T)^{-1}$, which is proportional to the susceptibility: a drop in the spin susceptibility is seen below T^* before it strongly increases due to defects [522,543].

The minor ESR signal shifts to lower fields and can be clearly identified as a separate maximum below $T = 2.5$ K. In Figure 66(d) the angular dependence of the ESR signal is displayed, revealing two low-temperature features with a large anisotropy of about 10 mT, which are symmetrically shifted by $\pm 22^\circ$ with respect to the main signal. A similar behavior has been reported for κ -(BEDT-TTF)₂Cu[N(CN)₂]Cl, due to crystallographically inequivalent adjacent layers [582–584], depicted in Figure 6. For the monoclinic symmetry of κ -(BEDT-TTF)₂Cu₂(CN)₃, this explanation does not hold; hence stacking faults in the crystal are suggested to cause the doubling of the line. As the temperature is reduced further to the mK range, this ESR line separates even more. From its pronounced dependence on the external magnetic field and the particular anisotropy shown in Figure 66(d), the minor ESR feature is assigned to

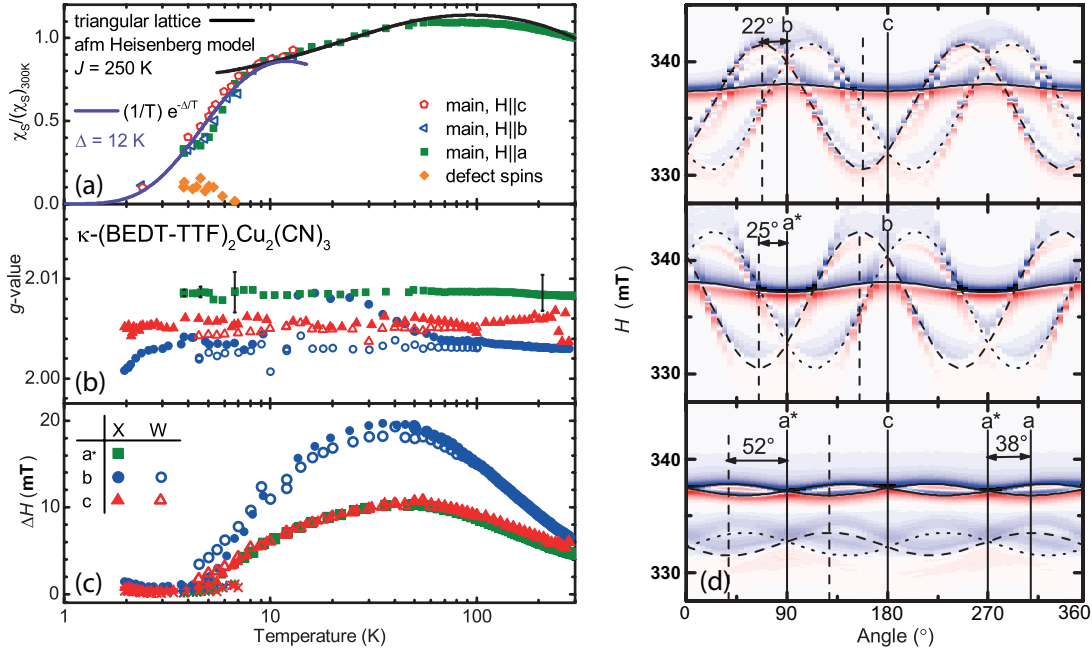


Figure 66. Temperature dependence of the (a) spin susceptibility χ_S , (b) g -value, and (c) line width ΔH obtained from fits to the ESR spectra measured in the three directions $H \parallel a^*, b, c$ for κ -(BEDT-TTF) $_2$ -Cu $_2$ (CN) $_3$ single crystals. The experiments have been performed in the X-band (9.5 GHz; solid symbols) and the W-band (95 GHz; open symbols). The spin susceptibility is described by an antiferromagnetic Heisenberg model on a triangular lattice at elevated temperatures. Below $T^* = 6$ K an exponential decay of the main signal evidences the opening of a spin gap $\Delta = 12$ K. Below T^* we notice the simultaneous appearance of the lone-spin component: The orange diamonds corresponds to the defect spins; the green \times , blue $+$, and red \times indicate the respective line width. The g -value does not exhibit any change with temperature within the experimental uncertainty estimated as 5% of the line width. The line width $\Delta H(T)$ is basically independent of the measurement frequency and field; it is largest along the b -direction. The minimum of $\Delta H(T)$ around $T \approx 3$ K coincides with features that can be identified in specific heat data at the same temperature [544,563]. Note the logarithmic temperature scale. (d) Anisotropy of the X-band ESR resonance field of κ -(BEDT-TTF) $_2$ -Cu $_2$ (CN) $_3$ measured at $T = 2$ K. Besides the main signal (solid line) from the BEDT-TTF radical, additional lines (dashed lines) appear at low-temperatures. The main line has its maximum along the crystallographic b -direction whereas the maxima of the defect signals are shifted by an angle of $\pm 22^\circ$ in the bc -plane. Similar shifts can be identified for the other directions: $\pm 25^\circ$ in the a^*b -plane $\pm 38^\circ$ in the a^*c -plane. The mirror-image doubling of the signal corresponds to the two distinct orientations of the molecules that occur due to stacking faults. (data from [558]).

defect spins, which can interact with local magnetic moments of the Cu $^{2+}$ sites in the otherwise non-magnetic Cu $^+$ anion layers [529,562] by dipolar coupling eventually forming some weakly coupled antiferromagnetic state [558]. Its strength might vary from sample to sample, but the effect in general is robust. The findings are in agreement with the μ SR experiments by Pratt *et al.* [580] and the suggestion of Riedl *et al.* analyzing the low-temperature magnetic torque measurements [548,557].

Figure 67(a) summarizes the present understanding of the ground state in κ -(BEDT-TTF) $_2$ Cu $_2$ (CN) $_3$ [520,548,558]: below T^* , spin singlets form a valence-bond solid accompanied by a lattice distortion, similar to a spin-Peierls coupling. There remain numerous orphan spins, *i.e.* local magnetic moments that might interact by dipolar coupling with each other, but also with magnetic moments in the anions layers. Although there exists no long-range magnetic order, the valence-bond solid does influence the low-temperature phase diagram compared to the spin-less case sketched in Figure 42(b). In Figure 67(b) we suggest a revised phase diagram resembling the quantum spin liquid candidate κ -(BEDT-TTF) $_2$ Cu $_2$ (CN) $_3$ where the transition to the

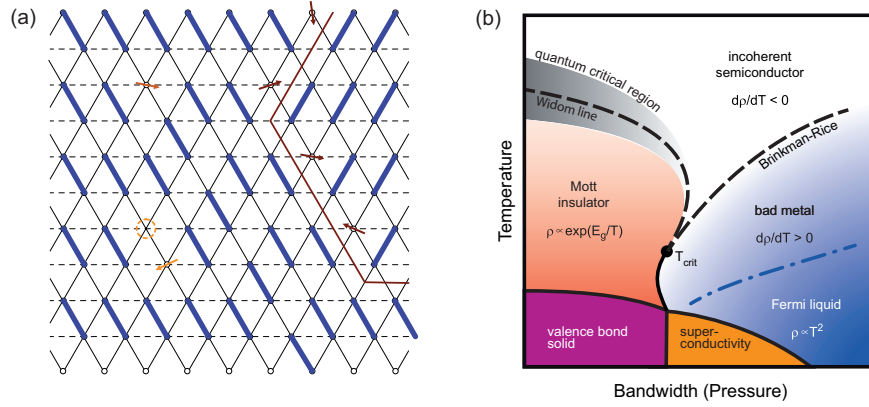


Figure 67. (a) Quasi-static valence-bond solid on an anisotropic triangular lattice, as suggested for κ -(BEDT-TTF) $_2$ Cu $_2$ (CN) $_3$ [520,548,558]. The spin singlets indicated in blue preferably form along the $(b \pm c)$ -directions; domain walls between the valence-bond patterns indicated in red. Local valence-bond defects can occur at various kinds of grain boundaries; a local spin $\frac{1}{2}$ can also be caused by the breaking of a singlet bond probably due to an anion layer vacancy, emphasized by the red circle. (b) The valence bond solid state (violet) will affect the low-temperature phase boundaries sketched in Figure 42. In the case of κ -(BEDT-TTF) $_2$ Cu $_2$ (CN) $_3$ the insulating phase is next to the superconducting state.

superconducting state is assumed vertical since no experimental data are available due to low temperatures [131,362,363].

It is crucial to extend this sort of low-temperature ESR investigations to other spin-liquid compounds in order to conclude whether the case of κ -(BEDT-TTF) $_2$ Cu $_2$ (CN) $_3$ is particular. The effect of Cu $^{2+}$ ions, for instance should not be an issue in the κ -(BEDT-TTF) $_2$ Ag $_2$ (CN) $_3$ and β' -EtMe $_3$ Sb[Pd(dmit) $_2$] $_2$ salts. However, the formation of a disordered valence-bond solid implying the opening of a spin gap could be a general scenario [190,503,585,586]. In this regard, the recently synthesized compound κ -(BEDT-TTF) $_2$ Cu[Au(CN) $_2$]Cl is of interest as it possesses no disorder in the anions [74].

5.5. Randomness

This brings us to the long debate whether the quantum-spin-liquid properties in the organic compounds originate solely from geometrical frustration or whether some sort of randomness or disorder might be crucial [517]. The interplay between mutual interaction and quenched disorder is a fundamental issue not only in condensed matter research but also in the physics of cold atoms. Recently this was further investigated theoretically in three and two dimensions [517–520,587,588].

Within randomness-induced quantum-spin-liquid models, disorder supports the cooperative action of quantum fluctuations and triangular frustration in the stabilization of a quantum-spin-liquid state [517,520]. This is important since the frustrated triangular lattices in two dimensions are unable to destroy the long-range magnetic order on their own [513–515]. Randomness helps constituting the quantum spin liquid in two-dimensional organics; its nature is two-fold: (i) The intrinsic randomness originates in the charge sector and acts via charge-spin coupling; Hotta [589] suggests that quantum electric dipoles are formed on the dimers, which interact with each other and thus modify the exchange coupling J between the spins on the dimers, crucial for the formation of the spin-liquid state. Experimentally, only inhomogeneous charge fluctuations are observed [490,590,591], which indicate fluctuating electric dimers at the

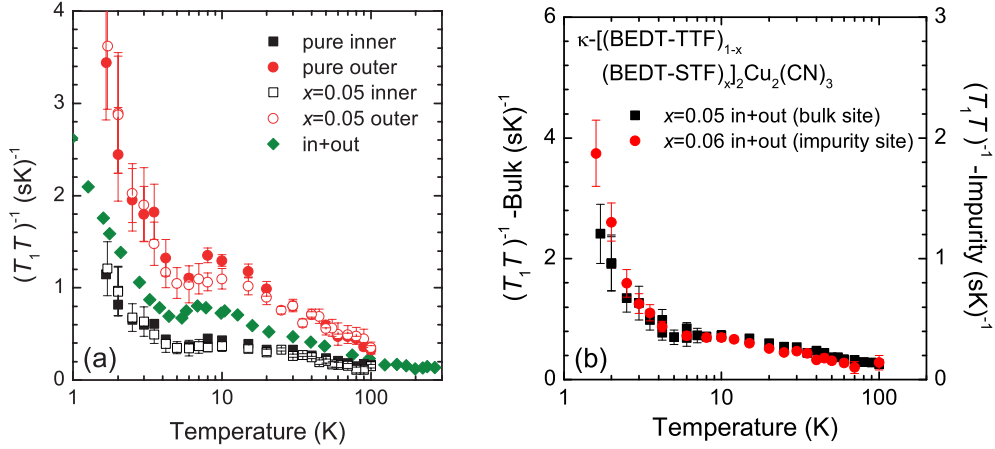


Figure 68. (a) Temperature dependence of $(T_1 T)^{-1}$ for the pure and $x = 0.05$ crystals of κ -[(BEDT-TTF) $_{1-x}$ (BEDT-STF) $_x$] $_2$ Cu $_2$ (CN) $_3$. The green diamonds indicate data of a pure samples without distinguishing inner and outer sites [489,543]. (b) Mean value of $(T_1 T)^{-1}$ of the associated inner and outer sites for bulk and impurity sites. The results of the bulk site refer to the left axis, and the results of the impurity site are plotted with the right axis [489].

rate of about 0.1 THz. We discuss this topic in Section 6.1. (ii) The extrinsic quenched randomness comes into play as a result of disorder in the anion layers [Figures 6(h) and (i)], and was revealed to be inherent to κ -(BEDT-TTF) $_2$ Cu $_2$ (CN) $_3$ and κ -(BEDT-TTF) $_2$ Ag $_2$ (CN) $_3$ [523,556]; this aspect is crucial for understanding the dc transport and electrodynamic properties of these materials in general and is discussed in Sections 4.4 and 6.2. Hence, the quenched randomness originating in the anions might provide a spatially random effective interaction to the spin degrees of freedom.

κ -(BEDT-TTF) $_2$ Cu[N(CN) $_2$]Cl is an antiferromagnetically ordered Mott insulator at low temperatures with a coupling t'/t far from frustration. Extended x-ray irradiation of 500 h (0.5 MGy/h) introduces sufficiently strong disorder to suppress the antiferromagnetic state in κ -(BEDT-TTF) $_2$ Cu[N(CN) $_2$]Cl. It was suggested [307,592] that the system evolves towards a quantum spin liquid, because the antiferromagnetic ordering observed in the pristine crystal disappears; no spin freezing, spin gap, nor critical slowing down are observed by 1 H-NMR experiments, instead gapless spinon excitations emerge.

Saito *et al.* went the other way by slightly modifying the BEDT-TTF molecules with partially replacing sulfur by selenium in the inner rings [489]. As discussed in Section 4.2, BEDT-STF substitution enlarges the bandwidth and drives the system across the Mott transition [Figure 49(b)]. However, the magnetic characteristics of κ -[(BEDT-TTF) $_{1-x}$ (BEDT-STF) $_x$] $_2$ Cu $_2$ (CN) $_3$ with $x = 0.05$ are quantitatively similar to those of the pristine crystals (Figure 68). Moreover, magnetically the substituted sites are also the same as in the bulk. NMR spectra from the impurity site suggest a decrease in local spin susceptibility and that no staggered moments are induced. Thus, the results indicate that the static and dynamic susceptibilities do not change, even at very low temperatures. This led the authors to the conclusion that disorder might already play a role in the pure compound and that the observed magnetic quantum-spin-liquid properties are not solely caused by geometrical frustration.

This idea was extended to λ -(BEDT-STF) $_2$ GaCl $_4$ [593], where also site-selective NMR was utilized to investigate the non-magnetic insulating phase of the stripe lattice system consisting of triangular and square tilings. As the temperature decreases antiferromagnetic spin fluctuations develop. The spin-lattice relaxation rate T_1^{-1} is

strongly enhanced, but saturates below 3.5 K with no indications of long-range magnetic order. λ -(BEDT-STF)₂GaCl₄ is a disordered electronic system where a novel quantum disordered state is realized. The non-magnetic ground state is discussed in terms of geometrical frustration, disorder, and the quantum critical point between the antiferromagnetic phase and the spin gap phase.

In a new class of hybrid organic crystals [EDT-TTF-CONH₂]₂[BABCO] Szirmai *et al.* [594] suggested that a quantum-spin-liquid state is introduced not by frustration – which is only $t : t' : t'' = 1.00 : 0.75 : 0.60$ – but mainly by disorder that originates in the molecular rotor BABCO[−] [595,596]. Despite the rather strong coupling of $J \approx 314$ K, the compound does not show indications of a magnetic phase transition down to 20 mK. From a variety of advanced magnetic probes (multi-frequency ESR, ¹H-NMR, zero-field μ SR), the authors conclude that intrinsic randomness due to the configuration of the frozen BCO Brownian rotors causes subtle disorder potential that suppresses magnetic order. The ¹H-NMR relaxation rate T_1^{-1} exhibits a weak increase below 10 K following an unusual power law, similar to κ -(BEDT-TTF)₂Cu₂(CN)₃ and other quantum-spin-liquid candidates, cf. Figures 68 and 79. The electron spin relaxation rate of μ SR spectra exhibits only a slow change with temperatures without a critical slowing down in the temperature range from 0.5 K down to 20 mK, which is a universal characteristic of several quantum-spin-liquid compounds [580,597–599].

Dynamic magnetic inhomogeneities are indicated by the strong field dependence of T_1^{-1} observed at around 1 K in κ -(BEDT-TTF)₂Cu₂(CN)₃ and κ -(BEDT-TTF)₂-Ag₂(CN)₃ [360,522,543]. Disorder is also identified in magnetically coupled defect spins linked to the frustrated BEDT-TTF organic lattice discussed in previous Section 5.4. Defect spins coupled to kagome and triangular lattices are also observed in inorganic quantum spin liquids herbertsmithite ZnCu₃(OH)₆Cl₂ [600,601] and 1T-TaS₂ [602]. The observation of disorder outside frustrated lattices might present a common feature of quantum-spin-liquid candidates; further studies are needed to clarify the interplay between the defect spins and the inherent frustrated lattices, as well as whether the presence of this disorder is related to the establishment of quantum-spin-liquid states.

6. Coupling of Quantum Electric and Magnetic Dipoles

The hallmark of the spin-liquid state is the absence of long-range magnetic order and the presence of persistent spin dynamics down to $T = 0$. From a quantum mechanical point of view there is no unique ground state, but a superposition of numerous equivalent solutions. The random variation in time leads to tiny fluctuations. This implies that the electronic distribution is neither solely determined nor static. In Chapter 5, we discussed the example of quantum spin liquids, where strongly correlated spins residing on the spin-frustrated lattice fluctuate and thus prevent an antiferromagnetic ordering even at absolute zero temperature. Likewise, a quantum electric dipole liquid are expected to emerge in frustrated dielectrics with fluctuating electric dipoles residing on a triangular lattice in two dimensions and preventing long-range order [603,604]. In this regime these aspects are not isolated but a certain coupling can be expected. In other words, the development of some magnetic order might affect the dielectric properties and vice versa; in general this also acts on the crystal lattice via magnetoelastic and piezoelectric coupling. While multiferroicity in inorganic compounds has drawn significant attention for the last twenty years [102,605–607], similar observations in organic charge-transfer compounds remain elusive [608–610].

In the subsequent Sections, we first give an overview of relevant theoretical stud-

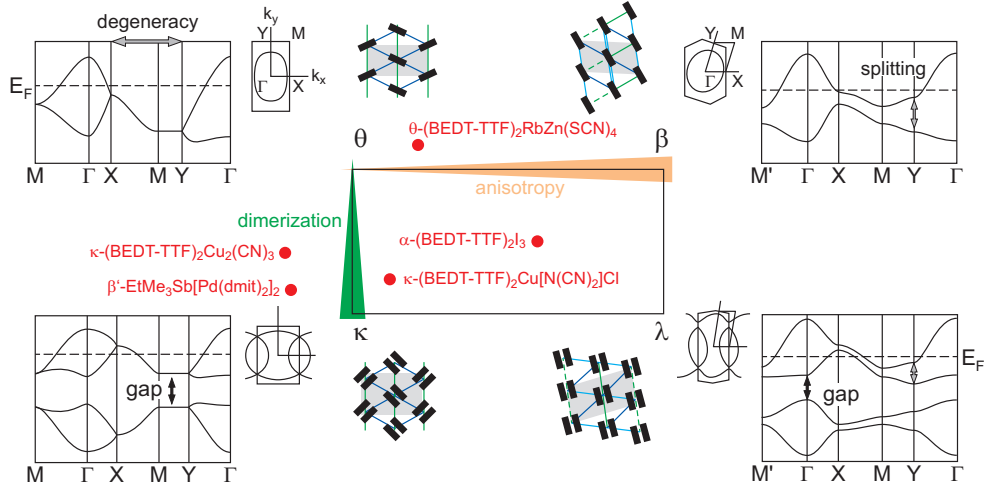


Figure 69. The classification of quarter-filled electronic system in the weak-coupling regime. The θ - (α -) and β -type with weak or no dimerization form a triangular lattice in unit of molecule, whereas those with strong dimerization, κ - and λ -type do so in unit of dimer. The distortion of the ideal triangular lattice in terms of unequal bonds is described by the anisotropy (after [92,611]).

ies concerning the interplay between spin and charges and of the experimental efforts to disclose electric dipoles in quantum spin liquids κ -(BEDT-TTF) $_2$ Cu $_2$ (CN) $_3$ and κ -(BEDT-TTF) $_2$ Ag $_2$ (CN) $_3$ and in antiferromagnet κ -(BEDT-TTF) $_2$ Cu[N(CN) $_2$]Cl (Sections 6.1 and 6.2). We continue with a unique example of a quantum liquid composed of both magnetic and electric dipoles in κ -H $_3$ (Cat-EDT-TTF) $_2$ (Section 6.3), followed by a presentation of a quantum electric dipole liquid with glassy signatures and an exotic coupling with magnetic degrees of freedom in κ -(BEDT-TTF) $_2$ Hg(SCN) $_2$ Br.

6.1. Quantum electric dipoles

Due to the A_2B stoichiometry of most BEDT-TTF salts with monovalent anions B^- , the systems are supposed to possess a quarter-filled conduction band; dimerized structures, such as the κ - or λ -phases (Figure 2), however, lead to half-filled bands. In the latter case, on-site Coulomb repulsion U dominates the electronic interactions, and the compounds serve as prime models for Mott physics. subject of Chapter 4. In the former case, however, inter-site Coulomb interaction V cannot be neglected; the α -, β - and θ - compounds (Figure 2) are the most important and heavily studied ones. A general classification of these quasi-two dimensional organic conductors is given by Hotta's minimal model based on an anisotropic triangular lattice [92,127,611]. The main factors that determine the band structure are dimerization and anisotropy, *i.e.* geometrical frustration, as illustrated in Figure 69. The inter-molecular Coulomb interaction V governs the degree of geometrical frustration in the limit of strong dimerization; the dimerization is given by strength of interaction t_d within the molecular dimer.

When dimerization is negligibly small but finite, the charge degrees of freedom are governed by V and the transfer integral t along the nearest neighbor bonds. In this limit, the system tends to a charge-ordered insulator, as discussed in Chapter 3. Frustration weakens the inter-site repulsion and finally destroys charge order; an exotic metallic state exists with limited charge mobility. The compounds are paramagnetic with no tendency towards magnetic order. As the dimerization t_d develops, the elec-

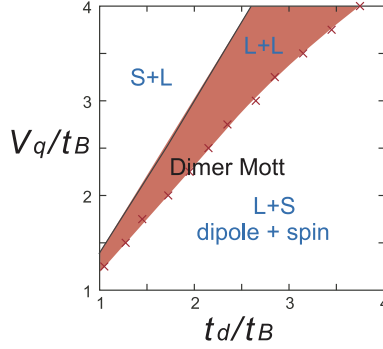


Figure 70. Phase diagram calculated within an effective dipolar-spin model by Hotta [589]. t_B and t_d are the interdimer and intradimer hopping integrals, and V_q is the intersite Coulomb interaction. S+L, L+S and L+L denote a charge ordered spin liquid, a spin-ordered charge liquid, and a charge-spin liquid phase, respectively (after [589]).

tron becomes confined within the dimer (dimer Mott insulator, cf. Chapter 4) but still delocalized, providing the possibility that dielectric degrees of freedom form a so-called ‘quantum electric dipole’, which is subject to fluctuations and correlations depending on t_d and V . The electric moments start to compete as frustration weakens V , leading to some unusual dielectric properties. Exchange coupling of the spins associated with those dielectric moments may give rise to some nontrivial magnetic behavior, as depicted in Figure 70. Increasing t_d suppresses the dielectric moments, while the spin degrees of freedom become more important. By weakening the interaction strength and approaching the insulator-metal transition (for instance, by reducing the effect of on-site repulsion U/t), spatial fluctuations of electrons develop and nontrivial long-range spin exchange interactions when the geometrical frustration becomes large. The long-range antiferromagnetic order may be destroyed and a quantum spin liquid state appears, as discussed in Chapter 5.

Based on the extended Hubbard model with on-site and nearest-neighbor interaction V that includes intra- as well as inter-dimer terms on a model lattice of κ compounds, Hotta [589] considered quantum electric dipoles as depicted in Figure 71. In order to describe the observations on κ -(BEDT-TTF) $_2$ Cu $_2$ (CN) $_3$, she suggests that at low temperatures κ -(BEDT-TTF) $_2$ Cu $_2$ (CN) $_3$ falls in the dipolar-spin liquid phase, where both spins and charges remain short-range ordered. The dielectric anomaly that develops below 50 K in most of these charge transfer salts [458,523,576,608,612–614] could be explained under the condition that electric dipoles exist when the charge is unbalanced within the dimers. A similar conclusion of ferroelectric charge order (dipolar order) is obtained by mean field and classical Monte Carlo methods [251].

Very recently Powell and collaborators performed a comprehensive study on several κ -(BEDT-TTF) $_2X$ salts combining first-principle density functional calculations with empirical relationships for the Coulomb interactions [615] in order to evaluate the model of Hotta [92,589], Naka and Ishihara [251] developed for the coupled dipolar and spin degrees of freedom. The transverse-field in the Ising model is governed by the intradimer coupling t_d , which is significantly smaller in κ -(BEDT-TTF) $_2$ Hg(SCN) $_2$ Cl and κ -(d8-BEDT-TTF) $_2$ Cu[N(CN) $_2$]Br, compared to κ -(BEDT-TTF) $_2$ Cu[N(CN) $_2$]Cl or κ -(BEDT-TTF) $_2$ Ag $_2$ (CN) $_3$. More important, however, is the more one-dimensional arrangement in the mercury-containing compounds compared to the others, which are in the quasi-two-dimensional limit. We should note, however, that all these models do not include the underlying ionic lattice and coupling to phonons.

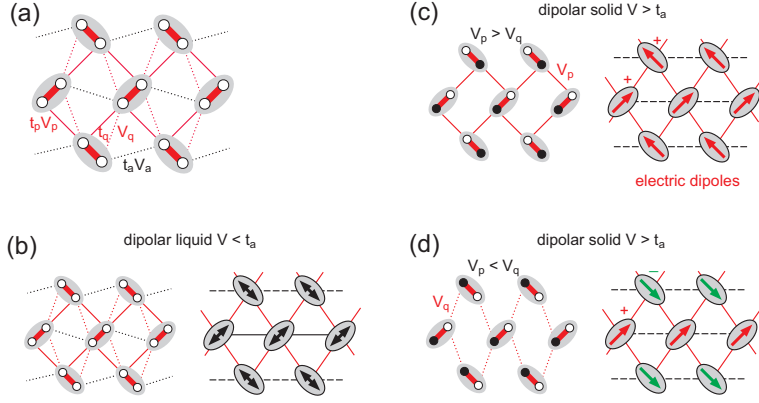


Figure 71. (a) In this κ -type lattice structure the molecules are presented by circles, the shaded area and bold red line represent the dimers (t_d , V_d). The interactions between the dimers are indicated by the overlap t_q and t_p and by the Coulomb repulsion V_q and V_p . (b) Unpolarized and (c,d) polarized configurations of quantum dipoles, depending on the hierarchy of interactions. Charges avoid neighboring alignment along the bond with strong interaction (according to [589]).

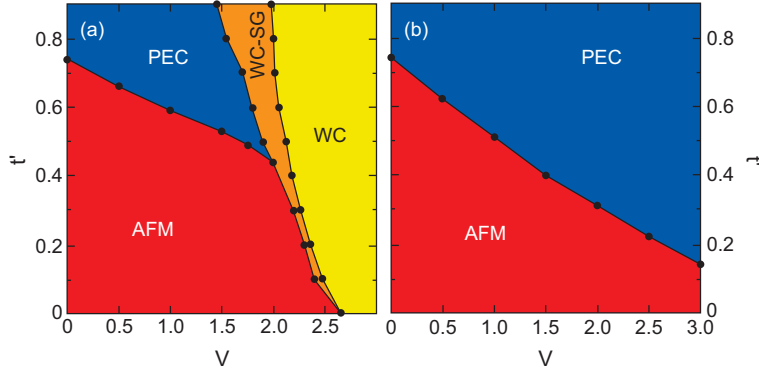


Figure 72. (a) Ground state phase diagrams from self-consistent calculations by Dayal *et al.* on periodic 4×4 lattice as a function of t' and $V = V_x = V_y$, $V' = 0$, for $U = 6$, $\alpha = 1.1$, $\beta = 0.1$, and $K_\alpha = K_\beta = 2.0$. (b) Same as panel (a), but with $V = V_x = V_y = V'$. Here antiferromagnetic (AFM) and paired-electron crystal (PEC) phases are shown together with Wigner crystal (WC) and spin gap phase. Lines are guides to the eye. (from [190,616]).

An interplay of spins with charges and bonds is pursued in the exact diagonalization study by Clay, Mazumdar and collaborators [190,571,616,617] on the extended Hubbard model with both Holstein- and Peierls-type of electron-lattice couplings on the anisotropic triangular lattice. The freezing of bonds and charges simultaneously with a spin-Peierls singlet formation results in a so-called ‘paired-electron crystal’, which exhibits moderate degrees of charge disproportionation and lattice displacement compared to those of the charge ordered state at larger V . The geometrical frustration completely replaces the charge ordered phases with the novel paired-electron crystal. As shown above, geometrical frustration in V destabilizes charge order against the dimer Mott insulator; however, compared to the pure dimer Mott case, the pair-electron crystal is more significantly stabilized, due to the spin degrees of freedom or to the spontaneous lattice modulation instead of the intrinsic dimerization. Figure 72 illustrates how electron-electron interaction affect the ‘paired electron crystal’. As U increases moderately, the coupling t' also increases. The phase diagram depends critically on the form of nearest neighbor interaction V . With $V_x = V_y = V$ but the diagonal term $V' = 0$, the Wigner crystal is found for sufficiently strong V ,

along with a narrow region, where it coexists with a spin gapped phase. Since most two-dimensional charge transfer salts have a tendency towards triangular lattices, the assumption $V' = 0$ is not realistic. For $V_x = V_y = V'$ the Wigner crystal is completely replaced by the paired electron crystal.

Fukuyama *et al.* considered the crossover from a quarter-filled system with charge-ordered ground state to the dimer Mott insulator due to strong dimerization [618]. At high energy (in the range of eV, *i.e.* optical frequencies) the dimer Mott insulator is stable, whereas at very low energy (10^{-10} eV \approx 10 kHz) charge order becomes dominant leading to extended domains of different charge polarities. As a consequence, domain walls form in the system, giving rise to the dielectric anomaly observed. This aspect is presented in full detail in Section 3.4.

Despite considerable experimental efforts, no spectroscopic evidence has been obtained for sizeable charge disproportionation in any of these κ -phase quantum spin liquid candidates and antiferromagnets [490,523]. There is a broad consensus that static charge order is less than 1%. This is supported by the most recent x-ray diffraction measurements of κ -(BEDT-TTF)₂Cu₂(CN)₃ and κ -(BEDT-TTF)₂Ag₂(CN)₃ by Foury-Leylekian *et al.* [71,72]. At the same time, the new data provide evidence for the symmetry breaking of the non-polar mean P2₁/c structure thereby proving the presence of non-equivalent crystallographic sites and allowing the formation of electric dipoles. Interestingly, despite the fact that the structural signatures of symmetry breaking are not weak, the resulting static charge disproportionation is negligibly small and in the range of the error bar. However, fluctuating electric dipoles might be concluded from dynamic charge fluctuations inferred from the charge-sensitive molecular-vibrational modes observed in Raman and infrared spectroscopy [590,591], which are broader than those of typical BEDT-TTF compounds; similar conclusion are drawn from NMR experiments. These fluctuating dipoles may show up in the microwave [575] and terahertz response [619], but the latter has been demonstrated to involve coupled anion-dimer vibrations instead [556]. Lastly, these fast charge fluctuations cannot account for the dielectric response in the audio- and radio-frequency range. We discuss this topic in subsequent Section 6.2.

6.2. *Ferroelectric-like signatures in quantum spin liquid and antiferromagnetic states*

An anomalous dielectric peak shows up as an ubiquitous property independent of the nature of the ground state in the spin sector [458,523,576,608,610,620]: in spin liquid compounds κ -(BEDT-TTF)₂Cu₂(CN)₃ and κ -(BEDT-TTF)₂Ag₂(CN)₃ (Figure 73), as well as in κ -(BEDT-TTF)₂Cu[N(CN)₂]Cl with antiferromagnetic ground state [Figure 74(c)].

The relaxor-type dielectric response suggests a short-range ferroelectric-like order [576,621] and the existence of domains of low symmetry equivalent with the average high symmetry, in accord with density functional (DFT) calculations and structural refinements [71,72,523,556,620]. However, both spectroscopic [490,523,610,620] and structural measurements [71,72] consistently demonstrate the equally distributed charge in quantum spin liquid compounds. Moreover, the persistence of strong quantum fluctuations due to charge or dipolar fluctuations in the kHz-MHz frequency range is unlikely because no Barrett-like behavior of the dielectric constant [cf. Equation (12)] has been detected.

Since no appreciable static electric dipoles have been found, the dielectric anomaly

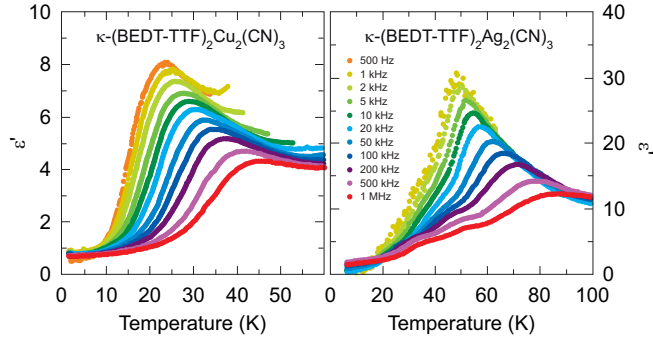


Figure 73. Temperature dependence of the real part of dielectric function ϵ' measured with the ac electric field applied $E \parallel a^*$ *i.e.* along the direction perpendicular to the molecular layers (a) of κ -(BEDT-TTF) $_2$ Cu $_2$ (CN) $_3$ and (b) of κ -(BEDT-TTF) $_2$ Ag $_2$ (CN) $_3$ (after [610]).

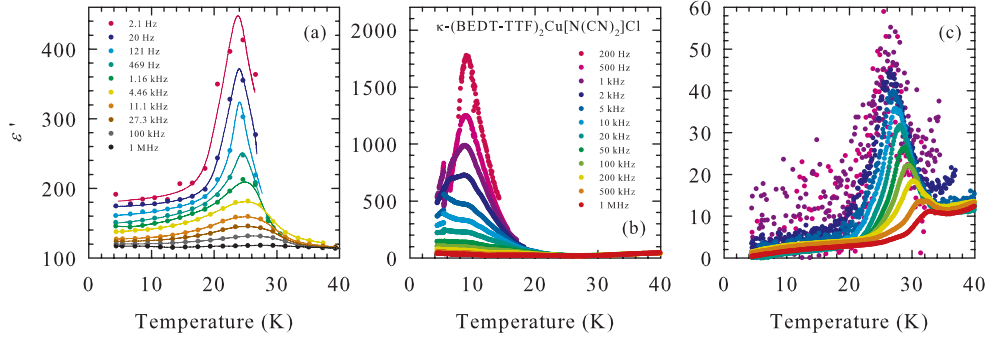


Figure 74. Temperature dependence of the real part of dielectric function ϵ' measured with the ac electric field applied $E \parallel b$, *i.e.* along the direction perpendicular to the molecular layers of three different single crystals of κ -(BEDT-TTF) $_2$ Cu[N(CN) $_2$]Cl. Different behaviors are observed ranging from (a) Curie-like at the magnetic transition $T_N \approx 25$ K suggesting multiferrocity, over (b) Curie-like at 8 K to (c) relaxor-like (after [608,610]).

in quantum spin liquid compounds has been attributed to the cooperative motion of charged domain walls within random domain structure [115,458,610].

In the BEDT-TTF-based quantum spin liquids, this structure originates from the cyanide groups located at the inversion centers bridging the polymeric CuCN/AgCN chains in the anionic layer. In the β' -EtMe $_3$ Sb[Pd(dmit) $_2$] $_2$ with quantum spin liquid ground state, disorder occurs due to two equally probable orientations of the Et groups (static disorder) and to internal rotational degrees of freedom of the Me groups (dynamic disorder); both Et and Me groups reside in the non-conducting cations [620]. Interestingly, a quantum-spin-liquid state is not established in β' -Me $_4$ P[Pd(dmit) $_2$] $_2$ and β' -Me $_4$ Sb[Pd(dmit) $_2$] $_2$: here static disorder is absent, but dynamic disorder is still present and causes a relaxor peak in $\epsilon'(T)$ [621]. In all cases, the disorder-induced domain structure is mapped onto the organic dimers and results in relaxor dielectric response with glassy signatures. The charged domain walls increasingly contribute to the dielectric constant, and the response time gets longer as the temperature is lowered because screening becomes weak when the number of charge carriers is reduced [458,523]. The domain structure changes significantly under x-ray irradiation: the relaxor peak shifts to lower temperatures with extended irradiation before a second feature emerges and becomes dominant, which is attributed to the direct response of anion defects [488].

The broadened charge-sensitive molecular vibrational modes observed in Raman and infrared spectroscopy [490,590,591] also infer inhomogeneous charge fluctuations;

however, these fast fluctuations cannot be invoked for explaining the dielectric response in kHz-MHz frequency range. Similar conclusions on the presence of an inhomogeneous charge distribution are drawn from the dc conductivity behavior showing variable range hopping, as well as from the broadening of NMR linewidth [458,492,622].

In order to shed light on the microscopic understanding of the observed dielectric anomalies in kHz-MHz range, Fukuyama *et al.* proposed a one-dimensional tight binding model with on-site and inter-site Coulomb repulsion [618]. The approach reveals that charge fluctuations are possible in the boundary region between Mott and charge order insulator. At low frequencies, oscillations occur in the double-well potential corresponding to a small charge disproportionation of opposite charge polarity; importantly, spatially extended domain walls connecting two respective domains are also present; they give rise to the observed dielectric response. The structural results of Foury-Leylekian *et al.* support the relevancy of this theoretical consideration as they evidence a symmetry breaking; however the tiny inter-dimer charge imbalance is hardly above the resolution limit [71,72]. The extension to a larger number of randomly distributed domains, which lift off the inversion symmetry in the anionic layers, is straightforward, as identified by density-functional theory calculations of Lazić *et al.*; the calculations find the ground state quasi-degenerate in energy and with reduced symmetry [523,556,620].

On the other hand, a long-range dipolar order has been proposed to occur in κ -(BEDT-TTF)₂Cu[N(CN)₂]Cl acting as a driving force for the antiferromagnetic ground state [608]. The inferred multiferroicity is based on the Curie-like dielectric peak [Figure 74(a)], as well as on the observed hysteresis and time-dependent phenomena in the vicinity of the antiferromagnetic transition at $T_N \approx 25$ K. Intriguing results obtained on another single crystal of κ -(BEDT-TTF)₂Cu[N(CN)₂]Cl suggest that ferroelectricity is proximate to the magnetic and superconducting phases [Figure 74(b)] [610]. However, the relaxor-like dielectric peak as depicted in Figure 74(c) has been observed in the most number of single crystals studied by different groups; most importantly, no symmetry breaking has been detected until now [623]. Since there is no disorder in the anionic layers, the tendency to phase segregation has been invoked, in order to support the relevancy of the charged domain wall motion scenario [610]. Thus, further experimental efforts are vital in search for structural inversion symmetry breaking in order to clarify the ferroelectric-like signatures in this antiferromagnetic system.

6.3. Quantum electric dipoles in a quantum spin liquid

A quantum liquid consisting of both electric and magnetic dipoles might be realized in the hydrogen-bonded single-molecular Mott insulator κ -H₃(Cat-EDT-TTF)₂, in which Cat-EDT-TTF spin- $\frac{1}{2}$ dimers are arranged on a two-dimensional triangular lattice as depicted in Figure 75 [526,527]. The moderately one-dimensional frustration $t'/t \approx 1.25$ is distinct from 0.83 of quantum spin liquid candidates κ -(BEDT-TTF)₂Cu₂(CN)₃ and κ -(BEDT-TTF)₂Ag₂(CN)₃ (see Section 5.1), but close to the κ -(BEDT-TTF)₂B(CN)₄ with $t'/t \approx 1.44$ [624]. This material, similar to κ -H₃(Cat-EDT-TTF)₂ compound, maintains a magnetically disordered Mott insulating state with enhanced quantum fluctuations over a wide temperature range, but in contrast to κ -H₃(Cat-EDT-TTF)₂ undergoes a phase transition below 5 K into a spin-gapped phase.

The discovery of the purely organic metal κ -H₃(Cat-EDT-TTF)₂ by Mori and collaborators [80,81,526,625] is of particular interest in so far, as the organic molecules are

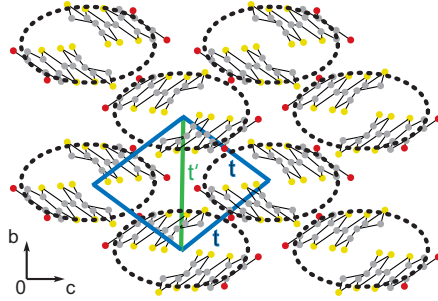


Figure 75. For $\kappa\text{-H}_3(\text{Cat-EDT-TTF})_2$ the molecules are arranged in dimers that constitute an anisotropic triangular lattice within the conduction layer. The inter-dimer transfer integrals t and t' are defined along the sides of rhomboids and along one diagonal, respectively (after [526]).

linked by hydrogen bonds as illustrated in Figure 9. Figure 62 shows the temperature dependence of the dielectric constant $\varepsilon'(T)$, which exhibits a quantum paraelectric behavior as described by the Barrett formula [542]:

$$\varepsilon'(T) = A + \frac{C}{(T_1/2) \coth(T_1/2T) - T_C} \quad , \quad (12)$$

where $C = n\mu^2/k_B$ is the Curie constant, n the density of dipoles, μ the dipole moment, and k_B the Boltzmann constant. $T_C = -6.4$ K is the Curie-Weiss temperature of ferroelectric order in the absence of strong quantum fluctuations; while T_1 is the characteristic crossover temperature from the classical Curie-Weiss regime to the quantum paraelectric regime. From Figure 62 we see that quantum fluctuations become important below $T_1 \approx 8$ K. The development of strong quantum fluctuations may be associated with enhanced proton fluctuations arising from the zero-point motion of hydrogen atoms, which persist down to low temperatures. Cooperative action between proton and electron degrees of freedom induce intra- or inter-dimer charge fluctuations, and thereby a disordered state of quantum electric dipoles develops at low T . Interestingly, the quantum spin liquid state emerges simultaneously with the quantum electric dipolar liquid. Shimozawa *et al.* suggested that the localized spins couple with the zero-point motion of the protons. First principle density functional theory (DFT) calculations confirm this idea [626]. The potential energy surface for the H atom is very shallow near the minimum points; hence, there is a certain probability that the proton is delocalized between the two oxygen atoms. Overall results thereby suggest that the quantum proton fluctuations give rise to a combined quantum liquid consisting of electric and magnetic dipoles. Interestingly, the Barrett-like behavior of the dielectric constant $\varepsilon'(T)$ is absent in the other organic quantum-spin-liquids candidates consisting of π -electron molecular layers that are separated by the anion layers.

Deuterated crystals, however, undergo an ordering transition at $T_{CO} = 185$ K leading to a charge disproportionation ($+0.94e : +0.06e$) associated with deuterium localization within the Cat-EDT-TTF layers. The resistivity abruptly jumps at that temperature with a hysteresis of 4 K [81]. The D_3 -compound exhibits a small and constant permittivity and a non-magnetic ground state below the phase transition at 185 K. In other words, the quantum-disorder due to the fluctuating proton bond is crucial for the low-temperature properties, in the spin sector as well as for the electric dipoles. And *vice versa*, the arrangement of the charge order and formation of spin singlets in the charge-rich dimers lead to the non-magnetic ground state of κ -

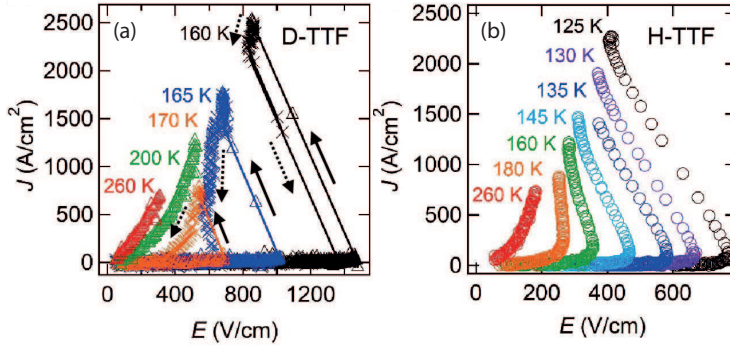


Figure 76. J versus E curves of (a) κ -H₃(Cat-EDT-TTF)₂ and (b) the deuterated analogue at several temperatures as indicated. The solid and dashed arrows represent the voltage-increasing and voltage-decreasing processes, respectively. The hysteresis appears only in the deuterated compound but not in the hydrogenated one (after [627]).

D₃(Cat-EDT-TTF)₂. As displayed in Fig. 63(b), the heat capacity of the deuterated compound remains at smaller values for the entire temperature range due to the lack of spin contributions. Except for very low T , $C_p T^{-1}$ increases linearly with T^2 but the Sommerfeld γ_e term is much smaller. An additional Schottky term infers paramagnetic spins due to disorder.

Measuring the current density–electric field characteristics of κ -D₃(Cat-EDT-TTF)₂ above and below the charge-ordering transition Ueda *et al.* found a negative differential resistance and hysteresis, which is considered to be induced by the deuterium dynamics [627]. Applying a pulsed voltage, the initial charge-ordered state changes to a metastable state through a high-conducting (excited) state, which results in the appearance of the hysteresis, as illustrated in Figure 76(a). Raman spectroscopy suggests that this metastable state is a non-charge-ordered dimer-Mott state. The results can be understood by considering the temperature-dependent dynamics of hydrogen-bonded deuterium (*i.e.*, localization/fluctuations) coupled to the π -electrons in the conducting layers. Figure 76(b) shows that on the contrary the hydrogen analogue κ -H₃(Cat-EDT-TTF)₂, which is a dimer-Mott insulator without charge-ordering phase transition, does not exhibit such hysteretic behavior, but it does display a similar negative differential resistance as well, indicating that some degree of proton localization is present. This idea is confirmed by DFT calculations [626], which find another H-localized state with reduced symmetry which lies only 2 meV above the optimized state with minimum energy. The quasi-degenerate electronic state implies that random domains are present; domain wall motion may be responsible for the nonlinear effects.

It is interesting to recall the cooperative charge dynamics observed in the charge-ordered state of α -(BEDT-TTF)₂I₃, where also a negative differential resistance is observed (Figure 22) with a significant change in shape of the measured resistivity in time [262,263]. In Section 3.4.3 we discussed how the findings of negative differential resistance and switching to transient states are explained by cooperative domain-wall dynamics inherent to the ferroelectric state driven by charge-ordering.

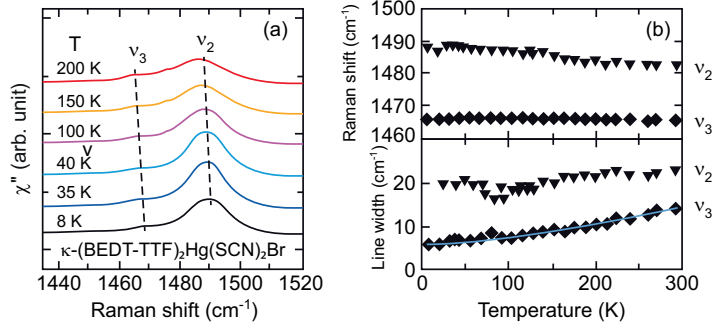


Figure 77. (a) Raman spectra of κ -(BEDT-TTF) $_2$ Hg(SCN) $_2$ Br in the region of the molecular vibrations ν_2 and ν_3 at temperatures between 200 and 8 K. (b) No splitting due to charge ordering is observed. For the ν_2 mode, the linewidth increases below 80 K. For comparison, the behavior of the charge-insensitive ν_3 band is shown; its linewidth decreases continuously from 300 K down to low temperatures (after [129]).

6.4. Quantum electric dipoles with glassy signatures

6.4.1. Quantum electric dipole lattice

Recently, Drichko and collaborators suggested that κ -(BEDT-TTF) $_2$ Hg(SCN) $_2$ Br may serve as an example of a quantum dipole liquid, based on Raman scattering investigations [129]. The system is *a priori* a good candidate because electric dipoles are arranged on a triangular lattice with moderate frustration (Figure 7) [589]. Raman and infrared vibrational spectroscopy shows that static charge order is absent [129,285] despite a pronounced metal-insulator transition at $T_{\text{MIT}} = 80$ K, the origin of which is still elusive. Charge fluctuations are invoked to explain the behavior observed in the $\nu_2(a_g)$ Raman band: Figure 77 demonstrates that the band broadens on cooling and that the linewidth goes through a slight minimum at around T_{MIT} before it increases again below. The explanation starts from the two types of BEDT-TTF molecules with charge $+0.6e$ and $+0.4e$, respectively, that are present in the charge-ordered sister system κ -(BEDT-TTF) $_2$ Hg(SCN) $_2$ Cl (Section 3.5); it is assumed ad hoc that these charges are also present in κ -(BEDT-TTF) $_2$ Hg(SCN) $_2$ Br, but fluctuate between two molecules in a dimer; the assumption is in line with our estimate of charge fluctuations indicated by the broad $\nu_{27}(b_{1u})$ mode as discussed in Section 3.5. Applying Kubo’s two-states-jump model [149,162], the shape of the band can be mimicked assuming charge fluctuations with an exchange frequency $\omega_{\text{ex}} \approx 30 - 40\text{cm}^{-1}$.

Most important, the Raman spectra in the A_{1g} channel reveal a broad feature around 40cm^{-1} of non-phonon origin that grows strongly below $T_{\text{MIT}} = 80$ K and attains maximum intensity below around 40 K, shown in Figure 78(a). The energy of mode is lower than expected for magnetic excitations; instead it is associated with the exchange frequency of charge fluctuations $\omega_{\text{ex}} \approx 30 - 40\text{cm}^{-1}$. The results are interpreted as fluctuating dipoles forming a quantum electric dipole liquid state.

6.4.2. Glassy behavior

Along this line one expects a quantum paraelectric behavior described by the Barrett formula [542], Eq. (12), as it is observed in other compounds with a triangular lattice, such as BaFe $_{12}$ O $_{19}$ and κ -H $_3$ (Cat-EDT-TTF) $_2$ [527,603] (Figure 62). Instead, the dielectric response of κ -(BEDT-TTF) $_2$ Hg(SCN) $_2$ Br exhibits only a weak relaxor-like behavior in the audio and radio-frequency range, which is screened by the conduction electrons [285]. Simultaneous fits of $\epsilon'(\omega)$ and $\epsilon''(\omega)$ to the generalized Debye

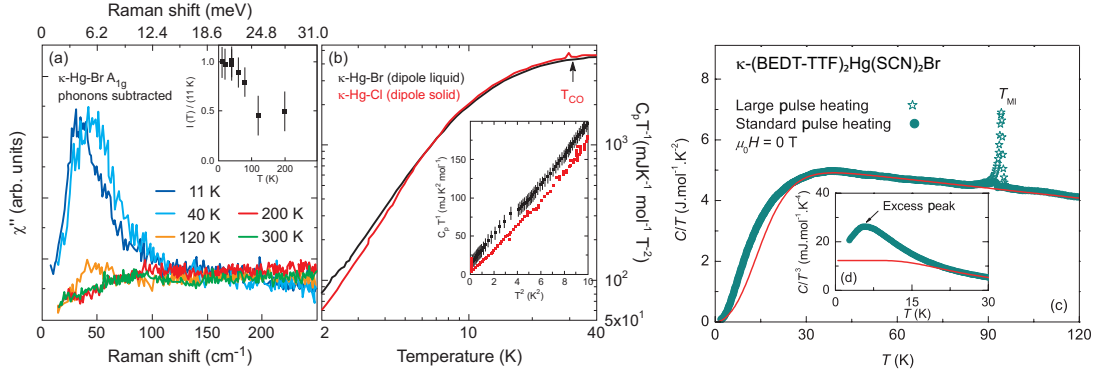


Figure 78. (a) Temperature dependence of the collective mode in the A_{1g} scattering channel for κ -(BEDT-TTF) $_2$ Hg(SCN) $_2$ Br, determined by subtracting phonons from the full Raman spectrum. Inset shows the intensity of the mode as a function of temperature. (b) Temperature dependence of the heat capacity C_p for κ -(BEDT-TTF) $_2$ Hg(SCN) $_2$ Cl (red line) and κ -(BEDT-TTF) $_2$ Hg(SCN) $_2$ Br (black line) below $T = 40$ K. The two curves deviate from each other below approximately 6 K. The inset shows the low-temperature data with linear behavior of heat capacity for κ -(BEDT-TTF) $_2$ Hg(SCN) $_2$ Br. (c) Temperature dependence of specific heat of κ -(BEDT-TTF) $_2$ Hg(SCN) $_2$ Br. The C/T^3 vs. T plot demonstrates the excess contribution from the Boson peak located at around $T = 5$ K (after [129,633]).

formula (see Section 3.4.2) disclose a strongly diminishing dielectric constant and a broadening of the relaxation time distribution when the temperature decreases; this behavior might indicate glassy freezing [628]. The mean relaxation time τ_0 follows the Arrhenius type of gradual slowing down. When we take the temperature where τ_0 extrapolates to the value of 100 s as the glass transition, we obtain $T_g \approx 5$ K. In the glassy phenomenology, the Arrhenius behavior is characteristic of strong slow-cooled glass formers and implies that glassy dynamics involves only local rearrangements of charge configurations. From this point of view, the low-frequency Raman mode is interpreted as a Boson peak arising from charge fluctuations between two molecular dimer sites. In analogy to the charge-density wave phenomenology, we speculate that the low-frequency Raman mode (Boson peak) and the dielectric mode in kHz-MHz range represent fingerprints of the same phenomenon [629,630]: the formation of dipole liquid state occurs on the local scale and bears glassy signatures. This interpretation is in accord with previous observations: systems with strong Boson peaks above T_g tend to be those with strong liquid character [206,631,632].

Also specific heat measurements reveal the presence of a Boson peak below $T = 20$ K, as displayed in Figure 78. The significant non-Debye behavior indicating an excess of low-energy vibrational states [633] is often taken as a universal signature of heterogeneity and glassy properties of the liquid state [634]. Importantly, the entropy associated with the excess peak is significantly larger than what is expected for the pure magnetic entropy of a spin- $\frac{1}{2}$ system, indicating that the glassy state should be mainly attributed to heterogeneity in the charge sector. Since no estimates of the Boson peak frequency, either on the basis of specific heat or low-frequency Raman data exist, we cannot finally conclude on their common origin. This issue is certainly worth clarifying in future studies.

6.4.3. Coupling to magnetic degrees of freedom

While in the regular dimer Mott insulator the magnetic coupling between the dimers in κ -(BEDT-TTF) $_2$ Hg(SCN) $_2$ Br is given by $J \approx 20$ meV (Table 1), unequal charge distribution on the dimers causes a renormalization [92,589] to $J_{DS} \approx 6 - 7$ meV,

as consistently estimated from ESR and Raman experiments [129,633]; still too high to assign the 40 cm^{-1} -peak observed in Figure 78(a) to purely magnetic excitations. From other metallic BEDT-TTF salts close to the charge-order transition, it is known [143,635–637] that charge fluctuations can cause collective modes present in optical spectra. The coupling of these electric dipole fluctuations to $S = \frac{1}{2}$ spins on a triangular lattice might serve as mechanism for spin-liquid behavior [589,638]. Starting with a Kugel-Khomskii type Hamiltonian, Naka and Ishihara show that the spin-charge interaction promotes an instability of the long-range magnetic ordered state around a parameter region where two spin-spiral phases merge [638]. As a matter of fact, the fluctuating dipole liquid is rather similar to an orbital liquid [500,501]. Specific heat measurements down to low temperatures are also consistent with the idea of a spin-liquid behavior in κ -(BEDT-TTF)₂Hg(SCN)₂Br, since a linear term is present only in the Br-compound but not in the Cl-analogue, where the electric dipoles are well ordered [Figure 78(b)]. It is interesting to recall the proposal of Mazumdar and Clay [190,571,616,617] about a paired electron crystal where magnetic interaction acts as a driving force for the charge order in a frustrated dimer lattice and a singlet ground state. In the case of κ -(BEDT-TTF)₂Hg(SCN)₂Cl, where an abrupt charge-ordered phase occurs at $T_{\text{CO}} = 30 \text{ K}$ (Figure 40), it is likely that the long-range magnetic order must be excluded below $T_{\text{CO}} = 30 \text{ K}$, as discussed below.

At the first sight, evidence of magnetic properties in the charge-ordered state of κ -(BEDT-TTF)₂Hg(SCN)₂Cl is pretty vague. In the region of T_{CO} , one finds a kink in dc resistivity together with a decrease of the susceptibility; this might be seen as tendency to a spin-gapped state. On the other hand, early ESR data suggested antiferromagnetic state formation slightly below T_{CO} [639], while more recent ESR and specific heat measurements on samples from different sources failed to detect any signature of magnetic transition [76]. Although there is general agreement of both results, the details seem to be affected by impurities.

Recently, the absence of long-range magnetic order is also concluded from ¹H nuclear magnetic resonance data on κ -(BEDT-TTF)₂Hg(SCN)₂Cl [640]. This study reveals a classical Korringa temperature dependence in the metallic state; in other words $(T_1 T)^{-1} \approx 1000 \text{ Ks}$ remains constant from ambient temperatures down to $T_{\text{CO}} = 30 \text{ K}$. There the relaxation rate is strongly enhanced due to charge order, but otherwise the NMR spectra do not change when passing the phase transition; in fact no signature of long-range magnetic order was observed down to 25 mK. A maximum in the relaxation rate T_1^{-1} occurs around 5 K, similar to previous observations in the spin liquid candidates κ -(BEDT-TTF)₂Cu₂(CN)₃ and κ -(BEDT-TTF)₂Ag₂(CN)₃ around 1 K, as plotted in Figure 79(a) [360,522,543]. The strong field dependence of T_1^{-1} observed at that temperature [(Figure 79(b))] is taken as indication of contributions for dynamic inhomogeneities. It seems that the low-temperature NMR properties of all these frustrated materials are dominated by extrinsic magnetic contributions rather than by intrinsic spin degrees of freedom.

While antiferromagnetism is quite common in charge transfer salts, there has been only one report on indications of weak ferromagnetic order: shortly after the discovery of superconductivity in slightly pressurized κ -(BEDT-TTF)₂Cu[N(CN)₂]Cl at a record temperature of $T_c = 12.8 \text{ K}$ by the Argonne group [641], they observed an antiferromagnetic transition near $T_N = 45 \text{ K}$ followed by a weak ferromagnetic hysteresis below 22 K [642]. As depicted in Figure 52(b), NMR, ESR und SQUID experiments confirm the antiferromagnetic ground state below 26 K; the weak ferromagnetic moment results from a canting of the ordered spins at lower temperatures [343,612,643].

In this context, the recent discovery of weak ferromagnetic order in κ -(BEDT-

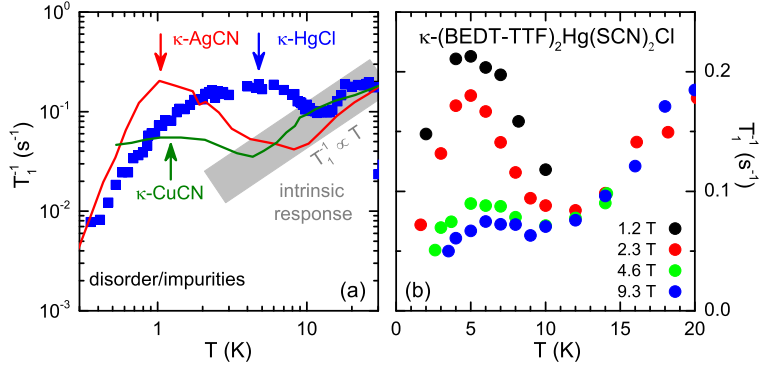


Figure 79. (a) Temperature dependence of the ^1H -NMR relaxation rate of several spin liquid candidates. At temperatures above the maximum, the T_1^{-1} data in the insulating state of $\kappa\text{-(BEDT-TTF)}_2\text{Hg(SCN)}_2\text{Cl}$ (indicated by $\kappa\text{-HgCl}$) [640] coincide with the paradigmatic quantum spin liquid compounds $\kappa\text{-(BEDT-TTF)}_2\text{-Cu}_2(\text{CN})_3$ [522] and $\kappa\text{-(BEDT-TTF)}_2\text{Ag}_2(\text{CN})_3$ [360]. Here, T_1^{-1} follows a field-independent approximately linear T dependence suggesting that this is the intrinsic response with $J \approx 200$ K. (b) Upon increasing B_0 the maximum is strongly suppressed and shifts to higher temperatures. This behavior is observed for the other compounds, too [360,522,543] (after [640]).

$\text{-TTF)}_2\text{Hg(SCN)}_2\text{Br}$ below $T = 20$ K was fairly surprising [633]. As discussed in Sections 3.5 and 6.4.1, the material is known to undergo a smooth metal-insulator transition at 80 K, which is neither a Mott nor a charge-order transition and also not associated with structural changes [77,285]. In the spin sector, the heat capacity shows a finite linear term γ_e [129], while the spin susceptibility and ESR spectroscopy [633] suggest that frustrated spins in the molecular dimers suppress long-range antiferromagnetic order, forming a spin-glass-type ground state of the triangular lattice below 40 K, which locally contains ferromagnetic polarons. Interestingly, this estimate of T_g corresponds to the energy of low-frequency Raman mode located at 40 cm^{-1} , which attains maximum intensity around $T = 40$ K. Moreover, most recent ^{13}C -NMR investigation finds weak NMR line broadening starting right below T_{MIT} and strongly developing below 40 K. The spin-lattice relaxation time forms a broad maximum centered around 5 K indicating a dynamical slowing down of magnetic fluctuations. Overall results are interpreted as disordered charge disproportionation and antiferromagnetism developed at short-range scales [644]. Considering both, the charge and spin sectors, we suggest for $\kappa\text{-(BEDT-TTF)}_2\text{Hg(SCN)}_2\text{Br}$ an exotic quantum liquid state with glassy nature, that consists of entangled fluctuating electric dipoles and spins. Below $T_{\text{MIT}} = 80$ K, composite charge-spin clusters develop upon cooling, the dynamics gradually slows down and freezes at low temperatures. More efforts in future research, experimental as well theoretical, are needed in order to further elaborate this scenario.

7. Summary and Prospects

Organic solids including charge-transfer, radical cation and anion salts and single-molecular materials represent a fascinating class of strongly correlated electrons systems in two dimensions. These materials host a broad range of quantum phenomena, which stay at the center stage of condensed-matter physics today: electronic ferroelectricity, massless Dirac fermions, quantum criticality, correlation-driven metal-insulator phase transition, quantum liquid states of spin and electric dipoles.

7.1. *Electronic ferroelectricity*

Organic charge transfer salts attract attention because some of them exhibit ferroelectricity of electronic origin that arises from charge order instead of cooperative displacements of ions observed in conventional ferroelectrics. The charge ordering is controlled by strong on-site and inter-site Coulomb interactions and is found in a number of weakly dimerized materials with effectively quarter-filled bands. However, ferroelectricity is established only if the van den Brink and Khomski requirement for the coexistence of non-equivalent sites with different charge density and non-equivalent bonds is fulfilled in the charge-ordered state.

The most prominent example is certainly α -(BEDT-TTF)₂I₃, for which charge-order-driven ferroelectricity below the metal-insulator phase transition at $T_{CO} = 135$ K is demonstrated unambiguously in numerous experiments including optical and THz-wave second-harmonic-generation, x-ray scattering, Raman and infrared vibrational spectroscopy, electron-spin and nuclear magnetic resonance and polarization switching. The phase transition is of first order as evidenced by an abrupt onset of second-harmonic-generation signal, charge imbalance and charge and spin gaps. Observation of near-field images of its spatial evolution corroborates these findings. The dynamic response of ferroelectric domains subjected to ultrafast external stimuli has been extensively studied by time-resolved measurements of electrical conductivity and femtosecond pump-probe spectroscopy and by now a rather fair understanding is achieved. New emergent phases, memory effect, photo-induced metallic state; overall, these observations strongly support a purely electronic mechanism of ferroelectricity with only minor involvement of electron-phonon interaction.

At longer time scales, the non-linear response observed by time- and field-dependent transport exhibits two distinct regimes, both of which are in line with domain wall motion. At low temperatures the behavior involves thermally excited topological defects over an electric field dependent potential barrier, whereas at temperatures closer to the phase transition the negative differential resistance behavior can be simulated consistently by a two-state model of excited charge carriers with the high mobility. The dynamic response in kHz-MHz frequency range studied by dielectric spectroscopy displays the two-mode response deeper in the charge ordered state than expected from a Curie-like peak. The anomalous response indicates the presence of disorder arising due to intrinsic heterogeneity but no consensus has been reached yet how to explain these observations. A plausible mechanism may involve the motion of two types of domain walls. No doubt, a thorough study of the topology of domain structure is highly desired in order to reach a consistent understanding of the dielectric response as well as of the low level of switchable polarization.

For the related compound, *i.e.* the slowly-cooled θ -(BEDT-TTF)₂RbZn(SCN)₄, charge order and ultrafast dynamics has been clearly identified, while the experimental evidence for polar order is not complete and its recognition is mostly based on a Curie-like dielectric peak. From a unifying view of experimental data and current theoretical approaches, it becomes rather clear that the stabilization of charge-order driven ferroelectricity takes place by a cooperative action between Coulomb repulsion – both on-site and inter-site – and coupled molecular-anion subsystems. There are also examples, such as β'' -(BEDT-TTF)₂SF₅CHFCF₂SO₃, where some degree of charge order exists at all temperatures, but it is not associated with a metal-insulator phase transition, and the van den Brink and Khomski requirement is not fulfilled.

Glassy phases in the vicinity of charge order have been identified in two charge transfer salts with a frustrated triangular lattice of molecular units. Charge order

can be avoided by rapid cooling in θ -(BEDT-TTF)₂RbZn(SCN)₄ or by replacing Rb by Cs in θ -(BEDT-TTF)₂CsZn(SCN)₄. Slow charge dynamics and glassy freezing are demonstrated by resistance fluctuation spectroscopy: upon reducing the temperature, a broad peak shifts to lower frequency and its linewidth strongly increases. The development of slow dynamics is correlated with the growth of two-dimensional charge clusters observed by x-ray diffuse scattering. Metastability of the charge glass phase in θ -(BEDT-TTF)₂RbZn(SCN)₄ is demonstrated by the time-evolution of the resistivity and nuclear magnetic resonance spectra at a fixed temperature; the obtained data show time-temperature-transformation curves commonly observed for crystallization of structural, ionic glasses and metallic alloys. Additional fingerprints of glassy state – charge vitrification and non-equilibrium aging phenomena – are demonstrated in θ -(BEDT-TTF)₂CsZn(SCN)₄ by means of the resistivity and resistance fluctuations spectroscopy: faster cooling results in a higher glass transition temperature, the resistivity behavior in time can be described by the stretched exponential function with the relaxation time obeying the gradual slowing down law; the equilibrium states at high temperature and non-equilibrium below the glass transition follow the same dynamics.

Overall, the data show that the interplay of long-range interactions and geometric frustration takes a primary role in the formation of charge glass; theoretical considerations confirm these observations and suggest θ -(BEDT-TTF)₂RbZn(SCN)₄ and θ -(BEDT-TTF)₂CsZn(SCN)₄ as prominent examples of a self-generated Coulomb glass. However, in real materials the lattice degrees of freedom are involved in the creation of the electronic crystal states, both the charge glass as well as the charge order; the extent to which they influence the crystallization mechanism remains to be clarified.

Finally, among those two-dimensional organic materials, in which organic molecules are paired in dimers and organized on an anisotropic triangular lattice, charge ordering presents a prominent topic because a link to the magnetic degrees of freedom was proposed. Until now, charge ordering below the metal-insulator transition at $T_{CO} = 30$ K and a Curie-like non-dispersive dielectric peak are detected only in κ -(BEDT-TTF)₂-Hg(SCN)₂Cl. There remain some open issues concerning the potentially polar nature of the charge-ordered state. The charge pattern and the symmetry space-group changes are not identified yet; this fact, together with indications that charge order melts below 15 K, calls for more efforts in x-ray diffraction measurements. The dielectric investigations were conducted only for an electric field applied perpendicular to molecular layers where anionic contribution cannot be avoided; certainly, in-plane measurements are needed.

7.2. Dirac electrons

The Dirac electron state in the two-dimensional organic solid α -(BEDT-TTF)₂I₃ emerges under high pressure as evidenced by the electrical conductivity, Hall effect, specific heat, nuclear magnetic resonance, magnetotransport and optical conductivity measurements. These measurements also indicate that low-mobility massive holes coexist with high-mobility massless Dirac carriers. Theoretical considerations reveal that with increasing pressure, a topological transition occurs from a charge-ordered insulator to a zero-gap state with a pair of Dirac electrons of finite mass; their existence is characterized by a special structure of the Berry curvature inside the Brillouin zone. Angle-resolved photoemission spectroscopy is certainly the most desirable tool to verify modifications of the energy spectrum associated with the topological transition; unfortunately the material and parameter range constitutes a real challenge. Here

molecular engineering might provide the possibility to enlarge the orbitals towards Dirac electrons at ambient conditions.

The outstanding feature of the Dirac state in α -(BEDT-TTF)₂I₃ is that the Dirac cones are fixed at the Fermi energy and are shifted away from the high crystallographic symmetry points in the first Brillouin zone, they are strongly anisotropic and tilted in the wavevector-energy space, very much in contrast to graphene with the isotropic Dirac cones at the corners of the first Brillouin zone. Consequently, the low-energy electronic and magnetic response show significant deviations from theoretical expectations for simple Dirac systems. The electronic correlations, long-range and short-range Coulomb interactions, induce non-uniform cone re-shaping and bandwidth reduction together with an emergent ferrimagnetic spin polarization. The long-range part is responsible for anomalous spin dynamics and excitonic fluctuations in the vicinity of the charge-order state. Effects of correlations are also observed in dc resistivity and in optical studies; interaction among Dirac electrons can be modified by temperature and pressure. Numerical studies around the critical region of the charge ordering and Dirac state show how the system passes through a phase change when increasing the intersite Coulomb interaction, which varies upon changing the external pressure: from massless Dirac via massive Dirac state coexistent with the charge order into the charge-ordered state with no Dirac cones. The much smaller gap extracted from dc resistivity compared to the one found in optics, is a result of the conduction of domain walls between ferroelectric domains with opposite polarization.

It remains unclear whether a true zero-gap Dirac state is realized in α -(BEDT-TTF)₂I₃; spin-orbit coupling is suggested to may be responsible for that it is not the case.

7.3. *Mott metal-insulator phase transition*

Organic charge-transfer salts turn out to constitute ideal model systems for studying the quantum-critical nature of the Mott transition and to verify different scenarios occurring in strongly correlated systems. For κ -(BEDT-TTF)₂X compounds a first-order Mott transition is observed up to the critical endpoints between $T_{\text{crit}} = 20$ and 40 K. Introducing disorder blurs the discontinuity and a smeared first-order transition remains.

The bandwidth-controlled Mott criticality involves fluctuations in electron and lattice degrees of freedom. A material-independent quantum critical scaling of the dc resistivity, bifurcating into a Fermi liquid metal or Mott insulator, is identified regardless of the ground state; the findings reveal the incoherent charge transport in the crossover region at high temperatures as predicted by dynamical mean-field theory calculations. Hook's law of elasticity breaks down close to the critical endpoint due the coupling of the critical electronic system to the lattice; critical elasticity shows the universal properties of an isostructural solid-solid endpoint with mean-field critical exponents.

The coexistence region of insulating and metallic phases below the critical endpoint, that is a result of the first-order Mott transition, is experimentally determined by dc conductivity measurements under varying pressure. Nuclear magnetic resonance, ac susceptibility and spatially resolved magneto-optical spectroscopy studies uncover the regime where antiferromagnetic and superconducting phases spatially coexist evidencing percolative superconductivity, whereas their competition deep in the Fermi liquid part of the phase diagram is revealed by ultrasonic velocity and attenuation

measurements. The phase separation in the critical region of the phase diagram is also supported by slowing down of electron dynamics demonstrated by fluctuation spectroscopy.

Calculations by dynamical mean field theory find a first-order phase transition with a coexistence region on both sides limited by spinodal lines that end at the critical point at finite temperatures. In the high-temperature region above the critical point quantum critical transport spreads out, following the quantum Widom line; it separates the more-insulating from the more metallic features. The predicted behavior is successfully verified experimentally combining optical and transport measurements of three highly-frustrated materials with no magnetic order β' -EtMe₃Sb[Pd(dmit)₂]₂, κ -(BEDT-TTF)₂Cu₂(CN)₃ and κ -(BEDT-TTF)₂Ag₂(CN)₃. The genuine phase diagram of Mott insulators is established: quantum Widom line, the back-bending towards the critical endpoint and metallic fluctuations close to the first-order phase boundary are found.

Visualization of the real-space phase coexistence in the critical region is still limited to about 10 μm , disabling a direct proof that metallic regions coexist in the insulating background; scanning near-field microscopy at cryogenic temperatures is a desirable tool in future studies. Hence, at present indirect approaches must be employed. Tuning the bandwidth by hydrostatic pressure and chemical substitution enables us to follow the temperature-dependent dc transport and dielectric constant from the strongly correlated Mott insulator via the range of phase coexistence into the metallic regime; no hysteresis is observed. The spatial coexistence of correlated insulating and metallic regions is successfully testified by a strongly enhanced dielectric constant, when approaching the first-order transition; this behavior uncovers percolative nature of the first-order Mott transition. The experimental findings are supported by dynamical mean-field theory calculations including spatial inhomogeneities in a hybrid approach.

When the system is tuned into the metallic state, coherent electronic charge transport emerges, this is highlighted via the Fermi-liquid behavior including quadratic temperature dependence of dc resistivity and ω - T scaling in the optical conductivity. As a matter of fact, in these organic conductors Fermi-liquid behavior is observed over a wider temperature and frequency range than in any inorganic compound, owing to the fact that the intrinsic energy scales (bandwidth, Fermi energy) are fairly low. The upper limit of the Fermi liquid regime is given by deviations of the scattering rate from the T^2 and ω^2 -lines.

At low temperatures, in the Fermi-liquid regime, the data exhibit a gradual increase of the effective mass indicating that the electronic correlations become stronger when approaching the Mott transition from the metallic side; the findings are in agreement with the Brinkman-Rice theory and dynamical mean-field calculations. The comprehensive set of optical data evidences the universality of Landau's Fermi liquid concept upon varying the correlation strength.

At higher temperatures above the Fermi liquid range, a bad metal regime is found as commonly observed for strongly correlated materials; and resistivity even exceeds the Ioffe-Regel-Mott limit. Reduction of the low-frequency spectral weight is in agreement with theoretical calculations. The displacement and finally disappearance of the Drude peak is accompanied by a transfer of spectral weight to energies above 1 eV. The phenomenon was ascribed to strong correlations, but arguments were raised that this might not be the main cause for all correlated organic materials.

Effects of disorder on the Mott transition were studied for different interaction and disorder strength by dynamical mean-field theory; the resulting Anderson-Hubbard phase diagram displays a correlated disordered metallic phase, surrounded by An-

derson and Mott insulating phases. With increasing disorder the coexistence region gets smaller; when disorder becomes large enough (larger than twice the bandwidth), the critical temperature abruptly goes to zero and the coexistence region disappears. In this regime, the effects of interaction and disorder are found to be comparably important for charge localization.

Experimentally, x-ray irradiation of the Mott insulator κ -(BEDT-TTF)₂Cu[N-(CN)₂]Cl results in a shift of spectral weight from the interband transition to low energies where the Drude-like behavior is present. The result that disorder can make the system more metallic agrees with theoretical considerations; recent calculations find that the random potential broadens the bandwidth and moves the system away from the Mott transition. In addition, recently it was found that x-ray irradiation can induce slow electronic fluctuations caused by a synergistic effect between the Mott boundary and randomness indicating the formation of electronic Griffiths phase. On the other hand, κ -(BEDT-TTF)₂Cu₂(CN)₃ is much less susceptible to x-ray irradiation; the resistivity decreases but even for large doses the effect is not significant. However, effects of inherent disorder on the transport properties are clearly observed for several κ -(BEDT-TTF)₂X quantum-spin-disordered Mott insulators and can be explained within the Mott-Anderson localization theory. While at high temperatures the transport properties is dominated by the correlation strength, upon lowering temperature variable-range hopping transport takes over; the most disordered material, κ -(BEDT-TTF)₂Cu₂(CN)₃, exhibits the lowest dc resistivity and the highest charge-carrier density, indicating that it is located closest to the insulator-metal transition.

7.4. *Quantum spin liquid versus magnetic order*

Quantum spin liquids are quantum disordered ground states of strongly correlated spins, in which the ground state is a superposition of multiple configurations and quantum fluctuations are important enough to prevent conventional magnetic long-range order. At this point, there are four prominent triangular organic solids, which are considered candidates for the realization of a quantum spin liquid state: charge-transfer salts κ -(BEDT-TTF)₂Cu₂(CN)₃, κ -(BEDT-TTF)₂Ag₂(CN)₃, β' -EtMe₃Sb[Pd(dmit)₂]₂ and the hydrogen-bonded single-molecular compound κ -H₃(Cat-EDT-TTF)₂.

These materials are Mott insulators, in which – despite the relatively large exchange coupling – there is no experimental indication of magnetic ordering: the susceptibility, specific heat and nuclear magnetic resonance show no singular features related to phase transitions. Initially, it was proposed that the key variable is frustration – spatial anisotropy – measured by the ratio of the next-nearest-neighbor and nearest-neighbor transfer integral, which is close to unity for κ -(BEDT-TTF)₂-Cu₂(CN)₃, κ -(BEDT-TTF)₂Ag₂(CN)₃ and β' -EtMe₃Sb[Pd(dmit)₂]₂, when estimated by the extended Hückel method. Recent evidence challenges this idea because calculations by density functional theory yield values closer to 0.8, as well as the more one-dimensional anisotropy value of about 1.3 for κ -H₃(Cat-EDT-TTF)₂.

Low-energy excitations are probed by thermal and optical properties: good evidence supporting spin liquid and gapless spin excitations – spinons – comes from specific heat displaying a large linear term for all four candidates. The Wilson ratio is slightly above unity, the value expected for free fermions; this result thus indicates that the same degrees of freedom determine the behavior of both the susceptibility and the specific heat. However, very recent electron-spin resonance measurements on κ -(BEDT-TTF)₂-

$\text{Cu}_2(\text{CN})_3$ observe a drop of the spin susceptibility, which can only be explained by the opening of a gap due to the formation of spin singlets. Interestingly, a finite residual linear term of thermal conductivity is only observed in $\kappa\text{-H}_3(\text{Cat-EDT-TTF})_2$, while it is fully suppressed in $\kappa\text{-(BEDT-TTF)}_2\text{Cu}_2(\text{CN})_3$ leading to the suggestion of a gap opening. In $\beta'\text{-EtMe}_3\text{Sb}[\text{Pd}(\text{dmit})_2]_2$, in contrast to initial findings, most recent reports exclude the magnetic thermal conductivity as well. The absence of reproducible finite residual thermal conductivity questions the presence of delocalized gapless low-energy excitations in these spin-liquid candidates; spinons may become localized due to the spin-lattice decoupling, or to disorder. On the other hand, the spinon contribution to the optical conductivity is successfully verified in $\beta'\text{-EtMe}_3\text{Sb}[\text{Pd}(\text{dmit})_2]_2$ in agreement with theory predicting a power-law absorption at low frequencies; similar experiments failed in the case of $\kappa\text{-(BEDT-TTF)}_2\text{Cu}_2(\text{CN})_3$ due to effects of metallic fluctuations in the vicinity of the Mott transition.

The legendary 6 K-anomaly in $\kappa\text{-(BEDT-TTF)}_2\text{Cu}_2(\text{CN})_3$ is omnipresent; effects observed in nuclear magnetic resonance, electron and muon spin resonance, in specific heat and thermal conductivity, in thermal expansion and ultrasonic velocity, and in microwave and dielectric response indicate coupled spin, lattice and charge degrees of freedom are involved. Various scenarios are suggested for the explanation of this anomaly, such as spin-chirality ordering, a spinon-pairing transition, or formation of an exciton condensate. A large sample-to-sample variations in the size of 6 K anomaly as well as in the microwave and dielectric anomalies are consistent with inhomogeneity and disorder. Theoretical considerations suggest disorder-induced spin defects may provide a comprehensive explanation of the low-temperature properties of $\kappa\text{-(BEDT-TTF)}_2\text{Cu}_2(\text{CN})_3$ and maybe other compounds, too. In this disorder-based approach, the 6 K anomaly can be interpreted as the formation of a valence bond solid. The formation of singlets yields the drop in susceptibility but leaves sufficient defects spins randomly placed due to disorder also induced from the anion layer. At this point, a comprehensive explanation of the low-temperature anomaly and its possible relation to a spin-liquid state in all quantum spin liquid candidates is still lacking.

It is intriguing that randomness appears to support the quantum spin liquid state: a nuclear magnetic resonance experiment on $\kappa\text{-(BEDT-TTF)}_2\text{Cu}[\text{N}(\text{CN})_2]\text{Cl}$ found that the antiferromagnetic ordering disappears, when crystals are irradiated by x-rays while spin-liquid properties emerge. Alloying $\kappa\text{-(BEDT-TTF)}_2\text{Cu}_2(\text{CN})_3$ with BEDT-STF molecules results in no change of magnetic properties suggesting inherent disorder is already present in $\kappa\text{-(BEDT-TTF)}_2\text{Cu}_2(\text{CN})_3$. The theoretically developed randomness-induced quantum spin-liquid models show disorder enhance cooperative action of quantum fluctuations and triangular frustration. Two inherent sources of randomness are anticipated: the intrinsic randomness is suggested to originate in the charge sector and to act via charge-spin coupling, while the extrinsic quenched randomness is due to disorder in the anion layers.

It remains a challenging task to verify the quantum spin liquid state experimentally. Certainly, a crucial open issue is the extent and influence of disorder and inhomogeneity. Whether any of these phenomena are also present in $\kappa\text{-H}_3(\text{Cat-EDT-TTF})_2$, and whether they are important for the formation of the quantum spin liquid state in organics remains to be clarified in future.

7.5. Quantum states of electric and magnetic dipoles

Although the spin liquid phase is insulating, anomalous charge dynamics in κ -(BEDT-TTF)₂Cu₂(CN)₃ and κ -(BEDT-TTF)₂Ag₂(CN)₃ are suggested for explaining the observed dielectric and low-energy optical responses. Several theoretical approaches have been developed to study the interplay of spins with charges on frustrated triangular lattice with dimerized sites. The approach based on extended Hubbard model considers quantum electric dipoles on organic dimers treating the inter-dimer interactions perturbatively; it results in the phase diagram, in which charge-spin liquid shares a common boundary with charge-ordered spin liquid and with spin-ordered charge liquid. An exact diagonalization study including electron-lattice coupling finds paired-electron crystal phase adjacent to the antiferromagnetic, spin gap and Wigner crystal phases.

Despite considerable efforts, no experimental evidence exists for sizeable electric dipoles; a negligibly small charge imbalance is found in vibrational spectroscopy and x-ray diffraction. But it has been shown that the symmetry of the non-polar mean P2₁/c structure is broken, *i.e.* that non-equivalent crystallographic sites exist. Whereas static electric dipoles are excluded, fluctuating dipoles may be concluded based on the unusually broad charge-sensitive molecular Raman and infrared modes. While these fast fluctuations cannot be invoked to explain the anomalous dielectric response in kHz-MHz range, suggestions were raised that they manifest in the microwave response; the terahertz response, however, was proven to be due to coupled dimer-anion vibrations instead.

Since no sizeable static electric dipoles are present, the dielectric anomaly in quantum spin liquids is attributed to the cooperative motion of charged domain walls. The walls are created within random domain structure induced by quenched disorder originating in the anion layer, as identified by density functional theory calculations. The domain wall scenario is also supported by an approach based on the one-dimensional tight binding model with on-site and inter-site Coulomb repulsion indicating that charge fluctuations occur in the boundary region between Mott and charge-order insulators. At low frequencies, oscillations occur in the double-well potential corresponding to a small charge disproportionation of opposite polarity; spatially extended domain walls connecting two respective domains may give rise to the observed dielectric response.

In κ -(BEDT-TTF)₂Cu[N(CN)₂]Cl an anomalous dielectric response shows up, which coincides with an antiferromagnetic state with signatures ranging from multiferroicity to ferroelectricity next to superconductivity; but relaxor-like response prevails in the majority of single crystals studied. Further experimental efforts are indispensable for the search for structural inversion-symmetry breaking in order to clarify the ferroelectric-like signatures in this antiferromagnetic system.

The low-temperature behavior of the hydrogen-bonded single-molecular compound κ -H₃(Cat-EDT-TTF)₂ is unique among organics in the way that it demonstrates a quantum liquid of electric dipoles established simultaneously with a quantum spin liquid. The dielectric constant follows the Barrett behavior revealing strong quantum fluctuations originating in the zero-point motion of hydrogen atoms; density functional theory suggests that proton fluctuations coupled to charges and spins give rise to a quantum liquid of electric and magnetic dipoles. The crucial importance of the fluctuating proton-bond is evidenced in the behavior of deuterated sister system κ -D₃(Cat-EDT-TTF)₂ showing no signatures of liquid phases; instead a charge-ordered state with spin gap is established. Under strong dc electric fields, the negative differ-

ential resistance is observed and attributed to the deuterium dynamics coupled to the electron system. A negative differential resistance behavior is also seen in κ -H₃(Cat-EDT-TTF)₂. This surprising result may be explained by density functional theory, which finds a quasi-degenerate electronic state implying random domains in the real space; the domain wall motion may be responsible for the nonlinear effects.

Another candidate for a quantum electric dipole liquid is given by κ -(BEDT-TTF)₂-Hg(SCN)₂Br because no evidence for charge ordering is detected. The $\nu_2(a_g)$ Raman band broadens on cooling and its shape is well described by Kubo's two-states-jump model assuming charge fluctuations with an exchange frequency $\omega_{ex} \approx 30 - 40 \text{ cm}^{-1}$. A broad feature of non-phonon origin around 40 cm^{-1} in the A_{1g} Raman channel is taken as a fingerprint of these very fluctuations; arguments are given that the energy of the mode is lower than expected for magnetic excitations. However, a quantum paraelectric behavior is not observed; dielectric response instead displays features characteristic of glassy dynamics indicating that the low-frequency Raman mode may be more appropriately interpreted as a Boson peak. The suggestion is supported by the significant non-Debye behavior found in the specific heat measurements; an excess of low-energy vibrational states, whose entropy is significantly larger than what is expected for the pure magnetic entropy, indicates heterogeneity and glassy properties mostly in the charge sector of the liquid state. But spins are coupled to fluctuating charges as also indicated by a finite linear term observed in the specific heat measurements consistent with a spin liquid behavior; a spin-glass-like phase develops at lower temperatures as implied by the spin susceptibility and electron spin resonance measurements. An idea of exotic quantum liquid state with glassy nature that consists of entangled fluctuating electric dipoles and spins is worth to be verified in future.

Theoretical considerations of spin-charge coupling suggest possible mechanisms of charge-driven instabilities towards a long-range magnetic state. Initially the charge-ordered κ -(BEDT-TTF)₂Hg(SCN)₂Cl was thought to tend to a magnetic transition at low temperatures. But the recent specific heat, electron spin resonance and nuclear magnetic resonance measurements give strong indications that magnetic order is absent and defect states dominate the properties at low temperatures. Nevertheless more efforts in this direction is needed to clarify the ground state in the spin sector and enable verification of current theoretical models based on dipolar-spin coupling.

7.6. Outlook

We live in a three-dimensional world, but physics in smaller number of dimensions reveals a qualitative change in the system's properties. Despite not being atomically thin as graphene, quasi-one- and two-dimensional organic materials have many characteristics linked to their reduced dimensionality. It is associated with the overlap of molecular orbitals provides the cornerstone of organic metallicity and modifies the way quantum fluctuations compete with long-range order. They developed as a workbench of real materials to discover novel aspects of matter such as Peierls distortion and charge and spin density waves in one-dimensional materials, electronic ferroelectricity and quantum spin liquids in two dimensions. Unconventional non-phonon-mediated superconductivity was first discovered and studied in low-dimensional organics; the knowledge gained helped a lot in the quest for high T_c superconductors since their discovery at the end of eighties.

While conducting polymers and organic semiconductors are implemented in a broad range of electronic devices, actual applications of crystalline two-dimensional organic

conductors did not surface until today; and one should not make any strong claims or serious predictions in this regard. Whether or not these materials eventually find useful applications, they keep expanding our understanding of fundamental science and offer paths to designing other materials with practical use.

The family of molecular quantum materials draws its strength from the versatility of the compounds and selectivity of their physical properties. It allows us to tune the interplay of various degrees of freedom in an unprecedented way, to reach unexplored areas of the phase diagram and to shift the frontier towards new states of matter. In roughly ten years, research in two-dimensional organic solids has made spectacular advances: it is amazing to see how the collaboration between theory and experiment enables us to realize what has been suggested in the past, but also to understand what has been observed years ago. Organic conductors always have been a niche in condensed matter science, the general interest is soaring since molecular solids have been realized as superior model compounds and often prime examples for investigating quantum phenomena. There is a historical record that supports this and justifies believing this should continue to be the case.

But the paradigm of successful science is shifting nowadays. Accomplishing the bright future of the field will require a stronger effort in materials synthesis and design. To this end important advances can be achieved by integrating machine learning applications. Experimentally, the organic materials are attractive because the sample can be prepared from commercially low-cost components we find in nature. The clever performance of making the targeted material will vitalize the field together with up-to-date experimental methods center on imaging, scattering and spectroscopy tools with increasing spatial and time resolution, including instrumentation for the individual investigator and the scientific user facilities. Reaching the goal equally requires the use of state-of-the-art computational facilities and synergy of numerical calculations and microscopic theory.

Only time will tell, but the potential for the continued growth of the field is here. We would be gratified if this paper turns out to be useful to this end and succeeds to drive enthusiasm of coming generations in physical and chemical sciences.

8. Acknowledgements

Working in the field of low-dimensional organic conductors for decades, we have enjoyed fruitful collaborations and illuminating discussions with numerous colleagues and students whom we all want to thank very much. In this context we would like to mention in particular M. Basletić, K. Biljaković, S. Brown, E. Canadell, R.T. Clay, M. Čulo, V. Dobrosavljević, N. Došlić, N. Drichko, M. Dumm, P. Foury-Leylekian, H. Fukuyama, S. Fratini, A. Girlando, B. Gorshunov, B. Gumhalter, C. Hotta, V. Ilakovac, S. Ishihara, T. Ivek, S. Kaiser, K. Kanoda, R. Kato, B. Korin-Hamzić, M. Lang, P. Lazić, W. Li, P. Littlewood, S. Mazumdar, J. Merino, O. Milat, J. Müller, M. Pinterić, J.P. Pouget, B. Powell, A. Pustogow, R. Rösslhuber, G. Saito, Y. Saito, T. Sasaki, J.A. Schlueter, D. Schweitzer, R. Valentí, S. Winter, Y. Yoshida. The project was financially supported by the Deutsche Forschungsgemeinschaft (DFG), the Deutscher Akademischer Auslandsdienst (DAAD), the Croatian Ministry of Science and Education and by the Croatian Science Foundation. We acknowledge B. Gumhalter, T. Ivek, M. Pinterić, M. Prester, A. Pustogow and W. Strohmaier for their support and assistance during the preparation of this Review.

References

- [1] L. Pál, G. Grüner, A. Jánossy, and S. Sólyom (eds.) *Low-Dimensional Cooperative Phenomena*, NATO Advanced Study Institute, Series B Vol. 7, Plenum Press, New York, 1975 (Starnberg, Germany, 1974).
- [2] H. Schuster (ed.) *One-Dimensional Conductors*, Lecture Notes in Physics Vol. 34, Springer-Verlag, Berlin, 1975 (Saarbrücken, Germany, 1974).
- [3] L. Pál, G. Grüner, A. Jánossy, and S. Sólyom (eds.) *Organic Conductors and Semiconductors*, Lecture Notes in Physics Vol. 65, Springer-Verlag, Berlin, 1977 (Siófok, Hungary, 1976).
- [4] H. Keller (ed.) *Chemistry and Physics of One-Dimensional Metals*, NATO Advanced Study Institute, Series B Vol. 25, Plenum Press, New York, 1977 (Bolzano, Italy, 1976).
- [5] J. Miller and A. Epstein (eds.) *Synthesis and Properties of Low-Dimensional Materials*, Annals of the New York Academy of Sciences Vol. 313, New York Academy of Sciences, New York, 1978 (New York, U.S.A., 1977).
- [6] W. Hatfield (ed.) *Molecular Materials*, NATO Conference Series Vol. VI, Plenum Press, New York, 1979 (Les Arcs, France, 1978).
- [7] S. Barišić, A. Bjeliš, J. Cooper, and B. Leontić (eds.) *Quasi one-dimensional conductors I & II*, Lecture Notes in Physics Vol. 95 & 96, Springer-Verlag, Berlin, 1979 (Dubrovnik, Yugoslavia, 1978).
- [8] J. Devreese, R. Evrard, and V. van Doren (eds.) *Highly Conducting One-Dimensional Solids*, Plenum Press, New York, 1979.
- [9] L. Alcácer (ed.) *The physics and chemistry of low dimensional solids*, NATO Advanced Study Institute, Series C Vol. 56, Reidel, Dordrecht, 1980 (Tomar, Portugal, 1979).
- [10] J. Bernasconi and T. Schneider (eds.) *Physics in One Dimension*, Springer Series in Solid State Sciences Vol. 23, Springer-Verlag, Berlin, 1981 (Fribourg, Switzerland, 1980).
- [11] J. Miller (ed.) *Extended Linear Chain Compounds*, Vol. I-III, Plenum Press, New York, 1982-1983.
- [12] S. Tanaka and K. Uchinokura (eds.) *Physics and Chemistry of Quasi-One-Dimensional Conductors*, Vol. 143, Physica B & C, 1986 (Lake Kawaguchi, Japan, 1986).
- [13] D. Jérôme and L. Caron (eds.) *Low-Dimensional Conductors and Superconductors*, NATO Advanced Study Institute, Series B Vol. 155, Plenum Press, New York, 1987 (Magog, Canada, 1986).
- [14] P. Delhaes and M. Drillon (eds.) *Organic and Inorganic Low-Dimensional Crystalline Materials*, NATO Advanced Study Institute, Series B Vol. 168, Plenum Press, New York, 1987 (Minorca, Spain, 1987).
- [15] R.M. Metzger, P. Day, and G.C. Papavassiliou (eds.) *Lower-Dimensional Systems and Molecular Electronics*, NATO Advanced Study Institute, Series B Vol. 248, Plenum Press, New York, 1990 (Spetses Island, Greece, 1989).
- [16] G. Saito and S. Kagoshima (eds.) *The Physics and Chemistry of Organic Superconductors*, Springer Proceedings in Physics Vol. 51, Springer-Verlag, Berlin, 1990 (Tokyo, Japan, 1989).
- [17] V. Kresin and W.A. Little (eds.) *Organic Superconductivity*, Plenum Press, New York, 1990 (South Lake Tahoe, U.S.A., 1990).
- [18] D. Jérôme and H.J. Schulz, *Organic Conductors and Superconductors*, Adv. Phys. 31 (1982), pp. 299–490.
- [19] S. Kagoshima, H. Nagasawa, and T. Sambongi *One-Dimensional Conductors*, Springer-Verlag, Berlin, 1988.
- [20] T. Ishiguro, K. Yamaji, and G. Saito *Organic Superconductors*, 2nd ed. Springer-Verlag, Berlin, 1998.
- [21] H. Mori, *Materials Viewpoint of Organic Superconductors*, J. Phys. Soc. Jpn. 75 (2006), 051003.
- [22] D. Jérôme, *Historical approach to Organic Superconductivity*, in *The Physics of Organic Superconductors and Conductors*, , in *The Physics of Organic Superconductors and Con-*

- ductors, ed. A. Lebed. Springer-Verlag, Berlin, 2008, pp. 3–16.
- [23] W.A. Little, *A Look Back at the Consequences of an Innocent Question asked Fifty Years Ago on the possibility of Synthesizing an Organic Superconductor*, J. Supercond. Nov. Magn. 29 (2016), pp. 3–8.
- [24] H. Gutfreund, *The Formative Years of Ideas on High T_c Organic Superconductivity*, J. Supercond. Nov. Magn. 29 (2016), pp. 9–13.
- [25] A. Graja *Low-Dimensional Organic Conductors*, World Scientific, Singapore, 1992.
- [26] J.M. Williams, J.R. Ferraro, R.J. Thorn, K.D. Carlson, U. Geiser, H.H. Wang, A.M. Kini, and M.H. Whangbo *Organic Superconductors*, Prentice Hall, Englewood Cliffs, NJ, 1992.
- [27] J.P. Farges (ed.) *Organic Conductors*, Marcel Dekker, New York, 1994.
- [28] T. Giamarchi *Quantum Physics in One Dimension*, Oxford University Press, Oxford, 2004.
- [29] P. Batail (ed.) *Molecular Conductors*, Chem Rev. 104 (2004), No. 11.
- [30] S. Kagoshima, K. Kanoda, and T. Mori (eds.) *Organic Conductors: Special Topics*, J. Phys. Soc. Jpn. 75 (2006), No. 5.
- [31] N. Toyota, M. Lang, and J. Müller *Low-Dimensional Molecular Metals*, Springer Series in Solid-State Sciences Vol. 154, Springer-Verlag, Berlin, 2007.
- [32] A. Lebed (ed.) *The Physics of Organic Superconductors and Conductors*, Springer Series in Materials Science Vol. 110, Springer-Verlag, Berlin, 2008.
- [33] R. Kato (ed.) *Special Issue: Organic Conductors*, Crystals 2, 2012.
- [34] T. Mori *Electronic Properties of Organic Conductors*, Springer-Verlag, Tokyo, 2016.
- [35] M. Dressel (ed.) *Special Issue: Advances in Organic Conductors and Superconductors*, Crystals 8, 2018.
- [36] J. Wosnitza *Fermi Surfaces of Low-Dimensional Organic Metals and Superconductors*, Springer-Verlag, Berlin, 1996.
- [37] P. Coleman *Introduction to Many-Body Physics*, Cambridge University Press, Cambridge, 2015.
- [38] M. Imada, A. Fujimori, and Y. Tokura, *Metal-insulator transitions*, Rev. Mod. Phys. 70 (1998), pp. 1039–1263.
- [39] G. Saito, T. Enoki, K. Toriumi, and H. Inokuchi, *Two-dimensionality and suppression of metal-semiconductor transition in a new organic metal with alkylthio substituted {TTF} and perchlorate*, Solid State Commun. 42 (1982), pp. 557–560.
- [40] C. Strack, C. Akinci, V. Pashchenko, B. Wolf, E. Uhrig, W. Assmus, M. Lang, J. Schreuer, L. Wiehl, J.A. Schlueter, J. Wosnitza, D. Schweitzer, J. Müller, and J. Wykoff, *Resistivity studies under hydrostatic pressure on a low-resistance variant of the quasi-two-dimensional organic superconductor κ -(BEDT-TTF) $_2$ Cu[N(CN) $_2$]Br: Search for intrinsic scattering contributions*, Phys. Rev. B 72 (2005), 054511.
- [41] A. Girlando, *Charge Sensitive Vibrations and Electron-Molecular Vibration Coupling in Bis(ethylenedithio)-tetrathiafulvalene (BEDT-TTF)*, J. Phys. Chem. C 115 (2011), pp. 19371–19378.
- [42] M. Kozlov, K. Pokhodnia, and A. Yurchenko, *The assignment of fundamental vibrations of BEDT-TTF and BEDT-TTF- d_8* , Spectrochim. Acta A 43 (1987), pp. 323–329.
- [43] ———, *Electron molecular vibration coupling in vibrational spectra of BEDT-TTF based radical cation salts*, Spectrochim. Acta A 45 (1989), pp. 437–444.
- [44] J. Eldridge, C. Homes, J.M. Williams, A. Kini, and H. Wang, *The assignment of the normal modes of the BEDT-TTF electron-donor molecule using the infrared and Raman spectra of several isotopic analogs*, Spectrochim. Acta A 51 (1995), pp. 947–960.
- [45] H. Kobayashi, A. Kobayashi, Y. Sasaki, G. Saito, and H. Inokuchi, *The Crystal and Molecular Structures of Bis(ethylenedithio)tetrathiafulvalene*, Bull. Chem. Soc. Jpn. 59 (1986), pp. 301–302.
- [46] E. Demiralp, S. Dasgupta, and W.A. Goddard, *Electron-transfer boat-vibration mechanism for superconductivity in organic molecules based on BEDT-TTF*, J. Am. Chem. Soc. 117 (1995), pp. 8154–8158.

- [47] J.P. Pouget, P. Alemany, and E. Canadell, *Donor-anion interactions in quarter-filled low-dimensional organic conductors*, Mater. Horiz. 5 (2018), pp. 590–640.
- [48] T. Mori, A. Kobayashi, Y. Sasaki, H. Kobayashi, G. Saito, and H. Inokuchi, *The Intermolecular Interaction of Tetrathiafulvalene and Bis(ethylenedithio)tetrathiafulvalene in Organic Metals. Calculation of Orbital Overlaps and Models of Energy-band Structures*, Bull. Chem. Soc. Jpn. 57 (1984), pp. 627–633.
- [49] T. Mori, *Structural Genealogy of BEDT-TTF-Based Organic Conductors I. Parallel Molecules: β and β'' Phases*, Bull. Chem. Soc. Jpn. 71 (1998), pp. 2509–2526.
- [50] T. Mori, H. Mori, and S. Tanaka, *Structural Genealogy of BEDT-TTF-Based Organic Conductors II. Inclined Molecules: θ , α and κ Phases*, Bull. Chem. Soc. Jpn. 72 (1999), pp. 179–197.
- [51] T. Mori, *Structural Genealogy of BEDT-TTF-Based Organic Conductors III. Twisted Molecules: δ and α' Phases*, Bull. Chem. Soc. Jpn. 72 (1999), pp. 2011–2027.
- [52] K. Bender, I. Hennig, D. Schweitzer, K. Dietz, H. Endres, and H.J. Keller, *Synthesis, Structure and Physical Properties of a Two-Dimensional Organic Metal, Di[bis(ethylenedithio)tetrathiofulvalene] triiodide, (BEDT-TTF) $_2$ I $_3$* , Mol. Cryst. Liq. Cryst. 108 (1984), pp. 359–371.
- [53] K. Bender, K. Dietz, H. Endres, H.W. Helberg, I. Hennig, H.J. Keller, H.W. Schäfer, and D. Schweitzer, *(BEDT-TTF) $_2$ J $_3$: A Two-Dimensional Organic Metal*, Mol. Cryst. Liq. Cryst. 107 (1984), pp. 45–53.
- [54] B.H. Ward, J.A. Schlueter, U. Geiser, H.H. Wang, E. Morales, J.P. Parakka, S.Y. Thomas, J.M. Williams, P.G. Nixon, R.W. Winter, G.L. Gard, H.J. Koo, and M.H. Whangbo, *Comparison of the Crystal and Electronic Structures of Three 2:1 Salts of the Organic Donor Molecule BEDT-TTF with Pentafluorothiomehtylsulfonate Anions SF $_5$ CH $_2$ SO $_3^-$, SF $_5$ CHFSO $_3^-$, and SF $_5$ CF $_2$ SO $_3^-$* , Chem. Mater. 12 (2000), pp. 343–351.
- [55] U. Geiser, J.A. Schlueter, H.H. Wang, A.M. Kini, J.M. Williams, P.P. Sche, H.I. Zakowicz, M.L. van Zile, J.D. Dudek, P.G. Nixon, R.W. Winter, G.L. Gard, J. Ren, and M.H. Whangbo, *Superconductivity at 5.2 K in an Electron Donor Radical Salt of Bis(ethylenedithio)tetrathiafulvalene (BEDT-TTF) with the Novel Polyfluorinated Organic Anion SF $_5$ CH $_2$ CF $_2$ SO $_3^-$* , J. Am. Chem. Soc. 118 (1996), pp. 9996–9997.
- [56] H. Mori, S. Tanaka, and T. Mori, *Systematic study of the electronic state in θ -type BEDT-TTF organic conductors by changing the electronic correlation*, Phys. Rev. B 57 (1998), pp. 12023–12029.
- [57] G. Saito, *Molecular Metals and Superconductors*, in *Metal-insulator transitions revisited*, P. Edwards, C. Rao and N. Mott, eds., Taylor & Francis, London, 1995, pp. 231–267.
- [58] R.H. McKenzie, *A strongly correlated electron model for the layered organic superconductors κ -(BEDT-TTF) $_2X$* , Comment Condens. Matter Phys. 18 (1998), pp. 309–337.
- [59] T.J. Emge, H.H. Wang, P.C.W. Leung, P.R. Rust, J.D. Cook, P.L. Jackson, K.D. Carlson, J.M. Williams, M.H. Whangbo, and . al.et , *New cation-anion interaction motifs, electronic band structure, and electrical behavior in β -(ET) $_2X$ salts [ET = bis(ethylenedithio)tetrathiafulvalene; X = dichloroiodide, chlorobromoiodide]*, J. Am. Chem. Soc. 108 (1986), pp. 695–702.
- [60] A. Kobayashi, R. Kato, H. Kobayashi, S. Moriyama, Y. Nishio, K. Kajita, and W. Sasaki, *Crystal and Electronic Structures of a New Molecular Superconductor, κ -(BEDT-TTF) $_2$ I $_3$* , Chem. Lett. 16 (1987), pp. 459–462.
- [61] C.E. Campos, P.S. Sandhu, J.S. Brooks, and T. Ziman, *Extended Hückel tight-binding study of the effect of pressure and uniaxial stress on the electronic structure of α -(BEDT-TTF) $_2$ KHg(SCN) $_4$ and κ -(BEDT-TTF) $_2$ Cu(NCS) $_2$* , Phys. Rev. B 53 (1996), pp. 12725–12732.
- [62] A. Fortunelli and A. Painelli, *On the ab initio evaluation of Hubbard parameters. I. The analytical approach in the absence of orbital relaxation*, J. Chem. Phys. 106 (1997), pp. 8041–8050.
- [63] ———, *On the ab initio evaluation of Hubbard parameters. II. The κ -(BEDT-TTF) $_2$ Cu[N(CN) $_2$]Br crystal*, J. Chem. Phys. 106 (1997), pp. 8051–8058.

- [64] M. Rahal, D. Chasseau, J. Gaultier, L. Ducasse, M. Kurmoo, and P. Day, *Isothermal Compressibility and Pressure Dependence of the Crystal Structures of the Superconducting Charge-Transfer Salt κ -(BEDT-TTF)₂Cu(NCS)₂ [BEDT-TTF = Bis(ethylenedithio)tetrathiafulvalene]*, Acta Cryst. B 53 (1997), pp. 159–167.
- [65] J.A. Schlueter, U. Geiser, H. Wang, A.M. Kini, B.H. Ward, J.P. Parakka, R.G. Daugherty, M.E. Kelly, P.G. Nixon, R.W. Winter, G.L. Gard, L.K. Montgomery, H.J. Koo, and M.H. Whangbo, *Trifluoromethylsulfonyl-Based Salts of BEDT-TTF: Crystal and Electronic Structures and Physical Properties*, J. Solid State Chem. 168 (2002), pp. 524–534.
- [66] K. Nakamura, Y. Yoshimoto, T. Kosugi, R. Arita, and M. Imada, *Ab initio Derivation of Low-Energy Model for κ -ET Type Organic Conductors*, J. Phys. Soc. Jpn. 78 (2009), 083710.
- [67] H.C. Kandpal, I. Opahle, Y.Z. Zhang, H.O. Jeschke, and R. Valentí, *Revision of Model Parameters for κ -Type Charge Transfer Salts: an Ab-Initio Study*, Phys. Rev. Lett. 103 (2009), 067004.
- [68] E. Scriven and B.J. Powell, *Effective Coulomb Interactions within BEDT-TTF Dimers*, Phys. Rev. B 80 (2009), 205107.
- [69] U. Geiser, A. Schultz, H. Wang, D. Watkins, D. Stupka, J. Williams, J. Schirber, D. Overmyer, D. Jung, J. Novoa, and M. Whangbo, *Strain index, lattice softness and superconductivity of organic donor-molecule salts: Crystal and electronic structures of three isostructural salts κ -(BEDT-TTF)₂Cu[N(CN)₂]X (X=Cl, Br, I)*, Physica C 174 (1991), pp. 475–486.
- [70] T. Hiramatsu, Y. Yoshida, G. Saito, A. Otsuka, H. Yamochi, M. Maesato, Y. Shimizu, H. Ito, Y. Nakamura, H. Kishida, M. Watanabe, and R. Kumai, *Design and Preparation of a Quantum Spin Liquid Candidate κ -(ET)₂Ag₂(CN)₃ Having a Nearby Superconductivity*, Bull. Chem. Soc. Jpn. 90 (2017), pp. 1073–1082.
- [71] P. Foury-Leylekian, V. Ilakovac, V. Balédent, P. Fertey, A. Arakcheeva, O. Milat, D. Petermann, G. Guillier, K. Miyagawa, K. Kanoda, P. Alemany, E. Canadell, S. Tomić, and J.P. Pouget, *κ -(BEDTTTF)₂Cu₂(CN)₃ spin liquid: Beyond the average structure*, Crystals 8 (2018), 158.
- [72] P. Foury-Leylekian, V. Ilakovac, P. Fertey, V. Balédent, O. Milat, K. Miyagawa, K. Kanoda, T. Hiramatsu, Y. Yoshida, G. Saito, P. Alemany, E. Canadell, S. Tomić, and J.P. Pouget, *New insights about the structural properties of κ -(BEDTTTF)₂Ag₂(CN)₃ spin liquid*, Acta Cryst. B 76 (2020), pp. 581–590.
- [73] D. Guterding, R. Valentí, and H.O. Jeschke, *Influence of molecular conformations on the electronic structure of organic charge transfer salts*, Phys. Rev. B 92 (2015), p. 081109.
- [74] S. Tomeno, M. Maesato, Y. Yoshida, A. Kiswandhi, and H. Kitagawa, *Triangular-Lattice Organic Mott Insulator with a Disorder-Free Polyaniion*, Inorg. Chem. 59 (2020), pp. 8647–8651.
- [75] N. Drichko, R. Beyer, E. Rose, M. Dressel, J.A. Schlueter, S.A. Turunova, E.I. Zhilyaeva, and R.N. Lyubovskaya, *Metallic state and charge-order metal-insulator transition in the quasi-two-dimensional conductor κ -(BEDT-TTF)₂Hg(SCN)₂Cl*, Phys. Rev. B 89 (2014), 075133.
- [76] E. Gati, J.K.H. Fischer, P. Lunkenheimer, D. Zielke, S. Köhler, F. Kolb, H.A. Krug von Nidda, S.M. Winter, H. Schubert, J.A. Schlueter, H.O. Jeschke, R. Valentí, and M. Lang, *Evidence for Electronically Driven Ferroelectricity in a Strongly Correlated Dimerized BEDT-TTF Molecular Conductor*, Phys. Rev. Lett. 120 (2018), 247601.
- [77] M. Aldoshina, R. Lyubovskaya, S. Konovalikhin, O. Dyachenko, G. Shilov, M. Makova, and R. Lyubovskii, *A new series of ET-based organic metals: Synthesis, crystal structure and properties*, Synth. Met. 56 (1993), pp. 1905–1909.
- [78] R. Kato, *Development of π -Electron Systems Based on [M(dmit)₂] (M = Ni and Pd; dmit: 1,3-dithiole-2-thione-4,5-dithiolate) Anion Radicals*, Bull. Chem. Soc. Jpn. 87 (2014), pp. 355–374.
- [79] R. Kato, T. Fukunaga, H.M. Yamamoto, K. Ueda, and C. Hengbo, *Crystal struc-*

- ture and band parameters of mixed crystals derived from quantum spin liquid β' - $\text{EtMe}_3\text{Sb}[\text{Pd}(\text{dmit})_2]_2$ ($\text{dmit} = 1,3\text{-dithiol-2-thione-4,5-dithiolate}$), *phys. stat. sol. (b)* 249 (2012), pp. 999–1003.
- [80] T. Isono, H. Kamo, A. Ueda, K. Takahashi, A. Nakao, R. Kumai, H. Nakao, K. Kobayashi, Y. Murakami, and H. Mori, *Hydrogen bond-promoted metallic state in a purely organic single-component conductor under pressure*, *Nat. Commun.* 4 (2013), 1344.
- [81] A. Ueda, S. Yamada, T. Isono, H. Kamo, A. Nakao, R. Kumai, H. Nakao, Y. Murakami, K. Yamamoto, Y. Nishio, and H. Mori, *Hydrogen-Bond-Dynamics-Based Switching of Conductivity and Magnetism: A Phase Transition Caused by Deuterium and Electron Transfer in a Hydrogen-Bonded Purely Organic Conductor Crystal*, *J. Am. Chem. Soc.* 136 (2014), pp. 12184–12192.
- [82] A. Ueda, A. Hatakeyama, M. Enomoto, R. Kumai, Y. Murakami, and H. Mori, *Modulation of a Molecular π -Electron System in a Purely Organic Conductor that Shows Hydrogen-Bond-Dynamics-Based Switching of Conductivity and Magnetism*, *Chem. – Eur. J.* 21 (2015), pp. 15020–15028.
- [83] K. Yamamoto, Y. Kanematsu, U. Nagashima, A. Ueda, H. Mori, and M. Tachikawa, *Theoretical study of the H/D isotope effect on phase transition of hydrogen-bonded organic conductor $\kappa\text{-H}_3(\text{Cat-EDT-TTF})_2$* , *Phys. Chem. Chem. Phys.* 18 (2016), pp. 29673–29680.
- [84] J. Valasek, *Piezo-Electric and Allied Phenomena in Rochelle Salt*, *Phys. Rev.* 17 (1921), pp. 475–481.
- [85] C. K. M. Rabe and J.M. Triscone (eds.) *Physics of Ferroelectrics: A Modern Perspective*, Topics in Applied Physics Vol. 105, Springer-Verlag, Berlin, 2007.
- [86] M.E. Lines and A.M. Glass *Principles and Applications of Ferroelectrics and Related Materials*, Clarendon Press, Oxford, 1977.
- [87] E. Dagotto, *Complexity in Strongly Correlated Electronic Systems*, *Science* 309 (2005), pp. 257–262.
- [88] Y. Hu and S. Ren, *Electroresistance and electro-optic effects in molecular ferroelectrics*, *APL Mater.* 8 (2020), 080702.
- [89] E. Dagotto, T. Hotta, and A. Moreo, *Colossal Magnetoresistant Materials: the Key Role of Phase Separation*, *Phys. Rep.* 344 (2001), pp. 1–153.
- [90] H. Seo, *Charge Ordering in Organic ET Compounds*, *J. Phys. Soc. Jpn.* 69 (2000), pp. 805–820.
- [91] H. Yoshioka, Y. Otsuka, and H. Seo, *Theoretical Studies on Phase Transitions in Quasi-One-Dimensional Molecular Conductors*, *Crystals* 2 (2012), pp. 996–1016.
- [92] C. Hotta, *Theories on Frustrated Electrons in Two-Dimensional Organic Solids*, *Crystals* 2 (2012), pp. 1155–1200.
- [93] N. Ikeda, H. Ohsumi, K. Ohwada, K. Ishii, T. Inami, K. Kakurai, Y. Murakami, K. Yoshii, S. Mori, Y. Horibe, and H. Kito, *Ferroelectricity from iron valence ordering in the charge-frustrated system LuFe_2O_4* , *Nature* 436 (2005), pp. 1136–1138.
- [94] G.C. Milward, M.J. Calderon, and P.B. Littlewood, *Electronically soft phases in manganites*, *Nature* 433 (2005), pp. 607–610.
- [95] J. Hemberger, P. Lunkenheimer, R. Fichtl, H.A. Krug von Nidda, V. Tsurkan, and A. Loidl, *Relaxor ferroelectricity and colossal magnetocapacitive coupling in ferromagnetic CdCr_2S_4* , *Nature* 434 (2005), pp. 364–367.
- [96] T. Kimura, Y. Seiko, H. Nakamura, T. Siegrist, and A.P. Ramirez, *Cupric oxide as an induced-multiferroic with high T_c* , *Nat. Mater.* 7 (2008), pp. 291–294.
- [97] L.E. Cross, *Relaxor Ferroelectrics*, *Ferroelectrics* 76 (1987), pp. 241–267.
- [98] B.E. Vugmeister and M.D. Glinchuk, *Dipole glass and ferroelectricity in random-site electric dipole systems*, *Rev. Mod. Phys.* 62 (1990), pp. 993–1026.
- [99] R.A. Cowley, S.N. Gvasaliya, S.G. Lushnikov, B. Roessli, and G.M. Rotaru, *Relaxing with relaxors: a review of relaxor ferroelectrics*, *Adv. Phys.* 60 (2011), pp. 229–327.
- [100] T. Portengen, T. Östreich, and L. Sham, *Theory of electronic ferroelectricity*, *Phys. Rev. B* 54 (1996), pp. 17452–17463.
- [101] D.V. Efremov, J. van den Brink, and D.I. Khomskii, *Bond- versus site-centred ordering*

- and possible ferroelectricity in manganites, *Nat. Mater.* 3 (2004), pp. 853–856.
- [102] J. van den Brink and D.I. Khomskii, *Multiferroicity due to charge ordering*, *J. Phys.: Condens. Matter* 20 (2008), 434217.
- [103] N.A. Hill, *Why Are There so Few Magnetic Ferroelectrics?*, *J. Phys. Chem. B* 104 (2000), pp. 6694–6709.
- [104] T. Kimura, T. Goto, H. Shintani, K. Ishizaka, T. Arima, and Y. Tokura, *Magnetic control of ferroelectric polarization*, *Nature* 426 (2003), pp. 55–58.
- [105] S.W. Cheong and M. Mostovoy, *Multiferroics: a magnetic twist for ferroelectricity*, *Nature Materials* 6 (2007), pp. 13–20.
- [106] M. Chandra, S. Yadav, R.J. Choudhary, R. Rawat, A.K. Sinha, M.B. Lepeitit, and K. Singh, *Multiferroicity and magnetoelastic coupling in α -Mn₂O₃: A binary perovskite*, *Phys. Rev. B* 98 (2018), 104427.
- [107] L. Zhao, L. Muzica, U. Schwarz, and A.C. Komarek, *Multiferroicity in the frustrated spinel cuprate GeCu₂O₄*, *Phys. Rev. Materials* 2 (2018), 041402.
- [108] C. Gong, E.M. Kim, Y. Wang, G. Lee, and X. Zhang, *Multiferroicity in atomic van der Waals heterostructures*, *Nat. Commun.* 10 (2019), 2657.
- [109] K.F. Wang, J.M. Liu, and Z. Ren, *Multiferroicity: the coupling between magnetic and polarization orders*, *Adv. Phys.* 58 (2009), pp. 321–448.
- [110] S. Ishihara, *Electronic Ferroelectricity and Frustration*, *J. Phys. Soc. Jpn.* 79 (2010), 011010.
- [111] C. Ederer and N.A. Spaldin, *A new route to magnetic ferroelectrics*, *Nat. Mater.* 3 (2004), pp. 849–851.
- [112] S. Dong, H. Xiang, and E. Dagotto, *Magnetolectricity in multiferroics: a theoretical perspective*, *Natl. Sci. Rev.* 6 (2019), pp. 629–641.
- [113] S. Brazovskii, *Ferroelectricity and Charge-Ordering in Quasi-1D Organic Conductors*, in *The Physics of Organic Superconductors and Conductors*, , in *The Physics of Organic Superconductors and Conductors*, ed. A. LebedA. Lebed ed., Springer-Verlag, Berlin, 2008, pp. 313–355.
- [114] P. Monceau, *Electronic crystals: an experimental overview*, *Adv. Phys.* 61 (2012), pp. 325–581.
- [115] S. Tomić and M. Dressel, *Ferroelectricity in molecular solids: a review of electrodynamic properties*, *Rep. Prog. Phys.* 78 (2015), 096501.
- [116] P. Lunkenheimer and A. Loidl, *Dielectric spectroscopy on organic charge-transfer salts*, *J. Phys.: Condens. Matter* 27 (2015), 373001.
- [117] S. Horiuchi, R. Kumai, Y. Okimoto, and Y. Tokura, *Chemical approach to neutral-ionic valence instability, quantum phase transition, and relaxor ferroelectricity in organic charge-transfer complexes*, *Chem. Phys.* 325 (2006), pp. 78–91.
- [118] S. Horiuchi, T. Hasegawa, and Y. Tokura, *Molecular Donor-Acceptor Compounds as Prospective Organic Electronics Materials*, *J. Phys. Soc. Jpn.* 75 (2006), 051016.
- [119] S. Horiuchi and Y. Tokura, *Organic ferroelectrics*, *Nat. Mater.* 7 (2008), pp. 357–366.
- [120] S. Horiuchi, K. Kobayashi, R. Kumai, N. Minami, F. Kagawa, and Y. Tokura, *Quantum ferroelectricity in charge-transfer complex crystals*, *Nat. Commun.* 6 (2015), 7469.
- [121] G. Grüner, *The dynamics of charge-density waves*, *Rev. Mod. Phys.* 60 (1988), pp. 1129–1181.
- [122] G. Grüner *Density Waves in Solids*, Addison-Wesley, Reading, MA, 1994.
- [123] T. Vuletić, B. Korin-Hamzić, T. Ivek, S. Tomić, B. Gorshunov, M. Dressel, and J. Akimitsu, *The spin-ladder and spin-chain system (La,Y,Sr,Ca)₁₄Cu₂₄O₄₁: Electronic phases, charge and spin dynamics*, *Phys. Rep.* 428 (2006), pp. 169–258.
- [124] S. Ishihara, *Electronic ferroelectricity in molecular organic crystals*, *J. Phys.: Condens. Matter* 26 (2014), 493201.
- [125] H. Kino and H. Fukuyama, *Interrelationship among electronic states of α -(BEDT-TTF)₂I₃, (ET)₂MHg(SCN)₄ and κ -(ET)₂X*, *J.Phys.Soc.Jpn.* 64 (1995), pp. 4523–4526.
- [126] R.H. McKenzie, J. Merino, J.B. Marston, and O.P. Sushkov, *Theory of electronic ferroelectricity*, *Phys. Rev. B* 64 (2001), 085109.

- [127] H. Seo, C. Hotta, and H. Fukuyama, *Toward Systematic Understanding of Diversity of Electronic Properties in Low-Dimensional Molecular Solids*, Chem Rev. 104 (2004), pp. 5005–5036.
- [128] H. Kino and H. Fukuyama, *Phase diagram of two-dimensional organic conductors (BEDT-TTF)₂X*, J. Phys. Soc. Jpn. 65 (1996), pp. 2158–2169.
- [129] N. Hassan, S. Cunningham, M. Mourigal, E.I. Zhilyaeva, S.A. Torunova, R.N. Lyubovskaya, J.A. Schlueter, and N. Drichko, *Evidence for a quantum dipole liquid in an organic quasi-two-dimensional material*, Science 360 (2018), pp. 1101–1104.
- [130] A. Löhle, E. Rose, S. Singh, R. Beyer, E. Tafra, T. Ivek, E.I. Zhilyaeva, R.N. Lyubovskaya, and M. Dressel, *Pressure dependence of the metal-insulator transition in κ -(BEDT-TTF)₂Hg(SCN)₂Cl: optical and transport studies*, J. Phys.: Condens. Matter 29 (2017), 055601.
- [131] S. Singh, A. Löhle, A. Pustogow, R. Hübner, and M. Dressel, *Pressure-dependent transport on spin-liquid dimer Mott insulators*, (2015), unpublished.
- [132] E. Uykur, W. Li, C.A. Kuntscher, and M. Dressel, *Optical signatures of energy gap in correlated Dirac fermions*, npj Quantum Mater. 4 (2019), 19.
- [133] M. Dressel, G. Grüner, J.P. Pouget, A. Breining, and D. Schweitzer, *Field and frequency dependent transport in the two-dimensional organic conductor α -(BEDT-TTF)₂I₃*, J. Phys. (Paris) I 4 (1994), pp. 579–594.
- [134] N. Tajima, S. Sugawara, M. Tamura, Y. Nishio, and K. Kajita, *Electronic Phases in an Organic Conductor α -(BEDT-TTF)₂I₃: Ultra Narrow Gap Semiconductor, Superconductor, Metal, and Charge-Ordered Insulator*, J. Phys. Soc. Jpn. 75 (2006), 051010.
- [135] M. Hirata, K. Ishikawa, K. Miyagawa, M. Tamura, C. Berthier, D. Basko, A. Kobayashi, G. Matsuno, and K. Kanoda, *Observation of an anisotropic Dirac cone reshaping and ferrimagnetic spin polarization in an organic conductor*, Nat. Commun. 7 (2016), 12666.
- [136] N. Tajima, A. Ebina, M. Tamura, Y. Nishio, and K. Kajita, *Effects of Uniaxial Strain on Transport Properties of Organic Conductor α -(BEDT-TTF)₂I₃ and Discovery of Superconductivity*, J. Phys. Soc. Jpn. 71 (2002), pp. 1832–1835.
- [137] D. Schweitzer, P. Bele, H. Brunner, E. Gogu, U. Haeberlen, I. Hennig, I. Klutz, R. Świetlik, and H.J. Keller, *A stable superconducting state at 8 K and ambient pressure in α_t -(BEDT-TTF)₂I₃*, Z. Phys. B 67 (1987), p. 489–495.
- [138] P. Alemany, J.P. Pouget, and E. Canadell, *Essential role of anions in the charge ordering transition of α -(BEDT-TTF)₂I₃*, Phys. Rev. B 85 (2012), 195118.
- [139] D. Liu, K. Ishikawa, R. Takehara, K. Miyagawa, M. Tamura, and K. Kanoda, *Insulating Nature of Strongly Correlated Massless Dirac Fermions in an Organic Crystal*, Phys. Rev. Lett. 116 (2016), 226401.
- [140] F. Kagawa, T. Sato, K. Miyagawa, K. Kanoda, Y. Tokura, K. Kobayashi, and R. Kumai, *Charge-cluster glass in an organic conductor*, Nat. Phys. 9 (2013), pp. 419–422.
- [141] T. Sato, F. Kagawa, K. Kobayashi, K. Miyagawa, K. Kanoda, R. Kumai, Y. Murakami, and Y. Tokura, *Emergence of nonequilibrium charge dynamics in a charge-cluster glass*, Phys. Rev. B 89 (2014), 121102.
- [142] J. Merino and R.H. McKenzie, *Superconductivity Mediated by Charge Fluctuations in Layered Molecular Crystals*, Phys. Rev. Lett. 87 (2001), 237002.
- [143] S. Kaiser, M. Dressel, Y. Sun, A. Greco, J. J.A.Schlueter, G. Gard, and N. Drichko, *Bandwidth tuning triggers interplay of charge order and superconductivity in two-dimensional organic materials*, Phys. Rev. Lett. 105 (2010), 206402.
- [144] A. Pustogow, K. Treptow, A. Rohwer, Y. Saito, M. Sans Alonso, A. Löhle, J. J.A.Schlueter, and M. Dressel, *Charge order in β'' -phase BEDT-TTF salts*, Phys. Rev. B 99 (2019), 155144.
- [145] A. Pustogow, Y. Saito, A. Rohwer, J. J.A.Schlueter, and M. Dressel, *Coexistence of charge order and superconductivity in β'' -(BEDT-TTF)₂SF₅CH₂CF₂SO₃*, Phys. Rev. B 99 (2019), 140509.
- [146] N. Drichko, S. Kaiser, Y. Sun, C. Clauss, M. Dressel, H. Mori, J. Schlueter, E. Zhilyaeva, S. Torunova, and R. Lyubovskaya, *Interplay between Charge Order and Superconductivity*

- in Quasi-Two-Dimensional Organic Conductors Explored by Vibrational Spectroscopy*, Physica B 404 (2009), 490.
- [147] A. Girlando, *Calculations of the unrestricted geometry, leading to a boat shaped molecule; in the case of forced planar geometry, with D_2 symmetry, the HOMO-LUMO gap of the isolated molecule is 3.17 eV.*, (2011), unpublished.
- [148] A. Girlando, M. Masino, J. Schlueter, N. Drichko, S. Kaiser, and M. Dressel, *Spectroscopic characterization of charge order fluctuations in (BEDT-TTF) metals and superconductors*, phys. sta. sol. (b) 1-4 (2012), 201100722.
- [149] A. Girlando, M. Masino, S. Kaiser, Y. Sun, N. Drichko, M. Dressel, and H. Mori, *Charge-order fluctuations and superconductivity in two-dimensional organic metals*, Phys. Rev. B 89 (2014), 174503.
- [150] T. Ivek, M. Čulo, M. Kuveždić, E. Tutiš, M. Basletić, B. Mihaljević, E. Tafra, S. Tomić, A. Löhle, M. Dressel, and B. Korin-Hamzić, *Semimetallic and charge-ordered α -(BEDT-TTF) $_2$ I $_3$: on the role of disorder in dc transport and dielectric properties*, Phys. Rev. B 96 (2017), 075141.
- [151] K. Katano, T. Taniguchi, K. Ichimura, Y. Kawashima, S. Tanda, and K. Yamamoto, *STM observation of charge stripe in metallic phase of α -(BEDT-TTF) $_2$ I $_3$* , Phys. Rev. B 91 (2015), 125110.
- [152] Y. Takano, K. Hiraki, H. Yamamoto, T. Nakamura, and T. Takahashi, *Charge ordering in α -(BEDT-TTF) $_2$ I $_3$* , Synth. Met. 120 (2001), pp. 1081–1082.
- [153] T. Takahashi, Y. Nogami, and K. Yakushi, *Charge ordering in organic conductors*, J. Phys. Soc. Jpn. 75 (2006), 051008.
- [154] T. Kakiuchi, Y. Wakabayashi, H. Sawa, T. Takahashi, and T. Nakamura, *Charge Ordering in α -(BEDT-TTF) $_2$ I $_3$ by Synchrotron X-ray Diffraction*, J. Phys. Soc. Jpn. 76 (2007), 113702.
- [155] P. P. Guionneau, C. Kepert, G. Bravic, D. Chasseau, M. Truter, M. Kurmoo, and P. Day, *Determining the charge distribution in BEDT-TTF salts*, Synth. Met. 86 (1997), pp. 1973–1974.
- [156] R. Wojciechowski, K. Yamamoto, K. Yakushi, M. Inokuchi, and A. Kawamoto, *High-pressure Raman study of the charge ordering in α -(BEDT-TTF) $_2$ I $_3$* , Phys. Rev. B 67 (2003), 224105.
- [157] Y. Yue, M. Yamamoto, K. Uruichi, C. Nakano, K. Yakushi, S. Yamada, T. Hiejima, and A. Kawamoto, *Nonuniform site-charge distribution and fluctuations of charge order in the metallic state of α -(BEDT-TTF) $_2$ I $_3$* , Phys. Rev. B 82 (2010), 075134.
- [158] T. Ivek, B. Korin-Hamzić, O. Milat, S. Tomić, C. Clauss, N. Drichko, D. Schweitzer, and M. Dressel, *Electrodynamic response of the charge ordering phase: Dielectric and optical studies of α -(BEDT-TTF) $_2$ I $_3$* , Phys. Rev. B 83 (2011), 165128.
- [159] M. Maksimuk, K. Yakushi, H. Taniguchi, K. Kanoda, and A. Kawamoto, *The C=C Stretching Vibrations of κ -(BEDT-TTF) $_2$ Cu[N(CN) $_2$]Br and Its Isotope Analogues*, J. Phys. Soc. Jpn. 70 (2001), pp. 3728–3738.
- [160] M. Dressel and N. Drichko, *Optical Properties of Two-Dimensional Organic Conductors: Signatures of Charge Ordering and Correlation Effects*, Chem. Rev. 104 (2004), pp. 5689–5715.
- [161] T. Yamamoto, M. Uruichi, K. Yamamoto, K. Yakushi, A. Kawamoto, and H. Taniguchi, *Examination of the Charge-Sensitive Vibrational Modes in Bis(ethylenedithio)tetrathiafulvalene*, J. Phys. Chem. B 109 (2005), pp. 15226–15235.
- [162] K. Yakushi, *Infrared and Raman Studies of Charge Ordering in Organic Conductors, BEDT-TTF Salts with Quarter-Filled Bands*, Crystals 2 (2012), pp. 1291–1346.
- [163] R. Beyer, A. Dengl, T. Peterseim, S. Wackerow, T. Ivek, A.V. Pronin, D. Schweitzer, and M. Dressel, *Pressure-dependent optical investigations of α -(BEDT-TTF) $_2$ I $_3$: Tuning charge order and narrow gap towards a Dirac semimetal*, Phys. Rev. B 93 (2016), 195116.
- [164] S. Ishibashi, T. Tamura, M. Kohyama, and K. Terakura, *Ab Initio Electronic-Structure Calculations for α -(BEDT-TTF) $_2$ I $_3$* , J. Phys. Soc. Jpn. 75 (2006), 015005.
- [165] K. Miyagawa, A. Kawamoto, and K. Kanoda, *Charge ordering in a quasi-two-*

- dimensional organic conductor*, Phys. Rev. B 62 (2000), pp. 7679–7682.
- [166] R. Chiba, K. Hiraki, Y. Sakurai, T. Takahashi, H.M. Yamamoto, and T. Nakamura, *Extremely Slow Charge Fluctuations in the Metallic State of the Two-Dimensional Molecular Conductor θ -(BEDT-TTF)RbZn(SCN)₄*, Phys. Rev. Lett. 93 (2004), 216405.
- [167] M. Watanabe, Y. Noda, Y. Nogami, and H. Mori, *Transfer Integrals and the Spatial Pattern of Charge Ordering in θ -(BEDT-TTF)₂RbZn(SCN)₄ at 90K*, J. Phys. Soc. Jpn. 73 (2004), pp. 116–122.
- [168] K. Yamamoto, S. Iwai, S. Boyko, A. Kashiwazaki, F. Hiramatsu, C. Okabe, N. Nishi, and K. Yakushi, *Strong Optical Nonlinearity and its Ultrafast Response Associated with Electron Ferroelectricity in an Organic Conductor*, J. Phys. Soc. Jpn. 77 (2008), 074709.
- [169] S. Denev, T. Lummen, E. Barnes, A. Kumar, and V. Gopalan, *Probing Ferroelectrics Using Optical Second Harmonic Generation*, J. Am. Ceram. Soc. 94 (2011), p. 2699–2727.
- [170] K. Yamamoto, A. Kowalska, and K. Yakushi, *Direct observation of ferroelectric domains created by Wigner crystallization of electrons in α -[bis(ethylenedithio)tetrathiafulvalene]₂I₃*, Appl. Phys. Lett. 96 (2010), 122901.
- [171] Y. Takano, K. Hiraki, H. Yamamoto, T. Nakamura, and T. Takahashi, *Charge disproportionation in the organic conductor, α -(BEDT-TTF)₂I₃*, J. Phys. Chem. Solids 62 (2001), pp. 393–395.
- [172] J. Moldenhauer, C. Horn, K. Pokhodnia, D. Schweitzer, I. Heinen, and H. Keller, *FT-IR absorption spectroscopy of BEDT-TTF radical salts: charge transfer and donor-anion interaction*, Synth. Met. 60 (1993), pp. 31–38.
- [173] C. Clauss, N. Drichko, D. Schweitzer, and M. Dressel, *Charge gap in α -(BEDT-TTF)₂I₃*, Physica B 405 (2010), pp. S144–S146.
- [174] M. Hirata, K. Ishikawa, K. Miyagawa, K. Kanoda, and M. Tamura, *¹³C NMR study on the charge-disproportionated conducting state in the quasi-two-dimensional organic conductor α -(BEDT-TTF)₂I₃*, Phys. Rev. B 84 (2011), 125133.
- [175] R. Chiba, H. Yamamoto, K. Hiraki, T. Takahashi, and T. Nakamura, *Charge disproportionation in θ -(BEDT-TTF)RbZn(SCN)₄*, J. Phys. Chem. Solids 62 (2001), pp. 389–391.
- [176] R. Chiba, H. Yamamoto, K. Hiraki, T. Nakamura, and T. Takahashi, *Charge ordering in θ -(BEDT-TTF)₂RbZn(SCN)₄*, Synth. Met. 120 (2001), pp. 919–920.
- [177] N.L. Wang, H. Mori, S. Tanaka, J. Dong, and B. Clayman, *Far-infrared study of the insulator–metal transition in θ -(BEDT-TTF)RbZn(SCN)₄ (BEDT-TTF) = bis(ethylene-dithio)tetrathiafulvalene)*, J. Phys.: Condens. Matter 13 (2001), pp. 5463–5470.
- [178] K. Yamamoto, K. Yakushi, K. Miyagawa, K. Kanoda, and A. Kawamoto, *Charge ordering in θ -(BEDT-TTF)₂RbZn(SCN)₄ studied by vibrational spectroscopy*, Phys. Rev. B 65 (2002), 085110.
- [179] H. Seo, J. Merino, H. Yoshioka, and M. Ogata, *Theoretical Aspects of Charge Ordering in Molecular Conductors*, J. Phys. Soc. Jpn. 75 (2006), 051009.
- [180] H. Mori, S. Tanaka, T. Mori, A. Kobayashi, and H. Kobayashi, *Crystal structure and physical properties of M =Rb and Tl salts of (BEDT-TTF)MM'(SCN)₄ [$M, M' = Co, Zn$]*, Bull. Chem. Soc. Japan 71 (1998), pp. 797–806.
- [181] B. Rothaemel, L. Forró, J. Cooper, J. Schilling, M. Weger, P. Bele, H. Brunner, D. Schweitzer, and H. Keller, *Magnetic susceptibility of α and β phases of Di[bis(ethylenedithio)tetrathiofulvalene] triiodide (BEDT-TTF)₂I₃ under pressure*, Phys. Rev. B 34 (1986), pp. 704–712.
- [182] P. Lunkenheimer, B. Hartmann, M. Lang, J. Müller, D. Schweitzer, S. Krohns, and A. Loidl, *Ferroelectric properties of charge-ordered α -(BEDT-TTF)₂I₃*, Phys. Rev. B 91 (2015), 245132.
- [183] C. Kittel *Introduction to solid state physics*, 7th ed. John Wiley, New York, 1996.
- [184] A. Pustogow, A.S. McLeod, Y. Saito, D.N. Basov, and M. Dressel, *Internal strain tunes electronic correlations on the nanoscale*, Sci. Adv. 4 (2018), eaau9123.
- [185] H. Kino and H. Fukuyama, *On the Origin of the Phase-Transition of α -(BEDT-TTF)₂I₃*, Synth. Met. 70 (1995), pp. 921–922.
- [186] ———, *On the Phase-Transition of α -(ET)₂I₃*, J. Phys. Soc. Jpn. 64 (1995), pp. 1877–

- 1880.
- [187] H. Seo and H. Fukuyama, *J. Phys. Soc. Jpn.* 66 (1997), pp. 129–1252.
 - [188] H. Fukuyama, H. Seo, and H. Kino, *Interplay between structure and electronic properties in organic conductors*, *Physica B* 280 (2000), pp. 462–466.
 - [189] H. Seo and H. Fukuyama, *Charge order in organic conductors*, *Synth. Met.* 133-134 (2003), pp. 257–260.
 - [190] R. Clay and S. Mazumdar, *From charge- and spin-ordering to superconductivity in the organic charge-transfer solids*, *Phys. Rep.* 788 (2019), pp. 1–89.
 - [191] R.T. Clay, S. Mazumdar, and D.K. Campbell, *Charge Ordering in θ -(BEDT-TTF) $_2X$ materials*, *J. Phys. Soc. Japan* 71 (2002), pp. 1186–1189.
 - [192] N. Gomes, W. De Silva, T. Dutta, R.T. Clay, and S. Mazumdar, *Coulomb-enhanced superconducting pair correlations and paired-electron liquid in the frustrated quarter-filled band*, *Phys. Rev. B* 93 (2016), 165110.
 - [193] P. Alemany, J.P. Pouget, and E. Canadell, *Structural and electronic control of the metal to insulator transition and local orderings in the θ -(BEDT-TTF) $_2X$ organic conductors*, *J. Phys.: Condens. Matter* 27 (2015), 465702.
 - [194] J.P. Pouget, P. Alemany, and E. Canadell, *Donor-anion interactions in quarter-filled low dimensional organic conductors*, *Materials Horizons* 5 (2018), 590-640.
 - [195] K. Rossnagel, *On the origin of charge-density waves in select layered transition-metal dichalcogenides*, *J. Phys.: Condens. Matter* 23 (2011), 213001.
 - [196] J. Schlueter, B. Ward, U. Geiser, H. Wang, A. Kini, J. Parakkaa, E. Morales, H.J. Koo, M.H. Whangbo, R. Winter, J. Mohtasham, and G. Gard, *Crystal structure, physical properties and electronic structure of a new organic conductor β'' -(BEDT-TTF) $_2$ SF $_5$ CHFCF $_2$ SO $_3$* , *J. Mater. Chem.* 11 (2001), pp. 2008–2013.
 - [197] J. Dyre, *Colloquium: The glass transition and elastic models of glass-forming liquids*, *Rev. Mod. Phys.* 78 (2006), pp. 953–972.
 - [198] P.W. Anderson, *Ordering and Antiferromagnetism in Ferrites*, *Phys. Rev.* 102 (1956), pp. 1008–1013.
 - [199] J.P. Bouchaud, L.F. Cugliandolo, J. Kurchan, and M. Mézard, 1998 in *Out of Equilibrium Dynamics in Spin-Glasses and other Glassy Systems* World Science, Singapore, pp. 161–223.
 - [200] J. Merino, H. Seo, and M. Ogata, *Quantum melting of charge order due to frustration in two-dimensional quarter-filled system*, *Phys. Rev. B* 71 (2005), 125111.
 - [201] T. Sato, K. Miyagawa, and K. Kanoda, *Electronic crystal growth*, *Science* 357 (2017), pp. 1378–1381.
 - [202] F. Nad, P. Monceau, and H. Yamamoto, *Effect of cooling rate on charge ordering in θ -(BEDT-TTF)RbZn(SCN) $_4$* , *Phys. Rev. B* 76 (2007), 205101.
 - [203] J. Müller, *Fluctuation spectroscopy: A new approach for studying low-dimensional molecular metals*, *Chem. Phys. Chem.* 12 (2011), pp. 1222–1245.
 - [204] M. Ediger, *Spatially Heterogeneous Dynamics in Supercooled Liquids*, *Annu. Rev. Phys. Chem.* 51 (2000), pp. 99–128.
 - [205] J. Löffler, J. Schroers, and W. Johnson, *Time-temperature-transformation diagram and microstructures of bulk glass forming Pd $_{40}$ Cu $_{30}$ Ni $_{10}$ P $_{20}$* , *Appl. Phys. Lett.* 77 (2000), pp. 681–683.
 - [206] M. Ediger, C. Angell, and S. Nagel, *Supercooled Liquids and Glasses*, *J. Phys. Chem.* 100 (1996), pp. 13200–13212.
 - [207] S. Mahmoudian, L. Rademaker, A. Ralko, S. Fratini, and V. Dobrosavljević, *Glassy dynamics in geometrically frustrated Coulomb liquids without disorder*, *Phys. Rev. Lett.* 115 (2015), 025701.
 - [208] A.H. Castro Neto, F. Guinea, N.M.R. Peres, K.S. Novoselov, and A.K. Geim, *The electronic properties of graphene*, *Rev. Mod. Phys.* 81 (2009), pp. 109–162.
 - [209] T. Wehling, A. Black-Schafferc, and A. Balatsky, *Dirac materials*, *Adv. Phys.* 63 (2014), pp. 1–76.
 - [210] N.P. Armitage, E.J. Mele, and A. Vishwanath, *Weyl and Dirac semimetals in three-*

- dimensional solids*, Rev. Mod. Phys. 90 (2018), 015001.
- [211] N. Tajima, M. Tamura, Y. Nishio, K. Kajita, and Y. Iye, *Transport Property of an Organic Conductor α -(BEDT-TTF) $_2$ I $_3$ under High Pressure – Discovery of a Novel Type of Conductor*, J. Phys. Soc. Jpn. 69 (2000), pp. 543–551.
 - [212] N. Tajima, S. Sugawara, M. Tamura, R. Kato, Y. Nishio, and K. Kajita, *Transport properties of massless Dirac fermions in an organic conductor α -(BEDT-TTF) $_2$ I $_3$ under pressure*, Europhysics Letters (EPL) 80 (2007), 47002.
 - [213] N. Tajima and K. Kajita, *Experimental study of organic zero-gap conductor α -(BEDT-TTF) $_2$ I $_3$* , Sci. Technol. Adv. Mater. 10 (2009), 024308.
 - [214] N. Tajima and T. Morinari, *Tilted Dirac Cone Effect on Interlayer Magnetoresistance in α -(BEDT-TTF) $_2$ I $_3$* , J. Phys. Soc. Jpn. 87 (2018), 045002.
 - [215] K. Kajita, Y. Nishio, N. Tajima, Y. Suzumura, and A. Kobayashi, *Molecular Dirac Fermion Systems – Theoretical and Experimental Approaches*, J. Phys. Soc. Jpn. 83 (2014), 072002.
 - [216] S. Katayama, A. Kobayashi, and Y. Suzumura, *Pressure-Induced Zero-Gap Semiconducting State in Organic Conductor α -(BEDT-TTF) $_2$ I $_3$ Salt*, J. Phys. Soc. Jpn. 75 (2006), 054705.
 - [217] H. Kino and T. Miyazaki, *First-Principles Study of Electronic Structure in α -(BEDT-TTF) $_2$ I $_3$ at Ambient Pressure and with Uniaxial Strain*, J. Phys. Soc. Jpn. 75 (2006), 034704.
 - [218] A. Kobayashi, S. Katayama, Y. Suzumura, and H. Fukuyama, *Massless Fermions in Organic Conductor*, J. Phys. Soc. Jpn. 76 (2007), 034711.
 - [219] M.O. Goerbig, J.N. Fuchs, G. Montambaux, and F. Piéchon, *Tilted anisotropic Dirac cones in quinoid-type graphene and α -(BEDT-TTF) $_2$ I $_3$* , Phys. Rev. B 78 (2008), 045415.
 - [220] A. Kobayashi, S. Katayama, and Y. Suzumura, *Theoretical study of the zero-gap organic conductor α -(BEDT-TTF) $_2$ I $_3$* , Sci. Technol. Adv. Mater. 10 (2009), 024309.
 - [221] R. Kondo, S. Kagoshima, and J. Harada, *Crystal structure analysis under uniaxial strain at low temperature using a unique design of four-axis x-ray diffractometer with a fixed sample*, Rev. Sci. Instr. 76 (2005), 093902.
 - [222] R. Kondo, S. Kagoshima, N. Tajima, and R. Kato, *Crystal and Electronic Structures of the Quasi-Two-Dimensional Organic Conductor α -(BEDT-TTF) $_2$ I $_3$ and Its Selenium Analogue α -(BEDT-TSeF) $_2$ I $_3$ under Hydrostatic Pressure at Room Temperature*, J. Phys. Soc. Jpn. 78 (2009), 114714.
 - [223] T. Konoike, K. Uchida, and T. Osada, *Specific Heat of the Multilayered Massless Dirac Fermion System*, J. Phys. Soc. Jpn. 81 (2012), 043601.
 - [224] M. Hirata, K. Ishikawa, A. Kobayashi, K. Miyagawa, M. Tamura, C. Berthier, and K. Kanoda, *Anomalous spin correlations and excitonic instability of interacting 2D Weyle fermions*, Science 358 (2017), 6369.
 - [225] G. Montambaux, F. Piéchon, J.N. Fuchs, and M.O. Goerbig, *Merging of Dirac points in a two-dimensional crystal*, Phys. Rev. B 80 (2009), 153412.
 - [226] A. Kobayashi, Y. Suzumura, F. Piéchon, and G. Montambaux, *Emergence of Dirac electron pair in the charge-ordered state of the organic conductor α -(BEDT-TTF) $_2$ I $_3$* , Phys. Rev. B 84 (2011), 075450.
 - [227] D. Vanderbilt *Berry Phases in Electronic Structure Theory*, Cambridge University Press, Cambridge, 2018.
 - [228] T. Osada, *Chern Insulator Phase in a Lattice of an Organic Dirac Semimetal with Intracellular Potential and Magnetic Modulations*, J. Phys. Soc. Jpn. 86 (2017), 123702.
 - [229] ———, *Topological Properties of τ -Type Organic Conductors with a Checkerboard Lattice*, J. Phys. Soc. Jpn. 88 (2019), 114707.
 - [230] T. Osada and A. Kiswandhi, *Possible Current-Induced Phenomena and Domain Control in an Organic Dirac Fermion System with Weak Charge Ordering*, J. Phys. Soc. Jpn. 89 (2020), p. 103701.
 - [231] M. Inokuchi, H. Tajima, A. Kobayashi, T. Ohta, H. Kuroda, R. Kato, T. Naito, and H. Kobayashi, *Electrical and Optical Properties of α -(BETS) $_2$ I $_3$ and α -(BEDT-STF) $_2$ I $_3$* ,

- Bull. Chem. Soc. Jpn. 68 (1995), pp. 547–553.
- [232] T. Morinari and Y. Suzumura, *On the Possible Zero-Gap State in Organic Conductor α -(BEDT-TSF) $_2$ I $_3$ under Pressure*, J. Phys. Soc. Jpn. 83 (2014), 094701.
- [233] T. Naito, R. Doi, and Y. Suzumura, *Exotic Dirac Cones on the Band Structure of α -STF $_2$ I $_3$ at Ambient Temperature and Pressure*, J. Phys. Soc. Jpn. 89 (2020), 023701.
- [234] T. Naito, H. Kobayashi, and A. Kobayashi, *The Electrical Behavior of Charge-Transfer Salts Based on an Unsymmetrical Donor Bis(ethylenedithio)diselenadithiafulvalene (STF): Disorder Effect on the Transport Properties*, Bull. Chem. Soc. Jpn. 70 (1997), pp. 107–114.
- [235] T. Naito and R. Doi, *Band Structure and Physical Properties of α -STF $_2$ I $_3$: Dirac Electrons in Disordered Conduction Sheets*, Crystals 10 (2020), 4.
- [236] S. Kitou, T. Tsumuraya, H. Sawahata, F. Ishii, K.i. Hiraki, T. Nakamura, N. Katayama, and H. Sawa, *Ambient pressure Dirac electron system in quasi-two-dimensional molecular conductor α -(BETS) $_2$ I $_3$* , arXiv:2006.08978 (2020).
- [237] M. Monteverde, M.O. Goerbig, P. Auban-Senzier, F. Navarin, H. Henck, C.R. Pasquier, C. Mézière, and P. Batail, *Coexistence of Dirac and massive carriers in α -(BEDT-TTF) $_2$ I $_3$ under hydrostatic pressure*, Phys. Rev. B 87 (2013), 245110.
- [238] A. Mori, M. Sato, T. Yajima, T. Konoike, K. Uchida, and T. Osada, *Anisotropy of Dirac cones and Van Hove singularity in an organic Dirac fermion system*, Phys. Rev. B 99 (2019), 035106.
- [239] T. Tani, N. Tajima, and A. Kobayashi, *Field-Angle Dependence of Interlayer Magnetoresistance in Organic Dirac Electron System α -(BEDT-TTF) $_2$ I $_3$* , Crystals 9 (2019), 212.
- [240] Y. Tanaka and M. Ogata, *Correlation Effects on Charge Order and Zero-Gap State in the Organic Conductor α -(BEDT-TTF) $_2$ I $_3$* , J. Phys. Soc. Jpn. 85 (2016), 104706.
- [241] S.M. Winter, K. Riedl, and R. Valentí, *Importance of spin-orbit coupling in layered organic salts*, Phys. Rev. B 95 (2017), 060404.
- [242] T. Moriya, *The Effect of Electron-Electron Interaction on the Nuclear Spin Relaxation in Metals*, J. Phys. Soc. Jpn. 18 (1963), pp. 516–520.
- [243] A. Narath and H.T. Weaver, *Effects of Electron-Electron Interactions on Nuclear Spin-Lattice Relaxation Rates and Knight Shifts in Alkali and Noble Metals*, Phys. Rev. 175 (1968), pp. 373–382.
- [244] M. Hirata, K. Miyagawa, K. Kanoda, and M. Tamura, *Electron correlations in the quasi-two-dimensional organic conductor θ -(BEDT-TTF) $_2$ I $_3$ investigated by ^{13}C NMR*, Phys. Rev. B 85 (2012), 195146.
- [245] D. Ohki, M. Hirata, T. Tani, K. Kanoda, and A. Kobayashi, *Chiral excitonic instability of two-dimensional tilted Dirac cones*, Phys. Rev. Res. 2 (2020), 033479.
- [246] D. Ohki, Y. Omori, and A. Kobayashi, *Domain wall conductivity with strong Coulomb interaction of two-dimensional massive Dirac electrons in the organic conductor α -(BEDT-TTF) $_2$ I $_3$* , Phys. Rev. B 100 (2019), 075206.
- [247] D. Ohki, G. Matsuno, Y. Omori, and A. Kobayashi, *Optical Conductivity in a Two-Dimensional Extended Hubbard Model for an Organic Dirac Electron System α -(BEDT-TTF) $_2$ I $_3$* , Crystals 8 (2018), 137.
- [248] G. Matsuno, Y. Omori, T. Eguchi, and A. Kobayashi, *Topological Domain Wall and Valley Hall Effect in Charge Ordered Phase of Molecular Dirac Fermion System α -(BEDT-TTF) $_2$ I $_3$* , J. Phys. Soc. Jpn. 85 (2016), 094710.
- [249] Y. Omori, G. Matsuno, and A. Kobayashi, *Longitudinal Conductivity on Edge and Domain Wall Molecular Dirac Electron System α -(BEDT-TTF) $_2$ I $_3$* , J. Phys. Soc. Jpn. 86 (2017), 074708.
- [250] D. Ohki, G. Matsuno, Y. Omori, and A. Kobayashi, *Melting of Domain Wall in Charge Ordered Dirac Electron of Organic Conductor α -(BEDT-TTF) $_2$ I $_3$* , J. Phys. Soc. Jpn. 87 (2018), 054703.
- [251] M. Naka and S. Ishihara, *Electronic Ferroelectricity in a Dimer Mott Insulator*, J. Phys. Soc. Jpn. 79 (2010), 063707.

- [252] K. Yamauchi and P. Barone, *Electronic ferroelectricity induced by charge and orbital orderings*, J. Phys.: Condens. Matter 26 (2014), 103201.
- [253] J. Scott, *Ferroelectrics go bananas*, J. Phys.: Condens. Matter 20 (2008), 021001.
- [254] T. Ivek, B. Korin-Hamzić, O. Milat, S. Tomić, C. Clauss, N. Drichko, D. Schweitzer, and M. Dressel, *Collective Excitations in the Charge-Ordered Phase of α -(BEDT-TTF) $_2$ I $_3$* , Phys. Rev. Lett. 104 (2010), 206406.
- [255] K. Kodama, M. Kimata, Y. Takahide, N. Kurita, A. Harada, H. Satsukawa, T. Terashima, S. Uji, K. Yamamoto, and K. Yakushi, *Charge Transport in Charge-Ordered States of Two-Dimensional Organic Conductors, α -(BEDT-TTF) $_2$ I $_3$ and α' -(BEDT-TTF) $_2$ IBr $_2$* , J. Phys. Soc. Jpn. 81 (2012), 044703.
- [256] A.K. Jonscher, *The ‘universal’ dielectric response*, Nature 267 (1977), p. 673–679.
- [257] ———, *Dielectric relaxation in solids*, J. Phys. D: Appl. Phys. 32 (1999), pp. R57–R70.
- [258] F. Nad, P. Monceau, and H. Yamamoto, *Dielectric response in the charge-ordered θ -(BEDT-TTF) $_2$ RbZn(SCN) $_4$ organic compound*, J. Phys.: Condens. Matter 18 (2006), pp. L509–L514.
- [259] G. Catalan, J. Seidel, R. Ramesh, and J. Scott, *Domain wall nanoelectronics*, Rev. Mod. Phys. 84 (2012), pp. 119–156.
- [260] P. Bednyakov, T. Sluka, A. Tagantsev, D. Damjanovic, and N. Setter, *Formation of charged ferroelectric domain walls with controlled periodicity*, Sci. Rep. 5 (2015), 15819.
- [261] K. Tamura, T. Ozawa, Y. Bando, T. Kawamoto, and T. Mori, *Voltage oscillation associated with nonlinear conductivity in the organic conductor α -(BEDT-TTF) $_2$ I $_3$* , J. Appl. Phys. 107 (2010), 103716.
- [262] T. Ivek, I. Kovačić, M. Pinterić, B. Korin-Hamzić, S. Tomić, T. Knoblauch, D. Schweitzer, and M. Dressel, *Cooperative dynamics in charge-ordered state of α -(BEDT-TTF) $_2$ I $_3$* , Phys. Rev. B 86 (2012), 245125.
- [263] T. Peterseim, T. Ivek, D. Schweitzer, and M. Dressel, *Electrically induced phase transition in α -(BEDT-TTF) $_2$ I $_3$: Indications for Dirac-like hot charge carriers*, Phys. Rev. B 93 (2016), 245133.
- [264] S. Uji, K. Kodama, K. Sugii, Y. Takahide, T. Terashima, N. Kurita, S. Tsuchiya, M. Kohno, M. Kimata, K. Yamamoto, and K. Yakushi, *Kosterlitz-Thouless-Type Transition in a Charge Ordered State of the Layered Organic Conductor α -(BEDT-TTF) $_2$ I $_3$* , Phys. Rev. Lett. 110 (2013), 196602.
- [265] M. Sotome, N. Kida, Y. Kinoshita, H. Yamakawa, T. Miyamoto, H. Mori, and H. Okamoto, *Visualization of a nonlinear conducting path in an organic molecular ferroelectric by using emission of terahertz radiation*, Phys. Rev. B 95 (2017), 241102.
- [266] T. Iimori, T. Naito, and N. Ohta, *Unprecedented Optoelectronic Function in Organic Conductor: Memory Effect of Photoswitching Controlled by Voltage Pulse Width*, J. Phys. Chem. C 113 (2009), pp. 4654–4661.
- [267] T. Iimori and N. Ohta, *Tuning of electrical conductivity by photoirradiation and electric fields*, J. Phys. Chem. C 118 (2014), pp. 7251–7260.
- [268] T. Iimori, T. Naito, and N. Ohta, *Photoinduced Phase Transition in the Organic Conductor α -(BEDT-TTF) $_2$ I $_3$ at Temperatures near the Metal-Insulator Phase Transition*, Chem. Lett. 36 (2007), pp. 536–537.
- [269] S. Iwai, K. Yamamoto, A. Kashiwazaki, F. Hiramatsu, H. Nakaya, Y. Kawakami, K. Yakushi, H. Okamoto, H. Mori, and Y. Nishio, *Photoinduced Melting of a Stripe-Type Charge-Order and Metallic Domain Formation in a Layered BEDT-TTF-Based Organic Salt*, Phys. Rev. Lett. 98 (2007), 097402.
- [270] Y. Kawakami, T. Fukatsu, Y. Sakurai, H. Unno, H. Itoh, S. Iwai, T. Sasaki, K. Yamamoto, K. Yakushi, and K. Yonemitsu, *Early-Stage Dynamics of Light-Matter Interaction Leading to the Insulator-to-Metal Transition in a Charge Ordered Organic Crystal*, Phys. Rev. Lett. 105 (2010), 246402.
- [271] S. Miyashita, Y. Tanaka, S. Iwai, and K. Yonemitsu, *Charge, Lattice, and Spin Dynamics in Photoinduced Phase Transitions from Charge-Ordered Insulator to Metal in Quasi-Two-Dimensional Organic Conductors*, J. Phys. Soc. Jpn. 79 (2010), 034708.

- [272] Y. Tanaka and K. Yonemitsu, *Growth Dynamics of Photoinduced Domains in Two-Dimensional Charge-Ordered Conductors Depending on Stabilization Mechanisms*, J. Phys. Soc. Jpn. 79 (2010), 024712.
- [273] S. Iwai, *Photoinduced Phase Transitions in α -, θ -, and κ -type ET Salts: Ultrafast Melting of the Electronic Ordering*, Crystals 2 (2012), pp. 590–617.
- [274] H. Itoh, K. Itoh, K. Goto, K. Yamamoto, K. Yakushi, and S. Iwai, *Efficient terahertz-wave generation and its ultrafast optical modulation in charge ordered organic ferroelectrics*, Appl. Rev. Lett. 104 (2014), 173302.
- [275] H. Itoh, R. Fujiwara, Y. Kawakami, K. Yamamoto, Y. Nakamura, K. Kishida, and S. Iwai, *Modulation of terahertz emission in time-domain waveform via a photoinduced phase transition in a charge ordered organic ferroelectric*, Appl. Rev. Lett. 112 (2018), 093302.
- [276] Y. Tanaka and K. Yonemitsu, *Charge Order with Structural Distortion in Organic Conductors: Comparison between θ -(ET)₂RbZn(SCN)₄ and α -(ET)₂I₃*, J. Phys. Soc. Jpn. 77 (2008), 034708.
- [277] S. Miyashita and K. Yonemitsu, *Charge ordering in θ -(BEDT-TTF)₂RbZn(SCN)₄: Co-operative effects of electron correlations and lattice distortions*, Phys. Rev. B 75 (2007), 245112.
- [278] R. Świetlik, A. Lapiński, M. Polomska, L. Ouahab, and A. Ota, *Infrared and Raman investigations of the charge ordering phenomena in the monoclinic salts κ -(ET)₄[M(CN)₆][N(C₂H₅)₄]·2H₂O (M=Co^{III}, Fe^{III})*, J. Low Temp. Phys. 142 (2006), pp. 641–645.
- [279] A. Ota, L. Ouahab, S. Golhen, Y. Yoshida, M. Maesto, G. Saito, and R. Świetlik, *Phase transition from Mott insulating phase into the charge ordering phase with molecular deformation in charge-transfer salts κ -(ET)₄[M(CN)₆][N(C₂H₅)₄]·2H₂O (M=Co^{III} and Fe^{III})*, Chem. Mater. 19 (2007), pp. 2455–2462.
- [280] A. Lapiński, R. Świetlik, L. Ouahab, and S. Golhen, *Spectroscopic studies of the phase transition from the Mott insulation state to the charge-ordering state of κ -(ET)₄[M(CN)₆][N(C₂H₅)₄]·2H₂O (M=Co^{III} and Fe^{III}) salts*, Journal of Physical Chemistry A 17 (2013), pp. 5241–5250.
- [281] R.N. Lyubovskaya, O.A. Dyachenko, V.V. Gritsenko, S.G. Mkoyan, L.O. Atovmyan, R.B. Lyubovskii, V.N. Laukhin, A.V. Zvarykina, and A.G. Khomenko, *New Organic Metal (ET)₄(Hg₂Cl₆·C₆H₅Cl) – Synthesis, Structure, Properties*, Synth. Met. 42 (1991), pp. 1907–1910.
- [282] R. Lyubovskii, R. Lyubovskaya, and O. Dyachenko, *Physical properties of some ET-based organic metals and superconductors with mercury containing anions*, J. Phys. (Paris) I 6 (1996), pp. 1609–1630.
- [283] E.I. Zhilyaeva, O.A. Bogdanova, R.N. Lyubovskaya, R.B. Lyubovskii, K.A. Lyssenko, and M.Y. Antipin, *New organic conductors (BEDO-TTF)_mMHg(SCN)₄*, Synth. Met. 99 (1999), pp. 169–174.
- [284] R.B. Lyubovskii, S.I. Pesotskii, M. Gener, R. Rousseau, E. Canadell, J.A.A.J. Perenboom, V.I. Nizhankovskii, E.I. Zhilyaeva, O.A. Bogdanova, and R.N. Lyubovskaya, *Characterization of the Fermi surface of (BEDO-TTF)₅[CsHg(SCN)₄]₂ by magnetoresistance measurements and tight-binding band structure calculations*, J. Mater. Chem. 12 (2002), pp. 483–488.
- [285] T. Ivek, R. Beyer, S. Badalov, M. Čulo, S. Tomić, J.A. Schlueter, E.I. Zhilyaeva, R.N. Lyubovskaya, and M. Dressel, *Metal-insulator transition in the dimerized organic conductor κ -(BEDT-TTF)₂Hg(SCN)₂Br*, Phys. Rev. B 96 (2017), 085116.
- [286] T. Thomas, B. Hartmann, P. Lunkenheimer, H. Schubert, J.A. Schlueter, and J. Müller, *Low-Frequency Charge Carrier Dynamics in Ferroelectric κ -(BEDT-TTF)₂X – A Comparative Study of X = Cu[N(CN)₂]Cl and X = Hg(SCN)₂Cl*, phys. stat. sol. (b) 256 (2019), 1800746.
- [287] N. Hassan, K. Thirunavukkuarasu, Z. Lu, D. Smirnov, E. Zhilyaeva, S. Torunova, R. Lyubovskaya, and N. Drichko, *Melting of charge order in the low-temperature state of*

- an electronic ferroelectric-like system*, npj Quantum Mater. 5 (2020), 15.
- [288] S. Krohns and P. Lunkenheimer, *Ferroelectric polarization in multiferroics*, Physical Sciences Reviews 4 (2019), 20190015.
- [289] M. de Souza, L. Squillante, C. Sônego, P. Menegasso, P. Foury-Leylekian, and J.P. Pouget, *Probing the ionic dielectric constant contribution in the ferroelectric phase of the Fabre salts*, Phys. Rev. B 97 (2018), 045122.
- [290] N. Mott *Metal-Insulator Transitions*, 2nd ed. Taylor & Francis, London, 1990.
- [291] P. Edwards, C. Rao, and N. Mott (eds.) *Metal-insulator transitions revisited*, Taylor & Francis, London, 1995.
- [292] F. Gebhard *The Mott Metal-Insulator Transition: Models and Methods*, Springer Tracts in Modern Physics Vol. 137, Springer-Verlag, Berlin, 2010.
- [293] V. Dobrosavljević, N. Tevidi, and J. Valles *Conductor-Insulator Quantum Phase Transitions*, Oxford University Press, Oxford, 2012.
- [294] F.J. Morin, *Oxides Which Show a Metal-to-Insulator Transition at the Neel Temperature*, Phys. Rev. Lett. 3 (1959), pp. 34–36.
- [295] A. Jayaraman, D.B. McWhan, J.P. Remeika, and P.D. Dernier, *Critical Behavior of the Mott Transition in Cr-Doped V₂O₃*, Phys. Rev. B 2 (1970), pp. 3751–3756.
- [296] P. Limelette, A. Georges, D. Jérôme, P. Wzietek, P. Metcalf, and J.M. Honig, *Universality and Critical Behavior at the Mott Transition*, Science 302 (2003), pp. 89–92.
- [297] S. Lupi et al., *A microscopic view on the Mott transition in chromium-doped V₂O₃*, Nat. Commun. 1 (2010), 105.
- [298] P. Hansmann, A. Toschi, G. Sangiovanni, T. Saha-Dasgupta, S. Lupi, M. Marsi, and K. Held, *Mott–Hubbard transition in V₂O₃ revisited*, phys. stat. sol. (b) 250 (2013), pp. 1251–1264.
- [299] O. Nájera, M. Civelli, V. Dobrosavljević, and M.J. Rozenberg, *Resolving the VO₂ controversy: Mott mechanism dominates the insulator-to-metal transition*, Phys. Rev. B 95 (2017), 35113.
- [300] O. Nájera, M. Civelli, V. Dobrosavljević, and M.J. Rozenberg, *Multiple crossovers and coherent states in a Mott-Peierls insulator*, Phys. Rev. B 97 (2018), 045108.
- [301] Z. Shao, X. Cao, H. Luo, and P. Jin, *Recent progress in the phase-transition mechanism and modulation of vanadiumdioxide materials*, NPG Asia Materials 10 (2018), pp. 581–605.
- [302] S. Florens and A. Georges, *Slave-rotor mean-field theories of strongly correlated systems and the Mott transition in finite dimensions*, Phys. Rev. B 70 (2004), 035114.
- [303] T. Senthil, *Theory of a continuous Mott transition in two dimensions*, Phys. Rev. B 78 (2008), 045109.
- [304] A. Georges, G. Kotliar, W. Krauth, and M.J. Rozenberg, *Dynamical mean-field theory of strongly correlated fermion systems and the limit of infinite dimensions*, Rev. Mod. Phys. 68 (1996), pp. 13–125.
- [305] H. Terletska, J. Vučičević, D. Tanasković, and V. Dobrosavljević, *Quantum Critical Transport near the Mott Transition*, Phys. Rev. Lett. 107 (2011), 026401.
- [306] J. Vučičević, H. Terletska, D. Tanasković, and V. Dobrosavljević, *Finite-temperature crossover and the quantum Widom line near the Mott transition*, Phys. Rev. B 88 (2013), 75143.
- [307] T. Furukawa, K. Miyagawa, T. Itou, M. Ito, H. Taniguchi, M. Saito, S. Iguchi, T. Sasaki, and K. Kanoda, *Quantum Spin Liquid Emerging from Antiferromagnetic Order by Introducing Disorder*, Phys. Rev. Lett. 115 (2015), 77001.
- [308] A. Pustogow, M. Bories, A. Löhle, R. Rösslhuber, E. Zhukova, B. Gorshunov, S. Tomić, J.A. Schlueter, R. Hübner, T. Hiramatsu, Y. Yoshida, G. Saito, R. Kato, T.H. Lee, V. Dobrosavljević, S. Fratini, and M. Dressel, *Quantum spin liquids unveil the genuine Mott state*, Nat. Mater. 17 (2018), pp. 773–777.
- [309] R. Rösslhuber, A. Pustogow, E. Uykur, A. Böhme, A. Löhle, R. Hübner, J. Schlueter, and M. Dressel, *Phase coexistence at the first-order Mott-transition revealed by pressure-dependent dielectric spectroscopy of κ -(BEDT-TTF)₂Cu₂(CN)₃*,

- arXiv:1911.12273 (2019).
- [310] M.M. Radonjić, D. Tanasković, V. Dobrosavljević, K. Haule, and G. Kotliar, *Wigner-Mott scaling of transport near the two-dimensional metal-insulator transition*, Phys. Rev. B 85 (2012), 85133.
 - [311] X. Deng, J. Mravlje, R. Žitko, M. Ferrero, G. Kotliar, and A. Georges, *How Bad Metals Turn Good: Spectroscopic Signatures of Resilient Quasiparticles*, Phys. Rev. Lett. 110 (2013), 086401.
 - [312] L.P. Kadanoff, W. Götze, D. Hamblen, R. Hecht, E.A.S. Lewis, V.V. Palciauskas, M. Rayl, J. Swift, D. Aspnes, and J. Kane, *Static Phenomena Near Critical Points: Theory and Experiment*, Rev. Mod. Phys. 39 (1967), pp. 395–431.
 - [313] A. Georges and W. Krauth, *Physical properties of the half-filled Hubbard model in infinite dimensions*, Phys. Rev. B 48 (1993), pp. 7167–7182.
 - [314] M.J. Rozenberg, G. Kotliar, and X.Y. Zhang, *Mott-Hubbard transition in infinite dimensions. II*, Phys. Rev. B 49 (1994), pp. 10181–10193.
 - [315] R. Bulla, T.A. Costi, and D. Vollhardt, *Finite-temperature numerical renormalization group study of the Mott transition*, Phys. Rev. B 64 (2001), 045103.
 - [316] G. Kotliar and D. Vollhardt, *Strongly Correlated Materials: Insights From Dynamical Mean-Field Theory*, Physics Today 57 (March 2004), pp. 53–59.
 - [317] D. Vollhardt, *Dynamical mean-field theory for correlated electrons*, Ann. Phys. (Berl.) 524 (2012), pp. 1–19.
 - [318] J. Vučićević, D. Tanasković, M.J. Rozenberg, and V. Dobrosavljević, *Bad-Metal Behavior Reveals Mott Quantum Criticality in Doped Hubbard Models*, Phys. Rev. Lett. 114 (2015), 246402.
 - [319] H.E. Stanley *Introduction to Phase Transitions and Critical Phenomena*, Oxford University Press, New York and Oxford, 1971.
 - [320] M.E. Fisher and B. Widom, *Decay of Correlations in Linear Systems*, J. Chem. Phys. 50 (1969), pp. 3756–3772.
 - [321] G.G. Simeoni, T. Bryk, F.A. Gorelli, M. Krisch, G. Ruocco, M. Santoro, and T. Scopigno, *The Widom line as the crossover between liquid-like and gas-like behaviour in supercritical fluids*, Nature Phys. 6 (2010), pp. 503–507.
 - [322] B.J. Powell and R.H. McKenzie, *Quantum Frustration in Organic Mott Insulators: From Spin Liquids to Unconventional Superconductors*, Rep. Progr. Phys. 74 (2011), 056501.
 - [323] H.T. Dang, X.Y. Xu, K.S. Chen, Z.Y. Meng, and S. Wessel, *Mott transition in the triangular lattice Hubbard model: A dynamical cluster approximation study*, Phys. Rev. B 91 (2015), 155101.
 - [324] M. Pinterić, T. Ivek, M. Čulo, O. Milat, M. Basletić, B. Korin-Hamzić, E. Tafra, A. Hamzić, M. Dressel, and S. Tomić, *What is the origin of anomalous dielectric response in 2D organic dimer Mott insulators κ -(BEDT-TTF)₂Cu[N(CN)₂]Cl and κ -(BEDT-TTF)₂Cu₂(CN)₃?*, Physica B 460 (2015), pp. 202–207.
 - [325] T. Furukawa, K. Miyagawa, H. Taniguchi, R. Kato, and K. Kanoda, *Quantum criticality of Mott transition in organic materials*, Nat. Phys. 11 (2015), pp. 221–224.
 - [326] E. Gati, M. Garst, R.S. Manna, U. Tutsch, B. Wolf, L. Bartosch, H. Schubert, T. Sasaki, J.A. Schlueter, and M. Lang, *Breakdown of Hooke’s law of elasticity at the Mott critical endpoint in an organic conductor*, Sci. Adv. 2 (2016), e1601646.
 - [327] C. Castellani, C.D. Castro, D. Feinberg, and J. Ranninger, *New Model Hamiltonian for the Metal-Insulator Transition*, Phys. Rev. Lett. 43 (1979), pp. 1957–1960.
 - [328] G. Kotliar, E. Lange, and M.J. Rozenberg, *Landau Theory of the Finite Temperature Mott Transition*, Phys. Rev. Lett. 84 (2000), pp. 5180–5183.
 - [329] F. Kagawa, K. Miyagawa, and K. Kanoda, *Unconventional critical behaviour in a quasi-two-dimensional organic conductor*, Nature 436 (2005), pp. 534–537.
 - [330] F. Kagawa, T. Itou, K. Miyagawa, and K. Kanoda, *Transport criticality of the first-order Mott transition in the quasi-two-dimensional organic conductor κ -(BEDT-TTF)₂Cu[N(CN)₂]Cl*, Phys. Rev. B 69 (2004), 064511.
 - [331] F. Kagawa, K. Miyagawa, and K. Kanoda, *Magnetic Mott criticality in a κ -type organic*

- salt probed by NMR*, Nat. Phys. 5 (2009), pp. 880–884.
- [332] M. Sentef, P. Werner, E. Gull, and A.P. Kampf, *Charge and spin criticality for the continuous Mott transition in a two-dimensional organic conductor*, Phys. Rev. B 84 (2011), 165133.
- [333] M. de Souza, A. Brühl, C. Strack, B. Wolf, D. Schweitzer, and M. Lang, *Anomalous Lattice Response at the Mott Transition in a Quasi-2D Organic Conductor*, Phys. Rev. Lett. 99 (2007), 037003.
- [334] Y. Nakazawa and K. Kanoda, *Electronic structure of insulating salts of the κ -(BEDT-TTF)₂X family studied by low-temperature specific-heat measurements*, Phys. Rev. B 53 (1996), pp. 8875–8878.
- [335] S. Papanikolaou, R.M. Fernandes, E. Fradkin, P.W. Phillips, J. Schmalian, and R. Sknepnek, *Universality of Liquid-Gas Mott Transitions at Finite Temperatures*, Phys. Rev. Lett. 100 (2008), 026408.
- [336] L. Bartosch, M. de Souza, and M. Lang, *Scaling Theory of the Mott Transition and Breakdown of the Grüneisen Scaling Near a Finite-Temperature Critical End Point*, Phys. Rev. Lett. 104 (2010), 245701.
- [337] M. Zacharias, L. Bartosch, and M. Garst, *Mott Metal-Insulator Transition on Compressible Lattices*, Phys. Rev. Lett. 109 (2012), 176401.
- [338] M. de Souza and L. Bartosch, *Probing the Mott physics in κ -(BEDT-TTF)₂X salts via thermal expansion*, J. Phys.: Condens. Matter 27 (2015), 053203.
- [339] T. Sasaki, N. Yoneyama, and N. Kobayashi, *Mott transition and superconductivity in the strongly correlated organic superconductor κ -(BEDT-TTF)₂Cu[N(CN)₂]Br*, Phys. Rev. B 77 (2008), 054505.
- [340] M. Urai, T. Furukawa, Y. Seki, K. Miyagawa, T. Sasaki, H. Taniguchi, and K. Kanoda, *Disorder unveils Mott quantum criticality behind a first-order transition in the quasi-two-dimensional organic conductor κ -(ET)₂Cu[N(CN)₂]Cl*, Phys. Rev. B 99 (2019), 245139.
- [341] D. Vollhardt, *Dynamical Mean-Field Theory of Strongly Correlated Electron Systems*, JPS Conf. Proc. 30 (2020), 011001.
- [342] P. Limelette, P. Wzietek, S. Florens, A. Georges, T.A. Costi, C. Pasquier, D. Jérôme, C. Mézière, and P. Batail, *Mott Transition and Transport Crossovers in the Organic Compound κ -(BEDT-TTF)₂Cu[N(CN)₂]Cl*, Phys. Rev. Lett. 91 (2003), 016401.
- [343] S. Yasin, M. Dumm, B. Salameh, P. Batail, C. Mézière, and M. Dressel, *Transport studies at the Mott transition of the two-dimensional organic metal κ -(BEDT-TTF)₂Cu[N(CN)₂]Br_xCl_{1-x}*, Eur. Phys. J. B 79 (2011), pp. 383–390.
- [344] S. Lefebvre, P. Wzietek, S. Brown, C. Bourbonnais, D. Jérôme, C. Mézière, M. Fourmigué, and P. Batail, *Mott Transition, Antiferromagnetism, and Unconventional Superconductivity in Layered Organic Superconductors*, Phys. Rev. Lett. 85 (2000), pp. 5420–5423.
- [345] F. Kagawa, T. Itou, K. Miyagawa, and K. Kanoda, *Magnetic-Field-Induced Mott Transition in a Quasi-Two-Dimensional Organic Conductor*, Phys. Rev. Lett. 93 (2004), 127001.
- [346] J. Müller, J. Brandenburg, and J.A. Schlueter, *Magnetic-Field Induced Crossover of Superconducting Percolation Regimes in the Layered Organic Mott System κ -(BEDT-TTF)₂Cu[N(CN)₂]Cl*, Phys. Rev. Lett. 102 (2009), 047004.
- [347] J. Müller, B. Hartmann, and T. Sasaki, *Fine-tuning the Mott metal-insulator transition and critical charge carrier dynamics in molecular conductors*, Phil. Mag. 97 (2017), pp. 3477–3494.
- [348] K. Kanoda, *Electron correlation, metal-insulator transition and superconductivity in quasi-2D organic systems, (ET)₂X*, Physica C 282-287 (1997), pp. 299–302.
- [349] T. Vuletic, P. Auban-Senzier, C. Pasquier, S. Tomic, D. Jérôme, M. Heritier, and K. Bechgaard, *Coexistence of superconductivity and spin density wave orderings in the organic superconductor (TMTSF)₂PF₆*, Eur. Phys. J. B 25 (2002), pp. 319–331.
- [350] D. Fournier, M. Poirier, and K.D. Truong, *Competition between magnetism and superconductivity in the organic metal κ -(BEDT-TTF)₂Cu[N(CN)₂]Br*, Phys. Rev. B 76 (2007),

- 054509.
- [351] T. Sasaki and N. Yoneyama, *Spatial mapping of electronic states in κ -(BEDT-TTF)₂X using infrared reflectivity*, Sci. Technol. Adv. Mater. 10 (2009), 024306.
 - [352] T. Nishi, S. Kimura, T. Takahashi, T. Ito, H. Im, Y. Kwon, K. Miyagawa, H. Taniguchi, A. Kawamoto, and K. Kanoda, *The origin of the phase separation in partially deuterated κ -(ET)₂Cu[N(CN)₂]Br studied by infrared magneto-optical imaging spectroscopy*, Solid State Commun. 134 (2005), pp. 189–193.
 - [353] T. Nishi, S.i. Kimura, T. Takahashi, H. Im, Y.s. Kwon, T. Ito, K. Miyagawa, H. Taniguchi, A. Kawamoto, and K. Kanoda, *Magnetic-field-induced superconductor-insulator-metal transition in an organic conductor: An infrared magneto-optical imaging spectroscopic study*, Phys. Rev. B 75 (2007), 014525.
 - [354] T. Sasaki, N. Yoneyama, N. Kobayashi, Y. Ikemoto, and H. Kimura, *Imaging Phase Separation near the Mott Boundary of the Correlated Organic Superconductors κ -(BEDT-TTF)₂X*, Phys. Rev. Lett. 92 (2004), 227001.
 - [355] T. Sasaki, N. Yoneyama, A. Suzuki, N. Kobayashi, Y. Ikemoto, and H. Kimura, *Real Space Imaging of the Metal-Insulator Phase Separation in the Band Width Controlled Organic Mott System κ -(BEDT-TTF)₂Cu[N(CN)₂]Br*, J. Phys. Soc. Jpn. 74 (2005), pp. 2351–2360.
 - [356] J. Müller, *Fluctuation Spectroscopy: A New Approach for Studying Low-Dimensional Molecular Metals*, ChemPhysChem 12 (2011), pp. 1222–1245.
 - [357] J. Müller, J. Brandenburg, D. Schweitzer, and J.A. Schlueter, *Different electronic transport regimes in the quasi-two-dimensional organic conductors κ -(BEDT-TTF)₂X*, phys. stat. sol. (b) 249 (2012), pp. 957–961.
 - [358] I. Kézsmárki, Y. Shimizu, G. Mihály, Y. Tokura, K. Kanoda, and G. Saito, *Depressed Charge Gap in the Triangular-Lattice Mott Insulator κ -(ET)₂Cu₂(CN)₃*, Phys. Rev. B 74 (2006), 201101.
 - [359] S. Elsässer, D. Wu, M. Dressel, and J.A. Schlueter, *Power-law dependence of the optical conductivity observed in the quantum spin-liquid compound κ -(BEDT-TTF)₂Cu₂(CN)₃*, Phys. Rev. B 86 (2012), 155150.
 - [360] Y. Shimizu, T. Hiramatsu, M. Maesato, A. Otsuka, H. Yamochi, A. Ono, M. Itoh, M. Yoshida, M. Takigawa, Y. Yoshida, and G. Saito, *Pressure-Tuned Exchange Coupling of a Quantum Spin Liquid in the Molecular Triangular Lattice κ -ET₂Ag₂(CN)₃*, Phys. Rev. Lett. 117 (2016), 107203.
 - [361] J. Jeftic, U. Kindler, H. Spiering, and A. Hauser, *Helium gas pressure cell for pressures up to 1 kbar (0.1 GPa) in conjunction with the cold head of a closed-cycle He refrigerator*, Meas. Sci. Technol. 8 (1997), pp. 479–483.
 - [362] Y. Kurosaki, Y. Shimizu, K. Miyagawa, K. Kanoda, and G. Saito, Phys. Rev. Lett. 95 (2005), 177001.
 - [363] T. Furukawa, K. Kobashi, Y. Kurosaki, K. Miyagawa, and K. Kanoda, *Quasi-continuous transition from a Fermi liquid to a spin liquid in κ -(ET)₂Cu₂(CN)₃*, Nat. Commun. 9 (2018), 307.
 - [364] Y. Saito, R. Rösslhuber, A. Löhle, M.S. Alonso, A. Pustogow, A. Kawamoto, and M. Dressel, *Bandwidth-tuning from the insulating Mott quantum spin liquid to the superconducting Fermi liquid via chemical substitution in κ -[(BEDT-TTF)_{1-x}(BEDT-STF)_x]₂Cu₂(CN)₃*, arXiv:1911.06766 (2020).
 - [365] B. Knoll and F. Keilmann, *Near-field probing of vibrational absorption for chemical microscopy*, Nature 399 (1999), pp. 134–137.
 - [366] R. Hillenbrand and F. Keilmann, *Complex Optical Constants on a Subwavelength Scale*, Phys. Rev. Lett. 85 (2000), pp. 3029–3032.
 - [367] F. Keilmann and R. Hillenbrand, *Near-field microscopy by elastic light scattering from a tip*, Phil. Trans. R. Soc. Lond. A 362 (2004), pp. 787–805.
 - [368] M.M. Qazilbash, M. Brehm, B.G. Chae, P.C. Ho, G.O. Andreev, B.J. Kim, S.J. Yun, A.V. Balatsky, M.B. Maple, F. Keilmann, H.T. Kim, and D.N. Basov, *Mott transition in VO₂ revealed by infrared spectroscopy and nano-imaging*, Science 318 (2007), pp. 1750–

- 1753.
- [369] M.M. Qazilbash, M. Brehm, G.O. Andreev, A. Frenzel, P.C. Ho, B.G. Chae, B.J. Kim, S.J. Yun, H.T. Kim, A.V. Balatsky, O.G. Shpyrko, M.B. Maple, F. Keilmann, and D.N. Basov, *Infrared spectroscopy and nano-imaging of the insulator-to-metal transition in vanadium dioxide*, Phys. Rev. B 79 (2009), 075107.
 - [370] M.M. Qazilbash, A. Tripathi, A.A. Schafgans, B.J. Kim, H.T. Kim, Z. Cai, M.V. Holt, J.M. Maser, F. Keilmann, O.G. Shpyrko, and D.N. Basov, *Nanoscale imaging of the electronic and structural transitions in vanadium dioxide*, Phys. Rev. B 83 (2011), 165108.
 - [371] T.J. Huffman, D.J. Lahneman, S.L. Wang, T. Slusar, B.J. Kim, H.T. Kim, and M.M. Qazilbash, *Highly repeatable nanoscale phase coexistence in vanadium dioxide films*, Phys. Rev. B 97 (2018), 085146.
 - [372] H.T. Stinson, A. Sternbach, O. Najera, R. Jing, A.S. Mcleod, T.V. Slusar, A. Mueller, L. Anderegg, H.T. Kim, M. Rozenberg, and D.N. Basov, *Imaging the nanoscale phase separation in vanadium dioxide thin films at terahertz frequencies*, Nat. Commun. 9 (2018), 3604.
 - [373] O. Iakutkina, W. Luo, Y. Saito, A. Kuzmenko, and M. Dressel unpublished.
 - [374] S. Kirkpatrick, *Percolation and Conduction*, Rev. Mod. Phys. 45 (1973), pp. 574–588.
 - [375] D. Stauffer and A. Aharony *Introduction to Percolation Theory*, 2nd ed. CRC Press, Boca Raton, Florida, 1994.
 - [376] B. Bollobás and O. Riordan *Percolation*, Cambridge University Press, Cambridge, 2006.
 - [377] S. Torquato *Random Heterogeneous Materials*, Springer-Verlag, New York, 2002.
 - [378] T.C. Choy *Effective Medium Theory: Principles and Applications*, 2nd ed. Oxford University Press, Oxford, 2015.
 - [379] A.L. Efros and B.I. Shklovskii, *Nonmonotonic relaxation kinetics of confined systems*, phys. stat. sol. (b) 76 (1976), pp. 475–485.
 - [380] D.J. Bergman, *The dielectric constant of a composite material—A problem in classical physics*, Phys. Rep. 43 (1978), pp. 377–407.
 - [381] M. Hövel, B. Gompf, and M. Dressel, *Dielectric properties of ultrathin metal films around the percolation threshold*, Phys. Rev. B 81 (2010), 035402.
 - [382] ———, *Electrodynamics of ultrathin gold films at the insulator-to-metal transition*, Thin Solid Films 519 (2011), pp. 2955–2958.
 - [383] A. Pustogow, R. Rösslhuber, Y. Tan, E. Uykur, M. Wenzel, A. Böhme, A. Löhle, Y. Saito, A. Kawamoto, R. Hübner, J.A. Schlueter, V. Dobrosavljević, and M. Dressel, *Low-Temperature Dielectric Anomalies at the Mott Insulator-Metal Transition*, arXiv:1907.04437 (2019).
 - [384] T.G. Castner, N.K. Lee, G.S. Cieloszyk, and G.L. Salinger, *Dielectric Anomaly and the Metal-Insulator Transition in n-Type Silicon*, Phys. Rev. Lett. 34 (1975), pp. 1627–1630.
 - [385] T.F. Rosenbaum, R.F. Milligan, M.A. Paalanen, G.A. Thomas, R.N. Bhatt, and W. Lin, *Metal-insulator transition in a doped semiconductor*, Phys. Rev. B 27 (1983), pp. 7509–7523.
 - [386] M. Hering, M. Scheffler, M. Dressel, and H.v. Löhneysen, *Signature of electronic correlations in the optical conductivity of the doped semiconductor Si:P*, Phys. Rev. B 75 (2007), 205203.
 - [387] H.v. Löhneysen, *The metal-insulator transition in Si:P*, in *Festkörperprobleme Vol. 30*, U. Rössler ed., Springer-Verlag, Berlin, Heidelberg, 1990, pp. 95–111.
 - [388] ———, *Disorder, electron-electron interactions and the metal-insulator transition in heavily doped Si:P*, in *Advances in Solid State Physics Vol. 40*, B. Kramer ed., Springer-Verlag, Berlin, Heidelberg, 2000, pp. 143–167.
 - [389] ———, *Electron-electron interactions and the metal-insulator transition in heavily doped silicon*, Annalen der Physik 523 (2011), pp. 599–611.
 - [390] J. Merino and R.H. McKenzie, *Transport properties of strongly correlated metals: A dynamical mean-field approach*, Phys. Rev. B 61 (2000), pp. 7996–8008.
 - [391] M.J. Rozenberg, G. Kotliar, H. Kajueter, G.A. Thomas, D.H. Rapkine, J.M. Honig, and P. Metcalf, *Optical Conductivity in Mott-Hubbard Systems*, Phys. Rev. Lett. 75 (1995),

- pp. 105–108.
- [392] J. Merino, M. Dumm, N. Drichko, M. Dressel, and R.H. McKenzie, *Quasiparticles at the Verge of Localization near the Mott Metal-Insulator Transition in a Two-Dimensional Material*, Phys. Rev. Lett. 100 (2008), 086404.
 - [393] A.C. Jacko, J.O. Færestad, and B.J. Powell, *A unified explanation of the Kadowaki-Woods ratio in strongly correlated metals*, Nat. Phys. 5 (2009), pp. 422–425.
 - [394] M. Pinterić, S. Tomić, M. Prester, D. Drobac, and K. Maki, *Influence of internal disorder on the superconducting state in the organic layered superconductor κ -(BEDT-TTF)₂Cu[N(CN)₂]Br*, Phys. Rev. B 66 (2002), 174521.
 - [395] H. Ito, T. Ishiguro, M. Kubota, and G. Saito, *Metal-Nonmetal Transition and Superconductivity Localization in the Two-Dimensional Conductor κ -(BEDT-TTF)₂Cu[N(CN)₂]Cl under Pressure*, J. Phys. Soc. Jpn. 65 (1996), pp. 2987–2993.
 - [396] K. Kanoda, *Recent progress in NMR studies on organic conductors*, Hyperfine Interact. 104 (1997), pp. 235–249.
 - [397] D. Faltermeier, J. Barz, M. Dumm, M. Dressel, N. Drichko, B. Petrov, V. Semkin, R. Vlasova, C. Mezière, and P. Batail, *Bandwidth-controlled Mott transition in κ -(BEDT-TTF)₂Cu[N(CN)₂]Br_xCl_{1-x}: Optical studies of localized charge excitations*, Phys. Rev. B 76 (2007), 165113.
 - [398] M. Dumm, D. Faltermeier, N. Drichko, M. Dressel, C. Mezière, and P. Batail, *Bandwidth-controlled Mott transition in κ -(BEDT-TTF)₂Cu[N(CN)₂]Br_xCl_{1-x}: Optical studies of correlated carriers*, Phys. Rev. B 79 (2009), 195106.
 - [399] M. Dressel, D. Faltermeier, M. Dumm, N. Drichko, B. Petrov, V. Semkin, R. Vlasova, C. Mézière, and P. Batail, *Disentangling the conductivity spectra of two-dimensional organic conductors*, Physica B 404 (2009), pp. 541–544.
 - [400] K. Kadowaki and S. Woods, *Universal relationship of the resistivity and specific heat in heavy-Fermion compounds*, Solid State Commun. 58 (1986), pp. 507–509.
 - [401] K. Miyake, T. Matsuura, and C. Varma, *Relation between resistivity and effective mass in heavy-fermion and A15 compounds*, Solid State Commun. 71 (1989), pp. 1149–1153.
 - [402] Y. Maeno, K. Yoshida, H. Hashimoto, S. Nishizaki, S.i. Ikeda, M. Nohara, T. Fujita, A.P. Mackenzie, N.E. Hussey, J.G. Bednorz, and F. Lichtenberg, *Two-Dimensional Fermi Liquid Behavior of the Superconductor Sr 2RuO 4*, J. Phys. Soc. Jpn. 66 (1997), pp. 1405–1408.
 - [403] M. Dressel and G. Grüner *Electrodynamics of Solids*, Cambridge University Press, Cambridge, 2002.
 - [404] D.N. Basov, R.D. Averitt, D. Marelvan der , M. Dressel, and K. Haule, *Electrodynamics of correlated electron materials*, Rev. Mod. Phys. 83 (2011), pp. 471–541.
 - [405] M. Dressel, *Quantum criticality in organic conductors? Fermi liquid versus non-Fermi-liquid behaviour*, J. Phys.: Condens. Matter 23 (2011), 293201.
 - [406] B.J. Powell and R.H. McKenzie, *Half-Filled Layered Organic Superconductors and the Resonating-Valence-Bond Theory of the Hubbard-Heisenberg Model*, Phys. Rev. Lett. 94 (2005), 047004.
 - [407] N.W. Ashcroft and N.D. Mermin *Solid State Physics*, Saunders College, Philadelphia, 1976.
 - [408] A. Abrikosov, L. Gorkov, and I. Dzyaloshinski *Methods of Quantum Field Theory in Statistical Physics*, Prentice-Hall, Englewood, 1963.
 - [409] D. Pines and P. Nozières *The Theory of Quantum Liquids*, Vol. 1, Addison-Wesley, Reading, 1966.
 - [410] D.L. Maslov and A.V. Chubukov, *Optical response of correlated electron systems*, Rep. Progr. Phys. 80 (2017), 026503.
 - [411] L.D. Landau, *The Theory of a Fermi Liquid*, Sov. Phys. JETP 3 (1957), pp. 920–925.
 - [412] R.N. Gurzhi, *Mutual electron correlations in metal optics*, Sov. Phys. JETP 35 (1959), pp. 673–675.
 - [413] A. Rosch, *Optical conductivity of clean metals*, Ann. Phys. (Leipzig) 15 (2006), pp. 526–534.

- [414] C. Berthod, J. Mravlje, X. Deng, R. Žitko, D. van der Marel, and A. Georges, *Non-Drude universal scaling laws for the optical response of local Fermi liquids*, Phys. Rev. B 87 (2013), 115109.
- [415] U. Nagel, T. Uleksin, T. Rööm, R.P.S.M. Lobo, P. Lejay, C.C. Homes, J.S. Hall, A.W. Kinross, S.K. Purdy, T. Munsie, T.J. Williams, G.M. Luke, and T. Timusk, *Optical spectroscopy shows that the normal state of URu₂Si₂ is an anomalous Fermi liquid*, Proc. Nat. Acad. Sci. 109 (2012), pp. 19161–19165.
- [416] S.I. Mirzaei, D. Stricker, J.N. Hancock, C. Berthod, A. Georges, E. Heumenan , M.K. Chan, X. Zhao, Y. Li, M. Greven, N. Barišić, and D. Marelvan der , *Spectroscopic evidence for Fermi liquid-like energy and temperature dependence of the relaxation rate in the pseudogap phase of the cuprates*, Proc. Nat. Acad. Sci. 110 (2013), pp. 5774–5778.
- [417] D. Stricker, J. Mravlje, C. Berthod, R. Fittipaldi, A. Vecchione, A. Georges, and D. Marelvan der , *Optical Response of Sr₂RuO₄ Reveals Universal Fermi-Liquid Scaling and Quasiparticles Beyond Landau Theory*, Phys. Rev. Lett. 113 (2014), 087404.
- [418] A. Tytarenko, Y. Huang, A. Visserde , S. Johnston, and E. Heumenan , *Direct observation of a Fermi liquid-like normal state in an iron-pnictide superconductor*, Sci. Rep. 5 (2015), 12421.
- [419] T. Sasaki, I. Ito, N. Yoneyama, N. Kobayashi, N. Hanasaki, H. Tajima, T. Ito, and Y. Iwasa, *Electronic correlation in the infrared optical properties of the quasi-two-dimensional κ -type BEDT-TTF dimer system*, Phys. Rev. B 69 (2004), 064508.
- [420] A. Pustogow, *Unveiling Electronic Correlations in Layered Molecular Conductors by Optical Spectroscopy*; Dissertation Universität Stuttgart, 2017.
- [421] A. Pustogow, Y. Saito, A. Löhle, M. Sanz Alonso, A. Kawamoto, V. Dobrosavljević, M. Dressel, and S. Fratini, *Rise and Fall of Landau’s Quasiparticles While Approaching the Mott Transition*, (2020), unpublished.
- [422] V.J. Emery and S.A. Kivelson, *Superconductivity in Bad Metals*, Phys. Rev. Lett. 74 (1995), pp. 3253–3256.
- [423] S.A. Hartnoll, *Theory of universal incoherent metallic transport*, Nature Phys. 11 (2015), pp. 54–61.
- [424] O. Gunnarsson, M. Calandra, and J.E. Han, *Colloquium: Saturation of electrical resistivity*, Rev. Mod. Phys. 75 (2003), pp. 1085–1099.
- [425] N.E. Hussey, K. Takenaka, and H. Takagi, *Universality of the Mott–Ioffe–Regel limit in metals*, Phil. Mag. 84 (2004), pp. 2847–2864.
- [426] L.B. Ioffe and A.R. Regel, *Non-crystalline, amorphous and liquid electronic semiconductors*, Prog. Semicond. 4 (1960), pp. 237–291.
- [427] N.F. Mott, *Conduction in non-crystalline systems IX. the minimum metallic conductivity*, The Philosophical Magazine: A Journal of Theoretical Experimental and Applied Physics 26 (1972), pp. 1015–1026.
- [428] W. Li, A. Pustogow, R. Kato, and M. Dressel, *Transition of a pristine Mott insulator to a correlated Fermi liquid: Pressure-dependent optical investigations of a quantum spin liquid*, Phys. Rev. B 99 (2019), 115137.
- [429] K. Takenaka, M. Tamura, N. Tajima, H. Takagi, J. Nohara, and S. Sugai, *Collapse of Coherent Quasiparticle States in θ -(BEDT-TTF)₂I₃ Observed by Optical Spectroscopy*, Phys. Rev. Lett. 95 (2005), 227801.
- [430] B. Salameh, A. Nothardt, E. Balthes, W. Schmidt, D. Schweitzer, J. Stremper, B. Hinrichsen, M. Jansen, and D.K. Maude, *Electronic properties of the organic metals θ -(BEDT-TTF)₂I₃ and θ_T -(BEDT-TTF)₂I₃*, Phys. Rev. B 75 (2007), 054509.
- [431] T. Terashima, S. Uji, H. Aoki, M. Tamura, M. Kinoshita, and M. Tokumoto, *Three-dimensional fermi surface in θ -(BEDT-TTF)₂I₃*, Solid State Commun. 91 (1994), pp. 595–598.
- [432] A. Nothardt, E. Balthes, B. Salameh, W. Schmidt, D. Schweitzer, J. Stremper, B. Keimer, and D.K. Maude, *Quantum Oscillation Measurements on the Organic Superconductor θ -(BEDT-TTF)₂I₃*, Materials Science (Poland) 22 (2004), p. 299.
- [433] A. Nothardt, E. Balthes, W. Schmidt, B. Salameh, D. Schweitzer, J. Stremper, and D.

- Maude, *Investigations of Quantum Oscillations in θ - and θ_T -(BEDT-TTF) $_2$ I $_3$* , J. Low Temp. Phys. 142 (2006), pp. 539–542.
- [434] M. Tamura, K. Yakushi, H. Kuroda, A. Kobayashi, R. Kato, and H. Kobayashi, *Temperature Dependence of the Polarized Reflectance Spectra of the θ -Type of Bis(ethylenedithio)tetrathiafulvalenium Triiodide θ -(BEDT-TTF) $_2$ I $_3$: Estimation of Band Parameters*, J. Phys. Soc.Jpn. 57 (1988), pp. 3239–3247.
- [435] S. Fratini, S. Ciuchi, and D. Mayou, *Phenomenological model for charge dynamics and optical response of disordered systems: Application to organic semiconductors*, Phys. Rev. B 89 (2014), 235201.
- [436] L.V. Delacrétaz, B. Goutéraux, S.A. Hartnoll, and A. Karlsson, *Bad Metals from Fluctuating Density Waves*, SciPost Phys. 3 (2017), p. 025.
- [437] D.N. Basov and A.V. Chubukov, *Manifesto for a higher T_c* , Nat. Phys. 7 (2011), pp. 272–276.
- [438] O. Gunnarsson and K. Vafayi, *Comment on “Collapse of Coherent Quasiparticle States in θ -(BEDT-TTF) $_2$ I $_3$ Observed by Optical Spectroscopy”*, Phys. Rev. Lett. 98 (2007), 219802.
- [439] M.M. Radonjić, D. Tanasković, V. Dobrosavljević, and K. Haule, *Influence of disorder on incoherent transport near the Mott transition*, Phys. Rev. B 81 (2010), 075118.
- [440] T. Sasaki, *Mott-Anderson Transition in Molecular Conductors: Influence of Randomness on Strongly Correlated Electrons in the κ -(BEDT-TTF) $_2$ X System*, Crystals 2 (2012), pp. 374–392.
- [441] C. Walsh, P. Sémon, D. Poulin, G. Sordi, and A.M.S. Tremblay, *Local Entanglement Entropy and Mutual Information across the Mott Transition in the Two-Dimensional Hubbard Model*, Phys. Rev. Lett. 122 (2019), p. 067203.
- [442] ———, *Thermodynamic and information-theoretic description of the Mott transition in the two-dimensional Hubbard model*, Phys. Rev. B 99 (2019), 075122.
- [443] G. Sordi, C. Walsh, P. Sémon, and A.M.S. Tremblay, *Specific heat maximum as a signature of Mott physics in the two-dimensional Hubbard model*, Phys. Rev. B 100 (2019), 121105.
- [444] P.A. Lee and T.V. Ramakrishnan, *Disordered electronic systems*, Rev. Mod. Phys. 57 (1985), pp. 287–337.
- [445] D. Belitz and T.R. Kirkpatrick, *The Anderson-Mott transition*, Rev. Mod. Phys. 66 (1994), pp. 261–380.
- [446] K. Byczuk, W. Hofstetter, and D. Vollhardt, *Mott-Hubbard Transition versus Anderson Localization in Correlated Electron Systems with Disorder*, Phys. Rev. Lett. 94 (2005), 056404.
- [447] A.M. Finkel’shtein, *Influence of Coulomb interaction on the properties of disordered metals*, Sov. Phys. JETP (1983), pp. 97–108.
- [448] C. Castellani, C. Di Castro, P.A. Lee, and M. Ma, *Interaction-driven metal-insulator transitions in disordered fermion systems*, Phys. Rev. B 30 (1984), pp. 527–543.
- [449] M.A. Tusch and D.E. Logan, *Interplay between disorder and electron interactions in a $d=3$ site-disordered Anderson-Hubbard model: A numerical mean-field study*, Phys. Rev. B 48 (1993), pp. 14843–14858.
- [450] S.V. Kravchenko and M.P. Sarachik, *Metal-insulator transition in two-dimensional electron systems*, Rep. Progr. Phys. 67 (2004), pp. 1–44.
- [451] E. Abrahams (ed.) *50 Years of Anderson Localization*, World Scientific, Singapore, 2010.
- [452] V. Dobrosavljević and G. Kotliar, *Mean Field Theory of the Mott-Anderson Transition*, Phys. Rev. Lett. 78 (1997), pp. 3943–3946.
- [453] V. Dobrosavljević, A.A. Pastor, and B.K. Nikolić, *Typical medium theory of Anderson localization: A local order parameter approach to strong-disorder effects*, EPL (Europhysics Letters) 62 (2003), pp. 76–82.
- [454] M.C.O. Aguiar, V. Dobrosavljević, E. Abrahams, and G. Kotliar, *Effects of disorder on the non-zero temperature Mott transition*, Phys. Rev. B 71 (2005), 205115.
- [455] H. Bragança, M.C.O. Aguiar, J. Vučićević, D. Tanasković, and V. Dobrosavljević, *Ander-*

- son localization effects near the Mott metal-insulator transition, Phys. Rev. B 92 (2015), 125143.
- [456] L.K. Montgomery, *Chemical synthesis and crystal growth*, in *Organic Conductors*, , in *Organic Conductors*, ed. J. Farges J. Farges ed., Marcel Dekker, New York, 1994, pp. 138–145.
- [457] M. Lang, C. Strack, C. Akinci, B. Wolf, J.A. Schlueter, J. Wosnitzer, D. Schweitzer, J. Schreuer, and L. Wiehl, *Resistivity Studies on Different Variants of κ -(BEDT-TTF)₂Cu[N(CN)₂]Br: Evidence for Disorder and /or Defect-Induced Inelastic Scattering Contributions*, Journal of Low Temperature Physics 142 (2006), pp. 191–197.
- [458] M. Pinterić, M. Čulo, O. Milat, M. Basletić, B. Korin-Hamzić, E. Tafra, A. Hamzić, T. Ivek, T. Peterseim, K. Miyagawa, K. Kanoda, J.A. Schlueter, M. Dressel, and S. Tomić, *Anisotropic charge dynamics in the quantum spin-liquid candidate κ -(BEDT-TTF)₂Cu₂(CN)₃*, Phys. Rev. B 90 (2014), 195139.
- [459] X. Su, F. Zuo, J.A. Schlueter, M.E. Kelly, and J.M. Williams, *Structural disorder and its effect on the superconducting transition temperature in the organic superconductor κ -(BEDT-TTF)₂Cu[N(CN)₂]Br*, Phys. Rev. B 57 (1998), pp. 14056–14059.
- [460] T.F. Stalcup, J.S. Brooks, and R.C. Haddon, *Temporal processes in a polymeric anion-based organic superconductor*, Phys. Rev. B 60 (1999), pp. 9309–9312.
- [461] M.A. Tanatar, T. Ishiguro, T. Kondo, and G. Saito, *Nonmetal to metal crossover and ethylene ordering in the organic superconductor κ -(BEDT-TTF)₂Cu[N(CN)₂]Br*, Phys. Rev. B 59 (1999), pp. 3841–3844.
- [462] K. Saito, H. Akutsu, and M. Sorai, *Glass transition in the organic superconductor with the highest T_c under ambient pressure, κ -(ET)₂Cu[N(CN)₂]Br*, Solid State Commun. 111 (1999), pp. 471–475.
- [463] J. Müller, M. Lang, F. Steglich, J.A. Schlueter, A.M. Kini, and T. Sasaki, *Evidence for structural and electronic instabilities at intermediate temperatures in κ -(BEDT-TTF)₂X for X = Cu[N(CN)₂]Cl, Cu[N(CN)₂]Br and Cu(NCS)₂: Implications for the phase diagram of these quasi-two-dimensional organic superconductors*, Phys. Rev. B 65 (2002), 144521.
- [464] A.U.B. Wolter, R. Feyerherm, E. Dudzik, S. Süllow, C. Strack, M. Lang, and D. Schweitzer, *Determining ethylene group disorder levels in κ -(BEDT-TTF)₂ Cu[N(CN)₂]Br*, Phys. Rev. B 75 (2007), 104512.
- [465] K. Kanoda, K. Akiba, K. Suzuki, T. Takahashi, and G. Saito, *Magnetic-Field Penetration Depth of an Organic Superconductor: Evidence for Anisotropic Superconductivity of Gapless Nature*, Phys. Rev. Lett. 65 (1990), pp. 1271–1274.
- [466] K. Kanoda, Y. Tsubokura, K. Ikeda, T. Takahashi, N. Matsukawa, G. Saito, H. Mori, B. Hilti, and J. Zambounis, *Magnetic penetration depth of the κ -phase family of organic superconductors*, Synth. Met. 55-57 (1993), pp. 2865–2870.
- [467] D. Achkir, M. Poirier, C. Bourbonnais, G. Quirion, C. Lenoir, P. Batail, and D. Jérôme, *Microwave surface impedance of κ -(BEDT-TTF)₂Cu(NCS)₂, where BEDT-TTF is bis(ethylenedithio)tetrathiafulvalene: Evidence for unconventional superconductivity*, Phys. Rev. B 47 (1993), pp. 11595–11598.
- [468] L. Le, G. Luke, B. Sternlieb, W. Wu, U. Y.J., J. Brewer, T. Riseman, C. Stronach, G. Saito, H. Yamochi, H. Wang, A. Kini, K. Carlson, and W. J.M., *Muon-Spin-Relaxation Measurements of Magnetic Penetration Depth in Organic Superconductors (BEDT-TTF)₂X: X = Cu(NCS)₂ and Cu[N(CN)₂]Br*, Phys. Rev. Lett. 68 (1992), pp. 1923–1926.
- [469] D. Harshman, R. Kleiman, R. Haddon, S. Chichester-Hicks, M. Kaplan, L. Rupp Jr., T. Pfiz, D. Williams, and D. Mitzi, *Magnetic Penetration Depth in the Organic Superconductor κ -(BEDT-TTF)₂Cu(NCS)₂*, Phys. Rev. Lett. 64 (1990), pp. 1923–1926.
- [470] M. Lang, N. Toyota, T. Sasaki, and H. Sato, *Magnetic Penetration Depth of κ -(BEDT-TTF)₂Cu(NCS)₂: Strong Evidence for Conventional Cooper Pairing*, Phys. Rev. Lett. 69 (1992), pp. 1443–1446.
- [471] M. Dressel, O. Klein, G. Grüner, K. Carlson, H. Wang, and J. Williams, *Electro-*

- dynamics of the organic superconductors κ -(BEDT-TTF)₂Cu(NCS)₂ and κ -(BEDT-TTF)₂Cu[N(CN)₂]Br*, Phys. Rev. B 50 (1994), pp. 13603–13615.
- [472] M. Lang, *Quasi-Twodimensional Organic Superconductors*, Superconduct. Rev. 2 (1996), pp. 1–115.
- [473] M. Pinterić, S. Tomić, M. Prester, D. Drobac, O. Milat, K. Maki, D. Schweitzer, I. Heinen, and W. Strunz, *Probing the order parameter of the layered organic superconductor κ -(BEDTTTF)₂Cu[N(CN)₂]Br by ac susceptibility measurements*, Phys. Rev. B 61 (2000), pp. 7033–7038.
- [474] T. Sasaki, H. Oizumi, Y. Honda, N. Yoneyama, and N. Kobayashi, *Suppression of Superconductivity by Nonmagnetic Disorder in Organic Superconductor κ -(BEDT-TTF)₂Cu(NCS)₂*, J. Phys. Soc. Jpn. 80 (2011), 104703.
- [475] N. Yoneyama, T. Sasaki, N. Kobayashi, K. Furukawa, and T. Nakamura, *X-ray irradiation effect on magnetic properties of Dimer–Mott insulators: κ -(BEDT-TTF)₂Cu[N(CN)₂]Cl and β' -(BEDT-TTF)₂ICl₂*, Physica B 405 (2010), pp. S244–S246.
- [476] T. Sasaki, K. Sano, H. Sugawara, N. Yoneyama, and N. Kobayashi, *Influence of randomness on the Mott transition in κ -(BEDT-TTF)₂X*, phys. stat. sol. (b) 249 (2012), pp. 947–952.
- [477] T. Sasaki, H. Oizumi, N. Yoneyama, N. Kobayashi, and N. Toyota, *X-ray Irradiation-Induced Carrier Doping Effects in Organic Dimer-Mott Insulators*, J. Phys. Soc. Jpn. 76 (2007), 123701.
- [478] M. Matsumoto, H. Kato, Y. Kuwata, A. Kawamoto, N. Matsunaga, and K. Nomura, *Effect of X-ray Irradiation on the Organic Superconductor κ -(BEDT-TTF)₂Cu(NCS)₂ Probed by ¹³C-NMR*, J. Phys. Soc. Jpn. 81 (2012), 114709.
- [479] J.G. Analytis, A. Ardavan, S.J. Blundell, R.L. Owen, E.F. Garman, C. Jaynes, and B.J. Powell, *Effect of Irradiation-Induced Disorder on the Conductivity and Critical Temperature of the Organic Superconductor κ -(BEDT-TTF)₂Cu(SCN)₂*, Phys. Rev. Lett. 96 (2006), 177002.
- [480] K. Sano, T. Sasaki, N. Yoneyama, and N. Kobayashi, *Electron Localization near the Mott Transition in the Organic Superconductor κ -(BEDT-TTF)₂Cu[N(CN)₂]Br*, Phys. Rev. Lett. 104 (2010), 217003.
- [481] S. Dolanski Babić, N. Biškup, S. Tomić, and D. Schweitzer, *Electrical transport in the organic superconductor β -(BEDTTTF)₂AuI₂ [with BEDT-TTF = bis(ethylenedithio)tetrathiafulvalene]: Influence of x-ray-induced defects on the normal phase and superconducting ground state*, Phys. Rev. B 46 (1992), pp. 11765–11771.
- [482] T. Sasaki, N. Yoneyama, Y. Nakamura, N. Kobayashi, Y. Ikemoto, T. Moriwaki, and H. Kimura, *Optical Probe of Carrier Doping by X-Ray Irradiation in the Organic Dimer Mott Insulator κ -(BEDT-TTF)₂Cu[N(CN)₂]Cl*, Phys. Rev. Lett. 101 (2008), 206403.
- [483] T. Vojta, *Rare region effects at classical, quantum and nonequilibrium phase transitions*, J. Phys. A 39 (2006), pp. R143–R205.
- [484] V.N. Krivoruchko, *The Griffiths phase and the metal-insulator transition in substituted manganites (Review Article)*, Low Temperature Physics 40 (2014), pp. 586–599.
- [485] D. Tanasković, E. Miranda, and V. Dobrosavljević, *Effective model of the electronic Griffiths phase*, Phys. Rev. B 70 (2004), 205108.
- [486] E.C. Andrade, E. Miranda, and V. Dobrosavljević, *Electronic Griffiths Phase of the $d = 2$ Mott Transition*, Phys. Rev. Lett. 102 (2009), 206403.
- [487] R. Yamamoto, T. Furukawa, K. Miyagawa, T. Sasaki, K. Kanoda, and T. Itou, *Electronic Griffiths Phase in Disordered Mott-Transition Systems*, Phys. Rev. Lett. 124 (2020), 046404.
- [488] S. Sasaki, S. Iguchi, N. Yoneyama, and T. Sasaki, *X-ray Irradiation Effect on the Dielectric Charge Response in the Dimer–Mott Insulator κ -(BEDT-TTF)₂Cu₂(CN)₃*, J. Phys. Soc. Jpn. 84 (2015), 074709.
- [489] Y. Saito, T. Minamidate, A. Kawamoto, N. Matsunaga, and K. Nomura, *Site-specific ¹³C NMR study on the locally distorted triangular lattice of the organic conductor κ -(BEDT-TTF)₂Cu₂(CN)₃*, Phys. Rev. B 98 (2018), 205141.

- [490] K. Sedlmeier, S. Elsässer, D. Neubauer, R. Beyer, D. Wu, T. Ivek, S. Tomić, J.A. Schlueter, and M. Dressel, *Absence of charge order in the dimerized κ -phase BEDT-TTF salts*, Phys. Rev. B 86 (2012), 245103.
- [491] M. Čulo, E. Tafra, M. Basletić, S. Tomić, A. Hamzić, B. Korin-Hamzić, M. Dressel, and J. Schlueter, *Two-dimensional variable range hopping in the spin-liquid candidate κ -(BEDT-TTF)₂Cu₂(CN)₃*, Physica B 460 (2015), pp. 208–210.
- [492] M. Čulo, E. Tafra, B. Mihaljević, M. Basletić, M. Kuveždić, T. Ivek, A. Hamzić, S. Tomić, T. Hiramatsu, Y. Yoshida, G. Saito, J.A. Schlueter, M. Dressel, and B. Korin-Hamzić, *Hall effect study of the κ -(ET)₂X family: Evidence for Mott-Anderson localization*, Phys. Rev. B 99 (2019), 045114.
- [493] L. Pauling, *The structure and entropy of ice and of other crystals with some randomness of atomic arrangement*, J. Am. Chem. Soc. 57 (1935), pp. 2680–2684.
- [494] P. Anderson, *Resonating valence bonds: A new kind of insulator?*, Mater. Res. Bull. 8 (1973), pp. 153–160.
- [495] P. Fazekas and P.W. Anderson, *On the ground state properties of the anisotropic triangular antiferromagnet*, Phil. Mag. 30 (1974), pp. 423–440.
- [496] K.H. Fischer and J.A. Hertz *Spin Glasses*, Cambridge Studies in Magnetism Cambridge University Press, Cambridge, 1991.
- [497] P. Contucci and C. Giardinà *Perspectives on Spin Glasses*, Cambridge University Press, Cambridge, 2012.
- [498] H.T. Diep *Frustrated Spin Systems*, 2nd edition World Scientific, Singapore, 2013.
- [499] J.A. Mydosh, *Spin glasses: redux: an updated experimental/materials survey*, Rep. Progr. Phys. 78 (2015), 052501.
- [500] L. Balents, *Spin liquids in frustrated magnets*, Nature 464 (2010), pp. 199–208.
- [501] L. Savary and L. Balents, *Quantum spin liquids: a review*, Rep. Progr. Phys. 80 (2017), 016502.
- [502] Y. Zhou, K. Kanoda, and T.K. Ng, *Quantum spin liquid states*, Rev. Mod. Phys. 89 (2017), p. 025003.
- [503] I. Kimchi, A. Nahum, and T. Senthil, *Valence Bonds in Random Quantum Magnets: Theory and Application to YbMgGaO₄*, Phys. Rev. X 8 (2018), 031028.
- [504] J. Knolle and R. Moessner, *A Field Guide to Spin Liquids*, Annu. Rev. Condens. Matter Phys. 10 (2019), pp. 451–472.
- [505] Y. Li, P. Gegenwart, and A.A. Tsirlin, *Spin liquids in geometrically perfect triangular antiferromagnets*, J. Phys.: Condens. Matter 32 (2020), 224004.
- [506] C. Broholm, R.J. Cava, S.A. Kivelson, D.G. Nocera, M.R. Norman, and T. Senthil, *Quantum spin liquids*, Science 367 (2020), eaay0668.
- [507] K. Kanoda and R. Kato, *Mott Physics in Organic Conductors with Triangular Lattices*, Annu. Rev. Condens. Matter Phys. 2 (2011), pp. 167–188.
- [508] M. Dressel and A. Pustogow, *Electrodynamics of quantum spin liquids*, J. Phys.: Condens. Matter 30 (2018), 203001.
- [509] J. Wen, S.L. Yu, S. Li, W. Yu, and J.X. Li, *Experimental identification of quantum spin liquids*, npj Quantum Mater. 4 (2019), 12.
- [510] Y. Li, H. Liao, Z. Zhang, S. Li, F. Jin, L. Ling, L. Zhang, Y. Zou, L. Pi, Z. Yang, J. Wang, Z. Wu, and Q. Zhang, *Gapless quantum spin liquid ground state in the two-dimensional spin-1/2 triangular antiferromagnet YbMgGaO₄*, Sci. Rep. 5 (2015), 16419.
- [511] A. Ribak, I. Silber, C. Baines, K. Chashka, Z. Salman, Y. Dagan, and A. Kanigel, *Gapless excitations in the ground state of 1T-TaS₂*, Phys. Rev. B 96 (2017), 195131.
- [512] J.R. Chamorro, T.T. Tran, and T.M. McQueen, *The Chemistry of Quantum Spin Liquids*, arXiv:2006.10882 (2020).
- [513] D.A. Huse and V. Elser, *Simple Variational Wave Functions for Two-Dimensional Heisenberg Spin-Antiferromagnets*, Phys. Rev. Lett. 60 (1988), pp. 2531–2534.
- [514] B. Bernu, C. Lhuillier, and L. Pierre, *Signature of Néel order in exact spectra of quantum antiferromagnets on finite lattices*, Phys. Rev. Lett. 69 (1992), pp. 2590–2593.
- [515] L. Capriotti, A.E. Trumper, and S. Sorella, *Long-Range Néel Order in the Triangular*

- Heisenberg Model*, Phys. Rev. Lett. 82 (1999), pp. 3899–3902.
- [516] R. Kaneko, S. Morita, and M. Imada, *Gapless Spin-Liquid Phase in an Extended Spin 1/2 Triangular Heisenberg Model*, J. Phys. Soc. Jpn. 83 (2014), 093707.
- [517] K. Watanabe, H. Kawamura, H. Nakano, and T. Sakai, *Quantum Spin-Liquid Behavior in the Spin-1/2 Random Heisenberg Antiferromagnet on the Triangular Lattice*, J. Phys. Soc. Jpn. 83 (2014), 034714.
- [518] T. Shimokawa, K. Watanabe, and H. Kawamura, *Static and dynamical spin correlations of the $S = \frac{1}{2}$ random-bond antiferromagnetic Heisenberg model on the triangular and kagome lattices*, Phys. Rev. B 92 (2015), 134407.
- [519] H.Q. Wu, S.S. Gong, and D.N. Sheng, *Randomness-induced spin-liquid-like phase in the spin- $\frac{1}{2}$ $J_1 - J_2$ triangular Heisenberg model*, Phys. Rev. B 99 (2019), 085141.
- [520] H. Kawamura and K. Uematsu, *Nature of the randomness-induced quantum spin liquids in two dimensions*, J. Phys.: Condens. Matter 31 (2019), 504003.
- [521] A.N. Vasil'ev, M.M. Markina, and E.A. Popova, *Spin gap in low-dimensional magnets (Review)*, Low Temp. Phys. 31 (2005), pp. 203–223.
- [522] Y. Shimizu, K. Miyagawa, K. Kanoda, M. Maesato, and G. Saito, *Spin Liquid State in an Organic Mott Insulator with a Triangular Lattice*, Phys. Rev. Lett. 91 (2003), 107001.
- [523] M. Pinterić, P. Lazić, A. Pustogow, T. Ivek, M. Kuveždić, O. Milat, B. Gumhalter, M. Basletić, M. Čulo, B. Korin-Hamzić, A. Löhle, R. Hübner, M. Sanz Alonso, T. Hiramatsu, Y. Yoshida, G. Saito, M. Dressel, and S. Tomić, *Anion effects on electronic structure and electrodynamic properties of the Mott insulator κ -(BEDT-TTF) $_2$ Ag $_2$ (CN) $_3$* , Phys. Rev. B 94 (2016), 161105.
- [524] T. Itou, A. Oyamada, S. Maegawa, M. Tamura, and R. Kato, *Quantum spin liquid in the spin-1/2 triangular antiferromagnet EtMe $_3$ Sb[Pd(dmit) $_2$] $_2$* , Phys. Rev. B 77 (2008), 104413.
- [525] T. Itou, A. Oyamada, S. Maegawa, and R. Kato, *Instability of a quantum spin liquid in an organic triangular-lattice antiferromagnet*, Nat. Phys. 6 (2010), pp. 673–676.
- [526] T. Isono, H. Kamo, A. Ueda, K. Takahashi, M. Kimata, H. Tajima, S. Tsuchiya, T. Terashima, S. Uji, and H. Mori, *Gapless Quantum Spin Liquid in an Organic Spin-1/2 Triangular-Lattice κ -H $_3$ (Cat-EDT-TTF) $_2$* , Phys. Rev. Lett. 112 (2014), 177201.
- [527] M. Shimozawa, K. Hashimoto, A. Ueda, Y. Suzuki, K. Sugii, S. Yamada, Y. Imai, R. Kobayashi, K. Itoh, S. Iguchi, M. Naka, S. Ishihara, H. Mori, T. Sasaki, and M. Yamashita, *Quantum-disordered state of magnetic and electric dipoles in an organic Mott system*, Nat. Commun. 8 (2017), 1821.
- [528] K. Nakamura, Y. Yoshimoto, and M. Imada, *Ab initio two-dimensional multiband low-energy models of EtMe $_3$ Sb[Pd(dmit) $_2$] $_2$ and κ -(BEDT-TTF) $_2$ Cu(NCS) $_2$ with comparisons to single-band models*, Phys. Rev. B 86 (2012), 205117.
- [529] T. Komatsu, N. Matsukawa, T. Inoue, and G. Saito, *Realization of Superconductivity at Ambient Pressure by Band-Filling Control in κ -(BEDT-TTF) $_2$ Cu $_2$ (CN) $_3$* , J. Phys. Soc. Jpn. 65 (1996), pp. 1340–1354.
- [530] H.O. Jeschke, M. de Souza, R. Valentí, R.S. Manna, M. Lang, and J.A. Schlueter, *Temperature dependence of structural and electronic properties of the spin-liquid candidate κ -(BEDT-TTF) $_2$ Cu $_2$ (CN) $_3$* , Phys. Rev. B 85 (2012), 035125.
- [531] A. Jacko, L. Tocchio, H. Jeschke, R. Valentí, and H.O. Jeschke, *Importance of anisotropy in the spin-liquid candidate Me $_3$ EtSb[Pd(dmit) $_2$] $_2$* , Phys. Rev. B 88 (2013), 155139.
- [532] K. Oshima, T. Mori, H. Inokuchi, H. Urayama, H. Yamochi, and G. Saito, *Shubnikov-de Haas effect and the fermi surface in an ambient-pressure organic superconductor [bis-(ethylenedithiolo)tetrathiafulvalene] $_2$ Cu(CNS) $_2$* , Phys. Rev. B 38 (1988), pp. 938–941.
- [533] T. Hiramatsu, Y. Yoshida, G. Saito, A. Otsuka, H. Yamochi, M. Maesato, Y. Shimizu, H. Ito, and H. Kishida, *Quantum spin liquid: design of a quantum spin liquid next to a superconducting state based on a dimer-type ET Mott insulator*, J. Mater. Chem. C 3 (2015), pp. 1378–1388.
- [534] R. Kato and C. Hengbo, *Cation Dependence of Crystal Structure and Band Parameters in a Series of Molecular Conductors, β' -(Cation)[Pd(dmit) $_2$] $_2$ (dmit = 1,3-dithiole-2-*

- thione-4,5-dithiolate*), Crystals 2 (2012), pp. 861–874.
- [535] S. Yamashita, T. Yamamoto, Y. Nakazawa, M. Tamura, and R. Kato, *Galess spin liquid of an organic triangular compound evidenced by thermodynamic measurements*, Nat. Commun. 2 (2011), 275.
 - [536] S. Yamashita, Y. Nakazawa, A. Ueda, and H. Mori, *Thermodynamics of the quantum spin liquid state of the single-component dimer Mott system κ -H₃(Cat-EDT-TTF)₂*, Phys. Rev. B 95 (2017), 184425.
 - [537] T. Koretsune and C. Hotta, *Evaluating model parameters of the κ and β' -type Mott insulating organic solids*, Phys.Rev.B 89 (2014), 045102.
 - [538] L.F. Tocchio, A. Parola, C. Gros, and F. Becca, *Spin-liquid and magnetic phases in the anisotropic triangular lattice: The case of κ -(ET)₂X*, Phys. Rev. B 80 (2009), 064419.
 - [539] B. Kyung and A.M.S. Tremblay, *Mott Transition, Antiferromagnetism, and d-Wave Superconductivity in Two-Dimensional Organic Conductors*, Phys. Rev. Lett. 97 (2006), 046402.
 - [540] M. Laubach, R. Thomale, C. Platt, W. Hanke, and G. Li, *Phase diagram of the Hubbard model on the anisotropic triangular lattice*, Phys. Rev. B 91 (2015), 245125.
 - [541] A. Yamada, *Magnetic properties and Mott transition in the Hubbard model on the anisotropic triangular lattice*, Phys. Rev. B 89 (2014), 195108.
 - [542] J.H. Barrett, *Dielectric Constant in Perovskite Type Crystals*, Phys. Rev. 86 (1952), pp. 118–120.
 - [543] Y. Shimizu, K. Miyagawa, K. Kanoda, M. Maesato, and G. Saito, *Emergence of inhomogeneous moments from spin liquid in the triangular-lattice Mott insulator κ -(ET)₂Cu₂CN₃*, Phys. Rev. B 73 (2006), 140407.
 - [544] S. Yamashita, Y. Nakazawa, M. Oguni, Y. Oshima, H. Nojiri, Y. Shimizu, K. Miyagawa, and K. Kanoda, *Thermodynamic properties of a spin-1/2 spin-liquid state in a κ -type organic salt*, Nat. Phys. 4 (2008), pp. 459–462.
 - [545] T. Isono, S. Sugiura, T. Terashima, K. Miyagawa, K. Kanoda, and S. Uji, *Spin-lattice decoupling in a triangular-lattice quantum spin liquid*, Nat. Commun. 9 (2018), 1509.
 - [546] M. Yamashita, N. Nakata, Y. Kasahara, T. Sasaki, N. Yoneyama, N. Kobayashi, S. Fujimoto, T. Shibauchi, and Y. Matsuda, *Thermal-transport measurements in a quantum spin-liquid state of the frustrated triangular magnet κ -(BEDT-TTF)₂Cu₂(CN)₃*, Nat. Phys. 5 (2009), pp. 44–47.
 - [547] T. Osada, *Topological Insulator State due to Finite Spin–Orbit Interaction in an Organic Dirac Fermion System*, J. Phys. Soc. Jpn. 87 (2018), 075002.
 - [548] K. Riedl, R. Valentí, and S. Winter, *Critical spin liquid versus valence-bond glass in a triangular-lattice organic antiferromagnet*, Nat. Commun. 10 (2019), 2561.
 - [549] P. Prelovšek, K. Morita, T. Tohyama, and J. Herbrych, *Vanishing Wilson ratio as the hallmark of quantum spin-liquid models*, Phys. Rev. Research 2 (2020), 023024.
 - [550] Y. Okamoto, M. Nohara, H. Aruga-Katori, and H. Takagi, *Spin-Liquid State in the $S = 1/2$ Hyperkagome Antiferromagnet Na₄Ir₃O₈*, Phys. Rev. Lett. 99 (2007), 137207.
 - [551] G. Chen and Y.B. Kim, *Anomalous enhancement of the Wilson ratio in a quantum spin liquid: The case of Na₄Ir₃O₈*, Phys. Rev. B 87 (2013), 165120.
 - [552] T.K. Ng and P.A. Lee, *Power-Law Conductivity inside the Mott Gap: Application to κ -(BEDT-TTF)₂Cu₂(CN)₃*, Phys. Rev. Lett. 99 (2007), 156402.
 - [553] L.B. Ioffe and A.I. Larkin, *Gapless fermions and gauge fields in dielectrics*, Phys. Rev. B 39 (1989), pp. 8988–8999.
 - [554] A.C. Potter, T. Senthil, and P.A. Lee, *Mechanisms for sub-gap optical conductivity in Herbertsmithite*, Phys. Rev. B 87 (2013), 245106.
 - [555] A. Pustogow, Y. Saito, E. Zhukova, B. Gorshunov, R. Kato, T.H. Lee, S. Fratini, V. Dobrosavljević, and M. Dressel, *Low-Energy Excitations in Quantum Spin Liquids Identified by Optical Spectroscopy*, Phys. Rev. Lett. 121 (2018), 056402.
 - [556] M. Dressel, P. Lazić, A. Pustogow, E. Zhukova, B. Gorshunov, J.A. Schlueter, O. Milat, B. Gumhalter, and S. Tomić, *Lattice vibrations of the charge-transfer salt κ -(BEDT-TTF)₂Cu₂(CN)₃: Comprehensive explanation of the electrodynamic response in a spin-*

- liquid compound*, Phys. Rev. B 93 (2016), 081201.
- [557] T. Isono, T. Terashima, K. Miyagawa, K. Kanoda, and S. Uji, *Quantum criticality in an organic spin-liquid insulator κ -(BEDT-TTF)₂Cu₂(CN)₃*, Nat. Commun. 7 (2016), 13494.
 - [558] B. Miksch, A. Pustogow, M. Javaheri Rahim, M. Scheffler, A.A. Bardin, K. Kanoda, J.A. Schlueter, R. Hübner, and M. Dressel, *Gapped magnetic ground state in quantum spin-liquid candidate κ -(BEDT-TTF)₂Cu₂(CN)₃*, Science (2020) (in press); arXiv:2010.16155.
 - [559] M. Yamashita, N. Nakata, Y. Senshu, M. Nagata, H.M. Yamamoto, R. Kato, T. Shibauchi, and Y. Matsuda, *Highly Mobile Gapless Excitations in a Two-Dimensional Candidate Quantum Spin Liquid*, Science 328 (2010), pp. 1246–1248.
 - [560] P. Bourgeois-Hope, F. Laliberté, E. Lefrançois, G. Grissonnanche, S. Cotretde, R. Gordon, S. Kitou, H. Sawa, H. Cui, R. Kato, L. Taillefer, and N. Doiron-Leyraud, *Thermal Conductivity of the Quantum Spin Liquid Candidate EtMe₃Sb[Pd(dmit)₂]₂: No Evidence of Mobile Gapless Excitations*, Phys. Rev. X 9 (2019), 041051.
 - [561] J. Ni, B. Pan, B. Song, Y. Huang, J. Zeng, Y. Yu, E. Cheng, L. Wang, D. Dai, R. Kato, and S. Li, *Absence of Magnetic Thermal Conductivity in the Quantum Spin Liquid Candidate EtMe₃Sb[Pd(dmit)₂]₂*, Phys. Rev. Lett. 123 (2019), 247204.
 - [562] K. Padmalekha, M. Blankenhorn, T. Ivek, L. Bogani, J. Schlueter, and M. Dressel, *ESR studies on the spin-liquid candidate κ -(BEDT-TTF)₂Cu₂(CN)₃: Anomalous response below $T = 8$ K*, Physica B 460 (2015), pp. 211–213.
 - [563] R.S. Manna, M. de Souza, A. Brühl, J.A. Schlueter, and M. Lang, *Lattice Effects and Entropy Release at the Low-Temperature Phase Transition in the Spin-Liquid Candidate κ -(BEDT-TTF)₂Cu₂(CN)₃*, Phys. Rev. Lett. 104 (2010), 016403.
 - [564] M. Poirier, M. de Lafontaine, K. Miyagawa, K. Kanoda, and Y. Shimizu, *Ultrasonic investigation of the transition at 6 K in the spin-liquid candidate κ -(BEDT-TTF)₂Cu₂(CN)₃*, Phys. Rev. B 89 (2014), 045138.
 - [565] G. Baskaran, *Novel local symmetries and chiral-symmetry-broken phases in $S=(1/2)$ triangular-lattice Heisenberg model*, Phys. Rev. Lett. 63 (1989), pp. 2524–2527.
 - [566] H. Kawamura and S. Miyashita, *Phase Transition of the Two-Dimensional Heisenberg Antiferromagnet on the Triangular Lattice*, J. Phys. Soc. Jpn. 53 (1984), pp. 4138–4154.
 - [567] R. Moessner and S.L. Sondhi, *Resonating Valence Bond Phase in the Triangular Lattice Quantum Dimer Model*, Phys. Rev. Lett. 86 (2001), pp. 1881–1884.
 - [568] S.S. Lee, P.A. Lee, and T. Senthil, *Amperean Pairing Instability in the $U(1)$ Spin Liquid State with Fermi Surface and Application to κ -(BEDT-TTF)₂Cu₂(CN)₃*, Phys. Rev. Lett. 98 (2007), 067006.
 - [569] V. Galitski and Y.B. Kim, *Spin-Triplet Pairing Instability of the Spinon Fermi Surface in a $U(1)$ Spin Liquid*, Phys. Rev. Lett. 99 (2007), 266403.
 - [570] T. Grover, N. Trivedi, T. Senthil, and P.A. Lee, *Weak Mott insulators on the triangular lattice: Possibility of a gapless nematic quantum spin liquid*, Phys. Rev. B 81 (2010), 245121.
 - [571] H. Li, R.T. Clay, and S. Mazumdar, *The paired-electron crystal in the two-dimensional frustrated quarter-filled band*, J. Phys.: Condens. Matter 22 (2010), 272201.
 - [572] Y. Qi and S. Sachdev, *Insulator-metal transition on the triangular lattice*, Phys. Rev. B 77 (2008), 165112.
 - [573] R.S. Manna, M. de Souza, J.A. Schlueter, and M. Lang, *Field-induced length changes in the spin-liquid candidate κ -(BEDT-TTF)₂Cu₂(CN)₃*, phys. stat. sol. (c) 9 (2012), pp. 1180–1182.
 - [574] R.S. Manna, S. Hartmann, E. Gati, J.A. Schlueter, M. de Souza, and M. Lang, *Low-Temperature Lattice Effects in the Spin-Liquid Candidate κ -(BEDT-TTF)₂Cu₂(CN)₃*, Crystals 8 (2018), 87.
 - [575] M. Poirier, S. Parent, A. Côté, K. Miyagawa, K. Kanoda, and Y. Shimizu, *Magnetodielectric effects and spin-charge coupling in the spin-liquid candidate κ -(BEDT-TTF)₂Cu₂(CN)₃*, Phys. Rev. B 85 (2012), 134444.
 - [576] M. Abdel-Jawad, I. Terasaki, T. Sasaki, N. Yoneyama, N. Kobayashi, Y. Uesu,

- and C. Hotta, *Anomalous dielectric response in the dimer Mott insulator κ -(BEDT-TTF)₂Cu₂(CN)₃*, Phys. Rev. B 82 (2010), 125119.
- [577] K. Gregor and O.I. Motrunich, *Nonmagnetic impurities in a $S = \frac{1}{2}$ frustrated triangular antiferromagnet: Broadening of ¹³C NMR lines in κ -(ET)₂Cu₂(CN)₃*, Phys. Rev. B 79 (2009), 024421.
- [578] M. Yamashita, T. Shibauchi, and Y. Matsuda, *Thermal-Transport Studies on Two-Dimensional Quantum Spin Liquids*, ChemPhysChem 13 (2012), pp. 74–78.
- [579] S. Nakajima, T. Suzuki, Y. Ishii, K. Ohishi, I. Watanabe, T. Goto, A. Oosawa, N. Yoneyama, N. Kobayashi, F. L. Pratt, and T. Sasaki, *Microscopic Phase Separation in Triangular-Lattice Quantum Spin Magnet κ -(BEDT-TTF)₂Cu₂(CN)₃ Probed by Muon Spin Relaxation*, J. Phys. Soc. Jpn. 81 (2012), 063706.
- [580] F.L. Pratt, P.J. Baker, S.J. Blundell, T. Lancaster, S. Ohira-Kawamura, C. Baines, Y. Shimizu, K. Kanoda, I. Watanabe, and G. Saito, *Magnetic and non-magnetic phases of a quantum spin liquid*, Nature 471 (2011), p. 612–616.
- [581] M. Dumm, A. Loidl, B.W. Fravel, K.P. Starkey, L.K. Montgomery, and M. Dressel, *Electron spin resonance studies on the organic linear-chain compounds (TMTCF)₂X (C=S,Se; X=PF₆,AsF₆,ClO₄,Br)*, Phys. Rev. B 61 (2000), pp. 511–521.
- [582] Á. Antal, T. Fehér, A. Jánossy, E. Tátrai-Szekeres, and F. Fülöp, *Spin Diffusion and Magnetic Eigenoscillations Confined to Single Molecular Layers in the Organic Conductors κ -(BEDT-TTF)₂Cu[N(CN)₂]X (X = Cl, Br)*, Phys. Rev. Lett. 102 (2009), 086404.
- [583] Á. Antal, T. Fehér, N. Yoneyama, L. Forró, T. Sasaki, and A. Jánossy, *Spin and Charge Transport in the X-ray Irradiated Quasi-2D Layered Compound: κ -(BEDT-TTF)₂Cu[N(CN)₂]Cl*, Crystals 2 (2012), pp. 579–589.
- [584] Á. Antal, T. Fehér, B. Náfrádi, L. Forró, and A. Jánossy, *Two-dimensional Magnetism in κ -(BEDT-TTF)₂Cu[N(CN)₂]Cl, a Spin-1/2 Heisenberg Antiferromagnet with Dzyaloshinskii–Moriya Interaction*, J. Phys. Soc. Jpn. 84 (2015), 124704.
- [585] Y. Shimizu, H. Akimoto, H. Tsujii, A. Tajima, and R. Kato, *Mott Transition in a Valence-Bond Solid Insulator with a Triangular Lattice*, Phys. Rev. Lett. 99 (2007), 256403.
- [586] M. Tamura and R. Kato, *Variety of valence bond states formed of frustrated spins on triangular lattices based on a two-level system Pd(dmit)₂*, Sci. Techn. Adv. Mat. 10 (2009), 024304.
- [587] L. Liu, H. Shao, Y.C. Lin, W. Guo, and A.W. Sandvik, *Random-Singlet Phase in Disordered Two-Dimensional Quantum Magnets*, Phys. Rev. X 8 (2018), 041040.
- [588] K. Uematsu and H. Kawamura, *Randomness-Induced Quantum Spin Liquid Behavior in the $s = 1/2$ Random-Bond Heisenberg Antiferromagnet on the Pyrochlore Lattice*, Phys. Rev. Lett. 123 (2019), 087201.
- [589] C. Hotta, *Quantum electric dipoles in spin-liquid dimer Mott insulator κ -ET₂Cu₂(CN)₃*, Phys. Rev. B 82 (2010), 241104.
- [590] K. Yakushi, K. Yamamoto, T. Yamamoto, Y. Saito, and A. Kawamoto, *Raman Spectroscopy Study of Charge Fluctuation in the Spin-Liquid Candidate κ -(BEDT-TTF)₂Cu₂(CN)₃*, J. Phys. Soc. Jpn. 84 (2015), 084711.
- [591] Y. Nakamura, T. Hiramatsu, Y. Yoshida, G. Saito, and H. Kishida, *Optical Properties of a Quantum Spin Liquid Candidate Material, κ -(BEDT-TTF)₂Ag₂(CN)₃*, J. Phys. Soc. Jpn. 86 (2017), 014710.
- [592] M. Urai, K. Miyagawa, T. Sasaki, H. Taniguchi, and K. Kanoda, *Quantum Disordering of an Antiferromagnetic Order by Quenched Randomness in an Organic Mott Insulator*, Phys. Rev. Lett. 124 (2020), 117204.
- [593] Y. Saito, H. Nakamura, M. Sawada, T. Yamazaki, S. Fukuoka, N. Matsunaga, K. Nomura, M. Dressel, and A. Kawamoto, *Disordered quantum spin state in the stripe lattice system consisting of triangular and square tilings*, arXiv:1910.09963 (2019).
- [594] P. Szirmai, C. Mézière, G. Bastien, P. Wzietek, P. Batail, E. Martino, K. Mantulnikovs, A. Pisoni, K. Riedl, S. Cottrell, L.F. Christopher Baines, and B. Náfrádi, *Quantum spin liquid state in a hybrid of organic conductor and molecular rotor*, Proc. Nat. Acad. Sci.

- (2020) (in press).
- [595] C. Lemouchi, C. Mézière, L. Zorina, S. Simonov, A. Rodríguez-Forteza, E. Canadell, P. Wzietek, P. Auban-Senzier, C. Pasquier, T. Giamarchi, M.A. Garcia-Garibay, and P. Batail, *Design and Evaluation of a Crystalline Hybrid of Molecular Conductors and Molecular Rotors*, J. Am. Chem. Soc. 134 (2012), pp. 7880–7891.
- [596] C. Lemouchi, K. Iliopoulos, L. Zorina, S. Simonov, P. Wzietek, T. Cauchy, A. Rodríguez-Forteza, E. Canadell, J. Kaleta, J. Michl, D. Gindre, M. Chrysos, and P. Batail, *Crystalline Arrays of Pairs of Molecular Rotors: Correlated Motion, Rotational Barriers, and Space-Inversion Symmetry Breaking Due to Conformational Mutations*, J. Am. Chem. Soc. 135 (2013), pp. 9366–9376.
- [597] E. Kermarrec, P. Mendels, F. Bert, R.H. Colman, A.S. Wills, P. Strobel, P. Bonville, A. Hillier, and A. Amato, *Spin-liquid ground state in the frustrated kagome antiferromagnet MgCu₃(OH)₆Cl₂*, Phys. Rev. B 84 (2011), 100401.
- [598] B. Fåk, E. Kermarrec, L. Messio, B. Bernu, C. Lhuillier, F. Bert, P. Mendels, B. Koteswararao, F. Bouquet, J. Ollivier, A.D. Hillier, A. Amato, R.H. Colman, and A.S. Wills, *Kapellasite: A Kagome Quantum Spin Liquid with Competing Interactions*, Phys. Rev. Lett. 109 (2012), 037208.
- [599] L. Clark, J.C. Orain, F. Bert, M.A. De Vries, F.H. Aidoudi, R.E. Morris, P. Lightfoot, J.S. Lord, M.T.F. Telling, P. Bonville, J.P. Attfield, P. Mendels, and A. Harrison, *Gapless Spin Liquid Ground State in the S = 1/2 Vanadium Oxyfluoride Kagome Antiferromagnet [NH₄]₂[C₇H₄N][V₇O₆F₁₈]*, Phys. Rev. Lett. 110 (2013), 207208.
- [600] A. Zorko, M. Herak, M. Gomilšek, J. Tolvan, M. Velázquez, P. Khuntia, F. Bert, and P. Mendels, *Symmetry Reduction in the Quantum Kagome Antiferromagnet Herbertsmithite*, Phys. Rev. Lett. 118 (2017), 017202.
- [601] P. Khuntia, M. Velazquez, Q. Barthélemy, F. Bert, E. Kermarrec, A. Legros, B. Bernu, L. Messio, A. Zorko, and P. Mendels, *Gapless ground state in the archetypal quantum kagome antiferromagnet ZnCu₃(OH)₆Cl₂*, Nat. Phys. 16 (2020), pp. 469–474.
- [602] M. Klanjšek, A. Zorko, R. Žitko, J. Mravlje, Z. Jagličić, P. Kumar Biswas, P. Prelovšek, D. Mihailovic, and D. Arčon, *A high-temperature quantum spin liquid with polaron spins*, Nat. Phys. 13 (2017), pp. 1130–1134.
- [603] S.P. Shen, J.C. Wu, J.D. Song, X.F. Sun, Y.F. Yang, Y.S. Chai, D. Shang, S.G. Wang, J.F. Scott, and Y. Sun, *Quantum electric-dipole liquid on a triangular lattice*, Nat. Commun. 7 (2016), 10569.
- [604] B. Powell, *The expanding materials multiverse*, Science 360 (2018), pp. 1073–1074.
- [605] N.A. Spaldin and M. Fiebig, *The Renaissance of Magnetoelectric Multiferroics*, Science 309 (2005), pp. 391–392.
- [606] S. Dong, J.M. Liu, S.W. Cheong, and Z. Ren, *Multiferroic materials and magnetoelectric physics: symmetry, entanglement, excitation, and topology*, Adv. Phys. 64 (2015), pp. 519–626.
- [607] N.A. Spaldin, *Multiferroics beyond electric-field control of magnetism*, Proc. R. Soc. A 476 (2020), 20190542.
- [608] P. Lunkenheimer, J. Müller, S. Krohns, F. Schrettle, A. Loidl, B. Hartmann, R. Rommel, M. de Souza, C. Hotta, J. Schlueter, and M. Lang, *Multiferroicity in an organic charge-transfer salt that is suggestive of electric-dipole-driven magnetism*, Nat. Mater. 11 (2012), pp. 755–758.
- [609] M. Lang, P. Lunkenheimer, J. Müller, A. Loidl, B. Hartmann, N.H. Hoang, E. Gati, H. Schubert, and J.A. Schlueter, *Multiferroicity in the Mott Insulating Charge-Transfer Salt κ - (BEDT - TTF)₂Cu[N(CN)₂]Cl*, IEEE Trans. Magn. 50 (2014), pp. 1–7.
- [610] M. Pinterić, D. Rivas Góngora, v. Rapljenović, T. Ivek, M. Čulo, B. Korin-Hamzić, O. Milat, B. Gumhalter, P. Lazić, M. Sanz Alonso, W. Li, A. Pustogow, G. Gorgen Lesseux, M. Dressel, and S. Tomić, *Electrodynamics in Organic Dimer Insulators Close to Mott Critical Point*, Crystals 8 (2018), 190.
- [611] C. Hotta, *Classification of Quasi-Two Dimensional Organic Conductors Based on a New Minimal Model*, J. Phys. Soc. Jpn. 72 (2003), pp. 840–853.

- [612] M. Pinterić, M. Miljak, N. Biškup, O. Milat, I. Aviani, S. Tomić, D. Schweitzer, W. Strunz, and I. Heinen, *Magnetic anisotropy and low-frequency dielectric response of weak ferromagnetic phase in κ -(BEDT-TTF)₂Cu[N(CN)₂]Cl, where BEDT-TTF is Bis(ethylenedithio)tetrathiafulvalene*, Euro. Phys. J. B 11 (1999), pp. 217–225.
- [613] S. Tomić, M. Pinterić, T. Ivek, K. Sedlmeier, R. Beyer, D. Wu, J.A. Schlueter, D. Schweitzer, and M. Dressel, *Magnetic ordering and charge dynamics in κ -(BEDT-TTF)₂Cu[N(CN)₂]Cl*, J. Phys.: Condens. Matter 25 (2013), 436004.
- [614] S. Iguchi, S. Sasaki, N. Yoneyama, H. Taniguchi, T. Nishizaki, and T. Sasaki, *Relaxor ferroelectricity induced by electron correlations in a molecular dimer Mott insulator*, Phys. Rev. B 87 (2013), 075107.
- [615] A.C. Jacko, E.P. Kenny, and B.J. Powell, *Interplay of dipoles and spins in κ -(BEDT-TTF)₂X, where X = Hg(SCN)₂Cl, Hg(SCN)₂Br, Cu[N(CN)₂]Cl, Cu[N(CN)₂]Br, and Ag₂(CN)₃*, Phys. Rev. B 101 (2020), 125110.
- [616] S. Dayal, R.T. Clay, H. Li, and S. Mazumdar, *Paired electron crystal: Order from frustration in the quarter-filled band*, Phys. Rev. B 83 (2011), 245106.
- [617] R.T. Clay, S. Dayal, H. Li, and S. Mazumdar, *Beyond the quantum spin liquid concept in frustrated two dimensional organic superconductors*, phys. stat. sol. (b) 249 (2012), pp. 991–994.
- [618] H. Fukuyama, J.i. Kishine, and M. Ogata, *Energy Landscape of Charge Excitations in the Boundary Region between Dimer–Mott and Charge Ordered States in Molecular Solids*, J. Phys. Soc. Jpn. 86 (2017), 123706.
- [619] K. Itoh, H. Itoh, M. Naka, S. Saito, I. Hosako, N. Yoneyama, S. Ishihara, T. Sasaki, and S. Iwai, *Collective Excitation of an Electric Dipole on a Molecular Dimer in an Organic Dimer-Mott Insulator*, Phys. Rev. Lett. 110 (2013), 106401.
- [620] P. Lazić, M. Pinterić, D. RivasGongora, A. Pustogow, K. Treptow, T. Ivek, O. Milat, B. Gumhalter, N. Došlić, M. Dressel, and S. Tomić, *Importance of van der Waals interactions and cation-anion coupling in an organic quantum spin liquid*, Phys.Rev.B 97 (2018), 245134.
- [621] M. Abdel-Jawad, N. Tajima, R. Kato, and I. Terasaki, *Disordered conduction in single-crystalline dimer Mott compounds*, Phys. Rev. B 88 (2013), 075139.
- [622] T. Kawamoto, T. Mori, K. Takimiya, Y. Kataoka, Y. Aso, and T. Otsubo, *Organic superconductor with an incommensurate anion structure: (MDT-TSF)(AuI₂)_{0.44}*, Phys. Rev. B 65 (2002), 140508.
- [623] M. Matsuura, T. Sasaki, S. Iguchi, E. Gati, J. Müller, O. Stockert, A. Piovano, M. Böhm, J.T. Park, S. Biswas, S.M. Winter, R. Valentí, A. Nakao, and M. Lang, *Lattice Dynamics Coupled to Charge and Spin Degrees of Freedom in the Molecular Dimer-Mott Insulator κ -(BEDT-TTF)₂Cu[N(CN)₂]Cl*, Phys. Rev. Lett. 123 (2019), 027601.
- [624] Y. Yoshida, H. Ito, M. Maesato, Y. Shimizu, H. Hayama, T. Hiramatsu, Y. Nakamura, H. Kishida, T. Koretsune, C. Hotta, and G. Saito, *Spin-disordered quantum phases in a quasi-one-dimensional triangular lattice*, Nat. Physics 11 (2015), pp. 679–685.
- [625] H. Kamo, A. Ueda, T. Isono, K. Takahashi, and H. Mori, *Synthesis and properties of catechol-fused tetrathiafulvalene derivatives and their hydrogen-bonded conductive charge-transfer salts*, Tetrahedron Lett. 53 (2012), pp. 4385–4388.
- [626] T. Tsumuraya, H. Seo, R. Kato, and T. Miyazaki, *First-principles study of hydrogen-bonded molecular conductor κ -H₃(Cat-EDT-TTF/ST)₂*, Phys. Rev. B 92 (2015), 035102.
- [627] A. Ueda, K. Kishimoto, Y. Sunairi, J. Yoshida, H. Yamakawa, T. Miyamoto, T. Terashige, H. Okamoto, and H. Mori, *Hysteretic Current–Voltage Characteristics in the Deuterium-Dynamics-Triggered Charge-Ordered Phase of κ -D₃(Cat-EDT-TTF)₂*, J. Phys. Soc. Jpn. 88 (2019), 034710.
- [628] D. Starešinić, K. Biljaković, W. Brütting, K. Hosseini, P. Monceau, H. Berger, and F. Levy, *Wide-temperature-range dielectric response of the charge-density-wave system TaS₃*, Phys. Rev. B 65 (2002), 165109.
- [629] K. Biljaković, D. Starešinić, J. Lasjaunias, G. Reményi, R. Mélin, P. Monceau, and S. Sahling, *Charge density glass dynamics – Soft potentials and soft modes*, Physica B 407

- (2012), pp. 1741–1745.
- [630] G. Reményi, S. Sahling, K. Biljaković, D. Starešinić, J.C. Lasjaunias, J. Lorenzo, P. Monceau, and A. Cano, *Incommensurate Systems as Model Compounds for Disorder Revealing Low-Temperature Glasslike Behavior*, Phys. Rev. Lett. 114 (2015), 195502.
- [631] J. Schroeder, W. Wu, J. Apkarian, M. Lee, L. Hwa, and C. Moynihan, *Raman scattering and Boson peaks in glasses: temperature and pressure effects*, J. Non-Cryst. Solids 349 (2004), pp. 88–97.
- [632] T. Nakayama, *Boson peak and terahertz frequency dynamics of vitreous silica*, Rep. Prog. Phys. 65 (2002), pp. 1195–1242.
- [633] M. Hemmida, H.A. Krug von Nidda, B. Miksch, L.L. Samoilenko, A. Pustogow, S. Widmann, A. Henderson, T. Siegrist, J.A. Schlueter, A. Loidl, and M. Dressel, *Weak ferromagnetism and glassy state in κ -(BEDT-TTF)₂Hg(SCN)₂Br*, Phys. Rev. B 98 (2018), 241202.
- [634] M. Ando, O. Benzine, Z. Pan, J.L. Garden, K. Wondraczek, S. Grimm, K. Schuster, and L. Wondraczek, *Boson peak, heterogeneity and intermediate-range order in binary SiO₂-Al₂O₃ glasses*, Sci.Rep. 8 (2018), 5394.
- [635] J. Merino, A. Greco, R.H. McKenzie, and M. Calandra, *Dynamical properties of a strongly correlated model for quarter-filled layered organic molecular crystals*, Phys. Rev. B 68 (2003), 245121.
- [636] M. Dressel, N. Drichko, J. Schlueter, and J. Merino, *Proximity of the Layered Organic Conductors α -(BEDT-TTF)₂MHg(SCN)₄ ($M = K, NH_4$) to a Charge-Ordering Transition*, Phys. Rev. Lett. 90 (2003), 167002.
- [637] M. Dressel, N. Drichko, and S. Kaiser, *Collective charge-order excitations*, Physica C 470 (2010), pp. S589–S591.
- [638] M. Naka and S. Ishihara, *Quantum melting of magnetic order in an organic dimer Mott-insulating system*, Phys. Rev. B 93 (2016), 195114.
- [639] S. Yasin, E. Rose, M. Dumm, N. Drichko, M. Dressel, J. Schlueter, E. Zhilyaeva, S. Torunova, and R. Lyubovskaya, *Electronic and magnetic studies of κ -(BEDT-TTF)₂Hg(SCN)₂Cl*, Physica B 407 (2012), pp. 1689–1691.
- [640] A. Pustogow, T. Le, H.H. Wang, Y. Luo, E. Gati, H. Schubert, M. Lang, and S.E. Brown, *Impurity moments conceal low-energy relaxation of quantum spin liquids*, Phys. Rev. B 101 (2020), 140401.
- [641] J.M. Williams, A.M. Kini, H.H. Wang, K.D. Carlson, U. Geiser, L.K. Montgomery, G.J. Pyrka, D.M. Watkins, J.M. Kommers, S.J. Boryschuk, A.V.S. Crouch, W.K. Kwok, J.E. Schirber, D.L. Overmyer, D. Jung, and M.H. Whangbo, *From Semiconductor Semiconductor Transition (42 K) to the Highest-12.5 K Organic Superconductor, κ -(ET)₂Cu[N(CN)₂]Cl*, Inorg. Chem. 29 (1990), pp. 3272–3274.
- [642] U. Welp, S. Fleshler, W.K. Kwok, G.W. Crabtree, K.D. Carlson, H.H. Wang, U. Geiser, J.M. Williams, and V.M. Hitsman, *Weak ferromagnetism in κ -(ET)₂Cu[N(CN)₂]Cl, where (ET) is bis(ethylenedithio)tetrathiafulvalene*, Phys. Rev. Lett. 69 (1992), pp. 840–843.
- [643] K. Miyagawa, A. Kawamoto, Y. Nakazawa, and K. Kanoda, *Antiferromagnetic Ordering and Spin Structure in the Organic Conductor, κ -(BEDT-TTF)₂Cu[N(CN)₂]Cl*, Phys. Rev. Lett. 75 (1995), pp. 1174–1177.
- [644] T. Le, A. Pustogow, J. Wang, A. Henderson, J.A. Schlueter, and S.E. Brown, *Evidence of Slowing Magnetic Dynamics in κ -(BEDT-TTF)₂Hg(SCN)₂Br*, (2020), unpublished.